Influence of 3D Thermal Radiation on Cloud Development

Carolin Klinger

München 2015

Influence of 3D Thermal Radiation on Cloud Development

Carolin Klinger

Dissertation
an der Fakultät für Physik
der Ludwig–Maximilians–Universität
München

vorgelegt von
Carolin Klinger
aus Augsburg

München, Dezember 2015

Erstgutachter: Prof. Dr. Bernhard Mayer
Zweitgutachter: Prof. Dr. Markus Rapp
Tag der mündlichen Prüfung: 21.12.2015

Zusammenfassung

Hat dreidimensionaler (3D) thermischer Strahlungstransport einen Effekt auf die Wolkenentwicklung und muss thermischer 3D Strahlungstransport daher in wolkenauflösenden numerischen Modellen berücksichtigt werden? Welchen Einfluss haben 3D Erwärmungs- und Abkühlungsraten auf die Entwicklung von Wolken im Vergleich zu herkömmlichen eindimensionalen (1D) Approximationen? Zur Beantwortung dieser Fragen muss eine schnelle, aber dennoch möglichst genaue 3D Strahlungstransportparametrisierung an ein wolkenauflösendes numerisches Model gekoppelt werden. Zunächst wurde eine exakte Methode zur Berechnung dreidimensionaler thermischer Erwärmungs- und Abkühlungsraten entwickelt. Die Ergebnisse der Monte Carlo Simulationen dienten als Referenzwert um die 'Neighboring Column Approximation' (NCA) zu entwickeln. Die NCA wurde anschließend an das UCLA-LES, ein Grobstrukturmodel, gekoppelt. Somit konnten Effekte von 3D Erwärmungs- und Abkühlungsraten im Vergleich zu 1D Approximationen untersucht werden.
Zuerst wurden Unterschiede von 1D und 3D thermischen Erwärmungs- und Abkühlungsraten an Wolken untersucht. Hierfür wurden effiziente Monte Carlo Varianz-Reduktions Methoden entwickelt und in MYSTIC, ein Monte Carlo Strahlungstransportmodell implementiert. Mit den neu entwickelten Methoden ist es möglich, physikalisch korrekte 3D Erwärmungs- und Abkühlungsraten zu berechnen. Die Abhängigkeit von 1D und 3D Erwärmungs- und Abkühlungsraten von der Wolkengeometrie wurde am Beispiel einfacher geometrischer Wolkenformen (Würfel, Halbkugel) und Simulationen realistischer Wolkenfelder analysiert. Bei einer Modellauflösung von etwa 50 m bis 200 m konnten Abkühlungsraten von mehreren 100 K/d am Wolkenoberrand sowie einigen 10 bis 100 K/d an den Wolkenseiten gefunden werden. Die Abkühlung an den Wolkenseiten ist ein 3D Effekt, der von 1D Strahlungstransportlösungen nicht reproduziert wird. Am Wolkenboden ließen sich Erwärmungsraten von einigen 10 K/d feststellen. Erwärmungs- und Abkühlungsraten hängen von der Lage der Wolke in der Atmosphäre, dem Flüssigwassergehalt der Wolke, der Form der Wolke und der Geometrie des Wolkenfeldes (zum Beispiel dem Abstand zwischen Wolken) ab.
Basierend auf den Ergebnissen der exakten Erwärmungs- und Abkühlungsratensimulationen, wurde eine 3D Parametrisierung für thermische 3D Erwärmungs- und Abkühlungsraten entwickelt. Diese Parametrisierung, die 'Neighboring Column Approximation' (NCA), basiert auf einer 1D Strahlungstransportlösung und nutzt nur die direkten Nachbarsäulen einer Säule um die Erwärmungs- und Abkühlungsraten zu bestimmen. Die Methode kann in parallelisierten Wolkenmodellen verwendet werden. Mit der NCA ist es möglich, 3D Erwärmungs- und Abkühlungsraten an Wolkenseiten zu berechnen. Es wurde gezeigt, dass die Rechenzeit einer LES-Simulation nur um einen Faktor von 1.5 - 2 steigt, wenn die NCA anstelle einer herkömmlichen 1D Strahlungstransportlösung verwendet wird.

Die NCA wurde in das UCLA-LES implementiert. Mit dem UCLA-LES und der NCA war es zum ersten Mal möglich, die Effekte interaktiver thermischer 3D Strahlung auf die Entwicklung von Wolken zu untersuchen. Hierfür wurden Simulationen ohne Strahlung, mit 1D thermischer Strahlung und mit 3D thermischer Strahlung (NCA) durchgeführt und Unterschiede ermittelt. Zunächst wurden isolierte, einzelne Wolken untersucht. Insgesamt konnte gezeigt werden, dass ein genereller Einfluss von thermischer Strahlung auf Wolkenbildung und Wolkenentwicklung besteht. Abhängig von der Form der Wolke hat 3D thermische Strahlung die Entwicklung der Wolke beeinflusst oder den gleichen Effekt gezeigt, wie 1D thermische Strahlung. Einer der Hauptunterschiede in der Wolkenentwicklung beim Vergleich von Simulationen mit und ohne thermische Strahlung ist eine verstärkte Wolkenzirkulation, mit stärkeren Aufwinden in der Wolke und stärkeren Abwinden an der Wolkenseite. Diese veränderte Zirkulation führt zunächst zu einem verstärkten Wolkenwachstum, am Ende aber auch zu einer schnelleren Auflösung der Wolke.
Des weiteren wurden Simulationen eines Kumuluswolkenfeldes in einem 25 x 25 km^2 großen Gebiet mit 100 m horizontaler Auflösung analysiert. Zum ersten Mal konnte ein Wolkenfeld dieser Größe mit interaktiver 3D Strahlung simuliert werden. Im Mittel verstärken sich aufgrund thermischer Strahlung Auf- und Abwinde und Wolken wiesen einen erhöhten Flüssigwassergehalt auf. In der statistischen Analyse verschiedener Variablen zeigte sich, dass Wolken unter dem Einfluss von thermischer Strahlung horizontal ausgedehnter sind. Unter dem Einfluss von 3D thermischer Strahlung organisierten sich die Wolken bereits nach wenigen Stunden. Dies ist ein Hinweis darauf, dass konvektive Organisation durch den Einfluss 3D thermischer Strahlung beschleunigt werden könnte. Ein signifikanter Unterschied zwischen 1D und 3D thermischer Strahlung konnte in der statistischen Analyse anderer Variablen (wie zum Beispiel Flüssigwassergehalt oder Bedeckungsgrad) nicht gezeigt werden, aber ein genereller Effekt von thermischer Strahlung besteht.

Abstract

This thesis aims to answer the question if 3D effects of thermal radiative transfer need to be considered in cloud resolving simulations and if an influence of 3D thermal heating and cooling rates exists in contrast to common 1D approximations. To study this question with the help of a cloud resolving model, an accurate, yet fast parameterization of 3D radiative transfer is needed. First, an accurate 3D Monte Carlo model was developed which was used as benchmark for developing the fast 'Neighboring Column Approximation' (NCA), which was then coupled to the UCLA-LES to study the effects of 3D thermal heating and cooling rates in comparison to common 1D radiative transfer approximations.

First, differences between common 1D radiative transfer approximations and a correct 3D radiative transfer model were analyzed. For this, efficient Monte Carlo variance reduction methods have been developed and implemented in MYSTIC, a Monte Carlo radiative transfer model. The dependence of 1D and 3D heating and cooling rates on cloud geometry has been investigated by analyzing idealized clouds such as cubes or half spheres. Further more, 1D and 3D heating and cooling rates in realistic cloud fields were simulated and compared. It could be shown that cooling rates reach maximum values of several 100 K/d at cloud tops if the model resolution was between 50 m to 200 m. Additional cloud side cooling of several 10 to 100 K/d was found in 3D heating and cooling rate simulations. At the cloud bottom, modest warming of a few 10 K/d occurs. Heating and cooling rates depend on the vertical location of the cloud in the atmosphere, the liquid water content of the cloud, the shape of the cloud and the geometry of the cloud field (for example the distance between clouds).

Based on the results of a detailed analysis of exact simulations of 3D thermal heating and cooling rates, a fast, but still accurate 3D parameterization for thermal heating and cooling rates has been developed. This parameterization, the 'Neighboring Column Approximation' (NCA), is based on a 1D radiative transfer solution and uses the next neighboring columns of a column to estimate the 3D heating or cooling rate. The method can be used in parallelized models. With the NCA, it is possible to simulate 3D cloud side cooling and warming. It was shown that the NCA is a factor of 1.5 to 2 more expensive in terms of computational time when used in a cloud resolving model, compared to a 1D radiative transfer approximation.

The NCA was implemented in UCLA-LES, a cloud resolving, large-eddy simulation model. With the UCLA-LES and the NCA it was possible for the first time to study the effects of 3D interactive thermal radiation on cloud development. Simulations without radiation, with 1D thermal radiation and 3D thermal (NCA) radiation have been performed and differences have been analyzed. First, single, isolated clouds were investigated. Depending on the cloud shape, 3D thermal radiation changes cloud development in comparison to 1D thermal radiation. Overall it could be shown that a thermal radiation effect on cloud development exists

in general. Whether there is a differences between 1D and 3D thermal radiation on cloud development seems to depend on the specific situation. One of the main features of thermal radiation affecting a single cloud is a change in the cloud circulation. Stronger updrafts in the cloud core and stronger downdrafts at the cloud sides were found, causing an enhanced cloud development at first, but a faster decay of the cloud in the end.
Second, large scale simulations of a shallow cumulus cloud field in a 25 x 25 km^2 domain with 100 m horizontal resolution were analyzed. To the authors knowledge, this is the first time that a cloud field of this size and resolution was simulated including 3D interactive thermal radiation. It was shown that on average, updrafts, downdrafts and liquid water increases if thermal radiation is accounted for. While most variables (for example liquid water mixing ratio or cloud cover) did not show significant systematic difference between no-radiation simulation and the simulations with 1D and 3D thermal radiation, the cloud size (or horizontal extent) was larger in the simulations with interactive 3D thermal radiation. Convective organization set in after a few hours already. This is a clear indication that 3D thermal radiation could trigger convective organization.

Contents

Chapter 1

Introduction

When looking at the sky, one can hardly avoid seeing a cloud. Clouds are something common and usual to us, they often seem to be static. Looking at clouds for a longer time than just a short glimpse, it is obvious that clouds are by no means static. They are rather very dynamic and variable features at the sky. Many processes affect cloud formation and development. Due to the complexity of the Earth atmosphere system, simulating clouds and cloud development is a challenging task.

Clouds remain one of the biggest sources of uncertainty in climate and weather prediction (Boucher et al., 2013). Just recently, Bony et al. (2015) pointed out four key questions for a better understanding of climate prediction, in which clouds play the key role. Clouds strongly affect the energy budget in the atmosphere and transport heat and water by condensation and precipitation. Clouds feed back on the Earth's energy budget and therefore on surface temperature. They play an important but yet poorly quantified role in climate change. Model resolution and associated computational costs are the main source for the uncertainty in predicting cloud feedback. Today's climate models are run on a resolution of about 100 km in the horizontal, weather forecasting models on about 10 km, and regional weather forecasting models on about 3 km. It is obvious that clouds, which have a size of a few 100 meters to kilometers, can not be resolved if the grid box size is larger than the cloud itself. Higher model resolutions for large scale simulation are computationally too expensive to be performed even on today's supercomputers. It is therefore necessary to parameterize cloud processes in current weather prediction and climate models. To further improve weather and climate prediction, it is essential to improve the existing cloud and radiation parameterizations in numerical weather prediction and climate models.

One of the physical features affecting the development of clouds is radiation. Solar and thermal radiation drive weather and climate and strongly affect cloud formation. In the solar spectral range, radiation passes through the atmosphere and heats the surface. The near surface atmospheric air is heated and due to the lower density of warmer air, this air starts to rise. The thus generated updrafts transport moist air which condenses while rising and eventually forms clouds and precipitation. At the point in time when a cloud forms, this updraft can be weakened by the reduction of the irradiance at the surface. This reduced irradiance is caused by the shadow of the cloud or neighboring clouds. Next to the surface effect of radiation, absorption and emission of radiation occur in the atmosphere which is usually described by

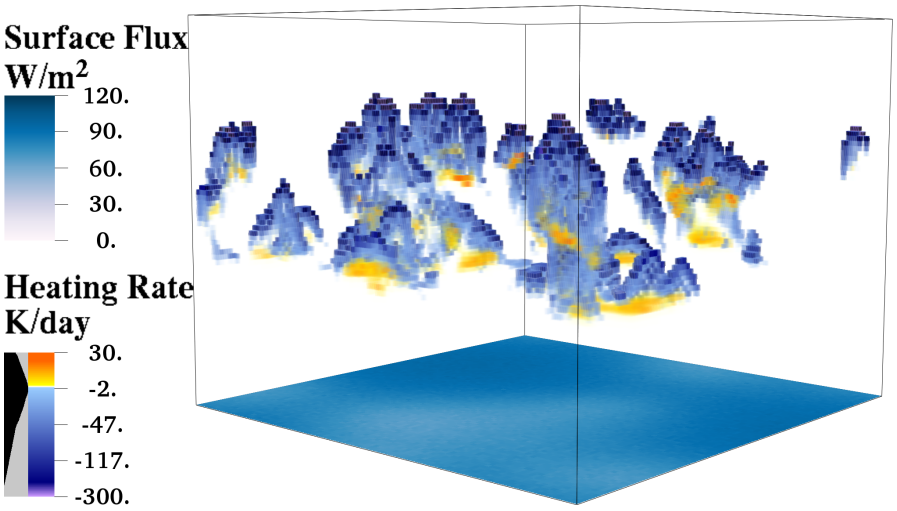

Figure 1.1: Thermal heating and cooling rates in a large eddy simulation cloud field and net surface irradiance in a 6.5 x 6.5 km^2 domain. The radiation simulation is performed with the Monte Carlo radiative transfer model MYSTIC (Mayer, 2009). The model resolution of the cloud is 66 m in the horizontal and 40 m in the vertical.

heating and cooling rates. These heating and cooling rates result from emitted and absorbed solar and thermal irradiance in the atmosphere. While the atmosphere absorbs solar radiation (which results in heating rates), it emits radiation in the thermal spectral range (resulting in cooling rates). The net result of both effects is a cooling of about 1 - 2 K/d in the atmosphere. However, heating or cooling rates can become orders of magnitude larger (several 100 K/d) at the interface between cloud and atmosphere. In the solar spectral range, the feedback onto the cloud is a warming at the illuminated cloud side. In the thermal spectral range strong cooling at the cloud top and cloud sides as well as modest warming at the cloud bottom occur. While there is a strong difference in surface irradiance in the solar spectral range due to the shadows at the surface (+/- some 100 W/m^2), the surface effect in the thermal spectral range remains small (+/- 30 W/m^2). The effects of thermal radiation are visualized in Figure 1.1.
Accurate radiative transfer models exist to calculate 3D heating and cooling rates (for example MYSTIC (Mayer, 2009), SHDOM (Evans, 1998)). These are often based on the Monte Carlo method and are computationally too expensive to be used to calculate diabatic heating (gain or loss of heat of a volume) in cloud resolving models. Due to the complexity and the computational cost of accurate 3D radiative transport, radiation is often treated poorly in todays cloud resolving models. At best, radiation is treated using a plane-parallel 1D approximation which neglects horizontal radiation transport.
Thermal radiation affects clouds in two different ways. First, radiation affects cloud dynamics. Former studies using 1D radiative transfer codes found that thermal cooling increases the liquid water content of clouds. In addition, the radiative cooling increases downward motion at the cloud sides, causing low level convergence which enhances vertical development in the cloud (Guan et al., 1995, 1997). Second, radiation changes cloud microphysical processes. Harrington et al. (2000) showed that thermal emission enhances cloud droplet growth. Furthermore, the critical supersaturation for cloud droplets is reduced by thermal cooling

(Marquis and Harrington, 2005) and collision and coalescence start earlier if thermal emission is accounted for (Hartman and Harrington, 2005a,b). Possibly, the radiative effect on droplet growth could close the existing gap in diffusional droplet growth theory. Diffusional droplet growth slows down considerably once a droplet has reached a size of 5 - 10 μm. However, the process of collision and coalescence becomes significant only for droplets with a size of at least 20 μm (Rogers, 1979).

The strengthened cooling of 3D thermal radiative transfer motivates to reexamine the influence of radiative cooling on clouds, to improve cloud, microphysics and radiation parameterizations in today's weather forecast and climate models. To my best knowledge, systematic studies of the 3D radiation effects have not been possible due to the lack of 3D radiation parameterizations and the high computational costs. Due to recent advances in supercomputing, such studies become feasible, but nevertheless require fast 3D radiation parameterizations.

This thesis focuses on the effect of thermal, especially 3D thermal radiative transfer and its influence on cloud development. The question if and how (3D) thermal radiation affects cloud development has to be answered. First, accurate benchmark results of the 3D thermal heating and cooling rates at clouds have to be identified. For this first essential step, the Monte Carlo Model MYSTIC (Monte Carlo code for the phYSically correct Tracing of photons In Cloudy atmospheres; Mayer (2009)) has been enhanced with different Monte Carlo methods to calculate 3D thermal heating rates. With the updated model, it is possible to study the 3D effects and important characteristics of thermal radiation which is a necessary step for the development of a 3D parameterization. Therefore, in a second step, such a parameterization was developed. The so called 'Neighboring Column Approximation' (NCA), a reasonable accurate and fast method for the calculation of 3D thermal heating rates can be used in cloud resolving models. This parameterization allows for the first time to study 3D thermal radiation effects on the evolution of clouds in detail. For this last step, the parameterization was implemented into the UCLA-LES, a large eddy simulation (LES), cloud resolving model. A multitude of simulations with varying degree of complexity were performed for the investigation of the radiation-cloud effects.

Chapter 2

Scientific Background

The Earth atmosphere system is a complex, non-linear system. The characteristics of this system are determined by atmosphere, ocean, ice, land surfaces, and the biosphere which interact with each other. Different forcings either of natural or anthropogenic origin affect the system and therefore weather and climate. While climate represents the mean state of the Earth atmosphere system (usually as an average over 30 years), weather takes place on much shorter time scales (within a few days). Mark Twain has been quoted: *climate is what you expect, weather is what you get.* To understand climate and weather, many processes and their interactions with each other have to be understood and considered. These processes include for example radiative transfer in the atmosphere, thermodynamics, fluid dynamics, and cloud physics.

Weather and climate are predicted with numerical models. Those numerical models solve differential equations that govern the physics of the Earth's atmosphere and their interactions (namely the Navier Stokes Equation, the continuity equation, the first law of thermodynamics, and the ideal gas law). Processes and the physics involved in the Earth atmosphere system have to be understood in order to parameterize them correctly in a numerical model. With increasing knowledge, current parameterizations in weather and climate models can be improved.

Understanding weather and climate implies to understand processes on very different scales in time and space. Atmospheric processes start at small scales, like small eddies or microphysical processes (few 10^{-3} m, few 10^{-3} s) and go up to large scales such as atmospheric waves (up to more than 1000 km, days to weeks). All these scales have to be represented in an atmospheric model. Whether processes can be solved physically correct or can only be represented in a parameterized way depends on the resolution of the model. Parameterizing means that complex physical processes are represented in a less complex way. It is not possible to solve the Earth atmosphere interactions without parameterizations, because of the high computational costs that would occur without parameterizations.

In this thesis, one of the important processes taking place on small scales (a few meters to a few 100 meters) will be addressed, the interaction between radiation and clouds. Ocean, the Earth's surface, the atmosphere, and radiation affect each other. Many processes (for example turbulence, heating rates or convection) and components (aerosols, cloud droplets or ice crystals) as well as their interactions have to be considered if cloud-radiation interactions are

studied (Fig. 2.1). Radiation modifies clouds, and, vice versa, clouds modify radiation. Both processes have to be understood on small scales to improve our knowledge about the physics involved. Understanding clouds and radiation on small scales can help to improve current radiative transfer and cloud parameterizations in weather prediction and climate models. This is essential, as insufficiently parameterizing clouds is still the greatest source of uncertainty in climate prediction (Boucher et al., 2013).

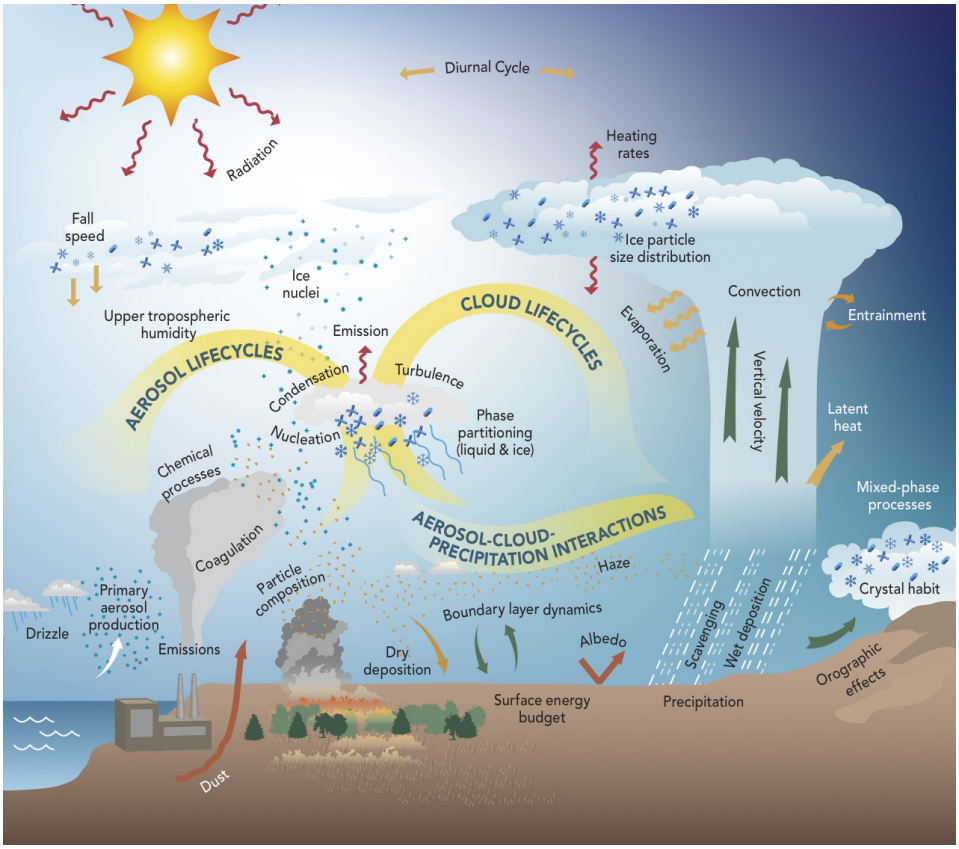

Figure 2.1: Atmospheric components and processes affecting clouds and radiation (ARM (2010), Figure 5).

The aim of this thesis is to study the effect of (3D) thermal radiation on cloud development. For this, a good understanding of radiation processes in the atmosphere, cloud processes, the interaction of both processes, and their representation in current cloud models is necessary. This section will therefore summarize the present state in radiative transfer in the atmosphere (Section 2.1) and continue with cloud processes (Section 2.2). Furthermore, the present knowledge about interaction between radiation and clouds (Section 2.3) and the current representation of radiation and clouds in climate, weather prediction as well as cloud resolving models (Section 2.4) will be summarized.

2.1 Radiative Transfer

This first section focuses on radiative transfer in the atmosphere. First, the role of radiation and clouds for the global energy budget will be addressed (Section 2.1.1). Radiative quantities, necessary for a physical description of radiation in the atmosphere are defined in Section 2.1.2. An overview about modeling radiative transfer with 1D approximations and in 3D is given in Section 2.1.3. If not stated otherwise, the information in this section is taken from Taylor (2005), Liou (2002) and Zdunkowski et al. (2007).

2.1.1 Clouds and the Global Energy Budget

Weather and climate are mainly driven by solar radiation entering the Earth's atmosphere. As the Earth is, to a good approximation, a sphere and its axis is tilted, the incoming solar radiation is not spread equally over the globe. In the tropics more energy arrives per surface area than in polar regions. This latitudinal imbalance causes differences in temperature and pressure which have to be compensated by the atmospheric circulation and the ocean circulation. Both circulations try to establish equilibrium by transporting energy from the tropics to higher latitudes. Due to the rotation of the Earth and the associated Coriolis force, these transport processes do not remain north-southward, but change into a west-east direction in the mid-latitudes. Additionally, these transport processes are perturbed by local phenomena such as orography or temperature contrasts between land and sea.
Changes in radiation lead to an imbalance in the energy budget of the Earth. Alterations in the radiation budget are related to changes in the incoming solar radiation, in the reflected radiation and in the outgoing longwave radiation. Following Trenberth et al. (2009), about 341 $\frac{W}{m^2}$ of solar radiation enter the Earth's atmosphere at top of atmosphere (TOA) in global annual average (Fig. 2.2). The incoming radiation has to pass the atmosphere before reaching the surface and interacts with the constituents of the atmosphere via scattering, absorption and emission. In the global mean, 30 % (102 $\frac{W}{m^2}$) of the incoming irradiance are reflected back to space (planetary albedo), 70 % are absorbed by molecules, aerosols and cloud particles as well as the surface. In equilibrium, the same amount of energy (239 $\frac{W}{m^2}$) is emitted to space in the thermal spectral range. Outgoing longwave radiation is absorbed by greenhouse gases (for example CO_2, CH_4, H_2O or O_3) in the atmosphere, resulting in a warming of the atmosphere. This process, known as the greenhouse effect, is a natural atmospheric process. Due to the natural greenhouse effect the temperature on the Earth is about $15°C$ in the mean, while it would be about $-19°C$ without it (Fourier, 1824; Arrhenius, 1896). Increased concentrations in greenhouse gases, mainly caused by industrial and traffic emissions, strengthen this effect which is known as the anthropogenic greenhouse effect.
Clouds play an important role in the global energy budget and therefore strongly affect climate and weather. Clouds regulate the Earth's average temperature in several ways. In the solar spectral range, 50 $\frac{W}{m^2}$ are reflected back to space (cooling effect), while in the thermal spectral range, clouds reduce the outgoing longwave radiation by 30 $\frac{W}{m^2}$ (warming effect). Clouds act as a kind of blanket in the thermal spectral range by trapping some of the energy that the lower troposphere and the Earth's surface emit. Therefore, the global net effect of clouds is a loss of 20 $\frac{W}{m^2}$. But how clouds behave in a changing climate and how the warming and cooling

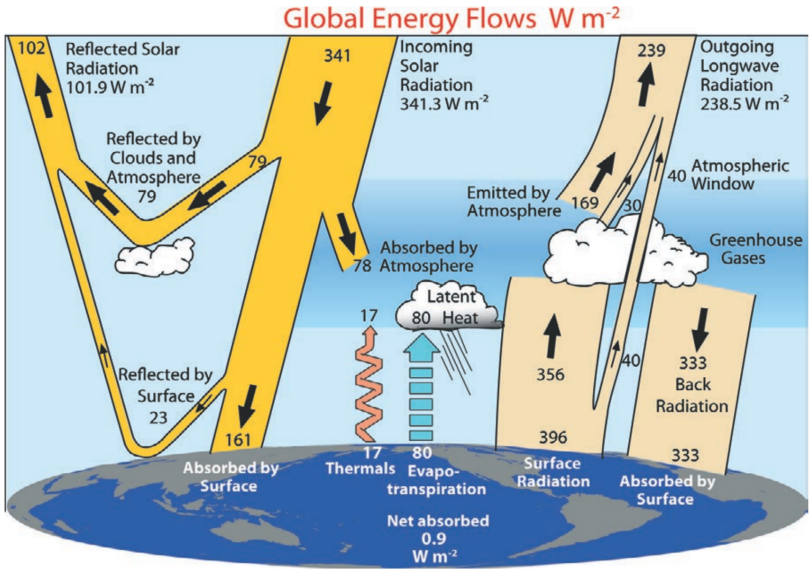

Figure 2.2: Earth's energy budget (Trenberth et al. (2009), Figure 1) showing the equilibrium between incoming solar and outgoing longwave radiation. About half of the incoming solar radiation is absorbed by the Earth's surface. This energy is transferred to the atmosphere by warming the air in contact with the surface (thermals), by evapotranspiration and by longwave radiation absorbed by clouds and greenhouse gases. The atmosphere in turn radiates longwave energy back to Earth as well as out to space.

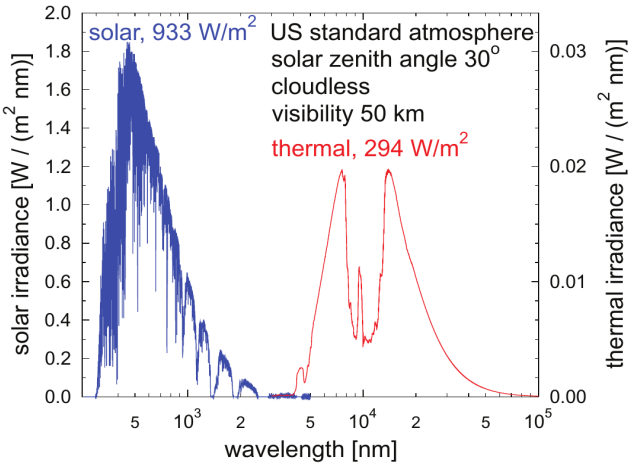

Figure 2.3: Downward solar and thermal irradiance at the Earth's surface (Mayer (2009), Figure 2.)

effects change in the future remains an open question (Boucher et al., 2013).

How much of the energy is trapped by clouds or reflected back to space depends on the characteristics of clouds (optical properties or cloud height) and is therefore highly variable. To estimate the effect of clouds on the Earth's climate is therefore a challenging task. In general, low clouds with high cloud cover (stratus clouds) are usually optically thick and reflect a large fraction of the incoming solar radiation back to space while the effect of emission is rather small as the temperature of low clouds is close to the one of the Earth's surface. High clouds

(cirrus clouds) on the other hand, are optically thin and reflection of solar radiation back to space is small. However, they absorb parts of the outgoing longwave radiation.
Solar (or shortwave) radiation includes ultraviolet, visible and near-infrared radiation (0.25 μm to 4 μm, Fig. 2.3, blue curve). Thermal (or longwave) radiation includes the wavelength spectrum from 4 μm to 100 μm (Fig. 2.3, red curve). The wavelength spectra of solar and thermal radiation overlap only in a small wavelength interval and can therefore be treated separately (Fig. 2.3). This is convenient, because the calculation of solar and thermal radiative transfer is fundamentally different. In the solar spectral range, scattering of light on atoms and molecules in the atmosphere is of high importance while the dominant feature in the thermal spectral range is emission and absorption by the Earth's atmosphere, its constituents and the surface. Radiative transport in the atmosphere is a challenging task, due to all the interactions of radiation with the atmospheric constituents (Fig. 2.1). A more detailed description of the processes involved in atmospheric radiative transport will be given in the following section.

2.1.2 Radiation Quantities and Physical Description

Radiative transfer describes the transport of electromagnetic energy through a medium (for example the atmosphere). The atmosphere consists of a number of different components (molecules, gases, particles, cloud droplets or ice crystals), which make radiative transport in the atmosphere a complex topic. For radiative transfer calculations, the atmosphere is, in a simple description, divided into layers or grid boxes, each containing specific optical properties. For each layer, or grid box, different aspects such as absorption, emission, reflection/scattering, and transmission of solar and thermal radiation have to be accounted for (Fig. 2.4).

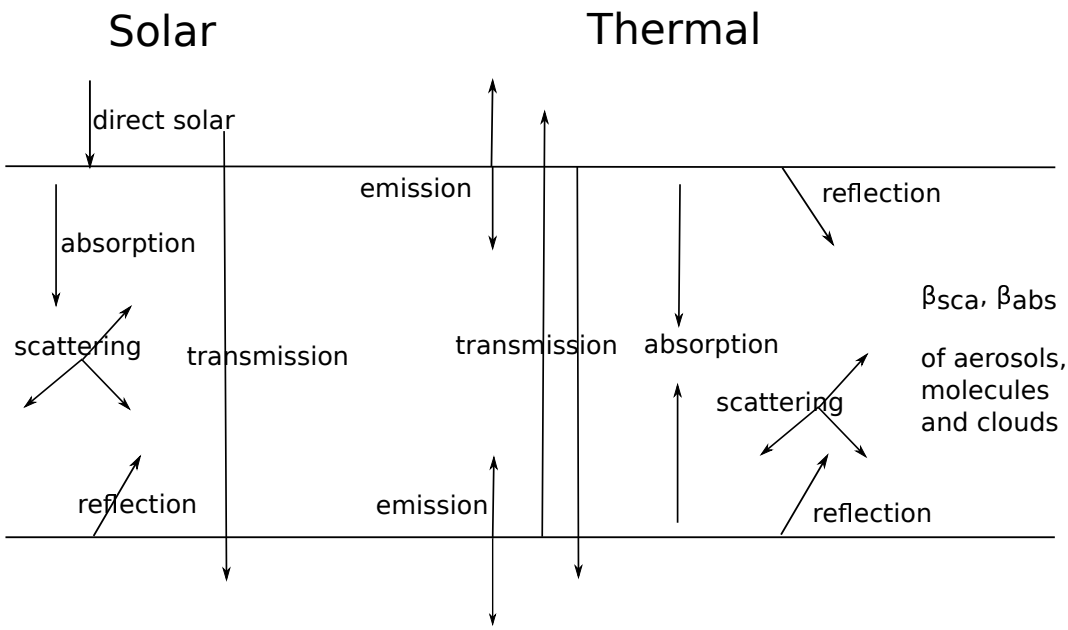

Figure 2.4: Schematic illustration of radiation processes in an atmospheric layer in the solar and thermal spectral range.

For the physical description of radiation and its interaction with matter, a few physical quantities are required:
The *Radiant Power* Φ $[W]$ is defined as the *Radiant Energy* dQ per time dt:

$$\Phi = \frac{dQ}{dt} \tag{2.1}$$

The radiant power Φ on a surface dA is the *Irradiance*, measured in $[\frac{W}{m^2}]$:

$$E = \frac{dQ}{dA\,dt} \tag{2.2}$$

The *Radiance* L is the irradiance per solid angle $d\Omega$ given in $\frac{W}{m^2\,sr}$:

$$L = \frac{dQ}{dA\,dt\,d\Omega\,\cos\theta} \tag{2.3}$$

θ is hereby the zenith angle, defined between the radiance direction $d\Omega$ and the normal of the surface, $dA\,cos\theta$ is the projection of the area dA perpendicular to the radiance direction.
In the atmosphere, radiation interacts with molecules, particles (also known as aerosols), and cloud droplets via scattering, reflection and absorption. For radiative transfer calculations, the following optical properties describe the composition of the atmosphere: β_{ext} is the *extinction coefficient* which is the sum of the *absorption* β_{abs} and *scattering coefficient* β_{sca} in $1/m$:

$$\beta_{\text{ext}} = \int_0^\infty \sigma(r,\lambda)\,n(r)\,dr = \beta_{\text{abs}} + \beta_{\text{sca}} \tag{2.4}$$

$n(r)$ and $\sigma(r,\lambda)$ are the number density of particles/droplets and the particle/droplet extinction cross section. r denotes the particle/droplet radius.
The fraction of scattering of the extinction is called *single scattering albedo* ω_0:

$$\omega_{\text{o}} = \frac{\beta_{\text{sca}}}{\beta_{\text{ext}}} \tag{2.5}$$

With the extinction coefficient, the *optical thickness* τ can be described:

$$\tau = \int_{s_1}^{s_2} \beta_{\text{ext}}\,ds \tag{2.6}$$

The optical thickness is a dimensionless quantity to show how strong radiation is modified by passing a medium.
The *effective radius* r_{eff} is defined as:

$$r_{\text{eff}} = \frac{\int r^3\,n(r)\,dr}{\int r^2 n(r) dr} \tag{2.7}$$

The optical thickness can be described by the effective radius r_{eff} (in μm) and the *liquid water path* (*lwp*, $[g/m^2]$) in the visible spectral range (Stephens, 1978). The approximation that

is made, in the limit of geometric optics, is $\sigma(r, \lambda) = 2\pi r^2$. As a rule of thumb, the optical thickness is then:

$$\tau \approx \frac{3\, lwp}{2\, \rho_{\mathrm{w}}\, r_{\mathrm{eff}}} \tag{2.8}$$

with:

$$lwp = \int_0^\infty lwc(z)\, dz \tag{2.9}$$

Hereby, the *liquid water content* (lwc, $[g/m^3]$) is:

$$lwc = \frac{4\,\pi\,\rho_{\mathrm{w}}}{3} \int_0^\infty n(r)\, r^3 dr \tag{2.10}$$

with the density of water ρ_{w} in kg/m^3.
Another variable to measure liquid water is the *liquid water mixing ratio* usually specified in $[g/kg]$:

$$r_{\mathrm{l}} = \frac{m_{\mathrm{w}}}{m_{\mathrm{d}}} \tag{2.11}$$

Where m_{w} and m_{d} are the mass of liquid water and dry air respectively.
Passing a medium, radiation interacts with it and is modified by scattering and absorption. The loss of radiance by extinction (β_{ext}) along a path ds and with a zenith angle of $\mu = cos\theta$ is described by *Lambert-Beer's law*:

$$L = L_0 \exp\left(-\frac{\tau}{\mu}\right) \tag{2.12}$$

Considering Eq. 2.12, an optical thickness of $\tau = 1$ reduces radiance to 1/e (37%).
The source of thermal radiation in the Earth's atmosphere is emission by the Earth's surface as well as by molecules, droplets, and particles in the atmosphere. *Planck's law* (Eq. 2.13) describes the amount of electromagnetic energy emitted by a black body as a function of its temperature and wavelength (Planck, 1901):

$$B(\lambda, T) = \frac{2hc^2}{\lambda^5} \frac{1}{\exp\left(\frac{hc}{\lambda k T}\right) - 1} \tag{2.13}$$

$B(\lambda, T)$ is the radiance emitted by a black body, $h = 6.62612 \cdot 10^{-34}\ Js$ the Planck constant, $c = 299792458\ m/s$ the speed of light, λ the wavelength, T the temperature in K and $k = 1.38065 \cdot 10^{-23}\ J/K$ the Boltzmann constant.
Integrating Planck's law (Eq. 2.13) over all wavelengths and $d\Omega$, *Stefan-Boltzmann-Law* describes the irradiance E emitted at temperature T:

$$E = \sigma\, T^4 \tag{2.14}$$

$\sigma = 5.67 \cdot 10^{-8}\ W/m^2/K^4$ is hereby the Stefan-Boltzmann-constant.
The amount of radiation which is actually emitted or absorbed by the atmosphere is modified by the spectral absorption or emission coefficients which are equal to each other according to Kirchhoff's law (Kirchhoff, 1890):

$$\epsilon_\lambda = \alpha_\lambda \tag{2.15}$$

with $0 < \epsilon_\lambda < 1$. The actually emitted radiance is therefore $\epsilon_\lambda \cdot B$. The combined interactions (emission, (multiple) scattering, and absorption) are described by the *radiative transfer equation*, Chandrasekhar (1950), an integro-differential equation:

$$\frac{1}{\beta_{\text{ext}}} \vec{s} \, \nabla L = -L + \frac{\omega_0}{4\pi} \int_{4\pi} p(\Omega', \Omega) L(\Omega') d\Omega' + (1 - \omega_0) \, B(T) \tag{2.16}$$

L is the radiance in direction $\vec{s}$ and $p(\Omega', \Omega)$ the scattering phase function. The radiative transfer equation is usually evaluated monochromatically (for a given wavelength or wavenumber). However, no analytical solution exists to solve the radiative transfer equation (Eq. 2.16) if scattering is accounted for. Often the scattering term (2nd term on the right side) is neglected in the thermal spectral range and the equation reduces to the *Schwarzschild equation* (Eq. 2.17) which is straightforward to solve numerically.

$$\frac{dL}{ds} = \beta_{\text{abs}} \left(B(T) - L \right) \tag{2.17}$$

Where $ds = dz/cos\theta$ is the distance under which radiation passes the atmosphere under incidence angle θ.

Emission and absorption of radiation cause cooling or heating of the air which are described by so-called heating or cooling rates. Heating or cooling rates are the temperature change per unit time $\frac{dT}{dt}$ of an atmospheric volume due to absorption and emission of radiation, usually specified in K/d. Emission and absorption can either be calculated directly or can be derived from the divergence of the net flux. In particular, the emitted minus absorbed electromagnetic power per volume $(\dot{q}_{\text{em}} - \dot{q}_{\text{abs}})$ equals the divergence of the net flux vector $\vec{E}_{\text{net}}$.

$$\frac{dT}{dt} = -\frac{1}{\rho c_{\text{p}}} (\dot{q}_{\text{em}} - \dot{q}_{\text{abs}}) = -\frac{1}{\rho c_{\text{p}}} \nabla \vec{E}_{\text{net}} \tag{2.18}$$

ρ is the density and c_{p} the specific heat capacity of the medium. The components of the net flux vector, $E_{\text{net,i}}$, are defined as the difference of the irradiance in positive and negative i directions, respectively. For finite volumes this relationship translates to

$$\dot{q}_{\text{em}} - \dot{q}_{\text{abs}} = \sum_{\text{i}=1}^{3} \frac{1}{\Delta x_i} \left(E_{\text{net,i}}(x_{\text{i}} + \Delta x_{\text{i}}) - E_{\text{net,i}}(x_{\text{i}}) \right) \tag{2.19}$$

2.1.3 1D and 3D Radiative Transfer

It was already pointed out in Section 2.1.2 that the solution of the radiative transfer equation (RTE, Eq. 2.16) is a challenging task. Especially in three dimensions when scattering and many different directions of radiation have to be taken into account and optical properties will no longer only vary with height but also in the horizontal (Fig. 2.5, left), solving the RTE becomes complex and no analytic solution exists.

Due to the complexity, different approximation for the solution of radiative transfer have been developed in the past, which are in general 1D approximation of radiative transfer. The basic assumption for a 1D approximation is the neglect of horizontal variability of radiative properties of the atmosphere and clouds (*plane-parallel approximation*). For 1D approximations it is assumed that optical properties may vary in the vertical but are constant in the horizontal direction (see Fig. 2.5, right). The radiative transfer equation is then solved for each layer and each wavelength. A 1D approximation is meaningful for example in cloudless sky or homogeneous, overcast clouds. However, as soon as finite clouds are present in the atmosphere, the 1D approximation lacks the effects of cloud sides (scattering, absorption and emission). The advantage of 1D approximations is the computational time. These approximations are usually fast. Some of the possible 1D approximation will be described in the following. 1D approximations, however, cause large uncertainties in the radiative transfer results.

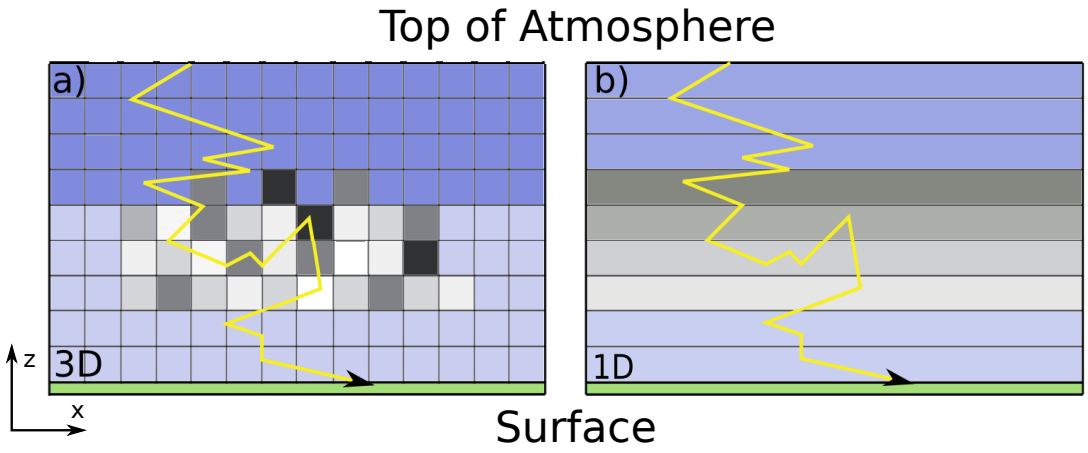

Figure 2.5: Schematic illustration of the difference between a 1D radiation approximation and a 3D calculation.

1D Radiative Transfer Approximation

In order to solve the radiative transfer problem in the atmosphere, a number of approximations (1D approximations) have been developed. These approximations are often computationally efficient but may introduce biases in the application, however, they are still state of the art in current cloud, weather and climate models. The most common approximation, which is widely used in climate, weather and cloud resolving models is the *two-stream approximation*. Also common is the *four-stream approximation*. Both methods are also found as *δ-two-stream* or *δ-four-stream* methods. The general underlying method of both approximations is the *discrete ordinate method*, which will be explain first, before a closer look is taken on the two-stream and four-stream approximation. The *δ-approximations* and its necessity will also be explained. The discrete ordinate method, and therefore the two-stream and four-stream approximation account for scattering and absorption. Furthermore, 1D radiative transfer approximations are usually applied as *independent column approximation* (ICA) in atmospheric models. The independent column approximation means that a 1D radiative transfer approximation is applied in every model column, assuming that each layer of the model column has an infinite extent

in the horizontal.
The primary goal of the *discrete ordinate method* is to reduce the RTE, an integro-differential equation, to a system of ordinary differential equations. For this ordinary system, eigenvalues can be found. For a detailed description, the reader is referred to the literature (for example Liou (1973, 2002) or Kourganoff (1952)) however, a brief overview (based on Liou (1973)) of the method shall be given:
The main problem for solving the RTE is scattering. To solve this problem, the scattering phase function is modified by the addition theorem of spherical harmonics. Then the phase function can be expanded in Legendre polynomials of a finite number. Applying the Gaussian quadrature formula provides a second order differential equation. After a few more mathematical tricks the upward and downward irradiance can be calculated as:

$$E_{up} = 2\,\pi \sum_{\mathrm{i}=1}^{n} a_{\mathrm{i}} \mu_{\mathrm{i}} L(\tau, \mu_{\mathrm{i}}) \tag{2.20}$$

$$E_{dn} = -2\,\pi \left[\sum_{\mathrm{i}=1}^{n} a_{\mathrm{i}} \mu_{\mathrm{i}} L(\tau, -\mu_{\mathrm{i}}) \; - \; S(\tau, -\mu_{\mathrm{i}}) \right] \tag{2.21}$$

$S(\tau, -\mu_{\mathrm{i}})$ is the direct solar irradiance which can be calculated by Lambert-Beer's law. μ_{i} is the discrete angle (one or more, depending on n for which the system is solved). a_{i} are weights, belonging to the discrete angles. The equations can be solved for a number (2n) of streams (2, 4, 8 and 16). More streams implies more discrete angles for which the RTE is solved and therefore higher accuracy of the result. The scattering phase function is approximated as a Legendre series with n terms and one receives n first order differential equations. This also implies n quadrature angles, which means n/2 angles (n/2 upward directed, n/2 downward directed). Each angle pair has a specific weight a_{i}.
The *two-stream approximation* is the most simple approximation. Various approaches exist. Sometimes, the two-stream approximation is applied by using the discrete ordinate method with n=1 and therefore two streams. More descriptive, one could say that the RTE is solved by calculating a solution for direct radiation and two additional diffuse radiation streams (an upward and a downward one) for a plan parallel layer. To get the direct and diffuse irradiance at the layer boundaries, the ingoing direct radiation and upwelling and downwelling diffuse radiation is needed as input. The two-stream approximation can then be expressed as:

$$\begin{pmatrix} E_{\mathrm{up}}^{\mathrm{i}-1} \\ E_{\mathrm{dn}}^{\mathrm{i}} \end{pmatrix} = \begin{pmatrix} a_{11} & a_{12} \\ a_{12} & a_{11} \end{pmatrix} \cdot \begin{pmatrix} E_{\mathrm{up}}^{\mathrm{i}} \\ E_{\mathrm{dn}}^{\mathrm{i}-1} \end{pmatrix} + \begin{pmatrix} a_{13} \\ a_{23} \end{pmatrix} \cdot E_{\mathrm{dir}}^{\mathrm{i}-1} \tag{2.22}$$

The layers i are counted from TOA to the surface. The direct solar radiation for each layer is:

$$E_{\mathrm{dir}}^{\mathrm{i}} = a_{33}\, E_{\mathrm{dir}}^{\mathrm{i}-1} \tag{2.23}$$

The two-stream coefficients (for example a_{11}) represent optical properties of a layer i and have the following, physical meaning:

- a_{11} transmission coefficient for diffuse radiation

- a_{12} reflection coefficient for diffuse radiation
- a_{13} reflection coefficient for the primary scattered solar radiation
- a_{23} transmission coefficient for the primary scattered solar radiation
- a_{33} transmission coefficient for the direct parallel solar radiation

The coefficient a_{33} is the only one needed to calculate the direct solar radiation ($E_{\mathrm{dir}}^{\mathrm{i}-1}$) and corresponds to Lambert-Beer's law ($a_{33} = exp(-\Delta s\, \beta_{\mathrm{ext}})$; Eq. 2.12). By setting the appropriate boundary conditions at top of the atmosphere and the surface (for the solar and the thermal radiation), the system of equations can be solved. In case of thermal radiation, only the first two coefficients (a_{11} and a_{12}) remain. The last term on the right of Eq. 2.22 has to be replaced by the upwelling and downwelling emitted irradiance of the layer. This method is used in most weather and climate models and is a computationally cheap approach.
The *four-stream approximation* is also a special case of discrete ordinate method. Here n=2 and therefore 4 streams are used for the calculation of diffuse fluxes. Two upward and two downward diffuse fluxes are represented, and, similar to the two-stream approximation, a direct stream is calculated. Due to the higher number of streams, scattering is represented more accurately. This method is also an analytic approximation. Computational time is higher than for the two-stream approach.
It has already been mentioned in the beginning of this section that a *δ-scaling approximation* is often applied to the two-stream and four-stream approximation. Two-stream and 4-stream approximations are working well for optically thick layers, but the radiative transfer solution is insufficient for optically thin layers. The reason for this is that scattering in the atmosphere is peaked in forward direction. To receive a better approximation, a part of the forward scattered radiation can be treated as non-scattered. Applying the δ-scaling, the angular distribution of the scattered radiation is improved. If a fraction f of scattered energy is put to the forward direction and at the same time, the scattering parameters (τ, w_0 and g) are reduced accordingly this problem can be solved. Mathematically, the phase function is written as a δ-peak in the forward direction and a smooth function in the other directions (Joseph et al., 1976).
In the thermal spectral range, scattering is often neglected and the *Schwarzschild equation* (2.17) is solved instead of the full radiative transfer equation. It describes the transmission of radiation of a particular frequency/wavelength in an absorbing medium. Thus, the radiance for one layer of optical thickness τ is:

$$L(\tau, \mu) = L(0, \mu)\, exp(\frac{(-\tau_{\mathrm{i}})}{\mu}) \; + \; B_{\mathrm{i}} \left(1 - exp(\frac{(-\tau_{\mathrm{i}})}{\mu})\right) \tag{2.24}$$

Here, $L(0)$ represents incoming radiance at a layer boundary, $exp(\frac{-\tau}{\mu})$ is the reduction of the radiance by absorption in a layer (what is still transmitted), and $B\, exp(\frac{-\tau}{\mu})$ is the emission of the atmospheric layer. Integrating over the zenith angle ($\mu = cos(\Theta)$) and solid angle $d\Omega$ one receives the irradiance E:

$$E = \int_{2\pi} L(\mu, \Phi)\, \mu\, d\Omega = 2\,\pi \int_0^1 L(\mu) \mu\, d\mu \tag{2.25}$$

3D Radiative Transfer - Monte Carlo Radiative Transfer

One way of solving the radiative transfer equation (Eq. 2.16) correct and in 3D is by using the *Monte Carlo method*. Monte Carlo is a stochastical approach and allows to solve the RTE without any simplifications for a 3D inhomogeneous medium. In the case of radiative transfer in the atmosphere, individual photons are traced through the atmosphere from their generation till their end, accounting for scattering, absorption, and reflection by using probability theory. In principle, the RTE can be solved without knowing it. With a Monte Carlo model, the individual physical processes are considered explicitely. For a detailed description, the reader is referred to the literature (for example Mayer (2009); Marshak and Davis (2005)). The basic principles will be described in the following.
For a Monte Carlo simulation, a modeling domain is defined and divided into layers and grid boxes (Fig. 2.6, left). In the beginning, photons have to be generated. In the atmosphere, two sources are available. In the solar spectral range, the source is the sun, in the thermal spectral range, the source is the atmosphere and the surface. Each photon has an initial location and direction. In case of solar radiation, the start location and direction are top of atmosphere and the solar zenith and azimuth angle (Fig. 2.6, right). In the thermal spectral range, the emitted radiance (and thus the number of emitted photons) is given by the product of the Planck function and the emission coefficient. The start location of photons is determined by randomly sampling from this distribution. The initial direction of the photons is isotropic.

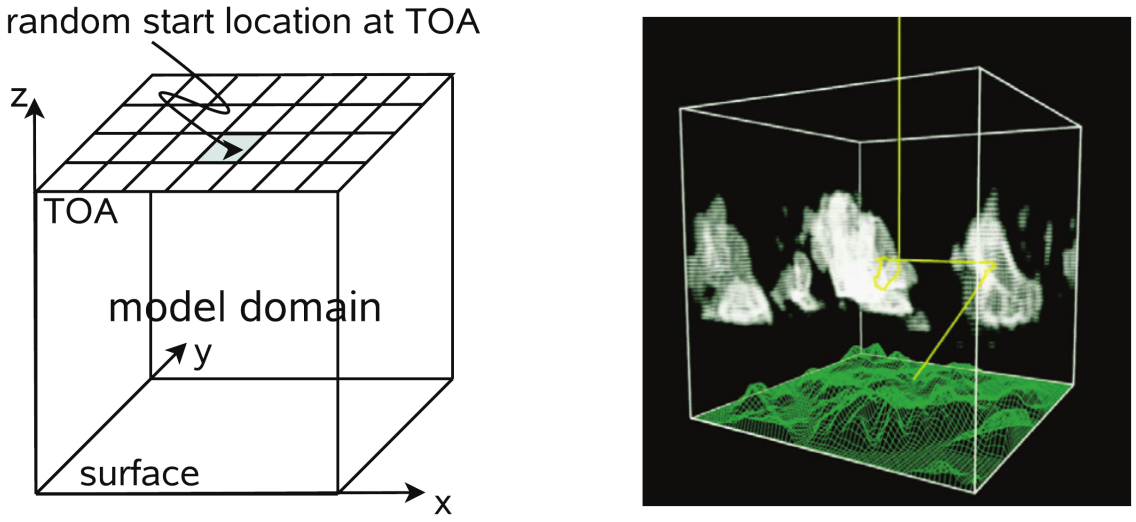

Figure 2.6: Left: Schematic illustration of a Monte Carlo modeling domain and the photon starting position in the solar spectral range (from (Mayer, 2009)). Right: Visualization of a photon path (yellow) in a Monte Carlo domain, passing clouds and showing inhomogeneous surface (from (Mayer, 2009), visualization of the Monte Carlo model MYSTIC)

After generation, the photon travels through the atmosphere. How far a photon can travel is determined by random sampling of Lambert-Beer's law (Eq. 2.12). At the destination location, the further travel of the photon has to be determined. Again per random number, the photon is either scattered or absorbed; if it hits the surface it can either be reflected or

absorbed. In case of scattering or reflection, the photon is assigned a new direction (again a random one, but following the scattering phase function), and the travel continues. If the photon is absorbed, its travel ends. The other possibility to end the photon journey would be the photon leaving the atmosphere at TOA.
With the Monte Carlo method, a variety of radiative transfer quantities, including radiance, irradiance or heating rates can be calculated. However, as this is a stochastical approach, the results are noisy. The noise can be reduced by tracing more photons, however, computational costs depend on the number of photons traced.
There are several possibilities to minimize the noise for a given computational time, which are so called *variance reduction techniques*. Another possibility is the backward tracing of photons. According to the reciprocity principle defined by Herman von Helmholtz, a path of light is reversible (von Helmholtz, 1853). Backward Monte Carlo is an efficient approach, when the result is only needed at a certain location (for example a cloud). When photons are traced backward, a certain amount of photons is started at a point (for example a grid box or the surface, for which the radiation should be calculated) and is traced to some place in the atmosphere (so to say, the place where it would start in reality). Therefore, every photon which is started contributes to the result.

Spectral Integration

The radiative transfer equation has to be solved monochromatically. Therefore the RTE only gives us information of a narrow wavelength band. To calculate for example integrated solar or thermal irradiance or heating rates, the RTE has to be integrated over all wavelengths, for which the solution is desired. The most straightforward approach are so-called *line by line* calculations where the RTE is solved for a large number of wavelengths, resolving all relevant spectral features and the result is integrated over wavelength. However, this is a computationally expensive approach as the line by line integration has to be performed for very narrow wavelength bands, because the components of the atmosphere change their spectral properties rapidly with wavelength, depending on the vibrational and rotational energies of the molecules.
An alternative to the line by line calculation are so called *k-distribution* methods. This method uses spectrally averaged data and a cumulative distribution of absorption coefficients. The gaseous spectral transmittance is grouped by the absorption coefficients and the usual wavelength integration can be replaced by an integration in absorption coefficient space. The reordered wavelength grid is smooth and monotonic and less sampling points are necessary to integrate the full radiation spectrum. For the k-distribution, the reordered wavelength grid is divided into bands and sub bands. The k-distribution is strictly valid for homogeneous atmospheres. However, the atmosphere is by no means homogenous, but varies with height. The *correlated-k distribution* assumes that spectral absorption cross sections of different layers are correlated. The correlated-k distribution was proven to be within 1% of a line by line calculation (Fu and Liou (1992); Goody et al. (1989)). Common correlated-k distributions are those by Fu and Liou (1992), Kato et al. (1999) or Mlawer et al. (1997).
A further simplified treatment of spectral integration is the so called *Monte Carlo spectral integration* (MCSI) as proposed by Pincus and Stevens (2009). This assumption is only meant

for use in time developing models where averaging over many time steps is possible. Here, only a single wavelength sub band of a correlated-k distribution is picked at each time step per model column when radiative transfer is applied in a cloud resolving model. The thus calculated irradiance of a sub band is weighted by the number of bands and the corresponding weight of the randomly sampled sub band of the correlated-k distribution. The MCSI reduces again the amount of computational time needed for the simulation significantly. It was shown that this approximation does not effect the overall result of a cloud resolving model. Due to averaging over multiple time steps, the randomly uncorrelated sampling does not affect the result. However, irradiance and heating rates will not be computed spectral fully integrated at each time step. At a single time step, the result of the MCSI contains random errors, compared to the full spectral calculation. The noise reduces however with increasing number of samples (time steps).

2.2 Clouds and Cloud Physics

This section gives an overview about clouds and cloud physics. Section 2.2.1 provides an overview about different cloud types in the atmosphere. The following section summarize important quantities of cloud physics (Section 2.2.2) and cloud microphysics (Section 2.2.2). The section is based on Taylor (2005), Rogers (1979), Houze (1993), and Bohren and Albrecht (1998) if not stated otherwise.

2.2.1 Clouds in the Atmosphere

Clouds are a remarkable and diverse feature at the sky. They consist of many small droplets of water or ice crystals, or even both, suspended in air. Many different forms of clouds exist. They are different in shape and size which usually corresponds to the dynamical processes which form the clouds. They appear over a wide range of scales in the atmosphere. On large scales, such as the synoptic scale ($>$ 2000 km, for example cloud systems), mesoscale (20 - 2000 km, for example cyclones) or on convective scale (0.2 - 20 km, for example evaporation, droplet growth or cumulus clouds). Their Latin names already explain parts of their appearance:

1. cumulus - heap or pile
2. stratus - layer
3. cirrus - lock of hair
4. nimbus - precipitation
5. altum - height

These five Latin names can be used in combinations or separated. Ten different cloud genera are defined by the World Meteorological Organization (WMO) (Table 2.1):

Clouds can be equally distributed, with nearly constant cloud cover, a rather uniform base and horizontally wide spread (*stratiform clouds*, Fig 2.7a) at the sky. Stratiform clouds usually

Type	Name	Height of Cloud Base
Low	Stratus Stratocumulus Cumulus	below 2 km
Middle	Altocumulus Altostratus Nimbostratus	between 2 and 6 km
High	Cirrus Cirrocumulus Cirrostratus	above 6 km
All levels	Cumulonimbus	below 2 km

Table 2.1: The ten cloud genera as defined by (World Meteorological Organization, 1975).

have small vertical velocities. *Cumulus clouds* (Fig 2.7b) have a finite extent with sharp edges and small to strong vertical velocities and different heights. They often seem to be bubbling or tower like. They can be isolated with only a few hundred meters to a kilometer in size or may grow high up in the atmosphere when they start clustering. Those tall cumulus clouds are called *cumulonimbus* and they often have an anvil like shape. Due to their height, the upper part of the cloud contains ice particles (Fig 2.7c). High clouds, so called *cirrus clouds*, have fine structures and consist of ice particles (Fig 2.7d). These are just a few examples of the huge variety of existing clouds.

As already pointed out in Section 2.1.1 clouds play an important role in the global energy budget and therefore in weather and climate, due to the different warming and cooling effects which they have. They modify radiation, release latent heat, transport heat, moisture and momentum vertically, and determine the surface hydrology (by precipitation).

In a simple description, a cloud forms when warm and moist air (with less density) rises, cools, and the water vapor condenses and forms a cloud. To form a cloud, two basic components are needed. *Water vapor* and *aerosols* have to be present. By *evaporation* over oceans, lakes, the surface, and vegetation, water vapor is released into the atmosphere, rises or is moved by advection. Aerosols, are small particles in the air. Their origin can be either natural (volcanic eruptions, desert dust, forest fires) or they can be of anthropogenic origin (combustion of fossil fuels). If aerosols are hygroscopic (if they absorb water), they become the basis of droplet formation. Water vapor condenses on them and over time, they grow by binding more and more water. They are therefore called *cloud condensation nuclei* (CCN).

Former studies, using 1D radiation approximations, have already looked at the effects of radiation on stratus clouds. Thermal radiation was found to be a key driver in stratus cloud development (for more information, see Section 2.3). Stratus clouds are horizontally homogeneous with limited cloud side area. They form if lower, moist atmospheric layers are cooled (for example during night or adiabatically through mechanical lifting). Cumulus clouds on the other hand have horizontally limited extent and have cloud side faces. They form from rising thermals. To study 3D effects of thermal radiation, finite cloud forms are necessary, because the 3D effect in the thermal spectral range is cloud side cooling. If horizontally homogeneous

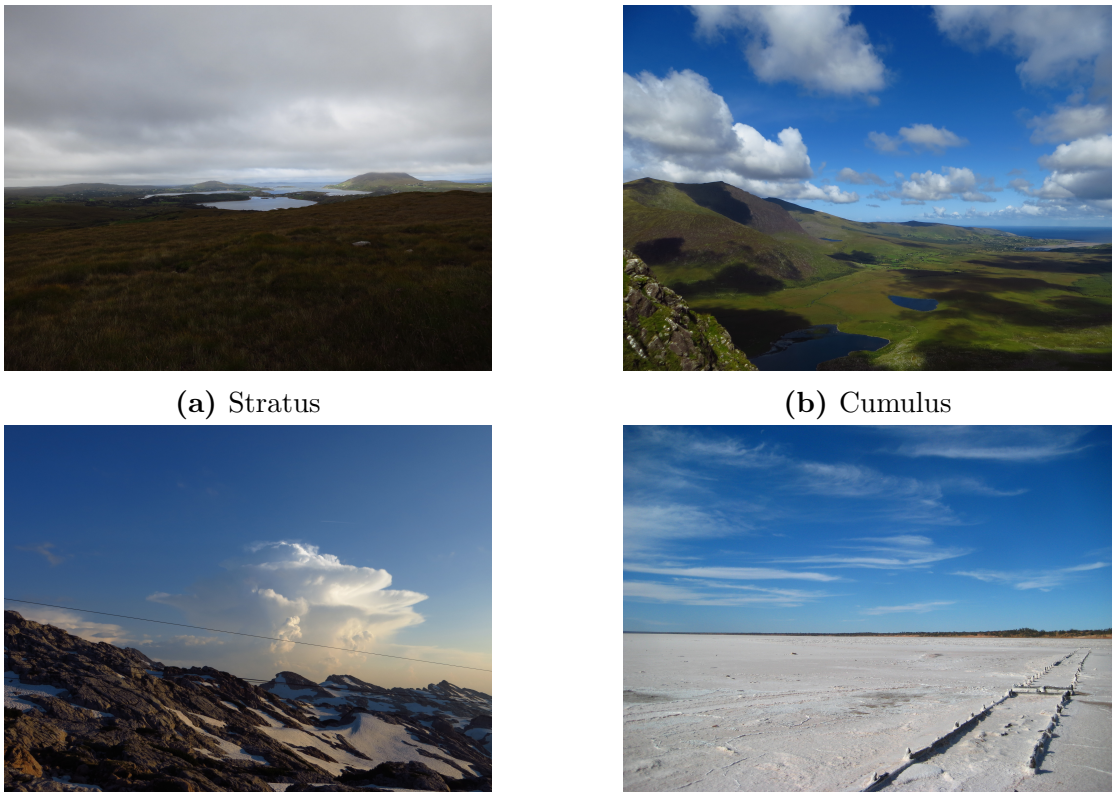

(a) Stratus **(b)** Cumulus

(c) Cumulonimbus **(d)** Cirrus

Figure 2.7: Photographs of different cloud types (Source: C.Klinger).

clouds (such as stratus) would be studied, there would hardly be any cloud side effect. The effects of additional cloud side cooling through side faces of cumulus clouds is, due to the missing 3D radiation parameterizations unknown.
For the rest of this work, the focus will therefore be on cumulus clouds. Cumulus clouds are regularly observed in the atmosphere. Usually, it is differentiated between shallow cumulus clouds and deep cumulus clouds. Shallow cumulus clouds have moderate updraft velocities and little precipitation which are often observed during fair weather periods over land and frequently over the oceans (Stevens et al., 2005). As the name already suggests, they are shallow clouds, with little vertical extend. They can often be observed in the trade wind region. As they are mainly non-precipitating, they dissappear simply by evaporation.
Deep cumulus clouds, with high vertical velocities and precipitation extend high up in the atmosphere. They are formed from shallow cumulus clouds, when the vertical motion continues and they can rise up to 10 km or more (Stevens et al., 2005). They are usually associated with precipitation.
In the following, a more detailed description of the dynamical and microphysical processes that form (shallow cumulus) clouds will be given.

2.2.2 Cloud Physics

The evolution of a cloud is often separated into two parts. One is the dynamical aspect, which usually describes the formation of clouds due to wind, temperature, humidity or the liquid water content of a cloud. The other aspect is the development of cloud droplets itself, and therefore the microphysical aspect.

Cloud Dynamics

Differential heating of the surface causes air to rise. Air cools while rising and if it cools down to the dew point (the point where the *relative humidity* reaches 100%), a cloud can form. The relative humidity RH is the ratio of the vapor pressure e to the saturation vapor pressure e_s:

$$RH = \frac{e}{e_\mathrm{s}} \tag{2.26}$$

To allow air to rise, the atmosphere has to be unstable. A common quantity used to describe the stability of the atmosphere is the *potential temperature*:

$$\theta = T \left(\frac{p_0}{p} \right)^{\frac{\mathrm{R_d}}{\mathrm{c_p}}} \tag{2.27}$$

This equation, also known as the *Poisson Equation*, describes the temperature an air parcel (with initial temperature T) would have, if it is moved adiabatically from its current pressure p to a reference pressure $p_0 = 1000\ hPa$. R_d is the specific gas constant for dry air and c_p the specific heat capacity for dry air.
The variation of θ with height can be described as:

$$\frac{d\theta}{dz} = \frac{\theta}{T} \left(\frac{dT}{dz} + \frac{g}{c_\mathrm{p}} \right) = \frac{\theta}{T} \left(\frac{dT}{dz} + \Gamma_\mathrm{dry} \right) \tag{2.28}$$

Here $\Gamma_\mathrm{dry} = \frac{g}{c_\mathrm{p}}$ is the *dry adiabatic lapse rate* ($9.8\ K/km$) and $\frac{\partial T}{\partial z}$ the *actual lapse rate* of the environment.
In a moist environment, the temperature has to be replaced by the *virtual (potential) temperature*:

$$T_\mathrm{v} = T(1 + \epsilon\, r_\mathrm{v}) \tag{2.29}$$

r_v is the *mixing ratio of water vapor* and $\epsilon = \frac{R_\mathrm{d}}{R_\mathrm{v}} = 0.61$ the ratio of the specific gas constants of dry air and water vapor. If the virtual potential temperature is desired, T has to be replaced by the potential temperature θ in Eq. 2.29. If condensation occurs, latent heat is released and the lapse rate changes to the *moist adiabatic lapse rate*.

$$-\frac{dT}{dz} = \Gamma_\mathrm{sat} = \frac{\Gamma_\mathrm{dry} \left(1 + \frac{l_\mathrm{v}\, r_\mathrm{s}}{R_\mathrm{d}\, T}\right)}{1 + \left(\frac{l_\mathrm{v}^2\, r_\mathrm{s}\, \epsilon}{c_\mathrm{p}\, R_\mathrm{d}\, T^2}\right)} \tag{2.30}$$

l_v is the *latent heat* of water and r_s the *saturation mixing ratio*. Γ_sat is always smaller than Γ_dry. If condensation occurs and liquid water is found in the atmosphere, the virtual temperature (Eq. 2.29) changes to:

$$T_\mathrm{v} = T(1 + \epsilon\, r_\mathrm{v} - r_\mathrm{l}) \tag{2.31}$$

where r_l is the *liquid water mixing ratio*.
With the above defined quantities, the stability criteria of the atmosphere can be defined and illustrated in Fig. 2.8:

- $\frac{\partial T}{\partial z} < -\Gamma_{dry}$: instable
- $\Gamma_{dry} < \frac{\partial T}{\partial z} < -\Gamma_{sat}$: conditionally unstable
- $-\Gamma_{sat} < \frac{\partial T}{\partial z}$: stable

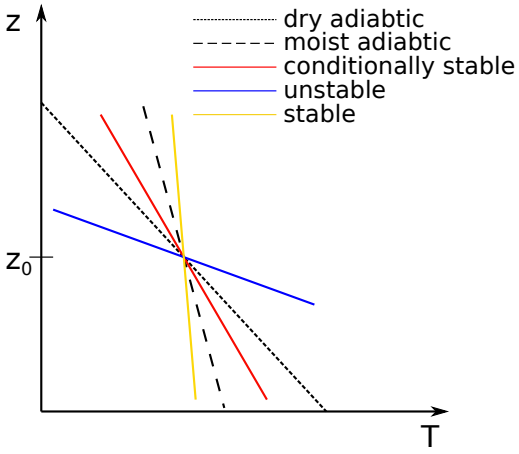

Figure 2.8: Schematic vertical profile of the change in temperature with height.

Two processes in the atmosphere may cause an air parcel to rise. One is forced or mechanic lifting. This usually happens if air masses move towards a barrier (for example mountain range) where the air is forced to rise. The other way of lifting air is by heating the surface by solar radiation. This is the process how cumulus (or convective clouds) form. Energy is conducted from the heated surface to the air in contact with the surface. The temperature of the air increases and the profile becomes unstable. From this moment on, the rising air causes mixing and overturning in this layer. By the time, the whole lower atmosphere gets affected by mixing and the temperature profile adjusts to a dry adiabatic lapse rate. While rising, the air parcel cools and the temperature eventually drops below the *dew point temperature* (T_d). This is the temperature where the relative humidity equals 100% and condensation starts (Fig. 2.9). The height in the atmosphere where condensation starts is called *lifting condensation level* (LCL), if the initial rise of the air parcel is due to mechanical lifting. If the air parcel is lifted by the heated surface and therefore convection, the height is called *convection condensation level* (CCL). In order to force convection, a certain initial temperature (*convective temperature*, T_c) at the surface has to be reached. The lifting of air can be described in a simplified way by the *elementary parcel theory*:
For this we assume an air parcel, which is isolated in an unstable environment and which, due to some heat disturbance at the surface, starts to rise. This process of rising, also called convection or buoyant convection describes the transformation of potential energy to kinetic energy. We consider an air parcel with temperature T, pressure p and density ρ. The environment may have temperature T', pressure p' and density ρ'. The *pressure gradient force* (first

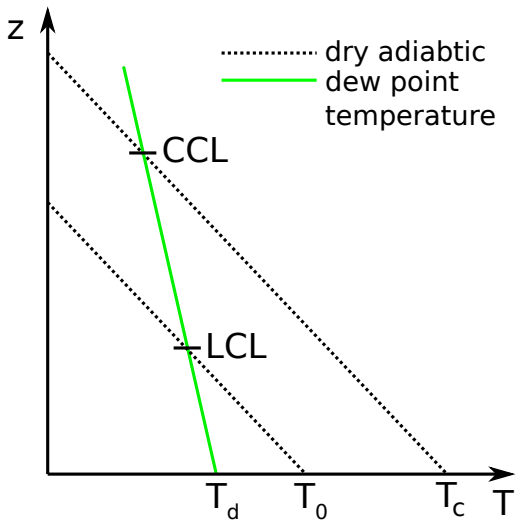

Figure 2.9: Schematic illustration of the lifting condensation level and convection condensation level.

term on the right) and the *gravitation* (second term on the right) act on the air parcel:

$$\delta F = -\frac{dp}{dz}\,\delta V - \delta m\, g \tag{2.32}$$

With the *hydrostatic equation*, the *ideal gas law*, and $p = p'$ this equation can be transformed to:

$$\delta F = \frac{T - T'}{T'}\, g\, \delta m = \frac{\rho' - \rho}{\rho}\, g\, \delta m \tag{2.33}$$

This equation describes *Archimedes' principle* that the upward buoyant force is equal to the weight of the body of the displaced medium. If $T > T'$, $\delta F > 0$ and the parcel will rise. The *equation of motion* for this parcel is therefore

$$\frac{d^2 z}{dt^2} = \frac{T - T'}{T'}\, g \tag{2.34}$$

The term $\frac{T-T'}{T'}$ is defined as *buoyancy* B. With $w = \frac{dz}{dt}$ the vertical velocity can be derived from Eq. 2.34 by integrating along a vertical distance Δz from z_0 to z_i. It then follows:

$$w^2 = w_\mathrm{o}^2 + 2\, g \int_{z_0}^{z_\mathrm{i}} B(z)\, dz \tag{2.35}$$

The latter term of Eq. 2.35 is the *convective available potential energy* (CAPE):

$$CAPE = g \int_{z_0}^{z_\mathrm{i}} B(z)\, dz \tag{2.36}$$

The CAPE is a measure for the available energy which causes convection and is directly proportional to an increase in kinetic energy of the buoyant parcel. It is a maximum estimation of the vertical velocity, due to several neglects in the elementary parcel theory:

1. neglect of the weight of condensed water
2. neglect of compensating downward motion
3. neglect of mixing with ambient air (entrainment)
4. neglect of aerodynamic drag

For all four negligence, correction can be added. This will not be described in detail here. A description of these processes can be found for example in Rogers (1979). The effects on the elementary parcel theory can be summarized as follows:
Considering the transport of condensed water (1) will have an effect on CAPE, by causing a reduced buoyancy. This can be seen from the calculation of the buoyancy (Eq. 2.34) when T and T' are replaced by the virtual temperature (considering liquid water, Eq. 2.31).
If the compensating downward motion (2) is considered, the stability criteria change. The downward motion of dry air partially compensates buoyancy. If dry air is entrained into the cloud (3) by turbulence, the relative humidity of the mixed air drops below 100% and some of the condensed water will evaporate and consequently the air is cooled by evaporation. Therefore, entrainment also reduces buoyancy. At cloud tops, entrainment can even cause negative buoyancy. Finally, the aerodynamic drag (4) also reduces buoyancy.

Cloud Microphysics

Cloud droplets form on so called cloud condensation nuclei (CCN). Those are hygroscopic aerosol particles on which water vapor condenses. CCN are essential for the formation of cloud droplets and therefore clouds and rain. Without them, the formation of droplets would hardly ever occur. For cloud droplet formation without CCN (so called *homogeneous nucleation*), relative humidities of 500% or more would be necessary, which are never found in the atmosphere. Instead, water vapor condenses onto aerosol which is called *heterogeneous nucleation*.
The critical quantity for droplet formation is the *relative humidity*. If air is cooled adiabatically while rising, the relative humidity rises and eventually reaches 100%. At this point, some of the aerosols (the more hygroscopic ones) start serving as CCN. If the air continues to rise and is cooled further, the air becomes *supersaturated*, which means that the relative humidity becomes slightly higher than 100%. The supersaturation hardly becomes larger than 1%, which in consequence means that there are always enough CCN around in the atmosphere to start cloud formation.
These findings are quantitatively explained by the *Köhler theory*. Homogeneous nucleation does not occur due to the *Kelvin effect*, which is an increase of saturation vapor pressure over curved surfaces compared to flat surfaces. Condensation nuclei reduce the power of the Kelvin effect. Water vapor can condense on droplets which reduces the curvature. This means, the larger an aerosol, the easier a cloud droplet will form. In addition, dissolved substances (aerosol) in water reduce the vapor pressure of a liquid. The fraction of water molecules in the liquid and at the surface decreases with increasing concentration of other molecules. The vapor pressure is reduced and cloud droplets can form more easily (*Raoult effect*). Both effects are combined in the *Köhler equation* (Köhler, 1936), which is the ratio of the saturation vapor

pressure $e_s(r)$ above a curved surface to the saturation vapor pressure e_s above a surface of pure water:

$$\frac{e_s(r)}{e_s} = \exp\left(\frac{\zeta}{r}\right) \cdot \frac{1-\eta^3}{1+(\xi-1)\eta^3} \tag{2.37}$$

with:

$$\zeta = \frac{2\gamma}{\rho_w R_v T}, \quad \eta = \frac{r_{ccn}}{r}, \quad \xi = \frac{iM_w\rho_{ccn}}{M_{ccn}\rho_w} \tag{2.38}$$

Here, γ is the surface tension, of water in $[N/m]$, ρ_w the density of water and ρ_{ccn} the density of the CCN in $[kg/m^3]$, M_w and M_{ccn} are molar masses of water and CCN (in $[kg/mol]$) respectively, r_{ccn} the radius of the CCN in $[m]$, R_v the specific gas constant of water vapor in $[J/kg/K]$, T the temperature of water in $[K]$ and i denotes the number of ions into which a molecule dissociates in aqueous solution. The first term of Eq. 2.37 describes the increase in saturation ratio over a droplet compared to a plain surface (Kelvin-effect), the second term shows the reduction of the vapor pressure due to a dissolved substance (Raoult-effect).
An example of the Köhler curve for a NaCl particle of initial radius 0.01 μm is given in Fig. 2.10. The crystal has a radius of 0.01 μm. The figure shows the Raoult- (blue) and Kelvin-effect (green). If the ratio of $e_s(r)$ and e_s equals 1, the saturation pressure above the droplet is the same as above a plane surface of pure water. In the beginning, the Raoult effect is the dominant effect. By the time, the droplet grows the concentration of the NaCl decreases and the Raoult effect becomes weaker and the Kelvin effect is dominating. At some point, the *critical radius* is reached, which is the maximum of the Köhler curve. For saturations below 100% the droplet will assume its equilibrium radius given by the Köhler curve. Once the supersaturation is large enough to let the droplet grow to the critical radius, the droplet will grow automatically.

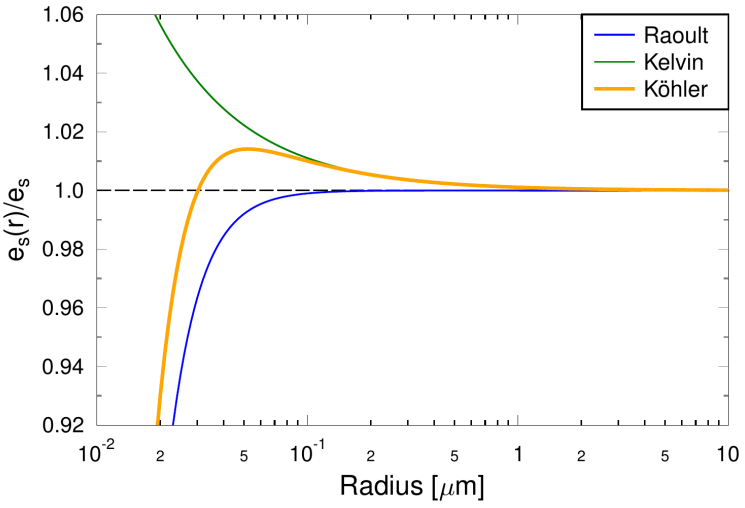

Figure 2.10: Köhler curve for a NaCl-CCN with $r_{ccn} = 0.01\ \mu m$ at T=288.15 K. Black: saturation pressure of pure water above an even surface, blue: Raoult effect; green: Kelvin effect; orange: Köhler curve (from Gödde, F. (2015), Figure 2.1).

Droplet growth (in particular its speed) is determined by *diffusional growth theory*. Diffusional growth is dominated by two processes. First, water vapor has to be transported to the droplet to condense on it. Secondly, during condensation, latent heat is released which has to be transported away from the droplet to the environment (both processes are illustrated in Fig. 2.11).

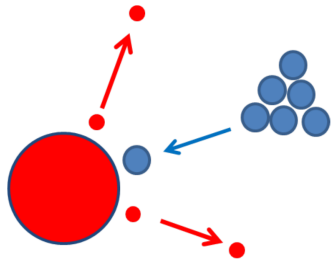

Figure 2.11: Schematic figure of diffusional growth. Blue: water vapor condensation on droplet; red: release of latent heat (From Gödde, F. (2015), Figure 2.2).

The transport of heat away from the droplet is essential for droplet growth, because the saturation pressure increases strongly with temperature. If the droplet would become warmer than its environment, it would evaporate. Diffusional growth can be described by the following equation:

$$\frac{dr}{dt} = \frac{1}{r}\frac{S^*}{\rho_\mathrm{w} C} \tag{2.39}$$

with $S^* = S - 1$ is the supersaturation and C:

$$C = \frac{l_\mathrm{v}^2}{R_\mathrm{v} K T_\infty^2} + \frac{R_\mathrm{v} T_\infty^2}{D e_\mathrm{s}(T_\infty)} \tag{2.40}$$

with l_v being the latent heat in [J/kg], R_v the specific gas constant of water vapor in $[J/kg/K]$, K is the thermal conductivity in [W/(m K)], T_∞ the temperature of the environment in $[K]$, e_s the saturation vapor pressure in [hPa] and D the diffusional constant in $[m^2/s]$. Eq. 2.39 combines both, the transport of heat way from the droplet and the transport of water vapor to the droplet. This equation is true for a droplet in radiative equilibrium, that is, the emitted thermal radiation is balanced by the incoming thermal radiation. This is not always true, especially at cloud sides and will be addressed later in this thesis.
If a cloud droplet has formed, it eventually grows further and becomes a rain droplet. The process for rain droplet formation is the so called *collision and coalescence*. The major source for collision is gravitation. If cloud droplets become large enough, they may fall downwards and collide with other droplets. Other sources for collision can be electromagnetic fields (for example in thunder storm clouds), or aerodynamic forces. If a droplet falls and collides with other droplets, coalescence does not necessarily take place. Droplets may bounce apart when they hit, they may coalesce and stay together or the may coalesce and separate again. The separation can take place immediately or after a while. Collision and coalescence start when cloud droplets have grown to a radius of about 20 μm (Mason, 1960). However, diffusional

growth usually slows down at 10 μm in the above described theory. The reduced growth for larger droplets can be seen in Eq. 2.39. Integrating the equation, one receives $r = \sqrt{\frac{2\,S^*\,t}{\rho_\mathrm{w}\,C}}$. For a constant C, S^*, and ρ_w, it follows that $r \propto \sqrt{t}$, which means that droplet growth slows down with droplet size. For this reason, droplets hardly grow beyond 10-15 μm. There is still a lack in droplet growth theory and no definite explanation has been found to account for the transition of cloud droplets to rain droplets. However, thermal radiative cooling of cloud droplets close to cloud tops and cloud sides might be one possible explanation. Considering radiative heating or cooling in droplet growth theory (for example Gödde, F. (2015)), Eq. 2.39 changes to:

$$\frac{dr}{dt} = \frac{1}{\rho_\mathrm{w}\,C}\left(\frac{S^*}{r} + F\,E_\mathrm{net}\right) \tag{2.41}$$

with the constants C (Eq. 2.40) and F:

$$F = \frac{l_\mathrm{v}}{R_\mathrm{v} K T_\infty^2} \tag{2.42}$$

Other derivation of Eq. 2.41 can be found for example in Roach (1976). More results from former studies about the effect of thermal radiation on droplet growth is given in Section 2.3.2. Comparing Eq. 2.41 to Eq. 2.39 one additional term (on the right) accounts for radiative heating or cooling. E_net is positive, if a droplet emits radiation and negative, if a droplet absorbs radiation. Thermal cooling occurs at cloud tops and cloud sides, and some of the cloud droplets are of course affected by cooling. Droplet growth will be enhanced for the droplets affected by thermal cooling.
To conclude this section, an overview over the different stages of droplets, their sizes and their occurrence in the atmosphere is given in Fig 2.12.

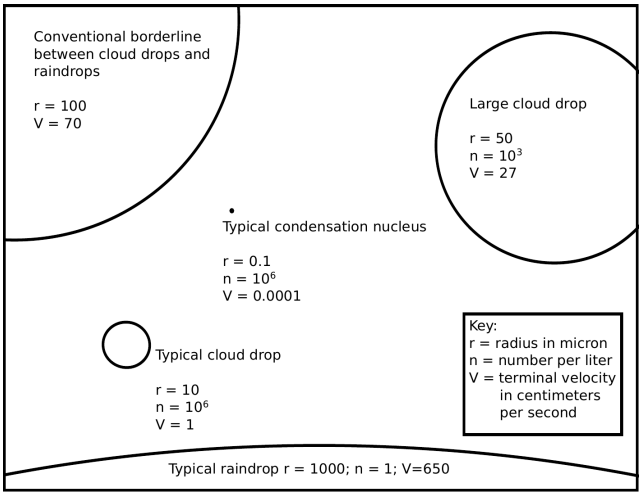

Figure 2.12: Illustration of different stages of a droplet (adapted from McDonald (1958), Figure 2).

2.3 Radiation Cloud Interactions

This section focuses on the interaction between radiation and clouds. Clouds and radiation interact with each other. On the one hand, clouds change radiation in the atmosphere. They scatter solar radiation back to space, cause shadows and therefore lower irradiance values at the surface, and they emit and absorb thermal radiation. Clouds affect the energy budget of the Earth atmosphere system and the modification of radiation by clouds is used in remote sensing to retrieve optical properties of clouds, either from space or from the surface. On the other hand, radiation affects the dynamics and microphysics of clouds. The effect of radiation on atmosphere and clouds is usually described by heating rates, the change in temperature and time (Eq. 2.18). In the following heating rates in the Earth's atmosphere and the interactions between radiation and cloud dynamics and microphysics will be described, with a particular focus on thermal radiation.

2.3.1 Heating Rates in the Atmosphere

The mathematical formulation to calculate heating or cooling rates in the atmosphere was already described in Section 2.1.2. But how is the distribution of heating or cooling rates in the atmosphere? During daytime, the general cooling in the atmosphere for cloudless conditions is about 0.5 to 1 K/d in the troposphere. At night, only thermal cooling occurs, resulting in a cooling rate of 1 to 2 K/d. However, heating or cooling rates can become orders of magnitude larger (several 100 K/d) at the interface between clouds and atmosphere which directly feed back onto the cloud. Solar radiation causes cloud side warming at the illuminated cloud side (Jakub and Mayer, 2015a; O'Hirok and Gautier, 2005) of about 100 K/d. In the thermal spectral range finite clouds show cooling at cloud tops and cloud sides as well as heating at the cloud bottom (Fig. 2.13). While there is a huge effect in the solar spectral range at the surface, depending on shadow or illuminated regions in the surface irradiance (Jakub and Mayer, 2015a; Wißmeier and Buras, 2012; Wapler and Mayer, 2008), the surface irradiance effects are much smaller in the thermal spectral range. Nevertheless, they exist. Ellingson (1982) showed that the neglect of cloud dimensions causes uncertainties in surface and TOA irradiance. For idealized cylindrical clouds more downwelling irradiance at the surface (of about 4%) and less upwelling irradiance at TOA (of about 8%) was found compared to flat-plate clouds. Heidinger and Cox (1996) found that about one third of the radiative forcing at the surface may be due to cloud side effects. But more relevant than these domain-averaged or surface effects are local effects in or close to the cloud: Former studies found thermal cooling rates up to 628 K/d in realistic 3D clouds (Kablick et al., 2011) or about 816 K/d in cylindrical clouds. Heating rates also vary locally within a cloud, especially in a 2D analysis (Mechem et al., 2008). Liou and Ou (1979) looked at finite cubic, rectangular and plan-parallel clouds at a wavelength of 10 μm with a 3D radiative transfer solution. They found that more cooling occurs at the tops of cubic clouds compared to plane-parallel clouds. Harshvardhan et al. (1981); Harshvardhan and Weinman (1982) also looked at cuboid clouds and cylindrical clouds and found, similar to Liou and Ou (1979) strong cooling at cloud tops and clouds sides and modest warming at the cloud bottom. The largest warming at cloud bottom occurs in

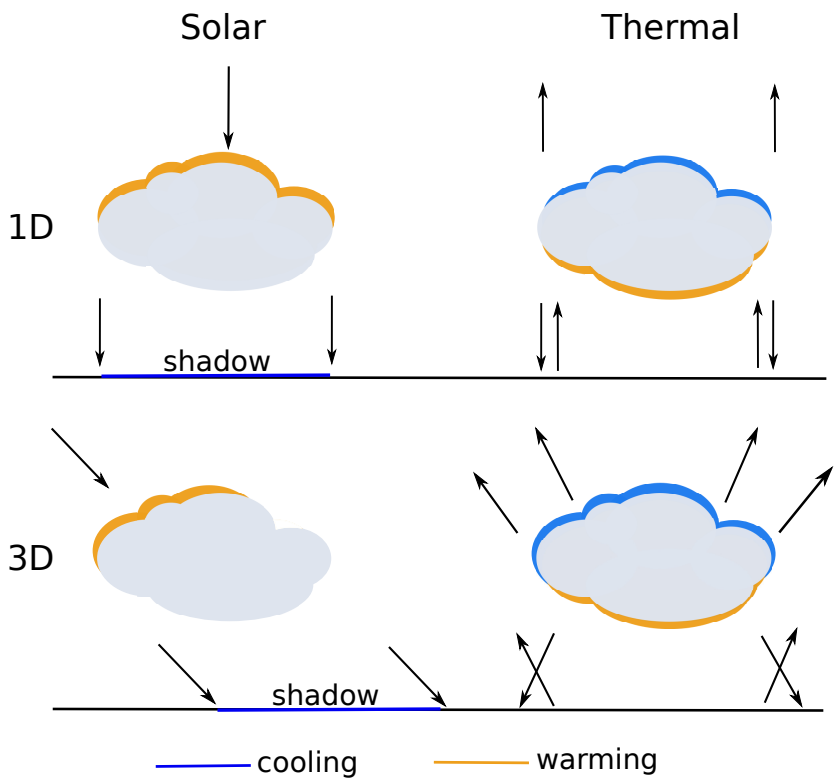

Figure 2.13: Schematic illustration of heating and cooling rates at a cloud in the solar and thermal spectral range for 1D and 3D radiation. In the solar spectral range the heating is at the illuminated cloud side, which is always at cloud top in a 1D approximation, while it varies with the solar zenith angle in a 3D radiation solution. In the thermal spectral range, additional cloud side cooling occurs in the 3D case, compared to the 1D radiation solution. At the surface, the shadow is shifted according to the solar zenith angle in the solar spectral range. In the thermal diffuse up- and downward radiation is spread more in the horizontal.

the center of the cubic cloud bottom, while it converges towards a light cooling at the side of the cubic cloud bottom. They found that the thermal cooling for finite, isolated cubic clouds can be up to three times the magnitude for plane-parallel clouds, due to the cooling through cloud sides. For plane-parallel clouds, emission occurs only at cloud top and bottom. For finite, isolated cubic clouds emission occurs at the top, bottom, and four side faces of the cloud. A factor of three in the emission remains. This factor varies with different aspect ratios of cuboid clouds. Harshvardhan et al. (1981); Harshvardhan and Weinman (1982) also state that clouds interact with each other and that the neglect of horizontal transport of radiation causes uncertainties in the radiation calculation. The uncertainties depend on the aspect ratio of the cuboid cloud and the cloud fraction. For an aspect ratio of 1 and a cloud cover between 0 and 0.5, the cooling of cubic clouds is a factor of 1.5 to 3 stronger respectively, compared to plane parallel clouds. For larger cloud side areas, this factor increases, for lower cloud side areas, the factor decreases. This last finding, concerning the importance of horizontal transport of radiation is further confirmed by Ellingson and Kolczynski (1980) and Ellingson (1982). Guan et al. (1995) used a simplified 3D radiation model to study cylindrical clouds. They also found the enhanced cooling due to 3D effects. They noted that the heating and

cooling rates are located close to the cloud side, in their case within the first 50 m of the cloud edge. Davies and Alves (1989) also found cloud cooling located at the first 50 m within a cloud. They performed high resolution (10 m) simulations of a stratocumulus cloud. Their average cooling rates were about 240 K/d but they found minimum coolings of more than 900 K/d. In their study, the heating and cooling rates were determined by the liquid water content and its gradient into the cloud. Ackerman et al. (1988) also found a dependence of the heating and cooling rates on cloud properties. They studied tropical anvils and found that the heating and cooling rates in the ice anvil depends on the ice water path. But heating rates do not only depend on liquid or ice water path. Radiation effects strongly depend on cloud geometry, cloud size, and cloud shape. Takara and Ellingson (1996) and Takara and Ellingson (2000) studied geometry and scattering effects in the thermal spectral range. While scattering effects are of minor importance and cause uncertainties up to 5% according to their latter study, cloud geometry plays an important role in terms of heating rates and fluxes. In addition, the magnitude of heating rates depends on particle size of a cloud (Fu et al., 1995) or and on liquid water content and droplet number concentration (Petters et al., 2012). They state that the aerosol indirect effect also affects heating rates. Very recent work of Lábó and Geresdi (2016) showed that an increasing droplet number concentration due to higher aerosol numbers increases the longwave cooling in clouds. They also looked at the dependence of the heating rates due to different microphysical parameterizations in cloud resolving models. They studied heating and cooling rates of a stratocumulus cloud, simulated with a bulk microphysics scheme and with resolved bin microphysics. Stronger cooling was found for bin microphysics. Although liquid water content was constant in all the simulations, the effective radius varied between the bulk and bin microphysical results which leads to different optical thicknesses of the clouds. This causes the difference in the cooling rates.
What most of these studies have in common is that the use of common 1D approximation of radiative transfer in comparison to 3D radiative transfer, and the common description of clouds as plan-parallel, homogenous layers in comparison to finite, 3D structures may cause huge uncertainties in the radiation simulations (Han and Ellingson, 1999; Takara and Ellingson, 1996, 2000; Heidinger and Cox, 1996; Ellingson, 1982; Liou and Ou, 1979). Also, a more recent study by Benassi et al. (2004) pointed out the differences in applying ICA, plane-parallel and 3D radiation. They showed that 1D approximations can be used in overcast cloud cases, but they also showed that horizontal transport of radiation is important in broken cloud fields, because thermal fluxes depend on the cloud fraction, optical depth and geometry.
In addition to all these modeling studies, there are also measurements of thermal heating rates available. During the POST (Physics of Stratocumulus Top) campaign, stratocumulus clouds were observed at the Californian coast (Gerber et al., 2013). During this flight campaign, cloud properties (liquid water content, droplet size) and irradiance were measured at the same time. It could be shown that measured thermal heating and cooling rates are in the same order of magnitude as simulated heating or cooling rates (Gerber et al., 2014).

2.3.2 Effect of Radiation on Cloud Dynamics and Microphysics

In the previous section, the phenomenological aspect of heating rates was described. But what happens if the heating and cooling of thermal (or solar) radiation at clouds interacts

with cloud dynamics and microphysics? Different hypotheses were raised in the past on the effect of thermal radiation on clouds. Horizontal differential heating (due to 3D thermal radiation) between cloud sides and the cloud center produces, according to Guan et al. (1995), a secondary circulation in the cloud and thus enhances cloud growth. The vertical differential heating and cooling in the longwave spectral range at clouds causes a destabilization of the cloud (Fu et al., 1995). The radiative destabilization, furthermore, generates buoyancy in the clouds (Sommerai, 1976) and thermal cooling causes radiation induced condensation (Sommerai, 1976). Thermal cooling does not only affect cloud dynamics, but also microphysics. Before a cloud volume is heated or cooled, a cloud droplet absorbs and emits radiation. Thus the cloud droplet gets warmer or cooler. By conduction of heat, the droplet restores equilibrium with its environment. These effects have to be accounted for in microphysical parameterizations, because they directly affect cloud droplet growth. Thermal cloud top cooling enhances cloud droplet growth (for example Roach (1976) or Harrington et al. (2000)). In the following, a more detailed look on these dynamical aspects, as well as additional changes in the microphysics of clouds due to radiation will be summarized:

Effect of Radiation on Cloud Dynamics

A number of studies exist, which focus on the effect of longwave radiation on ice clouds. Ramaswamy (1986) found that the longwave cooling is about one third stronger than solar heating in ice clouds. The heating or cooling rates, however, strongly depend on the ice water amount in the cloud and the ice crystal size. In very thin ice clouds, solar heating might even compensate thermal cooling. The effects of radiation on ice clouds and the ice cloud properties on heating and cooling rates cannot be separated, because one effect usually causes the other. Turbulence within the ice cloud increases due to longwave effects which in turn feeds back on the ice crystals themselves. Liu et al. (2003) looked at longwave effects in cold and warm cirrus clouds. Whether a cirrus is named cold or warm depends (in their study) on the height in the atmosphere and the temperature where the cirrus occurs. For cold and optically thin cirrus clouds they found longwave warming in the entire cloud, while for warm cirrus clouds, they observed the typical longwave cooling at cloud top and the warming effect at cloud bottom. They also found that the latent heat released by condensation was smaller than the longwave cooling. Again, they also observed effects in the cloud turbulence due to radiation which significantly affected the cloud development.
Mixed phase clouds were investigated by Smith et al. (2009). They looked at observations, combined with radiative transfer simulations. According to them longwave radiative effects are one of the major processes in the cloud water budget. Longwave warming at the cloud bottom causes evaporation, while longwave cooling at cloud top results in increased condensation.
Many studies found increased turbulence within the cloud due to longwave radiative effects. Davies and Alves (1989) and Fu et al. (1995) showed that cooling at the cloud top is a generator for turbulence in the cloud. Cloud bottom warming and cloud top cooling destabilizes the cloud, resulting in more turbulence. Fu et al. (1995) also found that the clear sky cooling enhances convection and precipitation. Petters et al. (2012) looked at radiative-dynamical

feedbacks of stratocumulus clouds in combination with the aerosol indirect effect. They found that liquid water path decreases when the droplet number increases. This in turn reduces longwave cooling, because longwave cooling depends on the liquid water content of a cloud. The cloud circulation is weaker, due to less cooling and the turbulence decreases. Larson et al. (2001) showed that longwave cooling on the one hand enhances condensation and thus increase liquid water content; on the other hand, radiation causes more entrainment and therefore a decrease in liquid water content. Therefore, two competing effects exists. It is unclear which one is the dominating effect. Heymsfield et al. (1991) stated that the effects of longwave cooling on cloud development depend on the cloud temperature. Larger effects of radiative cooling could be found in cold clouds, while in warm clouds latent heat release almost cancels the cooling effect. Curry and Herman (1985) also looked at the balance between latent heat release, evaporative cooling and radiative cooling. According to them 10% of the cloud top longwave cooling can be compensated by sensible heat fluxes from below, but some cooling always remains. They also found increased convection due to radiation, an increased liquid water content and enhanced droplet growth. Tao et al. (1993) found an increase in precipitation of 14-31% due to longwave effects and Tao et al. (1996) saw an increase in relative humidity, enhanced circulation and microphysical processes. Xu and Randall (1995) found a longer lifetime of clouds when simulating clouds with interactive radiation. Guan et al. (1997) divided the lifetime of a cloud in three stages. They used a simplified, axially symmetric, 3D radiative transfer model for their study. In the first stage, due to longwave radiation, an increase in maximum liquid water content as well as in the averaged values could be found. In return, the increased liquid water content, causes stronger cooling rates. In the second stage, cooling from radiation and evaporation causes a downward motion at the outer shell of the cloud, low level convergence and therefore a stronger cloud development. In the final stage of the cloud, the strong negative buoyancy caused by longwave cooling leads to a faster decay of the cloud. Yamaguchi and Randall (2012) traced individual cloud parcels in a stratocumulus cloud and investigated the effects on entrainment. Parcels affected by entrainment were found, due to the sinking motion, in cloud holes. Entrained air is brought down by negative buoyancy which results from radiative cooling, evaporation or mixing. Therefore, Yamaguchi and Randall (2012) separated radiative and evaporative cooling of an entrained cloud parcel to estimate the main contribution of the cooling. They found only a small fraction of the cooling in entrained parcels was due to radiative cooling. The main cooling was gained by mixing. The small contribution of radiative cooling to the total cooling of an entrained parcel can be explained by the location of the entrained parcels and the radiative cooling. Entrained parcels rested for a very short period in the radiatively cooled regions. The regions of strongest radiative cooling were located at cloud tops.

For the matter of completeness, two examples for the effect of solar radiation on cloud development will be shown. However, as the main focus of this thesis is on the effect of thermal radiation, this will be kept short. Generally the heating rates in the solar are about one third of the thermal cooling rates and are therefore compensated completely by the longwave cooling. Therefore studies focus on the cloud shadow effect, which is a very dominant feature in the solar spectral range. Schumann et al. (2002) studied the cloud shadow effect in the convective boundary layer with an idealized setup. They showed non-steady convective motion if the shadow of the cloud was located directly below the cloud and an reduction in the cloud

own buoyancy, compared to a shifted shadow. Markowski and Harrington (2005) also found an effect on thunderstorm dynamics if cloud shading is accounted for. (Wapler, 2007) found that the shadow at the surface causes asymmetries in the cloud development.

Effects of Radiation on Cloud Microphysics

Stephens (1983) showed that longwave cooling enhances ice crystal growth and suppresses evaporation of ice crystals. Another study with similar findings was published by Gu and Liou (2000). Again, radiation effects on ice clouds were studied. When ice water content reaches a certain value, longwave radiation effects become significant. In the very moment that radiative effects exist, ice crystal growth and sublimation are affected by the longwave heating or cooling. They also stated that the radiative effect is quite significant and that a larger number density of large ice crystal and a reduced number density of small ice crystals was observed in their simulations. Some studies focused on diffusional cloud droplet growth caused by longwave cooling. One of the first studies were those by Roach (1976) or Barkstrom (1978). Roach (1976) found enhanced droplet growth especially for droplets of 10 μm radius or more, Barkstrom (1978) stated that the growth rate is up to 20 times larger if thermal radiation is involved. Austin et al. (1995), Harrington et al. (2000), Marquis and Harrington (2005), and Lebo et al. (2008) had similar findings. Hartman and Harrington (2005a,b) found that the time for collection onset (the time when cloud droplets start growing to rain droplets by collection) is reduced if thermal emission is accounted for. Possibly, the radiative effect on droplet growth could close the existing gap in droplet growth theory. Up to now, droplet diffusional growth slows down at about 10 μm droplet size. However, the process of collision and coalescence only takes place when droplets have a minimum size of 20 μm (Rogers, 1979; Mason, 1960). Recent work of Brewster (2015) showed in a theoretical study that thermal cooling near the surface of a cloud droplet can affect supersaturation significantly. That change in supersaturation, according to Brewster (2015), is enough to provide the missing mechanism between non-radiative diffusional growth and turbulent coalescence growth.

2.4 Radiation and Clouds in Atmospheric Models

This section focuses on the different types of atmospheric models that exist, the representation of radiation in atmospheric models, as well as the representation of clouds in atmospheric models. The section is based on Holton (2003), if not stated otherwise.
Atmospheric models are required to study processes in the Earth's atmosphere. To describe the atmosphere, the domain investigated is split into grid boxes of different length and height. The size of such a grid box describes the process that can be investigated. A process (for example cloud formation or heat transport) is called *resolved* if the grid box size is much smaller than the scale of the process. Processes on smaller scales than the one resolved are referred to as *sub grid scale processes* and are parameterized.
Fig. 2.14 summarizes processes and scales resolved by different atmospheric models, which will be described in the following.
The whole range of spatial and temporal turbulence is resolved in so called *direct numerical*

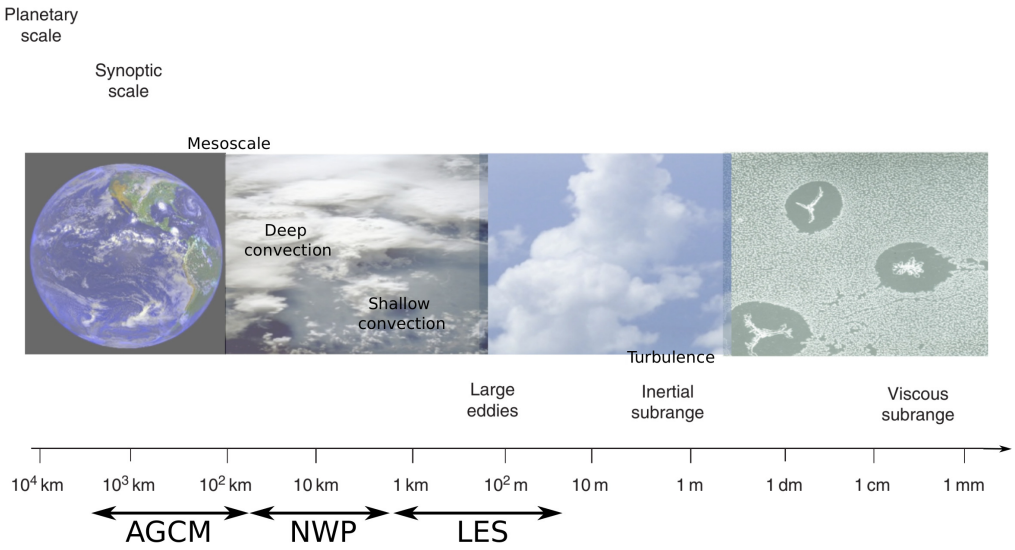

Figure 2.14: Atmospheric horizontal scales, corresponding processes and corresponding atmospheric models (adapted from ARM (2010), Figure 4 and Holton (2003), General Circulation Models, Figure 3).

simulations (DNS). DNS, however, are far too expensive in terms of computational cost and memory capacity that they could be used so solve atmospheric problems on larger domains than a few meters.

Large eddy simulation models (LES models) are models driven on a resolution of a few meters to a few hundred meters. They simulate energy containing eddies (where most of the *turbulent kinetic energy* (TKE) is stored), but still contain unresolved scales which are parameterized. But, because only a small fraction of the energy is stored in the unresolved, sub grid scale processes, it is assumed that the important features of the flow are insensitive to the parameterizations and that the models work correctly. LES are widely used to study boundary layer processes such as convection, entrainment, radiation or condensation. In this work, an LES model (UCLA-LES; Stevens et al. (2005)) will be used to study the effects of thermal radiation on cloud evolution.

If LES models are used, clouds are simulated by using microphysical schemes. Two types of microphysical schemes exist: *bulk microphysics schemes* and *spectral or bin microphysics schemes*. A detailed description about microphysical schemes in the past and present including various types is given in (Khain et al., 2015). Bin (or spectral) microphysical parameterizations are regarded to be the most sophisticated ones. They have the aim to calculate microphysics as accurate as possible by binning microphysical particles into different size regimes and compute the evolution of each of these size bins separately. The output of such a simulation is the size distribution of a specific hydrometeor (for example cloud droplets). They are used by today in LES models, but are too expensive to be used in operational models such as AGCMs or NWP-models. Spectral or bin models can have a huge amount of prognostic variables (100 - 300 variables) and their computational costs are by a factor of 5-20 larger compared to bulk microphysical schemes.

Bulk microphysical parameterizations do not explicitly calculate the size distribution of par-

ticles. Instead, moments of the size distribution (often described by a gamma or exponential distribution) are predicted. In a *one moment scheme*, only liquid water content is predicted, while in *two moment* or *three moment schemes* droplet concentration and liquid water content as well as droplet concentration, liquid water content, and radar reflectivity respectively are simulated.

Radiation is usually treated poorly, due to the enormous computational cost. A quite common approach is to add a representative cooling (for example 2.5 K/d) into the whole atmosphere instead of solving radiative transfer properly. At best, 1D interactive radiation is applied as independent column approximation to account for the 3D distribution of clouds. The 1D ICA radiation approximation introduces errors in a simulation, by failing to reproduce 3D effects (such as for example shifted shadows or cloud side cooling). 3D radiation schemes for LES or high resolution weather prediction models are currently developed (like in this work, or for example Jakub and Mayer (2015a)). Hogan and Shonk (2013) developed a 3D solar flux approximation for climate models.

Numerical weather prediction models (NWP models) are used to predict the weather for limited periods of time and areas. Their resolution ranges from about 3 km - 50 km, depending if they are driven as regional or global NWP models. If NWPs are driven as regional NWPs they do not govern the whole atmosphere, but only a certain region, they have boundaries in the horizontal and vertical (while AGCMs or global NWPs only have boundaries in the vertical). With a variety of different methods (for example nesting), boundary conditions are provided to a regional NWP model. They are often taken from global NWPs and the initial conditions are essential for a successful weather prediction.

Atmospheric general circulations models (AGCM) are models which describe the general circulation of the atmosphere. They are often also referred to as *climate models* and are used for climate prediction simulations. Their resolution (the grid box size in the horizontal) ranges in today's AGCMs between 50 - 250 km. Atmospheric processes smaller than this resolution (for example clouds or precipitation) are approximated by parameterizations. AGCMs usually cover the entire Earth and the Earth's atmosphere.

Radiation and clouds are poorly resolved in AGCM and NWP models. The most common approach for radiative transfer in atmospheric models is the two-stream method (Section 2.1.3). AGCMs or NWP models, due to their resolution, do not resolve cloud processes explicitly. Therefore cloud parameterizations are necessary. Those are called *cumulus convection parameterizations*. An overview about the history, current and future developments, aims and limitations of such parameterizations is for example given by Arakawa (2004). Different forms of convection parameterizations exist. One of the most basic assumptions is to look at a single grid box. A grid box is usually considered as cloudy, if the relative humidity reaches 100% and the atmosphere is unstable. However, this implies that a grid box is either covered completely by clouds (cloud fraction = 100%) or not cloudy at all (cloud fraction = 0%). Furthermore, it is known that different microphysical processes exist (Section 2.2). To avoid the complex treatment of microphysics (heterogeneous, homogeneous condensation or diffusional growth of droplets), it is for simplicity reasons assumed that there is always a sufficient number of CCN available in the model and condensation occurs whenever supersaturation is achieved. Many processes are still unresolved or neglected in cloud parameterizations in AGCM and NWP models, such as radiation effects, entrainment or microphysics. The poor treatment of clouds

feeds back on the radiation calculation in AGCM and NWP models. For radiative transfer, a fractional cloud cover, next to detailed optical properties such as liquid water content and effective radius of clouds, is essential. This however is not well represented by most atmospheric models and causes additional uncertainties in the radiation calculation, next to the neglect of 3D effects in the radiation calculation.
The resolution dependence of clouds is summarized in Fig. 2.15 and Fig. 2.16. Fig. 2.15 shows a cloud scene, required by the NASA satellite Aqua, by the moderate resolution imaging spectroradiometer (MODIS). The original scene is about 450 km in the horizontal and 300 km in the vertical with a resolution of 250 m. The image was modified to account for different model resolutions, representing AGCM, NWP and LES models. It can be seen that with decreasing model resolution more and more features of the clouds get lost. Fig. 2.16 shows visualizations of cumulus clouds from LES simulations at a resolution of 2 km and 50 m. The development of cloud and radiation parameterizations in the past has let to an artificial separation of both physical processes, although they are so closely linked in reality. One of the major tasks in the future will be to bring both processes together again. On the one hand this includes radiation parameterization that also affect the cloud development itself through heating and cooling via heating rats in the clouds, affecting microphysics, and dynamics. On the other hand, radiation parameterizations have to be capable of representing the effect of clouds on radiation fluxes. Cloud parameterizations have to be capable of describing the generation and dissipation of clouds and precipitation (in interaction with radiation).

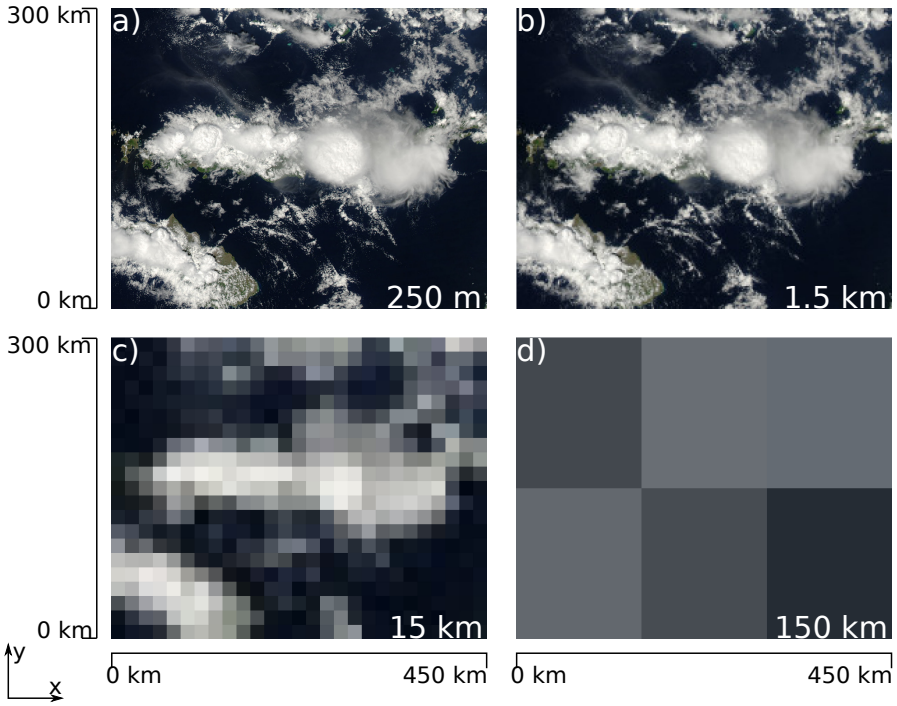

Figure 2.15: Schematic illustration of different model resolutions (Source of original picture: NASA/Jeff Schmaltz, LANCE/EOSDIS MODIS Rapid Response Team, NASA GSFC)

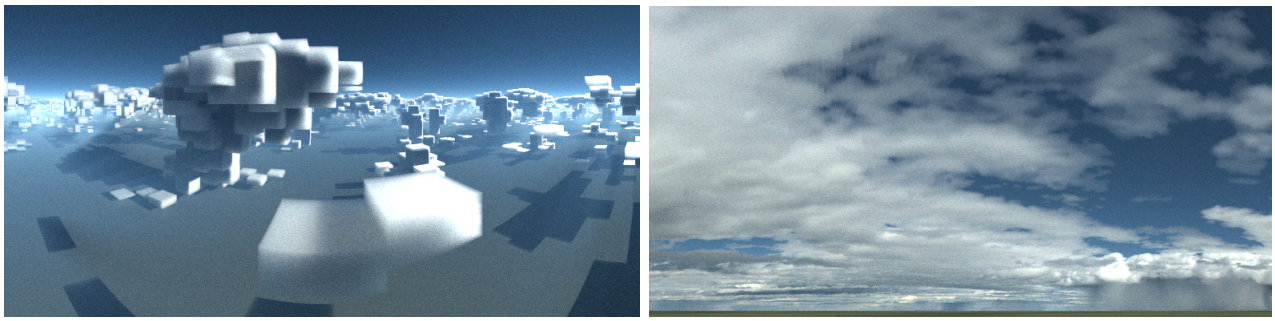

Figure 2.16: Visualization of a cumulus cloud field from a LES simulation with 2 km resolution (left) and with a resolution of 50 m (LES-Simulation, 2 km, left: Katrin Scheufele, EULAG Model; LES-Simulation 50 m; right: Christopher Moseley, UCLA-LES; Visualization with MYSTIC).

2.5 Summary and Thesis Outline

In this chapter, the close link between clouds and radiation, the complexity of clouds and radiation in the Earth atmosphere system and different approaches to model both processes on different scales and in different model types have been described and pointed out. Knowing that many approximations are made to model clouds and radiation in today's climate, weather, and cloud resolving models, it is obvious that improvements of the existing methods is desirable.

This thesis aims to improve our understanding of cloud-radiation and radiation-cloud interactions in the thermal spectral range in a 3D environment. It has also been shown that former studies found considerable uncertainties in model performance when 1D radiation approximations are applied and that thermal radiation has an effect on cloud development. However, the studies so far were only able to investigate these effects by using 1D radiation parameterizations. New methods to calculate 3D thermal radiative transport are necessary for the investigation in this thesis and have been developed. The effect of radiation on cloud development is analyzed by incorporating 3D radiation into a cloud resolving model and performing appropriate simulations (for more details see Chapter 3).

Chapter 3

Methods

Aim of this thesis is to quantify the effect of thermal radiation, especially 3D thermal radiation on cloud development. For this, a cloud model (in this thesis, the UCLA-LES; Stevens et al. (2005)) is needed which can be run with a 3D radiation scheme. However, up to today, such schemes do not exist. All existing 3D thermal radiation schemes are far too expensive to be used in a cloud resolving model. Therefore, such a scheme was developed within this thesis. For the development of a fast scheme, a benchmark model is required which allows accurate heating rate calculation. The MYSTIC Monte Carlo code (Mayer, 2009) was extended to allow reasonably fast calculations of thermal heating rates.
Three steps were necessary in order to study the effects of 3D thermal radiation on cloud development:

1) Quantify magnitude of typical thermal heating rates and provide accurate benchmark results by performing 3D radiative transfer simulations with an accurate radiative transfer model.

2) Develop a fast, but still reasonably accurate parameterization for the calculation of 3D thermal heating rates which can be implemented in a cloud resolving model, based on the knowledge gained in 1).

3) Implement the newly developed 3D thermal parameterization into a cloud resolving model and estimate the effect of thermal radiation on cloud development by a set of cloud simulations.

3.1 3D Thermal Heating Rate Calculation

The contents of Section 3.1 were published by Klinger and Mayer (2014). The following text and figures are adopted from the publication, with only a few editorial changes.
The first step of this thesis is to quantify (3D) thermal heating rates, gain knowledge about the difference between 1D and 3D thermal heating rates, their magnitude and their dependences for example on optical properties, geometry or model resolution. For this, new and fast, so called Monte Carlo variance reduction techniques for the calculation of 3D thermal heating

rates were developed and implemented into the Monte Carlo model MYSTIC (Mayer, 2009). The general idea about the Monte Carlo method was already explained in Section 2.1.3. In this section, the new approach for thermal heating rates developed for this work is explained. Forward and backward photon tracing methods are compared and new variance reduction methods to speed up the calculations are presented. It turns out that backward tracing is in most cases superior to forward tracing. Since heating rates may be either calculated as difference between emitted and absorbed power per volume or alternatively from the divergence of the net flux, both approaches have been tested. It was found that the absorption/emission method is superior (with respect to computational time for a given uncertainty) if the optical thickness of the grid box under consideration is smaller than about 5 while the net flux divergence may be considerably faster for larger optical thickness. In particular, the following three backward tracing methods are described: the first and most simple method (EMABS) is based on a random emission of photons in the grid box of interest and a simple backward tracing. Since only those photons which cross the grid box boundaries contribute to the heating rate, this approach behaves poorly for large optical thicknesses which are common in the thermal spectral range. For this reason, the second method (EMABS_OPT) uses a variance reduction technique to improve the distribution of the photons in a way that more photons are started close to the grid box edges and thus contribute to the result which reduces the uncertainty. The third method (DENET) uses the flux divergence approach where – in backward Monte Carlo – all photons contribute to the result, but in particular for small optical thickness the noise becomes large. The three methods have been implemented into MYSTIC (Monte Carlo code for the phYSically correct Tracing of photons In Cloudy atmospheres). All methods are shown to agree within the photon noise with each other and with a discrete ordinate code for a one-dimensional case. Finally a hybrid method (HYBRID) is built using a combination of EMABS_OPT and DENET, and application examples are shown. It should be noted that for the HYBRID application, only little improvement is gained by EMABS_OPT compared to EMABS.

3.1.1 Theoretical Background

For the general concepts of Monte Carlo photon tracing and the implementation in MYSTIC, the reader is referred to the literature, e.g. (Marshak and Davis, 2005; Mayer, 2009). In the following, aspects relevant for the calculation of thermal heating rates will be addressed. In forward Monte Carlo simulations, photons in the thermal infrared (IR) are emitted at random locations in the atmosphere, with a probability defined by the emission term (3rd term on the right side) of the radiative transfer equation (Eq. 2.16). In consequence, the emitted power per volume $\dot{q}_{\mathrm{em}}$ of a grid box in Eq. 2.18 can be calculated analytically according to

$$\dot{q}_{\mathrm{em}} = 4\pi\ \beta_{\mathrm{abs}}\ B(T) \tag{3.1}$$

where the factor 4π integrates the Planck radiance B(T) over the full hemisphere. It will be shown later, however, that the analytical calculation is not necessarily the fastest solution in a Monte Carlo calculation of heating rates. The atmosphere is usually divided into a number (N_{x}, N_{y}, N_{z}) of individual grid boxes with constant or linearly varying optical or microphysical

properties. $p(i,j,k)$ is the probability that a photon is emitted at a random location within grid box (i,j,k)

$$p(i,j,k) = \frac{B(T(i,j,k))\ \beta_{\text{abs}}(i,j,k)}{\sum_{\text{i,j,k}} B(T(i,j,k))\ \beta_{\text{abs}}(i,j,k)} \tag{3.2}$$

assuming constant optical properties and temperature within each individual grid box, and identical volumes for each grid box (the equation is easily generalized to non-uniform grid box volumes and temperature varying with height inside a grid box). Since molecular as well as cloud absorption coefficients are large in the thermal IR, photons are often absorbed spatially close to the emission and never reach the location where the radiation is to be calculated, for example the surface or TOA. They often don't even reach the boundary of the grid box where they are emitted and thus don't contribute to any irradiance or heating rate. In consequence, many photons are needed to get a statistical significant number of photons that contribute to the result which could be either the difference of photons emitted and absorbed in a specific volume (for the calculation of heating rates) or the amount of photons crossing a certain area element (for the calculation of irradiance). Backward Monte Carlo is an alternative: when photons are traced backward, photons are started at the location where the result is desired (for example an area element for the calculation of irradiance, or a grid box for the calculation of heating rates) and are traced until they are absorbed by the atmosphere or surface or leave the atmosphere at TOA (that is, the place where they would start in reality). For the backward calculation of fluxes or heating rates, every photon contributes to the result. According to the explanations above, there are two fundamentally different ways to calculate thermal heating rates in backward mode: The first method is to calculate the difference between the emitted and absorbed power in a volume while the second is based on net flux differences (Eq. 2.19). For the first method, the photon is started at a random location $\vec{x}_{\text{start}}$ in the grid box for which the heating rate is to be calculated and is traced through the atmosphere (from scattering to scattering), until the point $\vec{x}_{\text{end}}$ where it is absorbed (at the ground or in the atmosphere) or leaves the atmosphere at TOA. The "absorbed" photon is counted with a weight

$$W_{\text{abs}} = \beta_{\text{abs}}(\vec{x}_{\text{start}})\ B(T(\vec{x}_{\text{end}})) \tag{3.3}$$

In this implementation the start location of the photon is "recycled" to calculate a contribution to the emission of the grid box

$$W_{\text{em}} = -\beta_{\text{abs}}(\vec{x}_{\text{start}})\ B(T(\vec{x}_{\text{start}})) \tag{3.4}$$

Thus, a backward calculation of the absorption with a forward calculation of the emission is combined. It might seem more logical to do both calculations backward, but there is no reasonable way to calculate emission backwards since the emitted photon would have to be counted into the box where the photon path ends. This would, however, require that backward calculations were to be done for each grid box because each grid box might contribute to the backward emission of any other grid box. The heating rate is finally calculated by averaging the individual contributions W of all photons,

$$W = W_{\text{abs}} + W_{\text{em}} = \beta_{\text{abs}}(\vec{x}_{\text{start}})\ \left[B(T(\vec{x}_{\text{end}})) - B(T(\vec{x}_{\text{start}}))\right] \tag{3.5}$$

Obviously, the power emitted by a grid box could be easily calculated analytically according to Eq. 3.1. As will be shown later Eq. 3.5 converges more rapidly since the noise of the

emission and the noise of the absorption partially cancel which is not the case if the analytical expression for the grid box emission was used.
The advantage of the backward tracing is that only photons starting in the desired grid box need to be counted, while with forward tracing photons starting at any location in the atmosphere or the surface contribute to the result. It is immediately clear that photons which don't leave the grid box contribute little since temperature and absorption properties at the start and end locations are similar (or equal) and hence the weight is small. The second method is to calculate the net flux divergence Eq. 2.19. For this purpose, incoming and outgoing irradiance have to be calculated for the six faces of the grid box. In backward mode, photons are started inward and outward from the six faces and the 12 contributions to the net flux divergence have to be calculated independently. In the following the different methods to calculate the thermal heating rates in the Monte Carlo code MYSTIC are described, including the forward calculation and the two backward modes. Variance reduction methods to optimize each approach are introduced and their computational efficiency to determine the optimum method for the calculation of thermal heating rates is compared.

FORWARD – Forward calculation

In the standard forward photon tracing method, photons are emitted by the atmosphere or the surface. In this implementation, half of the photons are started from the surface with a probability proportional to $\epsilon_\mathrm{s} \cdot B(T_\mathrm{s})$ where ϵ_s is the surface emissivity and T_s is the surface temperature (both quantities may vary from grid box to grid box). The other half is emitted at random places in the atmosphere, sampling from the probability distribution in Eq. 3.2. Photons are traced from scattering to scattering until they are absorbed at the surface or leave the atmosphere at TOA. Absorption is considered by reducing the photon weight according to Lambert-Beer's law $exp(-\tau_\mathrm{abs})$ where τ_abs is the absorption coefficient integrated along the photon path. To convert the surface photon weights to absorbed power, the averaged weight is multiplied with the averaged emitted irradiance

$$\pi \, \frac{1}{N_\mathrm{x} N_\mathrm{y}} \sum_{\mathrm{i,j}} \epsilon_\mathrm{s} \; B(T_\mathrm{s}) \tag{3.6}$$

while for the atmospheric photons the average photon weight is multiplied with the averaged column-integrated emitted radiance

$$4\pi \, \frac{1}{N_\mathrm{x} N_\mathrm{y}} \sum_{\mathrm{i,j}} \int_0^{\mathrm{TOA}} \beta_\mathrm{abs}(i,j,k) \; B(T(i,j,k)) \; dz \tag{3.7}$$

These numbers are the average power emitted by the surface and the atmosphere (for completeness it is mentioned that in this implementation the Planck function varies linearly with height in each grid box and the temperature is actually specified at layer interfaces). Alternatively, one could have started photons at random locations in the atmosphere, not considering the probability distribution Eq. 3.2, and using $\beta_\mathrm{abs}(\vec{x}_\mathrm{start}) \cdot B(T(\vec{x}_\mathrm{start}))$ as photon weight. Since both absorption coefficient and temperature vary considerably in the atmosphere, this approach, however, turned out to be much more noisy than the described one. For the calculation of fluxes, the photon weights passing a given model level are counted while for the

determination of the absorbed energy, the fraction absorbed within a given grid box (again calculated by Lambert-Beer's law) is counted. Finally, the contributions of the atmosphere and surface are added.

EMABS – Backward Emission/Absorption

Here backward photon tracing is used to compute the difference of the power absorbed and emitted in a grid box. Photons are started at random locations in the grid box and absorption and emission of the grid box can be calculated according to Eq. 3.5. As mentioned above, the emitted power could be calculated analytically according to Eq. 3.1. However, it will be shown later that the statistical calculation is computationally more efficient for the purpose of calculating heating rates, as uncertainties cancel partially. In contrast to the forward calculation, this approach guarantees that all photons contribute to the result for the desired grid box. However, it is clear from Eq. 3.5 that the photon weight is proportional to the difference of the Planck functions at the start and the end of the photon trajectory. Photons which are absorbed close to the emission will contribute only little because the temperature difference is usually small. For optically thick grid boxes this method is therefore not efficient: most of the photons will be absorbed and emitted within the same grid box; if the temperature is considered constant in the grid box, they contribute zero; if the temperature is variable, their weights cancel to zero statistically. Only few photons, starting close to the edge, will "escape" from the grid box and might reach significantly different temperatures – these few photons will determine the heating rate. It would therefore be desirable to start more photons close to the grid box edges where they have a chance to escape the grid box and reach regions with temperatures different from those at the start location. This can be reached with variance reduction methods which are described in the following.

EMABS_OPT – Optimized Backward Emission/Absorption

One way to improve the performance of Monte Carlo codes are so-called "biasing" or "variance reduction" methods: photons may be forced to leave the grid box by starting them closer to the edge rather than evenly distributed over the volume. In order to keep the result correct, the photon weight needs to be adjusted accordingly. For example if the number of photons starting in a certain sub-area is doubled, their weight needs to be reduced by a factor of 2 accordingly.

A simple example

Imagine a volume V in which a number of photons N_0 is started at random locations. Each of the photons contributes with an individual weight to the result which is the average of all weights. Now, imagine that the volume is split into two sub-volumes V_1 and V_2, and that the number N_0 of photons started is split as well, according to the volume fraction $N_{01} + N_{02} = N_0$ with $N_{01} = V_1/V \cdot N_0$ and $N_{02} = V_2/V \cdot N_0$. If tracing the photons now and summing all weights, the same result is reached. Now let the number of photons be distributed unequally into $N'_{01} = N_{01}/\omega_1$ and $N'_{02} = N_{02}/\omega_2$ with

$$N'_{01} + N'_{02} = N_0. \tag{3.8}$$

To obtain a correct result, the photons have to be weighted with ω_1 and ω_2, respectively.

In a heating rate calculation, photons from the center of an optically thick grid box usually contribute less to the heating rate than photons starting closer to the edges. In the following it will be illustrated how to distribute the photon start positions in order to minimize the uncertainty of the result for a given total photon number: assume that photons from V_1 are less likely to leave the grid box than photons from V_2. For the heating rate calculation this means that the average photon weight W_1 (according to Eq. 3.5) for photons from V_1 will be smaller than W_2 for the photons from V_2. To optimize the uncertainty, the weights have to be known, and since they are not known a priori (but only after a full Monte Carlo calculation), they have to be estimated. It has to be noted already that the accuracy of this estimate does not affect the average but only the statistical noise and each approximation which is better than the implicit standard assumption ("V_1 and V_2 contribute equally to the result") will reduce the noise. For that purpose, it is assumed that all photons leaving the grid box will contribute the same amount to the result while those which don't leave the grid box don't contribute. The weights ω_1 and ω_2 are therefore determined by the fractions p_1 and p_2 of photons leaving the grid box which is called *escape probabilities*. With this approximation the Monte Carlo calculation is reduced to a simple yes/no experiment and the binomial distribution can be applied to calculate the uncertainty. The average photon numbers counted are simply $N_1 = p_1 N'_{01}$ and $N_2 = p_2 N'_{02}$ (both meaning averages in the limit of large photon numbers N_0).
The higher the escape probability, the more photons will contribute to the result and the smaller the uncertainty. The uncertainty of a result is quantified by the variance of the binomial distribution var $= \sigma^2$.

$$\sigma_1^2 = N_{01}\, p_1\, (1 - p_1) = N_{01}\, \alpha_1; \quad \sigma_2^2 = N_{02}\, p_2\, (1 - p_2) = N_{02}\, \alpha_2 \tag{3.9}$$

with

$$\alpha_1 = p_1\, (1 - p_1); \quad \alpha_2 = p_2\, (1 - p_2) \tag{3.10}$$

and for the new, unequal distribution:

$$\sigma_1'^2 = N'_{01}\, \alpha_1; \quad \sigma_2'^2 = N'_{02}\, \alpha_2 \tag{3.11}$$

(note that the averages and variances refer to photon number). The result of the calculation is

$$\text{avg} = \omega_1\, N_1 + \omega_2\, N_2 \tag{3.12}$$

and the variance is

$$\begin{aligned} \text{var} &= \omega_1^2\, \sigma_1'^2 + \omega_2^2\, \sigma_2'^2 \\ &= \omega_1\, N_{01}\, \alpha_1 + \omega_2\, N_{02}\, \alpha_2 \end{aligned} \tag{3.13}$$

Introducing the constraint Eq. 3.8 ω_2 is eliminated and

$$\text{var} = \omega_1\, N_{01}\, \alpha_1 + \frac{N_{02}^2}{N_0 - N_{01}/\omega_1}\, \alpha_2 \tag{3.14}$$

is obtained. The minimum is determined by setting the derivative $\frac{\partial \mathrm{var}}{\partial \omega_1}$ equal to 0 and by solving for ω_1:

$$\omega_1 = \frac{N_{01}}{N_0} + \frac{N_{02}}{N_0}\sqrt{\frac{\alpha_2}{\alpha_1}}; \quad \omega_2 = \frac{N_{02}}{N_0} + \frac{N_{01}}{N_0}\sqrt{\frac{\alpha_1}{\alpha_2}} \tag{3.15}$$

is obtained. From that the minimum variance can be calculated:

$$var_{\mathrm{opt}} = \frac{1}{N_0}(N_{01}\sqrt{\alpha_1} + N_{02}\sqrt{\alpha_2})^2 \tag{3.16}$$

To illustrate the results, a simple example with p_1=0.5 and identical photons numbers $N_{01} = N_{02} = N_0/2$ is shown. Table 3.1 shows the result for different p_2's, in particular the reduction in the variance by comparing it to the variance $\mathrm{var}_{\mathrm{std}}$ which would be obtained by distributing the photons equally instead of following Eq. 3.15 and Eq. 3.16. Obviously, the maximum improvement is a reduction of the variance by a factor of 2. This is not surprising because the best improvement is reached if p_2 is zero. The "standard" calculation would still trace half of the photons in each sub-volume and thus only half of the photons would contribute to the result. In the optimized calculation, all photons would be traced in the first sub-volume and the variance would be reduced by a factor of 2. It might seem disappointing that the maximum improvement is a factor of 2 in this example. However, it should be noted that the maximum reduction of the variance is actually $N_{01}/N_0 = V_1/V$ and for e.g. $V_1 = 0.1V$ (and $V_2 = 0.9V$) the maximum improvement would be a factor of 10. For this application this means that if a large number of photons from the interior of a grid box (V_2) can be distributed towards the edge (V_1) a large improvement may be reached. In the following, these consideration for an arbitrary number of grid boxes are generalized.

p_2	0.05	0.005	0.0005	0.0000
ω_1	0.718	0.571	0.522	0.500
ω_2	1.647	4.044	11.683	∞
$\mathrm{var}_{\mathrm{opt}}/\mathrm{var}_{\mathrm{std}}$	0.866	0.683	0.540	0.500

Table 3.1: Example calculation of the variance reduction.

General calculation

In this step, the principle idea of distributing the photons in two volumes to distributing photons into an arbitrary number N_{sub} of sub cubes is expanded. The example from 3.1.1 is easily generalized:

$$\omega_{\mathrm{i}} = \frac{1}{N_0}\frac{\sum_{\mathrm{j}=1}^{\mathrm{N_{sub}}} N_{0\mathrm{j}}\sqrt{\alpha_{\mathrm{j}}}}{\sqrt{\alpha_{\mathrm{i}}}} \tag{3.17}$$

is the weight of photons started in sub cube i and

$$var_{\mathrm{opt}} = \frac{1}{N_0}\left(\sum_{\mathrm{i}=1}^{\mathrm{N_{sub}}} N_{0\mathrm{i}}\sqrt{\alpha_{\mathrm{i}}}\right)^2 \tag{3.18}$$

is the minimum uncertainty.

In theory, it would be possible to divide the whole original grid box into equally-sized sub cubes. However, in the inner sub cubes, where the escape probability p_i and in consequence α_i are small, the photon weights become orders of magnitude larger than the weights of photons starting close to the edge, which will cause spikes in the Monte Carlo calculation; that is few contributions with very large weights which slows down convergence of the result. To avoid spikes and to save computational time and memory, only an outer layer of a specific *cut off optical thickness* (which will be optimized in section 3.1.2) is divided into sub cubes, leaving an inner cuboid with volume V_c and $N_{0\mathrm{c}} = V_\mathrm{c}/V \cdot N_0$. In addition to reduce the number of sub cubes, an upper limit is set to the photon weight and thus the magnitude of the spikes. The outer layer is again divided into a number of N_sub equally-sized sub cubes with certain optical thickness $\Delta\tau_\mathrm{sub}$, see Fig. 3.1, left. For the outer sub cubes the optimum photon weight is now

$$\omega_\mathrm{i} = \frac{1}{\sqrt{\alpha_\mathrm{i}}} \frac{\sum_{\mathrm{j}=1}^{\mathrm{N_{sub}}} N_{0\mathrm{j}}\sqrt{\alpha_\mathrm{j}} + N_{0\mathrm{c}}\sqrt{\alpha_\mathrm{c}}}{N_0} \tag{3.19}$$

For the inner cuboid, the optimum photon weight is:

$$\omega_\mathrm{c} = \frac{1}{\sqrt{\alpha_\mathrm{c}}} \frac{\sum_{\mathrm{j}=1}^{\mathrm{N_{sub}}} N_{0\mathrm{j}}\sqrt{\alpha_\mathrm{j}} + N_{0\mathrm{c}}\sqrt{\alpha_\mathrm{c}}}{N_0} \tag{3.20}$$

In consequence, the photon number to be started in the inner cuboid is $N'_{0\mathrm{i}} = \frac{N_{0\mathrm{i}}}{\omega_\mathrm{i}}$ and for the outer sub cubes $N'_{0\mathrm{c}} = \frac{N_{0\mathrm{c}}}{\omega_\mathrm{c}}$ with $\sum_{i=1}^{N_\mathrm{sub}} N'_{0\mathrm{i}} + N'_{0\mathrm{c}} = N_0$. To apply this method, one final piece is missing: The escape probability is not known a-priori and has to be estimated.

The escape probability

The escape probability is defined as the probability that a photon leaves its start grid box which is an estimate of its contribution to the heating rate. It is clear that the minimization of the uncertainty requires a reasonably accurate estimate of the escape probability. However, it has to be stressed that even a bad guess would only increase the noise of the result but would not affect the average. The escape probability of a sub cube certainly depends on the distance (measured in optical thickness τ units) from the grid box edges.

Consider a photon that is started somewhere in one of the sub cubes. The photon could escape through one of the 6 faces of the cube. First the escape probability for one of the six faces is calculated, in particular the lower xy plane, see Fig. 3.1, right. The probability of a photon escaping the grid box decreases exponentially with distance from the face according to Lambert-Beer's law $exp(-\frac{\tau_z}{\mu})$. For the estimation of the escape probability scattering is neglected, therefore $\tau = \tau_\mathrm{abs}$. The escape probability for the lower xy face is the average of the Lambert-Beer factor over the sub cube:

$$\begin{aligned} p \;=\; & \frac{1}{4\pi}\frac{1}{\Delta\tau^3}\int_{\mathrm{k}\Delta\tau}^{(\mathrm{k}+1)\Delta\tau}\int_{i\Delta\tau}^{(i+1)\Delta\tau}\int_{j\Delta\tau}^{(j+1)\Delta\tau} \\ & \int_0^{2\pi}\int_{\mu_g(\phi,\tau_x,\tau_y,\tau_z)}^{1} exp\left(-\frac{\tau_z}{\mu}\right) d\mu\, d\phi\, d\tau_y\, d\tau_x\, d\tau_z \end{aligned} \tag{3.21}$$

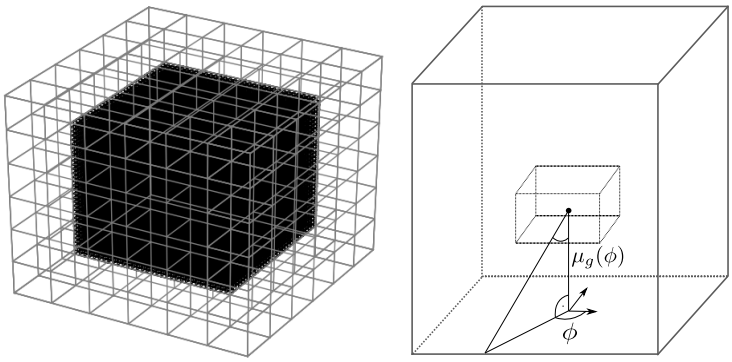

Figure 3.1: Left: Schematic figure of a grid box of optical thickness τ, divided into sub cubes and an inner cuboid. Right: illustration of the calculation of the escape probability for a given sub cube. The photon escapes through the lower xy plane. The escape probability is averaged over the sub cube and over the angles ϕ and μ_g.

where i, j, k is the index of the sub cube, counted from the respective face, starting from 0. $\Delta\tau$ is the optical thickness of the sub cube. This integral is complicated to evaluate and probably computationally expensive in the implementation since μ_g is a function of location within the sub cube and azimuth angle ϕ. Therefore more approximations are introduced. First, the Lambert-Beer factor varies fastest in the direction perpendicular to the considered face (in this example z) for which reason it is assumed that the Lambert-Beer factor is constant in the horizontal directions (in this example x and y); μ_g is also replaced by its average over the sub cube:

$$p \approx \frac{1}{4\pi}\frac{1}{\Delta\tau}\int_{k\Delta\tau}^{(k+1)\Delta\tau}\int_0^{2\pi}\int_{\mu_g(\phi)}^1 exp\left(-\frac{\tau_z}{\mu}\right)d\mu\, d\phi\, d\tau_z \tag{3.22}$$

This equation allows to calculate the escape probability for each face of the grid box. The total escape probability is the sum of the six individual escape probabilities. It is clear that the closest face contributes most to the total escape probability: The probability decreases with approximately a factor of $exp(-\Delta\tau)$ per k step. Therefore one final simplification is introduced: Only the escape through the closest face is considered and the other ones are neglected. To partially compensate the underestimation μ is integrated from 0 to 1 instead of μ_g to 1 – that is, the photons escape through only one horizontal plane extending to infinity rather than through the six faces. The biggest errors are expected for those points which have identical distances to two or three faces, that is, pixels lying on diagonals of the cube. Eq. 3.22 reduces to

$$p \approx p_{\text{an}} = \frac{1}{2}\frac{1}{\Delta\tau}\int_{k\Delta\tau}^{(k+1)\Delta\tau}\int_0^1 exp\left(-\frac{\tau_z}{\mu}\right)d\mu\, d\tau_z \tag{3.23}$$

which can be evaluated analytically to give

$$p_{\text{an}} = \frac{1}{2}\left[\left[\tau_z^2 Ei\left(-\frac{\tau_z}{\mu}\right) - \mu\, exp(-\frac{\tau_z}{\mu})(\mu-\tau_z)\right]_{\mu=0}^{\mu=1}\right]_{\tau=k\Delta\tau}^{\tau=(k+1)\Delta\tau} \tag{3.24}$$

where Ei is the "Exponential Integral" (Bronstein et al., 2006) which can be tabulated or is available as a function in various numerical packages. $\mu = 0$ has to be interpreted as $\lim_{\mu \to 0}$ and

$$p_{\text{an}} = \frac{1}{2} \left[\tau_z^2 Ei(-\tau_z) - exp(-\tau_z)(1 - \tau_z) \right]_{\tau=k\Delta\tau}^{\tau=(k+1)\Delta\tau} \tag{3.25}$$

is obtained. In the case of $k = 0$ the term in the brackets reduces to -1. To illustrate how well this approximation represents the escape probability, the approximation is compared to the real escape probability calculated by the Monte Carlo code (simply counting the number of photons escaping from each sub cube). Fig. 3.2 shows the results of the comparison. The approximated escape probability of most sub cubes lies close to the one-one-line and only those which have an identical distance to two or more faces (marked in orange) are underestimated considerably. In this particular example (20 x 20 x 20 = 8000 sub cubes), 28% of the data points have such a "special" location. The fit to all data points gives a slope of 0.85 with regression coefficient R^2=0.95, and if the "special" ones are excluded, a slope of 0.96 and a regression coefficient R^2=0.99 is obtained which confirms the high quality of the approximation. For this calculation a purely absorbing medium is assumed. The calculation was repeated by adding a scattering optical thickness of 20 with an asymmetry parameter of 0.8 (that is, the single scattering albedo was 0.5). The results (not shown) were hardly distinguishable which justifies the negligence of the scattering introduced earlier. In the thermal spectral range the asymmetry parameter is often larger than 0.9 (Hu and Stamnes, 1993) which means that a major fraction of the scattering is close to the forward direction and may thus be neglected for flux computations.
The performance of the approximation will be shown in Section 3.1.2 by comparing it to the maximum possible improvement.

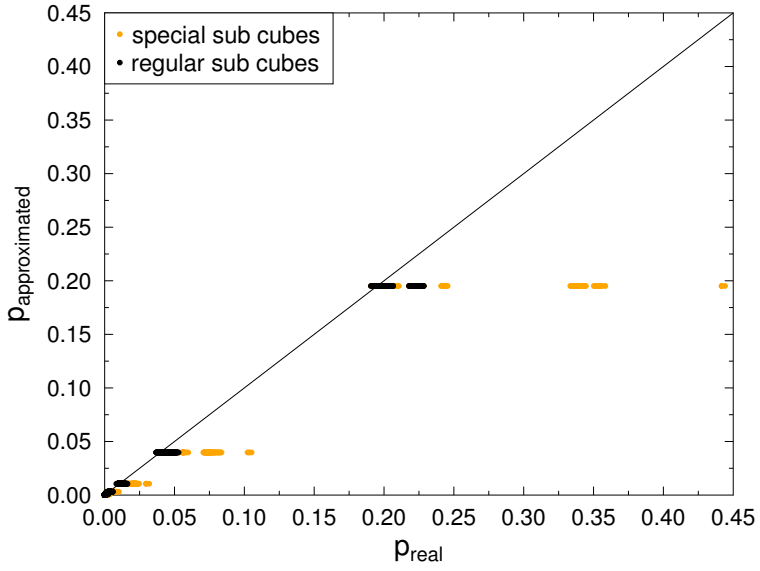

Figure 3.2: Comparison between real escape probability (calculated with Monte Carlo) and the approximated escape probability. The absorption optical thickness of the cube was 20 and the cube was divided into 20 x 20 x 20 = 8000 sub cubes.

Standard Deviation of the result

Here it is intended to determine the real uncertainty of the result which differs from the minimum variance var_{opt} since only an estimate of the escape probability is used to calculate the latter. The noise of a Monte Carlo calculation may be simply determined by repeating the calculation n times and determining the standard deviation of the n results. However, a much more accurate result is obtained when the standard deviation is calculated online from the individual photon weights according to

$$\sigma = \frac{1}{\sqrt{N_0}} \sqrt{\overline{W^2} - \overline{W}^2} \tag{3.26}$$

where $\overline{W}$ is the average photon weight and N_0 is the total number of photons started per grid box. Not going into detail here, it has to be pointed out that W has to be an estimate of the heating rate. For EMABS and EMABS_OPT each photon weight is already an estimate of the heating rate while for DENET one needs to consider that the heating rate is calculated as a weighted average of the in- and outgoing irradiance at the six faces which needs to be considered in the calculation of the standard deviation.

DENET – Net Flux Divergence

Section 3.1.1 has shown a possibility to make the calculation of thermal heating rates with the backward method faster and less uncertain. However, calculating heating rates from backward net flux differences according to Eq. 2.19 can speedup the calculation even more for high grid box optical thicknesses. In EMABS_OPT, the principle idea was to start more photons close to the face of the grid box because those photons leaving the grid box contribute more to the result. The backward net flux difference method might seem the ideal realization of this idea, since all photons are started on the faces and contribute to the result.
Following Eq. 2.19 backward inward and outward fluxes for the six faces have to be calculated. For this purpose, photons are randomly started at one of the six surfaces, with a probability given by the respective area fraction $A_{\text{x}}/(A_{\text{x}} + A_{\text{y}} + A_{\text{z}})$ etc. Since heating rates are usually small numbers resulting from differences of large numbers, it is mandatory to start identical photon numbers to compute the four components of the net flux difference in each spatial direction. For that purpose it has to be made sure that the photon number is a multiple of 4 and exactly one quarter for the inward and outward flux calculation at the left and right face are used, respectively. When distributing the photons randomly over the four contributions (rather than using exactly the same numbers), the noise increased considerably.

3.1.2 Results

In this section, the performance of the methods described above is evaluated and the optimum parameters for EMABS_OPT are determined. The results of the three methods are compared to each other and to one-dimensional simulations with an independent radiative transfer code. For these studies a non-scattering atmosphere was assumed. It will be shown in Section 3.1.2 that the effect of scattering in the atmosphere has an effect on the value of the heating rate but only little influence on the uncertainty and can therefore be neglected in the optimization

Parameter	Value
Number of photons	1200000
Temperature profile	US standard atmosphere
Background absorption coefficient	0.1 km^{-1}
Wavelength	[10 μm, 11 μm]
Surface albedo	0
Domain size	3 x 3 km^2
3D layer	1 km - 2 km
Number of grid boxes	3x3
Size of cloud	1 x 1 x 1 km^3
Single scattering albedo	0 (no scattering)

Table 3.2: Model input: a cubic cloud embedded in a moderately absorbing atmosphere.

process. The model input parameters are described in Table 3.2. Unless indicated otherwise, these settings were used for all simulations.

Optimization of EMABS_OPT

EMABS_OPT has two free parameters which have to be optimized: the size (in units of optical thickness) of the sub cubes has to be specified as well as the size of the outer layer (cutoff τ_{cut} in terms of optical thickness). Also, the way of calculating the emission (either analytical or at the 'real' location of the photon) has an influence on the uncertainty.

Analytical vs. statistical emission calculation

As described in Section 3.1.1, the emission of a grid box can be calculated either analytically (Eq. 3.1) or with a Monte Carlo approach (Eq. 3.4). It was found that estimating the emission via the Monte Carlo approach reduces the uncertainty of the standard photon distribution (EMABS) already by a factor of 1.5 - 1.8 for large optical thicknesses. Fig. 3.3 shows the standard deviation for the non-optimized EMABS method with an analytically calculated emission (yellow) and EMABS with the Monte Carlo emission (pink). For completeness the optimized photon distribution (EMABS_OPT) with the Monte Carlo emission (red) is already shown as well. It was found that for the optimized photon distribution EMABS_OPT, the noise of the heating rate caused by the analytical emission calculation is even higher than that of the non-optimized EMABS. This seems to be contra-intuitive since an analytical expression is certainly less noisy than a Monte Carlo calculation. As already outlined in 3.1.1, however, the noise of the emission partially cancels the noise of the absorption which reduces the noise of the heating rate. For this reason the statistical (Monte Carlo) calculation is used exclusively for further calculations and for developing EMABS_OPT.

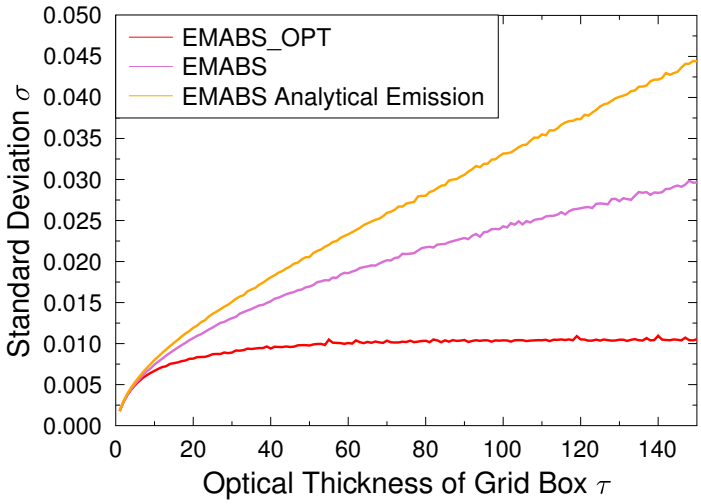

Figure 3.3: Influence of the estimation of the emission on the uncertainty of the result.

Optical thickness of the sub cubes

Fig. 3.4 shows the dependence of the result of EMABS_OPT on the optical thickness of the sub cubes in a non-scattering atmosphere. The optical thickness of the sub cubes $\Delta\tau$ was varied in steps of 0.5 from 0.5 to 5.0. The simulation was performed for different optical thicknesses of the grid box under investigation (1,5,10,50,100,150). In the case of $\Delta\tau$ being larger or equal to the optical thickness of the grid box itself, the grid box is not divided into sub cubes and the photons are distributed equally in the grid box which corresponds to using EMABS. A small increase in the uncertainty can be seen for larger optical thicknesses (50, 100, 150) if the sub cube optical thickness was larger than 1.5. Therefore a sub cube optical thickness of 1 is chosen as the standard value (a value as large as possible is desirable for reducing memory requirements of the algorithm).

Dependence on the cutoff optical thickness

For the cutoff optical thickness (the optical thickness of the outer shell in Fig. 3.1), a similar test was performed: The cutoff optical thickness varies from 1 to 20 in steps of 1 and the simulation was performed for different optical thicknesses (1,5,10,50,100,150) of the grid box. According to Section 3.1.2, the sub cube optical thickness is set to 1. Fig. 3.5 shows the uncertainty as a function of the cutoff optical thickness. It can be seen that the best results are achieved for a cutoff optical thickness between 6 and 12 for the outer layer. For smaller values, the photon distribution is obviously no longer ideal and the uncertainty is close to the one of EMABS. For larger values spikes (few photons with large weights) were found. Therefore a cutoff optical thickness of 10 was chosen.

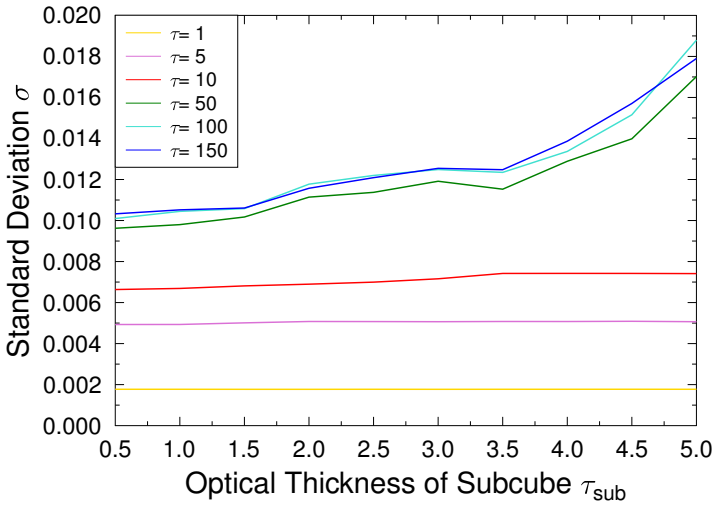

Figure 3.4: Dependence of the uncertainty on the sub cube optical thickness τ_{sub}.

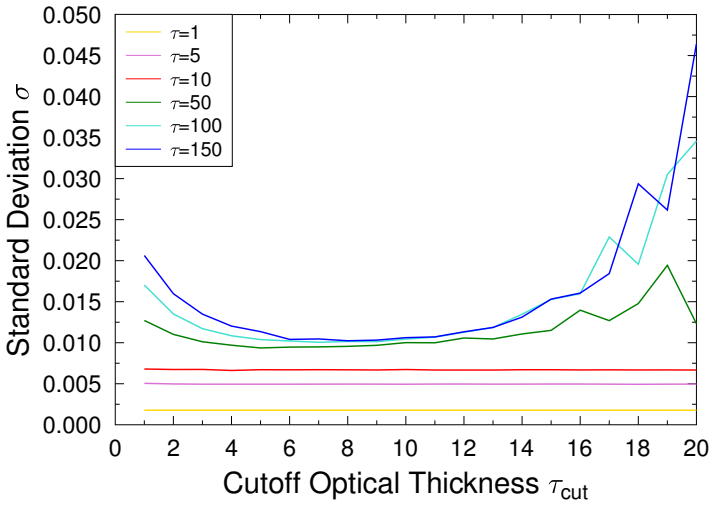

Figure 3.5: Dependence of the uncertainty of the result on the cut off optical thickness.

Uncertainty of the estimation of the escape probability

In Section 3.1.1, the escape probability was estimated introducing various assumptions and simplifications, see Fig. 3.2. In order to assess the quality of this approximation, the minimum possible standard deviation from Eq. 3.18 was calculated, using the "real" escape probabilities p_{real} determined by the Monte Carlo code as quotient of the number of photons leaving a grid box and photons started in a respective sub cube. As an example, the actual uncertainty of the heating rate of a cubic cloud between 1 and 2 km in a model domain of 2 x 2 km^2 is compared. The cloud had an absorption coefficient of 20 km^{-1} and a scattering coefficient of 20 km^{-1} with an asymmetry parameter of 0.8 and a single scattering albedo of 0.5. All other setup information can be taken from Table 3.2. For this example the actual uncertainty was

only 15% larger than the smallest possible uncertainty. It can thus be concluded that the assumptions for the limiting angles μ_g and the decision to consider only the maximum escape probability (to the nearest face) are justified.

Validation and comparison of the uncertainties of the methods

In the following, the different methods are compared to each other and to an independent radiative transfer code. The Monte Carlo noise for the three different approaches in order to determine the fastest method is quantified. For this section the term "uncertainty" always refers to the statistical uncertainty caused by the photon noise.

Comparison with DISORT for a 1D atmosphere

To validate the methods and their implementation, results of the three methods for a 1D atmosphere with the 1D discrete ordinate solver DISORT by Stamnes et al. (1988); Buras et al. (2011) which is also implemented in libRadtran are compared at first, thus guaranteeing identical input parameters of the different solvers. Simulations were done for the setup described in Table 3.2 except for the fact that a 1D atmosphere was simulated and the cloud therefore is a plane-parallel layer. Fig. 3.6 shows the heating rates for the three methods and the DISORT calculation as a function of the cloud optical thickness. The error bars are the standard deviations for the three Monte Carlo approaches. The results generally agree within 2σ of the respective Monte Carlo calculation. For larger optical thickness, EMABS (yellow) and EMABS_OPT (red) show considerable noise. The reduction of the standard deviation by the variance reduction method is obvious. The noise of DENET is small compared to the other two methods

Uncertainty as a function of grid box optical thickness

It is already clear from Fig. 3.6 that the uncertainty of the straightforward EMABS method increases with optical thickness while the uncertainty of the optimized EMABS_OPT approaches a constant value. Fig. 3.7 shows a quantitative comparison of the three backward methods. The uncertainty of DENET decreases slightly with increasing optical thickness, but approaches a constant value.
For all three methods the uncertainty depends on the optical thickness of the grid box under consideration. In general, the higher the optical thickness, the better EMABS_OPT and DENET work compared to EMABS. Fig. 3.7 shows the three methods compared to each other for increasing optical thicknesses (1 to 150). The number of photons and thus the computational time were equal for the three methods. The setup for the simulations again follows the description in Table 3.2, but a non-scattering atmosphere (as described in the table) was used and a scattering atmosphere for which a single scattering albedo of 0.5 was chosen by adding a scattering coefficient identical to the absorption coefficient. Hardly any differences are found between the uncertainties for the scattering and the non-scattering cases. EMABS_OPT is a clear improvement of EMABS; for an optical thickness of 150 (which is not uncommon in the

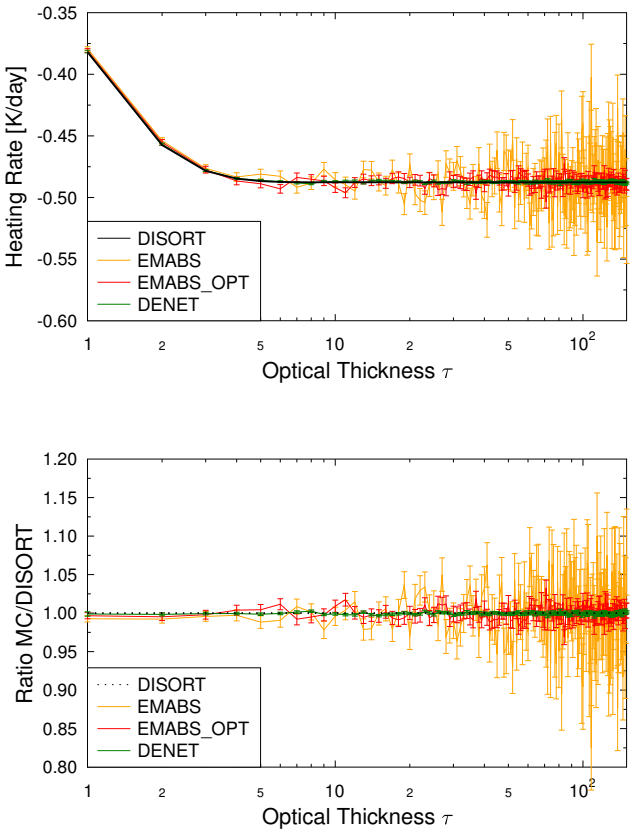

Figure 3.6: Comparison of the three different MYSTIC methods and DISORT. Error bars are 1 standard deviation. (Top) absolute values; (bottom) ratio of Monte Carlo simulations and DISORT.

thermal spectral range) the uncertainty is reduced by a factor of 4 which implies that a factor of 16 less photons need to be traced in order to reach the same uncertainty. Compared to EMABS, DENET reduces the uncertainty by even a factor of 10 or more for optical thicknesses higher than 100. This corresponds to a factor 100 in the photon number and thus in computational time. For optical thicknesses larger than about 4, DENET is the most efficient method while for an optical thickness of 1 the uncertainty of DENET is larger by more than a factor of 2, increasing towards smaller optical thickness. The reason is that for small optical thickness the net fluxes above and below (or left and right) of the cloud approach each other and the heating rate becomes a small difference of two large numbers, each with a large uncertainty. While the uncertainty of DENET is approximately constant, the uncertainty of EMABS and EMABS_OPT goes to zero for small optical thickness because the result is weighted with a small number, the absorption coefficient. The relative uncertainty of DENET, on the other hand, reaches its maximum for $\tau = 0$ where the absolute value of the heating rate assumes its minimum (0). From Fig. 3.7 it is clear, that the optimum (fastest) method would be a combination of a combination of EMABS_OPT and DENET. Only the cross-over point where DENET becomes more accurate than EMABS_OPT has to be determined which will be done in the next section.

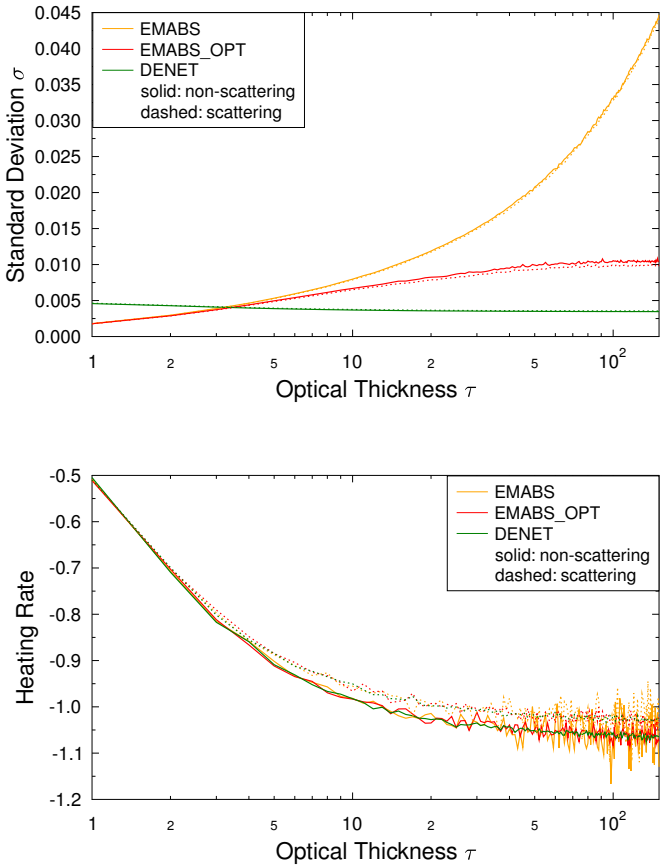

Figure 3.7: Dependence of the uncertainty of the result on the grid box optical thickness. The curves show the increase in uncertainty with increasing optical thickness, the black curves show that the result is much more stable with DENET. The picture shows that there is no dependence on scattering in the result.

Combining the best methods

For the cubic cloud example in section 3.1.2 it was found that EMABS and EMABS_OPT work best for low optical thicknesses (smaller than about 4) and DENET better for higher optical thicknesses (larger than about 4). To generalize the results a large number of calculations is performed, varying the absorption coefficient of the considered grid box as well as that of the surrounding grid boxes independently between 0 and 150. Fig. 3.8 illustrates the performance of DENET compared to EMABS_OPT. For this purpose the relative difference of the variance of both methods is used. Since the computational time is proportional to the variance

$$\frac{\sigma^2_{\text{DENET}} - \sigma^2_{\text{EMABS\_OPT}}}{\sigma^2_{\text{EMABS\_OPT}}} \tag{3.27}$$

may be interpreted as the difference in computational time between both methods: 0 indicates equal computational times, positive values indicate that EMABS_OPT performs better than DENET, with a number of 1 corresponding to a twice as large computational time of DENET and -0.5 corresponding to a half as large computational time of DENET.

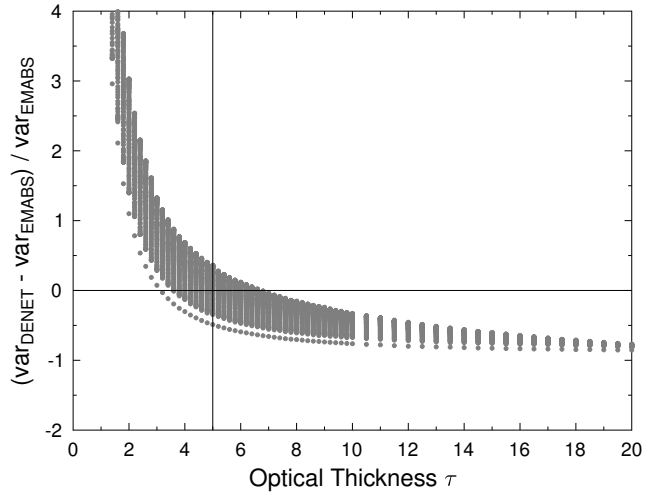

Figure 3.8: Illustration of the performance of DENET compared to EMABS_OPT as function of the grid box optical thickness. The y-axis shows the relative difference of the variance of DENET compared to EMABS_OPT which is an indicator for the computational time (see text for further explanation). The 0 line corresponds to equal computational times for both methods. The simulation was performed for varying absorption coefficients of the surrounding atmosphere.

The zero line is crossed at an optical thickness of 3 to 7, depending on the absorption coefficient of the surrounding grid boxes. Therefore an optical thickness of 5 was chosen as the cross-over point ($\tau_{\text{crossover}}$). With this simple assumption a slightly too high computational time, less than a factor of two for all calculated examples is introduced. In principle the cross-over might be parameterized as a function of the surroundings of the grid box which, however, is certainly difficult in a 3D world. Also, the results might look different for non-cubic grid boxes.
The best way to calculate thermal heating rates is therefore a combination of EMABS and DENET or EMABS_OPT and DENET. With an cross-over optical thickness of 5 between the methods it can be seen from Fig. 3.7 that hardly any difference exists between EMABS and EMABS_OPT. As EMABS_OPT might be a bit more expensive as far as computational time is concerned, EMABS would be sufficient for a 'hybrid' model. To fully exploit the optimization potential a hybrid method which uses EMABS_OPT for optical thickness smaller than $\tau_{\text{crossover}}$ and DENET for optical thickness larger than $\tau_{\text{crossover}}$ is implemented.

3.1.3 Application

A simple example - cubic clouds

To test the methods for a large optical thickness, a simple example of a 20 x 20 (in x and y) field, with a grid box size of 50 meters containing a cloud in the first 10 grid boxes of the x and y direction, and between 1 and 1.5 km altitude is performed. The cloud has a very high extinction coefficient of 0.75. Instead of a monochromatic simulation as in all previous calculations, an integration over the whole thermal spectral range is performed using the correlated-k approximation from Fu and Liou (1992) for the molecular absorption and the spectral cloud scattering and absorption properties from Hu and Stamnes (1993), both implemented in libRadtran. The profiles of pressure, temperature, water vapor, and ozone from the US standard atmosphere were used. A total number of 830 million photons were traced (that is 1,000 for each sub band of the (Fu and Liou, 1992) k-distribution and each grid box). Fig. 3.9 shows horizontal cross sections through different layers of the cloud for the HYBRID method. At the cloud base layer, a modest warming (about +25 K/d) can be found in the middle, while the cloud sides have a cooling effect. The middle layer also shows cooling at the cloud sides (-90 to -130 K/d as maximum values), while the inside shows nearly no heating or cooling (+0.08 to -0.08 K/d). The cooling at the cloud sides increases with height. The largest cooling rates are found at the cloud sides close to the top with about than -290 K/d. The cooling rate in the atmosphere around the cloud shows average values between -0.5 to -1.6 K/d, depending on the atmospheric level. To compare the performance of the various methods with each other, Table 3.3 shows the results for FORWARD, EMABS, EMABS_OPT, DENET and the two possible HYBRID combinations. Hybrid 1 uses EMABS and DENET

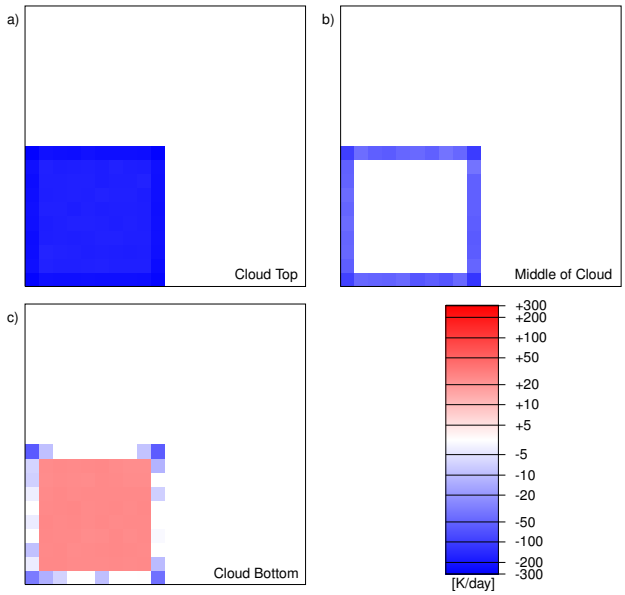

Figure 3.9: Heating rates at a) cloud top (1.45-1.5 km), b) middle layer (1.2-1.3 km), c) cloud base layer (1-1.05 km) in K/day.

Method	Total	Cloud Top	Cloudless
EMABS	-2.27 ± 0.14	-193.32 ± 23.18	-1.92 ± 0.068
EMABS_OPT	-2.27 ± 0.12	-192.77 ± 17.77	-1.92 ± 0.068
DENET	-2.20 ± 19.95	-190.80 ± 5.17	-1.72 ± 20.07
HYBRID 1	-2.27 ± 0.10	-193.10 ± 5.13	-1.92 ± 0.078
HYBRID 2	-2.26 ± 0.10	-194.24 ± 5.18	-1.92 ± 0.078
FORWARD	-2.31 ± 33.05	-196.24 ± 123.63	-1.99 ± 34.04

Table 3.3: Comparison of the performance of the different methods for a cubic cloud. The average heating rates and the corresponding averaged standard deviation (both in K/d) are shown for the whole scene, the cloud top grid boxes and cloudless grid boxes.

while Hybrid 2 uses EMABS_OPT and DENET. For each of these simulations the same setup was used as described above. This example shows the good performance of HYBRID for the overall scene and the superiority of the EMABS_OPT and DENET for optically thin and optically thick grid boxes, respectively. It can also be seen that the FORWARD method behaves poorly compared to the backward methods. The computational time on a standard office computer for this scene was about 90 minutes for EMABS, EMABS_OPT, HYBRID 1 and HYBRID 2; about 120 minutes for DENET and about 1000 minutes for FORWARD.

Realistic clouds

To test the methods for realistic clouds, a simulation for one of the cases from the Intercomparison of 3D Radiation Codes I3RC (Cahalan et al., 2005), in particular the "Cumulus LES" case shown in their Fig. 5 is performed. This cloud field contains 96 x 96 grid boxes of 0.06 km size in the x and y directions and height levels in steps of 0.04 km. The cloud is between 1.04 and 2.40 km. Background atmosphere and absorption parameterizations were as described in the above simple example. Fig. 3.10 shows five vertical cross section at 5 y-locations (pixels 34, 38, 49, 55, and 61). The cooling at the cloud tops can be seen as well as the modest warming at the cloud bottom. Probably most important is the strong cooling at the cloud sides which would be absent in any 1D approximation – typically used in cloud models, numerical weather forecast models, and climate models. The maximum positive heating rates was found with about 29 K/d at the cloud bottom, and the maximum cooling rate was found at the cloud top with about -351 K/d. In addition, Fig. 3.11 shows the horizontal cross section at 3 height levels of the cloud (z = 1.08, 1.48 and 1.84 km).

The computational time was about 6 s per grid box on a single standard PC processor. Since the number of grid boxes is large (96 times 96 times 75 = 691200) the total computational time is large: 48 days on a single processor. The relative uncertainty of the heating rates was about 1.5% (except for grid boxes with a heating rate close to zero where the relative error increases of course). The computational time depends linearly on the number of grid boxes and increases as the inverse square of the relative uncertainty. If e.g. the resolution was reduced by a factor of 2 in each direction, and an uncertainty of 10% was allowed, the computational time would decrease by a factor of 350. And if this computation was done e.g. on a

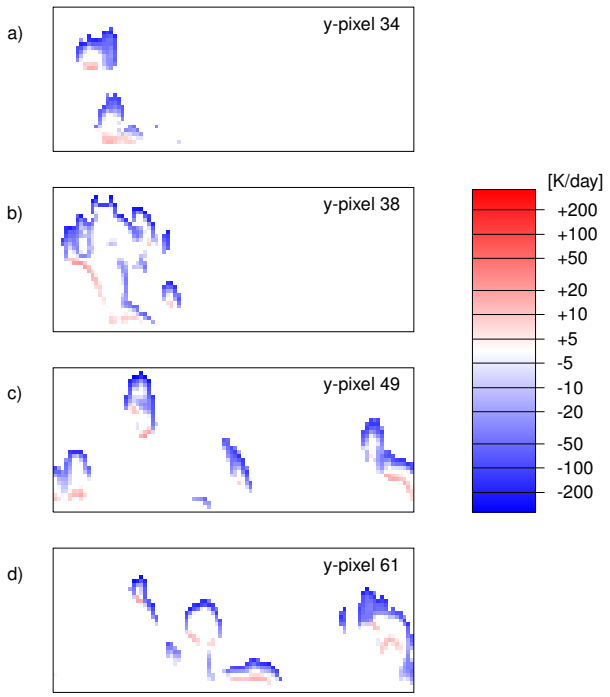

Figure 3.10: I3RC cumulus cloud field. A vertical cross-section through several y-grid boxes is shown. Modest warming can be found at the cloud base while strong cooling is found at the cloud sides and the cloud top.

64 processor cluster, the computational time would only be 3 min. As a side information, for the I3RC cloud, the optical thicknesses (generated by the Fu and Liou (1992) k-distribution) of the 60 m high grid boxes between 0 and 3 km varied between 0.00026 and 15600. The optical thickness of about 60% of these grid boxes was smaller than the cross-over optical thickness which implies that EMABS_OPT was used while the remaining 40% were calculated with DENET. It can be concluded that for a typical atmosphere and a typical k-distribution, both methods are equally important.

Summary Heating Rate Monte Carlo

Three fundamentally different Monte Carlo methods (one forward and two backward) to calculate 3D thermal heating rates in the atmosphere were developed. All three methods have been implemented into MYSTIC, the Monte Carlo code for the physically correct tracing of photons in cloudy atmospheres. All three methods are physically correct: no approximations were introduced which might bias the results. The results have been shown to agree within the inherent statistical noise of the Monte Carlo approach. The methods include the calculation of thermal emission, absorption, and scattering effects. For the backward tracing, which is more efficient than the forward tracing (at least for the EMABS_OPT and DENET) when thermal heating rates are concerned, two different approaches have been developed. In the first (EMABS) the difference between the emission and absorption of a grid box to calculate

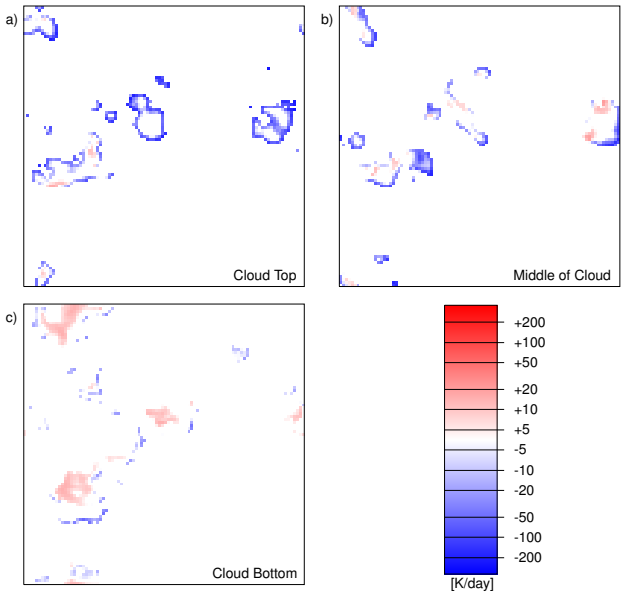

Figure 3.11: I3RC cumulus cloud field. A horizontal cross-section at three locations of the cloud (cloud base, middle and top) is shown. The increase of the cooling rate with height can be seen, as well as cloud base warming.

the heating rates is used. A sophisticated variance reduction method (EMABS_OPT) which reduces the computational time for a given Monte Carlo noise by an order of magnitude for grid box optical thicknesses of more than 100 (which are common in the thermal spectral range) is introduced. The second backward method (DENET) is based on a net-flux difference approach. DENET reduces the computational time for large grid box optical thicknesses by another order of magnitude. The results of all forward and backward methods agreed with each other and with the completely different DISORT method (for a 1D case) within the Monte Carlo noise.

In a sensitivity study it was shown that EMABS and EMABS_OPT perform best for grid box optical thickness smaller than 5 while DENET is a considerable improvement for large optical thickness. Since the optical thickness in a realistic atmosphere varies from grid box to grid box and from wavelength to wavelength (or sub band in a k-distribution), EMABS_OPT and DENET are combined to a 'hybrid' model which uses one or the other depending on the optical thickness of the grid box. For a realistic cloud field, it was found that both approaches were used equally frequent.

Although EMABS_OPT improves EMABS considerably for large optical thickness, hardly any difference between both was found for optical thickness smaller than 5. For that reason, one might rather combine EMABS and DENET and avoid the complex implementation of the variance reduction method EMABS_OPT.

3.2 3D Thermal Heating Rate Parameterization

The contents of Section 3.2 were published by Klinger and Mayer (2016). The following text and figures are adopted from the publication, with only a few editorial changes.
In this section, a reasonably accurate and fast parameterization for the calculation of 3D thermal heating rates which can be used in a cloud resolving model is described. 3D radiative transfer implies that photons may travel horizontally over large distances which is a technical problem for parallelized models where only limited subsets of the model domain are available on each processor. Therefore the aim has to be to develop an approximation which only needs access to few grid box columns around the column of interest.
Detailed studies of full 3D thermal heating rate effects (with the Monte Carlo Model MYSTIC) on which the development of the following method is based are shown in Section 4.1.
A fast and accurate method to calculate 3D heating and cooling rates in the thermal spectral range that can be used in cloud resolving models is presented. The parameterization considers net fluxes across horizontal box boundaries in addition to the top and bottom boundaries. Since the largest heating and cooling rates occur inside the cloud, close to the cloud edge, the method needs in first approximation only the information if a grid box is at the edge of a cloud or not. Therefore, in order to calculate the heating or cooling rates of a specific grid box, only the directly neighboring columns are used. The so-called "Neighboring Column Approximation" (NCA) is an analytical consideration of cloud side effects which can be considered a convolution of a 1D radiative transfer result with a kernel or radius of 1 grid-box (5 pt stencil) and which does usually not break the parallelization of a cloud resolving model. The NCA can be easily applied to any cloud resolving model that includes a 1D radiation scheme. Due to the neglect of horizontal transport of radiation further away than one model column, the NCA works best for model resolutions of about 100 m or lager.
In this paper the method is described and a set of applications of LES cloud field snap shots is shown. Correction terms, gains and restrictions of the NCA are described. Comprehensive comparisons to the 3D Monte Carlo Model MYSTIC and a 1D approximation are shown. In realistic cloud fields, the full 3D simulation with MYSTIC shows cooling rates up to 150 K/d (100 m resolution) while the 1D approximation shows maximum coolings of only 100 K/d. The NCA is capable of reproducing the larger 3D cooling rates. The spatial distribution of the heating and cooling is improved considerably. Computational costs are only a factor of 1.5-2 higher compared to a 1D approximation.

3.2.1 Theory and Method

Thermal Heating Rate Calculation

Thermal radiation plays an important role in the Earth's energy budget. Thermal radiation is emitted and absorbed by molecules and particles in the atmosphere as well as by the surface. In contrast to solar radiation, scattering is of minor importance in the thermal spectral range. Planck's law (Planck, 1901) describes the amount of energy emitted by a black body (Eq. 2.13), depending on the body's temperature and the wavelength. In the atmosphere, the amount of energy emitted or absorbed depends on the spectral emission or absorption coefficients which are equal to each other according to Kirchhoff's law (Kirchhoff (1890), Eq. 2.15).

The change in radiation while passing the atmosphere and the interaction of radiation with the atmosphere (emission, absorption, and scattering) are described by the radiative transfer equation (Eq. 2.16). By neglecting scattering, the RTE reduces to the Schwarzschild equation (Eq. 2.17) which is straightforward to solve (see Section 2.1.3).
To obtain the irradiance E or heating and cooling rates, radiances have to be calculated for a number of directions and integrated over solid angle. A possible approximation is to calculate the radiance for a specific representative direction μ_{rep} and to convert radiance to irradiance by multiplying with a factor π:

$$E = \int_{2\pi} L(\mu, \phi)\, \mu \, d\Omega = 2\pi \int_0^1 L(\mu)\, \mu \, d\mu \approx \pi \cdot L(\mu_{\text{rep}}) \tag{3.28}$$

(for a 1D plane parallel atmosphere in the thermal spectral range $L(\mu, \phi) = L(\mu)$ does not depend on azimuth ϕ). For each radiance distribution $L(\mu)$ there is always a μ_{rep} for which the approximation is actually an equality. However, if a specific μ_{rep} is chosen (and in the NCA $\mu_{\text{rep}} = \cos 45°$ will be used) then an approximation is used, the uncertainty of which will be assessed. To obtain integrated thermal irradiance or heating rates, Eq. 2.17 or Eq. 3.28 has to be solved for a number of wavelengths and the result has to be integrated over wavelength. The absorbed or emitted electromagnetic power per volume (often referred to as heating or cooling rate and measured as change of temperature with time $\frac{dT}{dt}$, [K/d]) was already defined in Eq. 2.18. The NCA utilizes the difference between emitted and absorbed power per volume.

Reference Model - MYSTIC

The necessary benchmark results for the development of the parameterization were calculated with the 3D Monte Carlo Model MYSTIC (Monte Carlo code for the phYSically correct Tracing of photons In Cloudy atmospheres, Mayer (2009)). MYSTIC is one of several solvers included in the libRadtran radiative transfer package by Mayer and Kylling (2005). The methods used for the calculation of the thermal heating rates are described in detail in Klinger and Mayer (2014). The specific setup for the reference simulations is described in Section 3.2.2.

The Neighboring Column Approximation - NCA

The parameterization described in this paper uses the irradiance from neighboring columns to estimate radiative fluxes into or out from the center column. It is therefore called Neighboring Column Approximation (NCA). The input to the NCA can be any 1D (independent-column; ICA) thermal irradiance profile (e.g. Schwarzschild, discrete-ordinate, or two-stream). 1D irradiance profiles from the column under consideration plus the four surrounding columns are needed to approximate the horizontal flux and thus the 3D heating and cooling rates. This has the advantage that the method can be used in parallelized cloud models. The essential assumption of the NCA is to calculate horizontal transport of radiation from and into the next model column, but horizontal transport beyond one neighboring column is neglected. As will be shown later, this assumption is well justified for model resolutions of about 100 m to several 100 m.
Fig. 3.12 illustrates what this assumption means for a real cloud field: the figure shows the

radiance distribution at a wavelength of 10 μm in a cloud field, seen from a cloud side at the upper edge of a cloud, looking outwards (see Fig. 3.12a). It shows the angular distribution of the radiance to be absorbed at the cloud edge with a field of view of -90° to 90° in the vertical and horizontal directions. The black sky above the clouds is a dominant feature for both pictures, a 3D MYSTIC calculation (b) and the NCA (c). In the atmospheric window around 10 μm, the cloudless sky contributes basically nothing. The large gray area at the bottom of both pictures is the cloud itself. In the 3D MYSTIC calculation neighboring clouds can be seen and these are neglected by the NCA. The white area (the ground) is visible in both calculations. The main features (sky, ground, own cloud) are accounted for in both methods. Only the radiation emitted by the neighboring cloud (clearly visible in Fig. 3.12b) is neglected by the NCA. Therefore only a small effect on the result from the neglect of horizontal transport of radiation beyond one neighboring column is expected. While these explanations refer to the absorbed thermal radiation and the uncertainties in the absorption, the emitted thermal radiation is calculated correctly anyway. Emission is taking place in the grid box itself and is not affected by the neighboring columns.

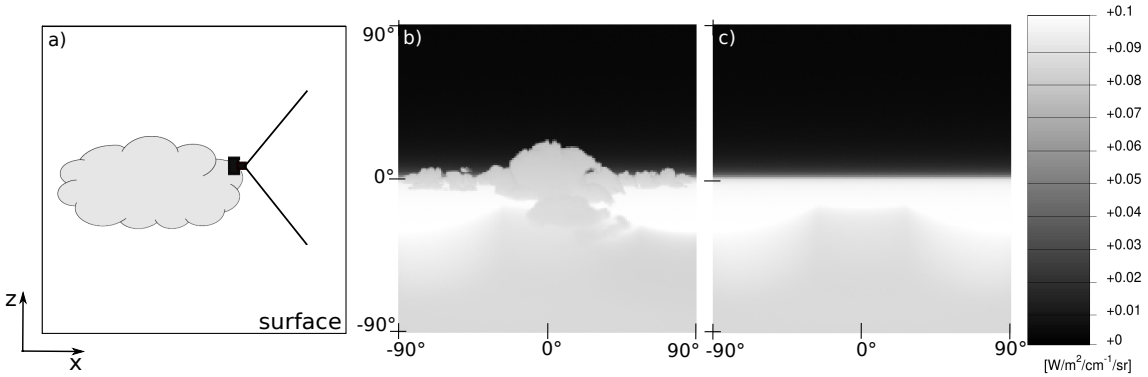

Figure 3.12: Schematic figure (a) of the observing position and angular thermal radiance distribution at 10 μm seen from a cloud side: (b) 3D MYSTIC simulation, (c) NCA simulation. The field of view covers the whole hemisphere. The black area represents the sky, gray areas clouds and the white are the ground. The figure shows the radiance distribution seen from a cloud side at cloud top, looking outwards.

From 1D to 3D

To obtain 3D heating and cooling rates with the NCA, the contributions from each side face as well as the top and bottom faces of a grid box (that is the emitted and absorbed energy through each face) have to be calculated. The mechanism is the same for each grid box face in principle: First, 1D irradiance results have to be converted to radiance. This is approximated by dividing the irradiance result by a factor π assuming isotropic radiance (see Eq. 3.28). For the contribution of the side faces of a grid box, the 1D radiance from the neighboring column is used (e.g. L_{s1} at level j+1 for the left neighboring column in Fig. 3.13b). The up- and downwelling contribution at the top and bottom faces of the grid box are calculated

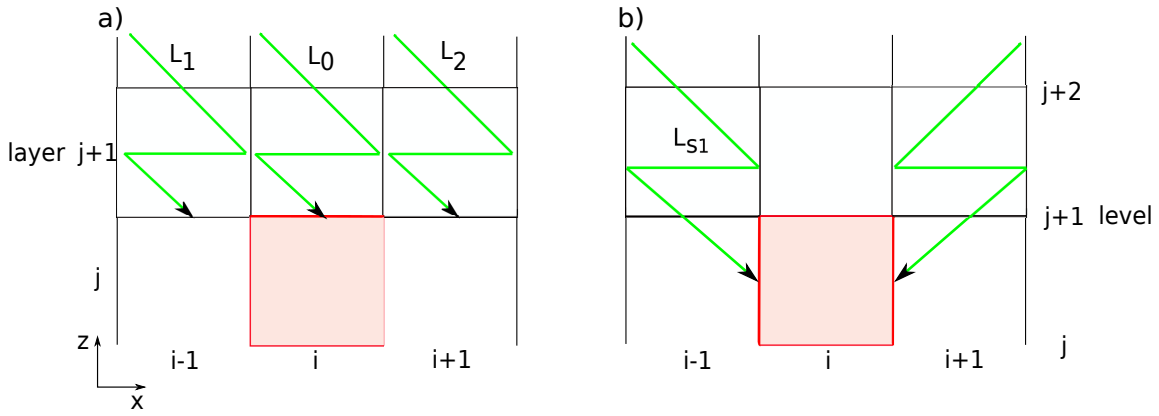

Figure 3.13: Schematic figure of the principle idea of the NCA. Left: contribution of the radiance (green) to the top face of the red grid box. Right: side face radiance contributions to the red grid box. The figure shows only the downwelling radiance. The same principle is applied for upwelling radiances.

as averages of the radiance over the 5 involved columns (e.g. L_0, L_1, L_2 at level j+2; see Fig. 3.13a).

The description of the mechanism, will focus on downwelling radiances through the upper and left faces of the grid box. The same calculations can be applied at the bottom face and the other side faces as well as for upwelling radiances.
It was already mentioned before that a representative direction $\mu_{\text{rep}} = \cos 45°$ will be used for the heating rate calculation by the NCA. In principle any angle could be used, however, the $\cos 45°$ assumption ensures that all directions (top, bottom, and sides) are treated consistently since the incidence angle on each side is the same.
It has to be noted that the 1D radiance which is used for the calculation of the 3D heating and cooling rates is not affected by the 45° assumption at the beginning. The fluxes converted to radiances depend only on the 1D approximation, which can vary, depending on the 1D approximation (e.g. Schwarzschild, two-stream). However, the estimated average incoming radiance at top/bottom of the grid box and the emitted and absorbed radiance which will be estimated from the 1D approximation will be affected by the 45° assumption.
From the incoming radiance L, a fraction is absorbed (L_{abs}). As an example, the absorbed amount of L in a plane-parallel, homogenous layer is:

$$L_{\text{abs}} = L \left[1 - \exp\left(-\beta_{\text{abs}} \frac{\Delta z}{\mu}\right)\right] \tag{3.29}$$

It then follows that the power $\dot{Q}$ [W] is:

$$\dot{Q} = \pi \int_0^{\Delta x} \int_0^{\Delta y} L_{\text{abs}}\, dx\, dy = \pi\, L_{\text{abs}}\, \Delta x\, \Delta y \tag{3.30}$$

The heating or cooling rate is defined as power per volume $\dot{q}$ in [W/m^3]:

$$\dot{q} = \frac{\dot{Q}}{V} = \pi\, L_{\text{abs}} \frac{\Delta x\, \Delta y}{\Delta x\, \Delta y\, \Delta z} = \pi \frac{L_{\text{abs}}}{\Delta z} \tag{3.31}$$

In the 3D application, L_{abs} also depends on the x and y direction and integrals become more complex (which is shown in the following). Depending on the direction over which the integrals are performed, the results will have factors of $\frac{1}{\Delta x}$, $\frac{1}{\Delta y}$ or $\frac{1}{\Delta z}$ which account for the grid box size and can therefore be seen as an area weight for the x, y, and z directions, respectively.

Top/bottom contributions:

Starting from a 1D ICA irradiance approximation, the radiance that arrives at the upper face of a grid box can be estimated. The radiance arriving there is, of course, dependent on the cloud field surrounding the grid box. For the neighboring column approximation it was decided to use information of all four neighboring columns (L_0, L_1, L_2 in the schematic projection of Fig. 3.13) because, if only the column radiance of the considered column (L_0 in Fig. 3.13a) would be used, potential shading by cloudy grid boxes, in the neighboring columns (e.g. radiances L_1, L_2 in Fig. 3.13a), above the layer in question, was neglected and large uncertainties were introduced. This average is calculated by starting one level above the grid box top and determining the slant transmission to the grid box top. Therefore, radiance from a level above (level j+2) is used and propagates through the layer above the one in question (layer j+1) with a zenith angle of 45° and perpendicular to the grid box face in azimuth. Fig. 3.14 illustrates the mechanism of this neighboring contribution for different grid box aspect ratios. The red box (i, j) is the one for which the heating rate is to be calculated. The green arrow indicates the incoming radiance (L_1) at top of the layer j+1. This incoming radiance is then propagated through the green shaded area with absorption coefficient $\beta_{\text{abs,i}-1}$ (Eq. 3.32) and the blue shaded area with $\beta_{\text{abs,i}}$ (Eq. 3.33) with a zenith angle of 45°. B_i and B_{i-1} are the average Planck functions of the grid boxes. Please note that layer indices j are omitted

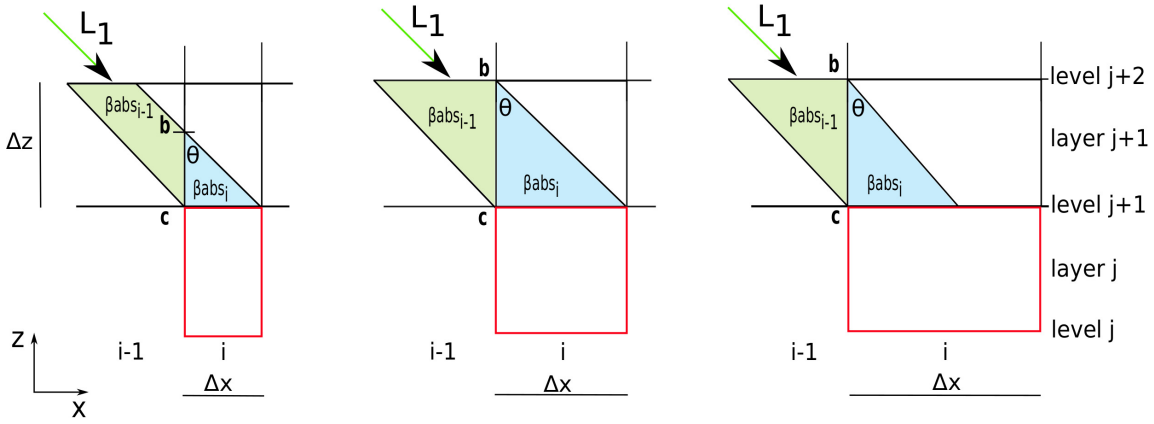

Figure 3.14: Schematic figure showing the neighboring column radiance contribution to the average incoming radiance for the heating rate calculation. The green arrow indicates the incoming radiance. The area (green and blue) that is passed by the radiation with an zenith angle of 45° is shown for the different optical properties of the grid boxes. The red grid box indicates the grid box for which heating or cooling rates are to be calculated. The distances a, b and c are geometric distances in the analytic solution which ensure that the integration can be performed for any grid box aspect ratio.

here for clarity since everything refers to one and the same layer above the considered grid box.

$$L_{1,\mathrm{trans}} = L_1 \, \exp(-\beta_{abs,i-1} \, s_{\mathrm{i}-1}) + B_{\mathrm{i}-1} \, [1 - \exp(-\beta_{\mathrm{abs,i}-1} \, s_{\mathrm{i}-1})] \tag{3.32}$$

$$L_{\mathrm{top,s1,path}} = L_{1,\mathrm{trans}} \, \exp(-\beta_{abs,i} \, s_{\mathrm{i}}) + B_{\mathrm{i}} \, [1 - \exp(-\beta_{\mathrm{abs,i}} \, s_{\mathrm{i}})] \tag{3.33}$$

$L_{\mathrm{top,s1,path}}$ (Eq. 3.33) corresponds to the radiance along one single path arriving at top of grid box (i,j) after passing the neighboring grid box (i-1, j+1) with an angle of 45°. The integration can be performed along z or along x. The integration is performed along z, substituting x by z and setting the integration borders from b to c:

$$\begin{aligned} L_{\mathrm{top,s1}} \; &= \tfrac{1}{c-b} \int_{\mathrm{b}}^{\mathrm{c}} [B_{\mathrm{i}} + (L_1 - B_{\mathrm{i}-1}) \, \exp(-\beta_{\mathrm{abs,i}-1} \, s_{\mathrm{i}-1}) \, \exp(-\beta_{\mathrm{abs,i}} \, s_{\mathrm{i}})] \; + \\ &\qquad [(B_{\mathrm{i}-1} \; - \; B_{\mathrm{i}}) \exp(-\beta_{\mathrm{abs,i}} \, s_{\mathrm{i}})] \, dz \end{aligned} \tag{3.34}$$

with:

$$s_{\mathrm{i}-1} = \tfrac{z}{cos\theta} \quad \text{from b to c in the neighboring grid box (i-1, j+1)}$$

and:

$$s_{\mathrm{i}} = \tfrac{\Delta z - z}{cos\theta} \quad \text{from b to c in the grid box (i, j+1)}$$

Then

$$\begin{aligned} L_{\mathrm{top,s1}} \quad &= \tfrac{1}{c-b} \left\{ B_{\mathrm{i}} \, (c-b) \; + (L_1 \; - \; B_{\mathrm{i}-1}) \, \tfrac{\cos\theta}{\beta_{abs,i} - \beta_{abs,i-1}} \, \exp\left(- \tfrac{\beta_{\mathrm{abs,i}} \, \Delta z}{\cos\theta} \right) \; \cdot \right. \\ &\qquad \left[\exp\left(\tfrac{(\beta_{abs,i} - \beta_{abs,i-1}) \, c}{\cos\theta} \right) - \exp\left(\tfrac{(\beta_{abs,i} - \beta_{abs,i-1}) \, b}{\cos\theta} \right) \right] \\ &\quad + (B_{\mathrm{i}-1} - B_{\mathrm{i}}) \, \tfrac{\cos\theta}{\beta_{abs,i}} \, \exp\left(- \tfrac{\beta_{\mathrm{abs,i}} \, \Delta z}{\cos\theta} \right) \, \left[\exp\left(\tfrac{\beta_{abs,i} \, c}{\cos\theta} \right) - \exp\left(\tfrac{\beta_{abs,i} \, b}{\cos\theta} \right) \right] \Big\} \end{aligned} \tag{3.35}$$

is obtained. For the other three neighboring columns plus the column under consideration, the procedure is analogous, only the input variables L_1 and β_{abs} have to be replaced accordingly. The analytic solution is valid for any aspect ratio.
After having calculated the four neighboring column radiances, the arithmetic average (L_{top}) of those 4 and L_0 is calculated.

$$L_{\mathrm{top}} = \frac{L_{\mathrm{top,s1}} + L_{\mathrm{top,s2}} + L_{\mathrm{top,s3}} + L_{\mathrm{top,s4}} + L_0}{5} \tag{3.36}$$

The $L_{\mathrm{top,si}}$ (i=1 ... 4) represent the four radiance contributions from the neighboring columns. Thus the incoming radiance at the top face of the grid box from which the heating or cooling rate contribution through the top face is estimated can be obtained. Testing different approaches it was found that the arithmetic mean of the five columns gave the best results compared to a 3D solution under the restrictions of the NCA.
Having now the incoming radiances, it can be continued with the calculation of heating or cooling rates. The heating or cooling rate is the difference between the emitted and absorbed power per volume (Eq. 2.18). For the calculation of the emitted and absorbed radiation of a grid box, it is assumed again that radiation passes the grid box with a zenith angle of 45° and perpendicular to the grid face in the azimuth.
First, the absorbed radiance through the top face of a grid box is calculated. With the angle

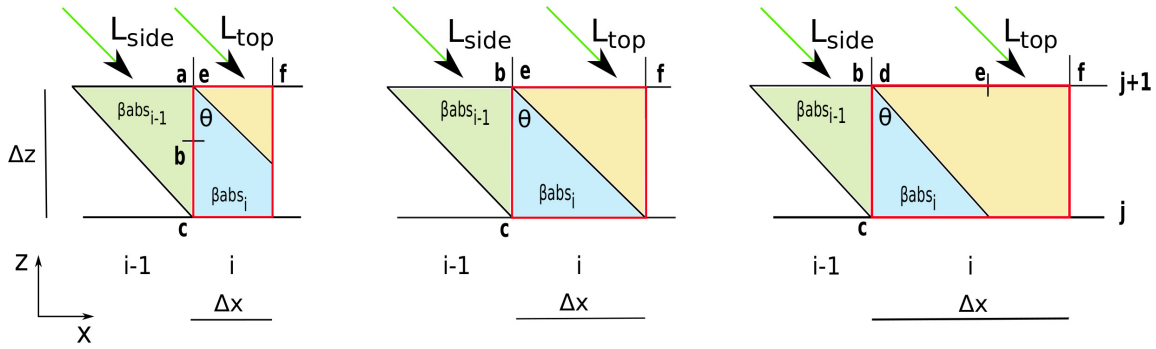

Figure 3.15: Schematic figure for the calculation of the emitted and absorbed power in a grid box through the left side face and the top face of a grid box. Similar to Fig. 3.14 the red grid box is the one for which heating rates are to be calculated. The green arrow indicates the incoming radiance in a neighboring column (L_{side}) for the side face contribution or the averaged radiance (described before) for the top face contribution (L_{top}). Again, different aspect ratios are considered in the calculation as well as the different optical properties of the passed grid boxes. The yellow area shows the absorption area for the top contribution, the blue area the absorption area for the side contribution. For the side contribution, radiation has to pass the green area before entering the red grid box.

of 45°, radiation passes the grid box only in the yellow shaded area of Fig. 3.15 in the case of downwelling radiance entering the grid box through the upper face (here only on the yellow contribution is considered; the green/blue side contributions will be explained later). The figure illustrates the three possible aspect ratio classes. Those are accounted for by setting the integration boundaries (d,e,f) accordingly. Depending on the aspect ratios, the integration boundaries consists of two or three components (see Fig. 3.15). The analytic solution shown in the following considers all kinds of aspect ratios. Generally, the absorption along one path through the grid box can be calculated as:

$$L_{\text{abs}} = \frac{1}{\Delta x} \int_{\text{d}}^{\text{f}} L_{\text{top}} \left[1 - \exp(-\beta_{\text{abs,i}}\, s)\right] dx \tag{3.37}$$

with L_{top} being the incoming radiance at the top of the grid box, L_{abs} being the absorbed radiance in the grid box, $\beta_{\text{abs,i}}$ being the absorption coefficient of the grid box and s the path through the grid box. The way s through the grid box (the yellow shaded area), is defined as:

$$s = \begin{cases} \frac{\Delta z}{sin\theta} & \text{from d to e} \\ \frac{\Delta x - x}{cos\theta} & \text{from e to f} \end{cases}$$

Inserting s into (Eq. 3.37) and solving the integral along x

$$\begin{aligned} \dot{q}_{\text{abs}} \quad &= L_{\text{top}} \cdot \tfrac{\pi}{\Delta x \cdot \Delta z} \left\{ (e-d) \left[1 - \exp\left(-\beta_{\text{abs,i}} \tfrac{\Delta z}{\sin\theta}\right)\right] + \right. \\ &\left. \left[(f-e) - \exp(\tfrac{-\beta_{\text{abs,i}} \Delta z}{\cos\theta}) \tfrac{\cos\theta}{\beta_{\text{abs,i}}} \left(\exp\left(\tfrac{f\,\beta_{\text{abs,i}}}{\cos\theta}\right) - \exp\left(\tfrac{e\,\beta_{\text{abs,i}}}{\cos\theta}\right)\right)\right] \right\} \end{aligned} \tag{3.38}$$

is obtained, with L_{top} being the incoming radiance at the top of the grid box, Δz being the height of the grid box, Δx the width of the grid box, θ being the zenith angle (45° in this case)

and $\beta_{\mathrm{abs,i}}$ being the absorption coefficient in the specific grid box. The emission ($\dot{q}_{\mathrm{em}}$) has to be calculated the same way and the quantity is easily obtained by replacing the radiance $\mathrm{L_{top}}$ by the averaged Planck function of the grid box.
For the lower face, the calculation is basically the same, just rotated by 180° and by using the upwelling irradiance as input for the absorption.

Side Contributions:
The side faces are considered in a similar way to top and bottom. For the side faces of a grid box, radiance is started at the grid box top level (j+1), transmitted through the neighboring grid box (i-1, j) (green shaded area in Fig. 3.15) until it enters the grid box of interest where a fraction of it is absorbed (blue shaded area in Fig. 3.15). The absorption is calculated from two steps. First, incoming radiance $\mathrm{L_{s1}}$ passes the neighboring grid box and L_{side} is obtained as:

$$L_{\mathrm{side}} = L_{\mathrm{s1}}\, \exp(-\beta_{\mathrm{abs,i-1}}\, s_{\mathrm{i-1}}) + B_{\mathrm{i-1}}\, [1 - \exp(-\beta_{\mathrm{abs,i-1}}\, s_{\mathrm{i-1}})] \tag{3.39}$$

Then, $\mathrm{L_{side}}$ passes the grid box in question and is absorbed:

$$L_{\mathrm{abs}} = L_{\mathrm{side}}\, [1 - \exp(-\beta_{\mathrm{abs,i}}\, s_{\mathrm{i}})] \tag{3.40}$$

Inserting Eq. 3.39 into Eq. 3.40, Eq. 3.41 is obtained which can be solved analytically.

$$L_{\mathrm{abs}} = \frac{1}{\Delta z} \int_{\mathrm{a}}^{\mathrm{c}} [B_{\mathrm{i-1}} + (L_{\mathrm{s1}} - B_{\mathrm{i-1}})\, \exp(-\beta_{\mathrm{abs,i-1}}\, s_{\mathrm{i-1}})]\, [1 - \exp(-\beta_{\mathrm{abs,i}}\, s_{\mathrm{i}})]\, dz \tag{3.41}$$

The path is defined:

$$s_{\mathrm{i-1}} = \tfrac{z}{cos\theta} \quad \text{from a to c in the neighboring grid box (i-1, j)}$$

and:

$$s_{\mathrm{i}} = \begin{cases} \frac{\Delta x}{sin\theta} & \text{from a to b in the grid box (i, j)} \\ \frac{\Delta z - z}{cos\theta} & \text{from b to c in the grid box (i, j)} \end{cases}$$

Integrating Eq. 3.41 along z from a to c $\dot{q}_{\mathrm{abs}}$ is received as:

$$\dot{q}_{\mathrm{abs}} = \frac{L_{\mathrm{abs,ab}} + L_{\mathrm{abs,bc1}} + L_{\mathrm{abs,bc2}} + L_{\mathrm{abs,bc3}} + L_{\mathrm{abs,bc4}}}{\Delta x} \cdot \pi \tag{3.42}$$

where

$$L_{\mathrm{abs,ab}} = \tfrac{1}{\Delta z} \left[1 - \exp\left(-\beta_{\mathrm{abs,i}}\, \tfrac{\Delta x}{\sin\theta}\right)\right] \left[B_{\mathrm{i-1}}\,(b-a) - (L_{\mathrm{s1}} - B_{\mathrm{i-1}})\, \tfrac{\cos\theta}{\beta_{\mathrm{abs,i-1}}}\right. \tag{3.43}$$

$$\left. \left[\exp\left(-\beta_{\mathrm{abs,i-1}} \tfrac{b}{\cos\theta}\right) - \exp\left(-\beta_{\mathrm{abs,i-1}} \tfrac{a}{\cos\theta}\right)\right]\right] \tag{3.44}$$

$$L_{\mathrm{abs,bc1}} = \frac{1}{\Delta z}\, B_{\mathrm{i-1}}\, (c - b) \tag{3.45}$$

$$L_{\mathrm{abs,bc2}} = -\frac{1}{\Delta z}\, (L_{\mathrm{s1}} - B_{\mathrm{i-1}})\, \frac{\cos\theta}{\beta_{\mathrm{abs,i-1}}} \left[\exp\left(-\beta_{\mathrm{abs,i-1}} \frac{c}{\cos\theta}\right) - \exp\left(-\beta_{\mathrm{abs,i-1}} \frac{b}{\cos\theta}\right)\right] \tag{3.46}$$

$$L_{\mathrm{abs,bc3}} = -\frac{1}{\Delta z}\left(L_{\mathrm{s1}} - B_{\mathrm{i-1}}\right)\frac{\cos\theta}{\beta_{\mathrm{abs,i}}-\beta_{\mathrm{abs,i-1}}} \exp\left(-\beta_{\mathrm{abs,i}}\frac{\Delta z}{\cos\theta}\right)\left[\exp\left(\frac{(\beta_{\mathrm{abs,i}}-\beta_{\mathrm{abs,i-1}})\,(c-b)}{\cos\theta}\right)\right] \tag{3.47}$$

$$L_{\mathrm{abs,bc4}} = -\frac{1}{\Delta z}\,B_{\mathrm{i-1}}\,\frac{\cos\theta}{\beta_{\mathrm{abs,i}}}\,\exp\left(-\beta_{\mathrm{abs,i}}\frac{\Delta z}{\cos\theta}\right)\left[\exp\left(\frac{c\,\beta_{\mathrm{abs,i}}}{\cos\theta}\right) - \exp\left(\frac{b\,\beta_{\mathrm{abs,i}}}{\cos\theta}\right)\right] \tag{3.48}$$

The emission is calculated analogously to the upper and lower contributions (Eq. 3.37) described before by replacing L_{top} with the averaged Planck emission of the layer, integrating over z and setting the integration boundaries to a, b, and c.
$\dot{q}_{\mathrm{abs}}$ and $\dot{q}_{\mathrm{em}}$ as derived from Eq. 3.42 and Eq. 3.38 are already area weighted, multiplied by π to account for the angular integration, and have the unit W/m^3.
Finally, the heating rate is the sum of all absorption and emission contributions through all six faces for upwelling and downwelling radiances of a grid box and divided by ρ and c_p to get the unit K/d (see Eq. 2.18).

Assumptions and Correction Factors

The NCA includes several assumptions:

- The first one is the neglect of scattering; this is usually a good approximation in the thermal spectral range where Rayleigh scattering is negligible and absorption by cloud droplets and particles is large; the related uncertainties will be discussed in Section 3.2.1.
- Horizontal travel of thermal radiation beyond the neighboring column is neglected; this causes a systematic bias because neighboring clouds (in particular if higher than the pixel under consideration) emit more thermal radiation than the cloudless sky and would therefore cause a reduced cooling; see also Fig. 3.12 where the neighboring clouds are bright spots.
- Finally, emission and absorption of a grid box are estimated by using a zenith angle of 45° and it is assumed that radiation hits the grid box faces perpendicular in the azimuth.

The first two assumptions and thus the existing bias are required in order to obtain a reasonably fast approximation of thermal radiative transfer and little can be done to change that. Inclusion of scattering or consideration of remote model columns would imply a significant increase in computational time. However, for the third approximation, a correction can be introduced by systematically comparing NCA and exact 3D MYSTIC simulations for an isolated grid box in an idealized set up. It will be shown in the following that the bias by the angle approximations can be corrected by a fit function. In particular it was found that the contribution by the grid box side and top faces to the heating/cooling rate is too strong or weak (depending on the aspect ratio of the grid box) for small optical thicknesses. To determine the error introduced by the simplifications, a one-layer, isothermal (288.2 K), non-scattering atmosphere with an isolated grid box in the middle of the domain was assumed (see Fig. 3.16). The heating rates were calculated for a wavelength of 10 μm. In the following, the calculated factor is always the quotient of NCA and Monte Carlo simulation. For the cloud

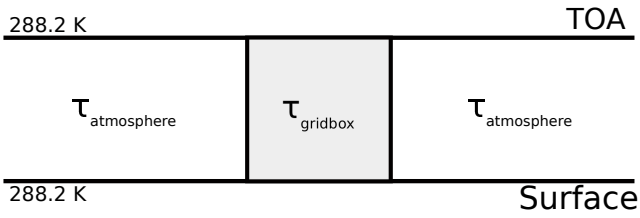

Figure 3.16: Idealized setup for the factor estimation. The optical thickness of the atmosphere $\tau_{\text{atmosphere}}$ and a grid box τ_{gridbox} are varied from 0.01 to 1000. Additionally, the aspect ratio of the grid box is changed. The simulations are performed at 10 μm in an isothermal atmosphere (288.2 K).

side correction factor estimation, the optical thickness was varied from 0.1 to 1000 for both the environment and the grid box and a variety of aspect ratios ($\Delta x/\Delta z$) ranging from 10 to 0.1 were investigated. The correction factor was found to be a function varying with aspect ratio and optical thickness of grid box and surroundings. The final fit curve was determined by a weighted fit, using the side contributions of the heating/cooling rate as weight, ensuring that the fit works best for large heating/cooling rates. As the factors converge to 1 for high optical thicknesses and to a constant value different from 1 for small optical thicknesses, the factors were found to approximately follow an inverse tangent *arctan*() (see Fig. 3.17). An example for the weighted fit is given in Fig. 3.18 for the side face correction. The black line is the weighted fit on all data points (varying with optical thickness). Gray dots indicate all factors given by various combinations of the optical thickness of the environment and the grid box. Red dots indicate the most relevant 50%, blue dots the most relevant 20% (those 50/20% with the highest weights). These factors give an indication for the development the of

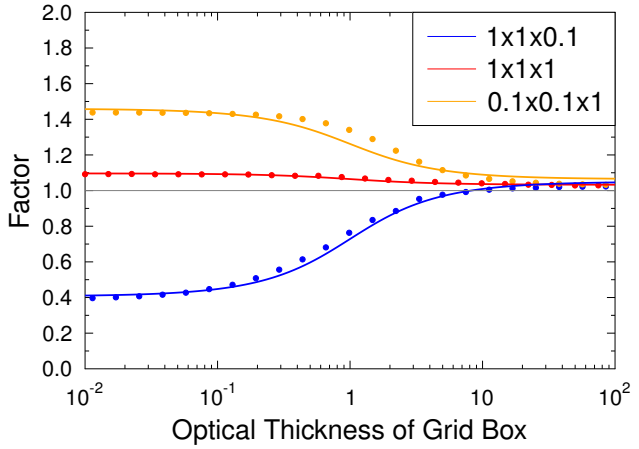

Figure 3.17: Example of the fitting curves. Three possible aspect ratios (0.1,1,10) for an atmosphere with small optical thickness (0.01 or 0.001, depending on the aspect ratio) and varying optical thickness of the grid box are shown. Solid lines show possible fit curves, dots show the actual factors estimated by the comparison of MYSTIC and the NCA.

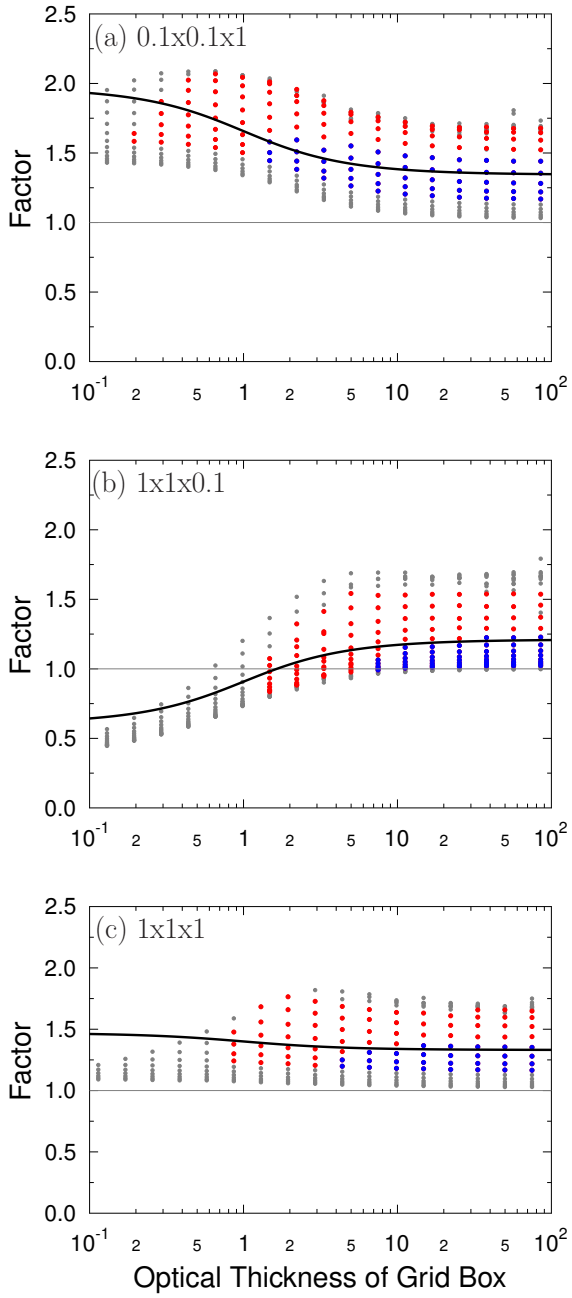

Figure 3.18: Correction factor for grid box side contributions. The black line shows the fit calculated by Eq. 3.49. Gray dots indicate all factors (depending on optical thickness of environment and of the grid box) for which the factor was estimated. The red and blue dots show the most significant 50% and 20% of those factors.

the fit curve. The correction factor (f_{side}) for the side contribution follows Eq. 3.49, with a_{side} and b_{side} following Eq. 3.50 and 3.51. The optical thickness $\tau_{abs,min}$ is the minimum optical

thickness of the grid box.

$$f_{\text{side}} = a_{\text{side}} \cdot arctan(\tau_{\text{abs,min}}) + b_{\text{side}} \tag{3.49}$$

$$a_{\text{side}} = 0.39 \cdot arctan(ln(\Delta x/\Delta z) - 0.24) \tag{3.50}$$

$$b_{\text{side}} = -0.67 \cdot arctan(ln(\Delta x/\Delta z) - 0.3) + 1.28 \tag{3.51}$$

The factor for the top contribution was estimated in a similar way. The top contribution to the absorption is independent of the incoming radiance, because the radiance was already calculated before. This is different to the side contribution, where the incoming radiance is directly linked to the absorption calculation (see Chapter 3.2.1). Therefore a constant optical thickness of 0.01 or 0.001 (depending on the aspect ratio of the grid box) is chosen and the optical thickness of the grid box is varied, similar to the side contribution, from 0.1 to 1000. From these results the correction factors for the top contribution can be estimated. Fig. 3.19 shows the fit functions (solid lines) for 5 different aspect ratios and the factors (dots). The correction factor (f_{top}) for the top contribution follows Eq. 3.52), with a_{top}, b_{top} and c_{top} following Eq. 3.53, 3.54 and 3.55.
The thus estimated factor can be divided from the side/top contributions of the heating rate. Applying this factor to the side/top contribution of the heating/cooling rate reduces the systematic overestimation by the NCA as well as the scatter (see Fig. 3.20).

$$f_{\text{top}} = arctan(\tau_{\text{abs,min}} \cdot \Delta x \cdot a_{\text{top}}) \cdot b_{\text{top}} + c_{\text{top}} \tag{3.52}$$

$$a_{\text{top}} = 0.6 \cdot arctan\left(7.35 \frac{\Delta x}{\Delta z}\right) - 0.35 \tag{3.53}$$

$$b_{\text{top}} = \frac{1 - c_{\text{top}}}{\frac{\pi}{2}} \tag{3.54}$$

$$c_{\text{top}} = 1.14 \cdot arctan(\frac{\Delta x}{\Delta z} - 0.36) + \frac{2.02}{0.48 \cdot \exp(\frac{\Delta x}{\Delta z})} - 0.84 \tag{3.55}$$

Isolated Cuboid Clouds

Heating rate results (in K/d) for a variety of grid boxes of different aspect ratios and with different optical properties in a realistic atmosphere are shown. These grid boxes are isolated. The results of the NCA to a full 3D Monte Carlo simulation with MYSTIC (MC), a 3D MYSTIC simulation without scattering (MC no-sca) and the NCA with a 1D Schwarzschild-solved background field (NCA) are compared. The setup and the results can be seen in Table 3.4 and Table 3.5. The Monte Carlo noise of the MYSTIC results is smaller than 1%. It was found that the neglect of scattering causes only small errors compared to the full 3D solution.

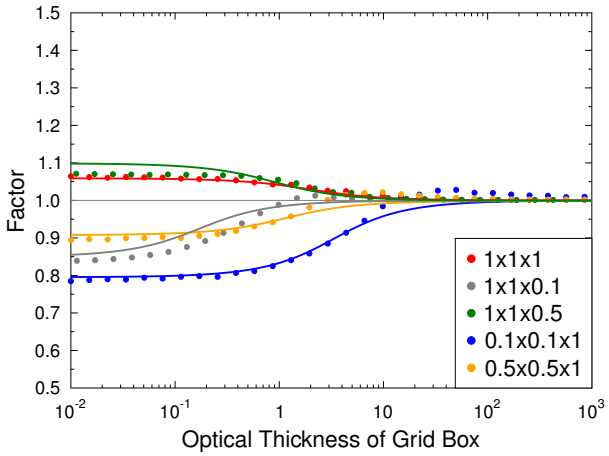

Figure 3.19: Correction factors for grid box top contributions. Solid lines show the fit curve gained by Eq. 3.52, dots show the actual factors estimated by the comparison of MYSTIC and the NCA.

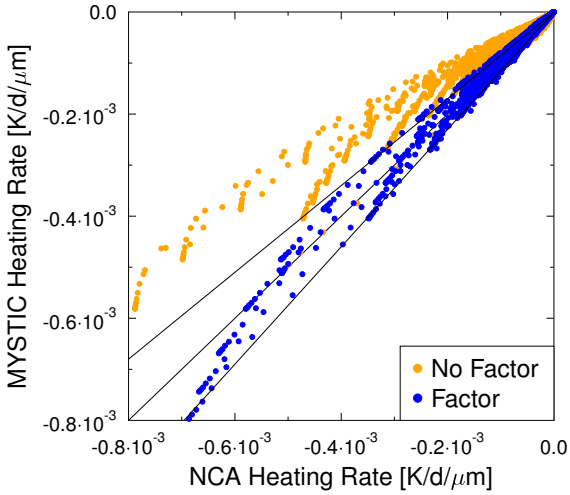

Figure 3.20: Comparison of heating rate side plus top contributions for various optical thicknesses and aspect ratios with (red) and without (blue) the correction factors, NCA vs. MYSTIC. Black lines indicate the 1:1 line and a 15% offset lines. The heating rates where calculated in the atmospheric window for a wavelength of 10 μm

Parameter	Value
Number of Photons	1000000 per grid box
Temperature Profile	US Standard Atmosphere (Anderson et al., 1986)
Trace Gas Concentrations	US Standard Atmosphere (Anderson et al., 1986)
Molecular Absorption Param.	correlated-k (Fu and Liou, 1992)
Surface Emissivity	1

Table 3.4: Model input for the 3D MYSTIC cuboid simulations.

resolution (km^3)	τ	MC	MC_{no-sca}	NCA	% (NCA/MC)	% (NCA/MC_{no-sca})
1 x 1 x 1	0.1	-1.71	-1.71	-1.67	-2.3 %	-2.3 %
1 x 1 x 1	1	-5.49	-5.49	-5.28	-3.8 %	-3.8 %
1 x 1 x 1	100	-18.16	-18.83	-17.76	-2.2 %	5.68 %
0.5 x 0.5 x 1	0.1	-1.72	-1.72	-1.67	-2.9 %	-2.9 %
0.5 x 0.5 x 1	1	-5.85	-5.86	-5.58	-4.6 %	-4.8 %
0.5 x 0.5 x 1	100	-28.78	-29.80	-27.66	-3.9 %	7.1 %
0.1 x 0.1 x 1	0.01	-1.74	-1.74	-1.51	-13.2 %	-13.2 %
0.1 x 0.1 x 1	1	-6.44	-6.44	-5.37	-16.6 %	-16.6 %
0.1 x 0.1 x 1	100	-106.0	-109.64	-102.09	-4.0 %	-6.9 %
1 x 1 x 0.5	0.01	-2.21	-2.21	-2.26	2.26 %	2.26 %
1 x 1 x 0.5	1	-9.23	-9.24	-9.3	0.8 %	0.7 %
1 x 1 x 0.5	100	-24.99	-25.91	-25.97	3.9 %	0.2 %
1 x 1 x 0.1	0.01	-6.35	-6.31	-7.11	12.0 %	12.6 %
1 x 1 x 0.1	1	-37.97	-37.42	-40.45	6.5 %	8.1 %
1 x 1 x 0.1	100	-79.58	-82.50	-86.56	8.8 %	4.8 %

Table 3.5: Heating rate result comparison in K/d for grid boxes of different aspect ratio. Shown are the results for a full 3 dimensional MYSTIC calculation (MC), a MYSTIC calculation without scattering (MC_{no-sca}) and the NCA solver (NCA) using a standard Schwarzschild solution as 1D input field. Additionally, the percentage difference between the MYSTIC simulation with and without scattering and the NCA is shown. The MYSTIC results are within 1% uncertainty.

In general the difference between the MYSTIC 3D heating rates and those calculated by the NCA are about 2 % - 10 % for the isolated cuboid grid boxes. An exception is those grid boxes with extreme aspect ratios (0.1 x 0.1 x 1 km^3 and 1 x 1 x 0.1 km^3). This might be due to the fact that the correction fit is a weighted mean of all possible factors for the side contributions, which seems not to be the best approximation for this specific optical thickness and aspect ratio. However these kind of aspect ratios are not expected to occur often in the model application.

3.2.2 Results and Application

Realistic Cloud Fields

In a next step the parameterization is tested for a variety of real LES-cloud fields. The cloud field shown here is a cumulus cloud field (see Fig. 3.21) from a UCLA-LES (Stevens et al., 2005; Stevens, 2007) simulation. The simulation (Heinze et al., 2015) was performed within the HD$(CP)^2$ project (High Definition Clouds and Precipitation for Climate Prediction project). The whole simulations covers 19 days in April and May 2013. The computational domain is centered around a geographical latitude of 50.92°. The original field (960x960x144 grid boxes) has a grid box size of 50 m. The simulation was driven by a large scale forcing of 3 hourly COSMO-DE data of a 2° x 2° box around the center of the simulation domain. The cumulus

cloud field shown here is from May 2, 2013 at 12 UTC.
The heating rate results for a quarter of the scene are evaluated. To see how the NCA performs for different model resolutions, the cloud field was also averaged over 4/16 grid boxes to 100/200 m grid box size. The setup for the various simulations can be seen in Table 3.6.

Fig. 3.22 shows the comparison of the 1D ICA and 3D MYSTIC simulations (left) as well as the NCA and 3D MYSTIC simulations (right). The resolution decreases from 50 m (top) to 100 m (middle) to 200 m (bottom). Overall, the NCA agrees much better with the 3D MYSTIC results than the 1D ICA approximation. Especially the cloud side grid boxes (black dots) which show heating rates of about 0 K/d in the ICA are represented better by the NCA and shifted to higher values. The RMSE of the heating rates (see Table 3.7) is smaller for NCA vs. MYSTIC compared to ICA vs. MYSTIC. All cloudy grid boxes and also those grid boxes belonging to cloud sides are compared. In all cases, the RMSE were smaller for the NCA compared to the ICA. The bias (see also Table 3.7) shows that the NCA generally overestimates the cooling, while the ICA underestimates the cooling. However, overall the warming bias of the ICA is larger than the cooling bias of the NCA at cloud sides. For the total field (clearsky and cloudy grid boxes), the cool bias of the NCA is slightly higher than the warm bias of the ICA.

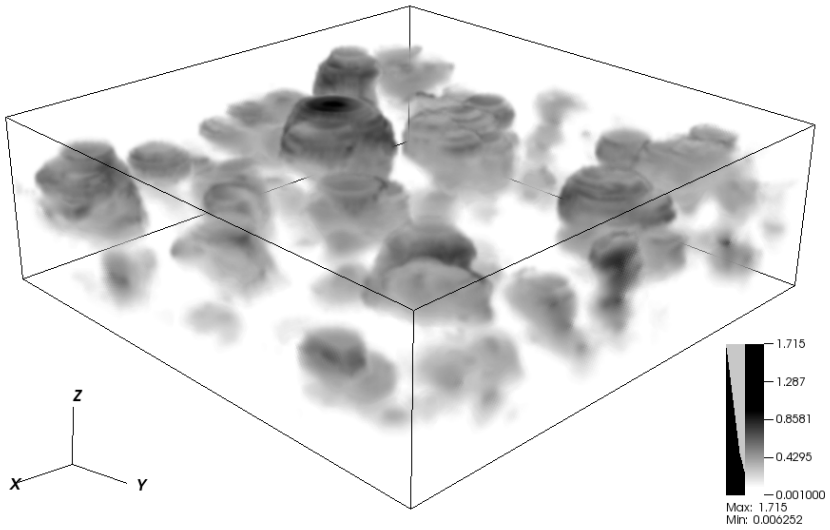

Figure 3.21: 3D distribution of the liquid water content of the cumulus cloud field (50 m resolution).

Parameter	Value
Number of Photons	1000 per grid box and spectral band
Temperature Profile	US Standard Atmosphere (Anderson et al., 1986)
Trace Gas Concentrations	US Standard Atmosphere (Anderson et al., 1986)
Molecular Absorption Param.	correlated-k (Fu and Liou, 1992)
Surface Albedo	0

Table 3.6: Model input for the 3D MYSTIC calculations.

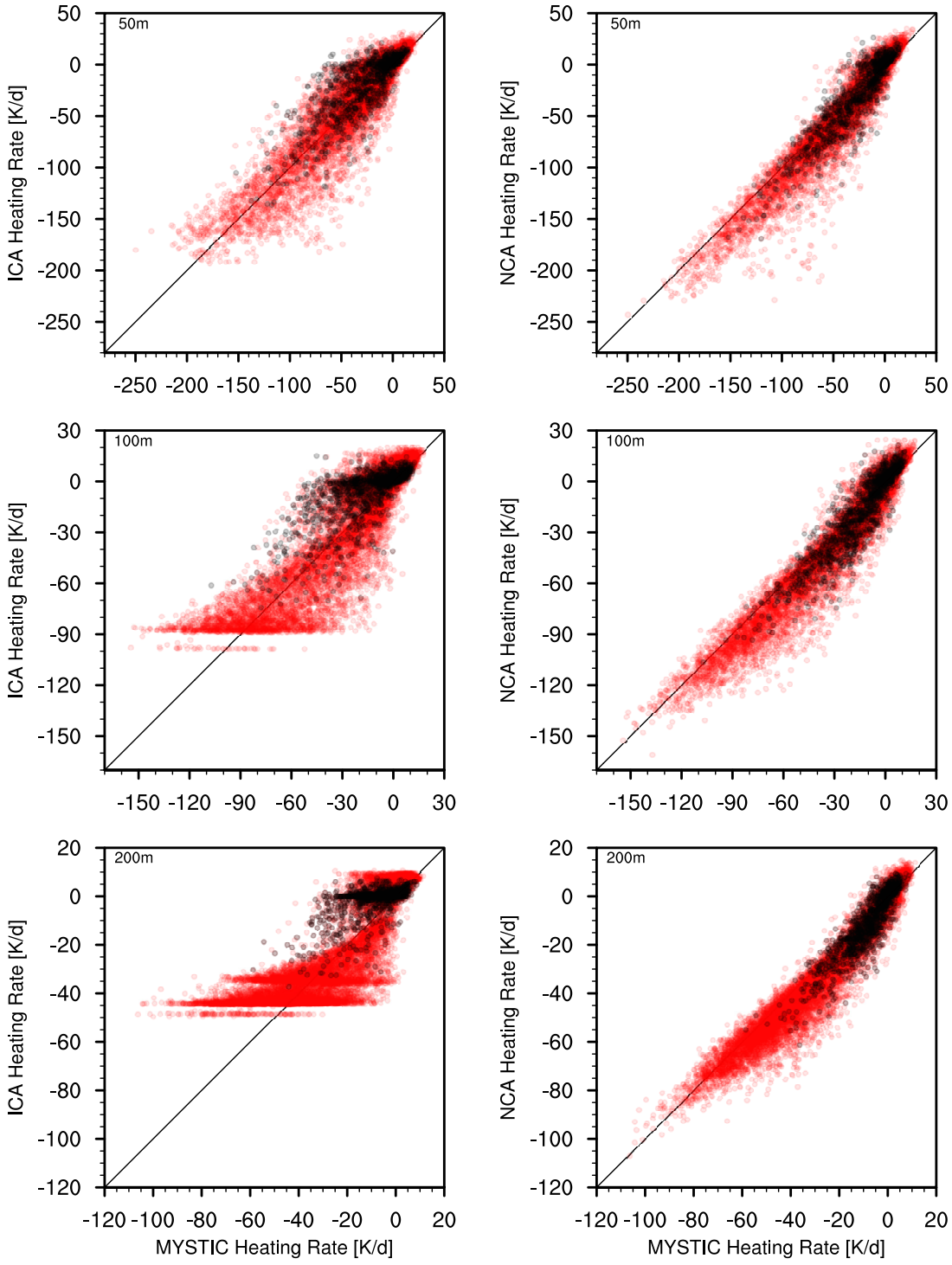

Figure 3.22: Comparison of the ICA (left) and the NCA (right) to full 3D MYSTIC results of a cumulus cloud field of different model resolution (top: 50 m; middle: 100 m; bottom: 200 m). Red dots show heating/cooling rates of all cloudy grid boxes, black dots the cloud side heating/cooling rates. The more transparent the colors, the less often the heating/cooling occurs.

	RMSE		bias	
case	ICA-MC3D	NCA-MC3D	ICA-MC3D	NCA-MC3D
50 m all	5.2	4.6	0.2	-0.4
100 m all	6.6	4.7	0.4	-0.9
200 m all	4.4	2.5	0.4	-0.6
50 m all cloud	14.9	13.0	1.3	-3.1
100 m all cloud	13.4	9.6	1.6	-3.3
200 m all cloud	11.8	6.8	3.28	-3.4
50 m cloud side	19.4	14.3	7.7	-2.5
100 m cloud side	15.9	10.4	9.0	-2.9
200 m cloud side	9.7	6.0	6.2	-2.7

Table 3.7: RMSE and bias for the cumulus cloud field with the 3 resolutions. The 3D MYSTIC simulation (MC3D) is compared to a 1D independent column (ICA) and the NCA (NCA) solution. Results of all grid boxes (clearsky and cloudy boxes) all cloudy grid boxes and cloud side grid boxes are shown.

Performance and Limitations

The performance of the NCA was tested by implementing the NCA into the UCLA-LES. UCLA-LES was run at the DKRZ (Deutsches Klimarechenzentrum), Hamburg, on an IBM Power 6 with a resolution of 100 m and 256 x 256 x 110 grid boxes on 512 cores. It could be shown that the NCA is only a factor of 1.5 - 2 more expensive than a 1D radiation approximation. The main step in computational cost occurs when considering radiation: even for 1D radiation (a delta-four-stream approximation, UCLA-LES), the CPU time increases by a factor of 30-50 compared to the calculation without radiation for the tested cases.
There are of course several assumptions which introduce systematic biases to the heating rate result. In particular, the consideration of only one neighboring grid box limits the applicability of the NCA to a range of model resolutions as will be outlined below. The assumptions were already pointed out in Section 3.2.1 and a correction factor for some of the assumptions was introduced. All other simplifications used for the NCA cause a slight overestimation of the heating or cooling rates.
One aspect which has to be considered when the method is applied is the model resolution. The NCA method allows horizontal transport of radiation, but only within a selected grid box and to its direct neighboring columns. Therefore cloud side effects can only be seen in the outermost grid box of a model cloud. Thermal heating and cooling occur within an optical thickness of 2 to 3, counted from the cloud edge, see also Klinger and Mayer (2014) (their Figures 10 and 11). Since the NCA cloud edge heating and cooling rates are restricted to the one grid box at the cloud edge, the NCA will perform best if the grid box optical thickness is 2-3 or larger. For optically thinner grid boxes, the NCA will miss part of the heating/cooling in all these boxes not directly at the edge of the cloud. An absorption optical thickness of 2-3 corresponds to a model resolution of 100-200 m. The smaller the grid box size, the more the cloud side cooling effects will be confined to the outermost grid box of a cloud and will not propagate into the cloud as it is found in reality, when the NCA is applied. Therefore it can

be concluded that the NCA works best for resolutions of about 100 m or larger (which could also be shown in the application example).

3.2.3 Summary and Conclusion

A fast and accurate method to calculate 3D thermal heating rates is presented. The method uses input from the directly neighboring columns of a gird box in a model domain and is therefore called Neighboring Column Approximation (NCA). The NCA may use the existing 1D ICA radiation code of a cloud resolving model or can be used with any 1D radiation code. It can therefore be easily applied in any cloud resolving model where a 1D radiation solver is implemented. Several assumptions were made to make this radiative transfer solution an analytic and fast approximation. Next to the neglect of horizontal transport of radiation beyond one neighboring column, scattering is neglected and radiation transport is approximated by using an effective zenith angle of 45°, perpendicular to the grid box faces in the azimuth. For the latter two assumptions, a correction function was found and implemented. An additional advantage of the method is that it can be used in parallelized models without breaking the parallelization. The computational costs of the NCA are only a factor of 1.5-2 higher compared to a 1D radiation approximation. The method performs best for model resolutions of about 100 m or coarser and a significant improvement towards common 1D radiative transfer approximations was shown. For isolated grid boxes, the NCA differed about 10% from an exact 3D Monte Carlo simulation. For a cloud field application with a resolution of 100 m, the RMSE for all cloudy grid boxes in the domain decreased from 13.6 K/d (ICA vs. MYSTIC) to 9.6 K/d (NCA vs. MYSTIC). Maximum cooling rates for the full 3D simulation with MYSTIC reach values of -150 K/d (100 m resolution) while the 1D approximation shows maximum coolings of -100 K/d. The NCA however is capable of reproducing the stronger 3D cooling rates.

3.2.4 Further Applications of the NCA

In addition to the application tests of the NCA shown in the work of Klinger and Mayer (2016), the relative BIAS of the performance of the NCA and a 1D ICA approximation in comparison to a 3D MYSTIC simulation for different cloud fields is shown in Table 3.8. The first five cloud fields are, as the name indicates, snap shots of different cumulus cloud field simulations at different resolutions (66 m, 50 m, 50 m, 100 m and 200 m). The last three cumulus cloud fields (Cumulus HPS) were also shown in the paper of Klinger and Mayer (2016). The last five simulations are stratus like cloud fields, again at different resolutions (55 m, 50 m, 100 m, 200 m, 80 m). Overall, the positive values of the NCA indicate an overestimation of the cooling, the negative values of the relative BIAS of the ICA simulations show a underestimated cooling. The NCA performs much better at cloud sides. Averaging over all shown cloud fields (total, last row), the absolute value of the relative bias is higher in the case of NCA than ICA.

Cloud Field	NCA (total)	NCA (side)	ICA (total)	ICA (side)
Cumulus (I3RC)	19 %	7 %	-9 %	-64 %
Cumulus	10 %	6 %	-6 %	-73 %
Cumulus (50 HPS)	11 %	9 %	-6 %	-28 %
Cumulus (100 HPS)	17 %	19 %	-7 %	-59 %
Cumulus (200 HPS)	14 %	30 %	-10 %	-81 %
Stratus (I3RC)	15 %	26 %	-2 %	-24 %
HPS 50	9 %	6 %	-3 %	-18 %
HPS 100	15 %	10 %	-1 %	-45 %
HPS 200	13 %	22 %	-1 %	-65 %
ASTEX	18 %	70 %	6 %	42 %
Total	12 %	14 %	-2 %	-37 %

Table 3.8: Relative bias of NCA and 3D MYSTIC and ICA and 3D MYSTIC for different cloud fields.

3.3 Large Eddy Simulations

3.3.1 The UCLA-LES

The last step of this thesis is a detailed study of the effects of thermal radiation and especially of 3D thermal radiation on the development of clouds. For this, a cloud resolving model is needed which is capable of simulating 3D thermal radiation.
For the cloud simulations in this thesis, the University of California, Los Angeles LES (UCLA-LES; Stevens et al. (2005); Stevens (2007)) was used. The UCLA-LES is a well established LES-model and took part in simulating well known cases such as BOMEX (Cheng et al., 2010), RICO (van Zanten et al., 2011) or DYCOMS (Stevens et al., 2005). The UCLA-LES includes bulk microphysics for warm clouds (Seifert and Beheng, 2001) and a 1D radiation scheme (δ-four-stream, Liou et al. (1988)), with a correlated-k molecular absorption parameterization (Fu and Liou, 1992). The Monte Carlo spectral integration (MSCI; Pincus and Stevens (2009)) is implemented. The prognostic variables of the model are the three components of the wind, the liquid water potential temperature (Θ_l), the total water mixing ration (r_t) and, microphysical variables like for example, rain water mixing ratio or ice properties, depending on the microphysics scheme. Sub-grid scale processes are parameterized by the Smagorinsky (1963) model. The parallelization of the model is a decomposition of the modeling domain into sub-domains in the x-y plane.
For the use of the UCLA-LES in this thesis, the model had to be adapted for 3D radiation. For this, the newly developed Neighboring Column Approximation (NCA; Section 3.2.1; Klinger and Mayer (2016)) was implemented into the model, making use of the already existing broadband spectral integration and the implemented 1D δ-four-stream scheme. With the NCA included, UCLA-LES is capable of simulating 3D thermal heating rates and the effect of 1D and 3D thermal radiation on cloud development can be studied.
The effect of thermal radiation on cloud development was studied following two approaches

of different complexity: First, idealized studies of heat bubble experiments were performed. This setup allows to isolate thermal radiation effects on a single cloud. Two different single cloud simulations were performed, one resulting in an axially symmetric, the other one in a non-symmetric single cloud. Second, the development of a shallow cumulus cloud field in a 25 x 25 km^2 was studied. Shallow cumulus clouds are a perfect target to study 3D thermal radiation effects on clouds, because of the moderate updraft velocities and the 3D structure of these clouds. More details on the specific setups of both simulation types are given in the following.

3.3.2 Idealized Studies of Heat Bubble Experiments

A heat bubble or plume is a common method for initializing convection and for studying its development. Studies initialized by heat bubbles have been performed for a long time, with numerical simulations or tank experiments. A detailed review about the heat bubble history is given in Yano (2014). In this thesis, the heat bubble method serves for the simulations of idealized single clouds, which allows to isolate effects of thermal radiation much better than in a realistic cloud field simulation. An initial temperature perturbation (the bubble) in the lower layers of a model causes air to rise and condense, forming a cloud. The temperature perturbation in the simulations performed in this study was an elliptical shaped volume of warmer air close to the surface with a radius of 500 m in the horizontal and 400 m in the vertical. The temperature perturbation was strongest in the middle of this ellipsoid and was set to 0.8 K. It decreased with distance from the center following a gaussian distribution. Two different single cloud simulations were performed. The first cloud was forced by a symmetric forcing placed in the middle of a modeling domain, resulting in an axially symmetric cloud (called *axially symmetric cloud* in the following). For the second cloud, the forcing was applied at the same location and with the same gaussian distribution, but a random noise was added to the temperature perturbation. This caused the resulting cloud to develop non-symmetrically and appear more realistic. This type of simulation is called *non-symmetric cloud* in the following. The random noise was implemented in such a way that the simulation could be repeated with the same random numbers at the same location for each of the performed simulations, causing the 'same' cloud to develop. The temperature perturbation was initialized at the initial time step. No additional temperature disturbances were applied later in the simulation. The simulation setup is described in Table 3.9 and the initial profile of the atmosphere is shown in Fig. 3.23. The sea surface temperature (SST), the basic state potential temperature (TH00) and the surface type are mentioned, because they are required to perform the simulation, but non of them had a strong effect on the development of the single cloud, which were driven by the initial bubble perturbation. These model variables are important for the large scale simulations (Section 3.3.3) and will be explained there. The heat bubble simulations were specifically set up in a way to study a single shallow cumulus cloud. Although it is not clear how radiation affects cloud development, it is expected that radiation effects will be stronger if the development of the cloud is not dominated by strong vertical updrafts. Heating and cooling rates act locally on the cloud. In a deep convective system where the air is in strong upward motion, the impact time of radiation is small. Therefore the initial forcing was chosen deliberately weak.

Model Variables	Value
Number of Grid Boxes	64 x 64
Number of z-levels	70
Resolution	100 m
Vertical Stretching	10 %
Surface Forcing	0.8 K
TH00	288 K
SST	288 K
CCN	$70 \cdot 10^6$ $1/dm^3$
Microphysics	warm clouds, no rain
Variable Output	every 100 s
Surface Type	fixed SST

Table 3.9: Model setup for the heat bubble simulations.

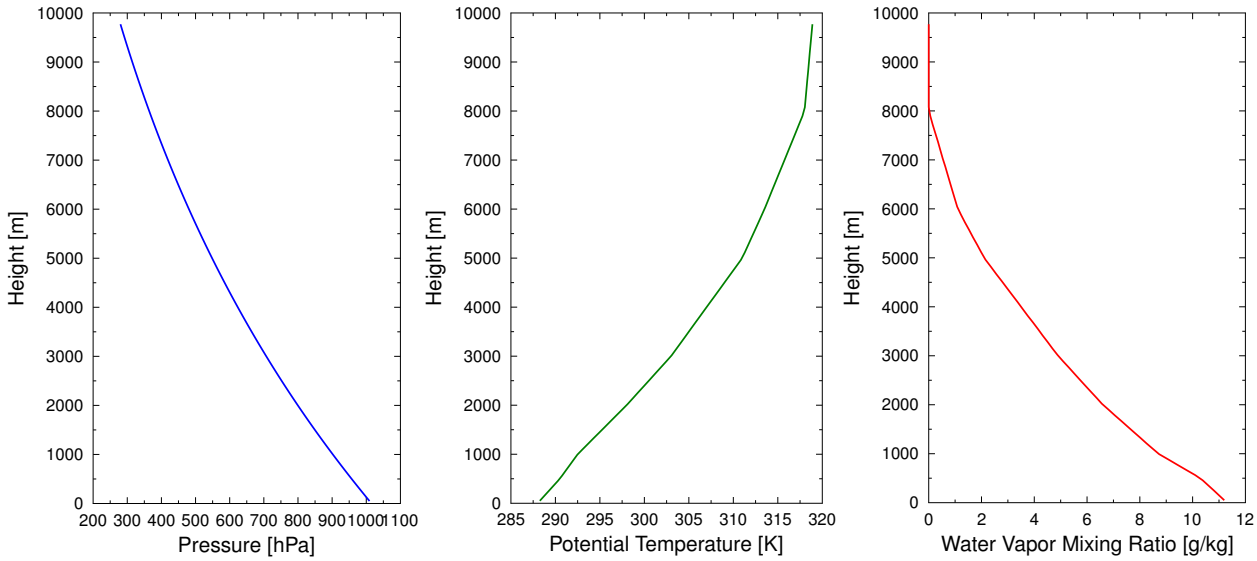

Figure 3.23: Initial profiles of pressure [hPa], potential temperature [K] and water vapor mixing ratio [g/kg] of the heat bubble simulations.

To study the effect of thermal radiation on cloud development, a reference simulation without the effect of radiation (case: *No-Radiation*) and simulations including 1D and 3D thermal radiation (cases: *Thermal 1D ICA* and *Thermal 3D NCA*) were performed and compared. For both simulations with thermal radiation, a full thermal correlated-k spectral integration (Fu and Liou, 1992) was performed. The simulations were performed locally at LMU Munich. Each of the simulations was performed on a single workstation with 8 cores.

3.3.3 Large Scale Shallow Cumulus Cloud Fields

Second, studies of shallow cumulus cloud fields were performed. Due to the three dimensional shape of shallow cumulus clouds and the moderate updraft velocities, they are a perfect target for the study of the effects of 3D thermal radiation on clouds. The environment was a ocean surface without orography. In order to estimate the effect of heating and cooling rates on cloud development, there was no interaction of surface fluxes with radiation allowed in all simulations performed in this study. The effects of the interaction between thermal radiation and the surface are supposed to be small. The setup was chosen to vary the complexity of the simulations step by step. First, simulations with prescribed fluxes of latent (180 W/m^2) and sensible heat (18 W/m^2) were performed. In a second step, the sea surface temperature was kept constant at 300 K and fluxes were allowed to develop with time. Only warm microphysics were considered.
Different radiation schemes were used in this simulations. Next to the 1D $\delta - four\ stream$ radiation solver, and the NCA, the *Tenstream Radiative Transfer solver* (Jakub and Mayer, 2015a,b) was implemented into UCLA-LES (done by Fabian Jakub). The Tenstream solver was developed for the calculation of solar radiative transfer, but is also capable of calculating thermal heating and cooling rates. The Tenstream solver includes a two-stream and Schwarzschild 1D radiation approximation. The NCA, based on the two-stream and Schwarzschild 1D approximation was also implemented in the Tenstream solver (for a full description of the method, the reader is referred to the paper (Jakub and Mayer, 2015a)). The advantage of the NCA, in comparison to the thermal solution of the Tenstream solver is that the NCA is faster in terms of computational time and that no additional software packages are needed when the NCA has to be applied (which is the case for most applications of the Tenstream solver).
Comparing the different radiation schemes allowed to study the effect which different radiation solver might have on the results of a cloud simulation.
In order to estimate the effect of thermal radiation on the development of clouds, all simulations were performed without and with thermal radiation. An overview of the simulation setup and the radiation combinations is given in Table 3.10 and 3.11.

The initial profiles follow Stevens et al. (2005) and can be seen in Fig. 3.24. The profiles have a dry inversion in about 1000 m height. Based on these profiles, fluxes and microphysics are varied following Table 3.10. All simulations were performed on 512 cores on Blizzard at DKRZ (Deutsches Klima Rechenzentrum, Hamburg), an IBM Power 6 with 64 cores/node.
Simulations with radiation are known to be computationally expensive, because the wavelength integration has to be performed at each time step. One way to reduce computational costs is the Monte Carlo spectral integration (MCSI) approach (Pincus and Stevens, 2009) (Section 2.1.3). In order to use this method in a 3D radiation application, modifications were necessary. Neighboring columns are communicating in a simulation with 3D radiation (in the NCA as well as the Tenstream method). Therefore, errors might occur if the radiation solutions are different in each model column (which they would be if the original MCSI method is applied, where the random sampling of sub bands is performed at each time step and for each model column). Therefore the method was modified to select a single wavelength band per time step, but for the whole modeling domain. Testing of this modification showed that the statistical results are still unmodified by this assumption (Jakub and Mayer, 2015b). All large

Model Variables	SC_fixed_flux	SC_fixed_SST
Number of Grid Boxes	256 x 256	256 x 256
Number of z-levels	110	110
Resolution x,y	100 m	100 m
Resolution z	30 m	30 m
Vertical Stretching	10 %	10 %
TH00	296 K	296 K
SST	-	300 K
CCN	$150 \cdot 10^6$ $1/dm^3$	$150 \cdot 10^6$ $1/dm^3$
Latent Heat	180 W/m^2	adjusting
Sensible Heat	18 W/m^2	adjusting
Microphysics	warm	warm and rain
Variable Output	every 300 s	every 300 s
Surface Fluxes	prescribed	adjusting
Restart	14400 s	21600 s

Table 3.10: Model input for shallow cumulus simulations.

Simulation	Radiation Type
SC_fixed_flux	No Radiation
	Thermal 1D Two-stream
	Thermal 1D δ-four-stream
	Thermal 1D Schwarzschild
	Thermal NCA Two-stream
	Thermal NCA δ-four-stream
	Thermal NCA Schwarzschild
	Thermal Tenstream
SC_fixed_SST	No Radiation
	Thermal 1D δ-four-stream
	Thermal 1D Schwarzschild
	Thermal NCA δ-four-stream
	Thermal NCA Schwarzschild
	Thermal Tenstream

Table 3.11: Radiation configurations for the different cumulus cloud field simulations.

scale simulations results shown in this work were performed by applying the MCSI approach. To save even more computational time, all simulations with thermal radiation were restarted after a certain time. The basic simulation implements a 1D thermal and solar radiation approximation with the same initial conditions shown in Tab. 3.10. After 4 h (Shallow Cumulus fixed flux, hereafter SC_fixed_flux) and 6 h (Shallow Cumulus fixed SST, hereafter SC_fixed_SST), the simulations were restarted with different thermal radiation solvers. Solar radiation was

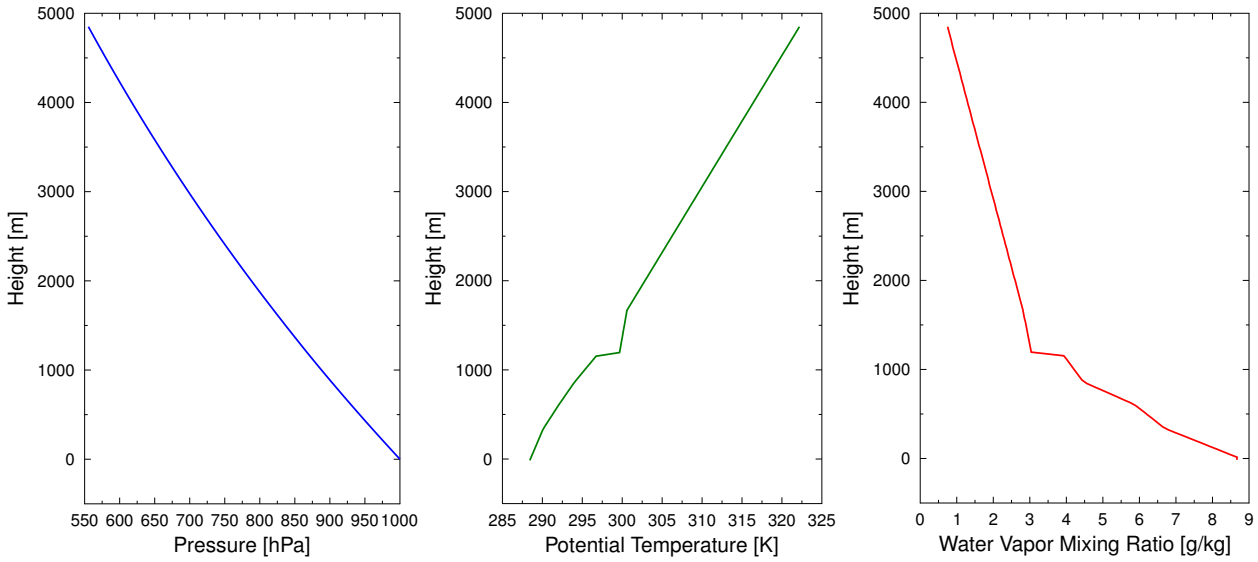

Figure 3.24: Initial profiles of pressure [hPa], potential temperature [K] and water vapor mixing ratio [g/kg] of the heat cumulus cloud field simulations.

switched off. The no-radiation simulation was started from the beginning, due to technical issues, no restart was performed here. The time of the restart was chosen at the moment where first clouds formed in the 1D solar and thermal simulations. The restarted simulations were performed for three different 1D solvers (Two-stream, Schwarzschild and δ-four-stream), the NCA (based on the same three 1D solvers) and the 3D Tenstream solution. The choice of using a simulation with combined 1D solar and thermal radiation as basis shall allow further investigation of the effects of solar and combined solar and thermal radiation with the same setup. A combined simulation of 1D solar and thermal radiation is used, because it is computationally cheaper than a combined simulation of 3D solar and thermal radiation.

Chapter 4

Results

The results of heating rate studies and the cloud resolving simulations are presented in this chapter. First, heating and cooling rates were systematically studied for characteristic idealized cloud geometries with the Monte Carlo model MYSTIC (Section 4.1). The effect of thermal radiation on cloud development is shown in Section 4.2.1 and 4.2.2. Finally, first attempts to study the effect of thermal radiation on cloud droplet growth are presented (Section 4.3).

4.1 Geometry Dependence of 3D Thermal Heating Rates

The effect of cloud geometry and the distance between individual clouds on 3D thermal heating rates (in comparison to 1D thermal heating rates) were studied in a comprehensive comparison in a bachelor thesis under my supervision (Akansu, 2014). In this work, heating rates were evaluated for cloud fields with five different geometrical cloud shapes. These shapes include a cube, a half sphere and a rhombic dodecahedron with the lower edge cut off, which represented clouds in an environment with small horizontal wind speeds; a parallelogram of 45 inclination, and a parallelogram of 22.5 inclination which represented wind shear. The distance between the individual clouds was varied between 25 m (or 50 m in case of parallelogram), 100 m, 500 m and 1000 m. All clouds had a similar horizontal extend and had the same cloud bottom height. For a detailed description of the effects, the reader is referred to the corresponding thesis (Akansu, 2014). A short summary of the effects is given here:
For the above mentioned cases, thermal heating rates were calculated with MYSTIC (Mayer, 2009; Klinger and Mayer, 2014). The heating rates were calculated in 3D and approximated in 1D (ICA). Constant liquid water content (0.266 g/m^3) and an effective radius (10 μm) were chosen for each cloudy grid box, which had a horizontal and vertical extend of 25 m. The optical properties correspond to an optical thickness $\tau = 1$ at 550 nm. The spectral integration was performed using the correlated-k distribution by Fu and Liou (1992) and the background atmosphere was the U.S. standard atmosphere (Anderson et al., 1986).
The analysis showed that 3D thermal heating and cooling occurred at all cloud interfaces. The cloud side cooling wasn't reproduced by the ICA. In the cloud interior, no heating or cooling was found. The heating or cooling was found at the outermost 100-250 m depending on the cloud shape and the distance between the individual clouds. The larger the distance between

the clouds, the stronger the cloud side cooling was in the 3D calculations. Cloud bottoms showed heating rates of about 30 K/d. The maximum cooling was located at cloud tops with about 200 K/d.
Furthermore, the magnitude of the heating or cooling rate varied with the distance between the clouds. For the 3D simulations, heating rates at the cloud bottom became smaller if the distance between the clouds increased, and turned into cooling at the very bottom edge for large distances (Fig. 4.1).

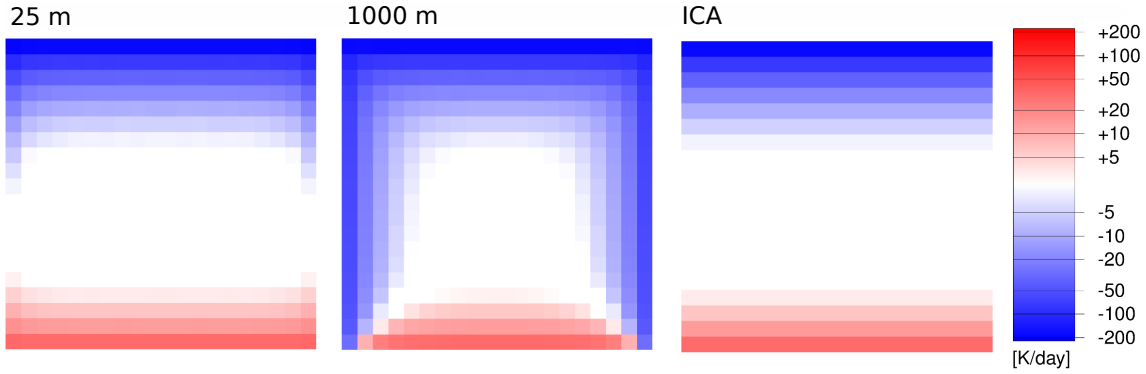

Figure 4.1: Vertical cross section through the center of the cube cloud (modified from Akansu (2014), Figure 5.1). The heating/cooling rate distribution is shown for two 3D MYSTIC simulations and varying distance between the cloud (25 m, 1000 m). In addition, the 1D approximation (ICA) is shown on the right. Cloud side cooling is neglected by the 1D approximation and becomes more and more important with increasing distance between the clouds.

Cooling rates at cloud top edges increased (in absolute value) if the distance became smaller, because the surface emission was shaded by the neighboring clouds and those emitted radiation at smaller temperatures than the surface. However, this behavior was not valid for all cases. It depended strongly on individual cloud geometries.
The dependence of the heating rates on the geometry of cubic clouds is visualized in Fig. 4.2. The figures show radiance distribution at 10 μm with a field of view of 360° in the horizontal and 130° in the vertical seen from the cloud top edge. Gray areas show areas where the radiance is emitted from clouds or the own cloud (left quarter), black areas show the sky and white areas the emission from the surface. It is instantaneously visible that the larger the distance between the clouds, the more the surface emission contributed to the heating or cooling rate at the cloud top edge. The smaller the distance, the more the emission from the neighboring clouds contributed to the heating or cooling rate. Although it is not obvious in Fig. 4.1, the cooling rate at the top edge slightly varied between 212 K/d (25 m), 213 K/d (100 m), 200 K/d (500 m) and 192 K/d (1000 m). The more dominant the surface emission was (white area in Fig. 4.2), the smaller was the absolute value of the cooling rate. However, this was no general trend in the heating rate. The largest cooling was found for 100 m distance and not for the 25 m distance. Although surface emission was shaded more for the 25 m distance, the close neighboring cloud which was also emitting radiation contributed more to the heating rate for the 25 m distance and thus reduced the cooling.
The ICA simulations were shown to be a reasonable approximation for small distances be-

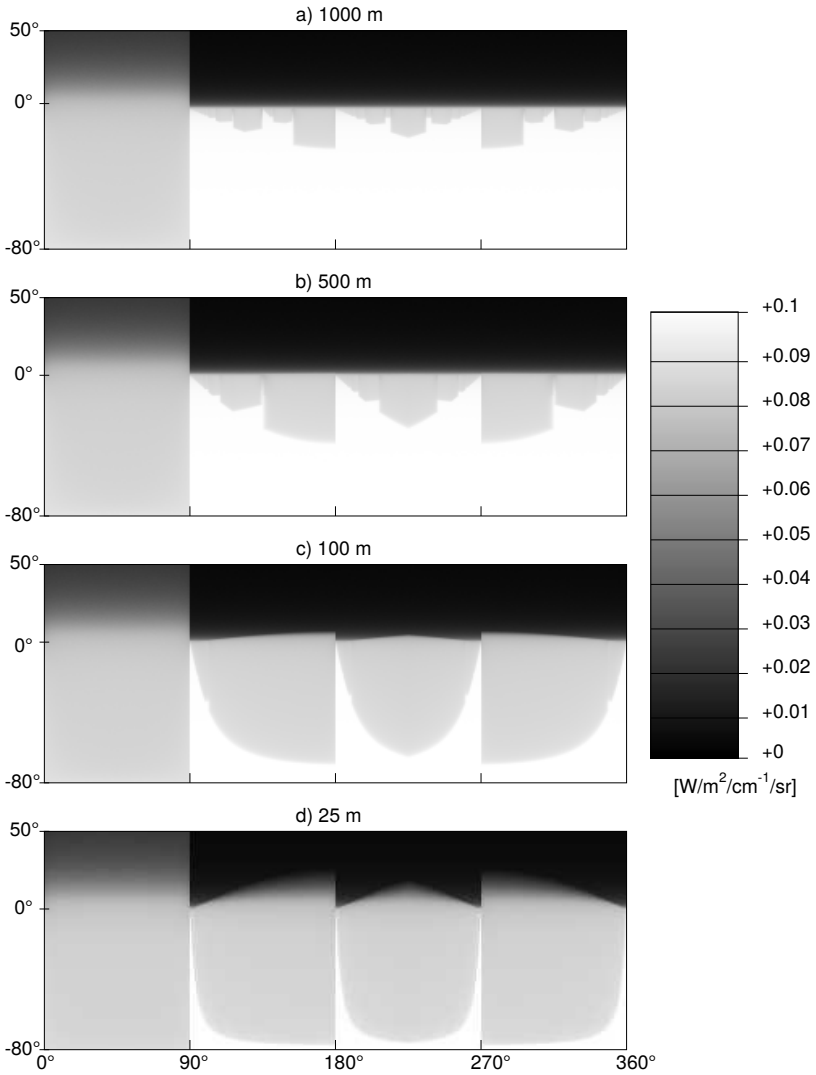

Figure 4.2: Radiance distribution seen from a cloud top edge. Gray areas show areas where radiance is emitted from clouds (the left quarter is the own cloud), black areas with nearly no emitted radiance are the sky and white areas show the emitted radiance from the surface. The simulation is performed at 10 μm. The field of view is 360° in the horizontal and 130° in the vertical. (From Akansu (2014), Figure 5.6.)

tween the clouds, but they failed to produce cloud side cooling which is stronger the larger the distance between the clouds (Fig. 4.1). The ICA also performed poorly for tilted clouds (parallelograms). While the 3D heating rates at the cloud bottom decreased with height, they increased in the ICA simulation (Fig. 4.3).

Studying the effect of different inclinations (the two different parallelograms) it was shown that cooling rates at the cloud side open to space showed higher absolute values for the 45° parallelograms than for the 22.5° parallelograms.

Finally, averaged values of heating and cooling rates were calculated for the different clouds

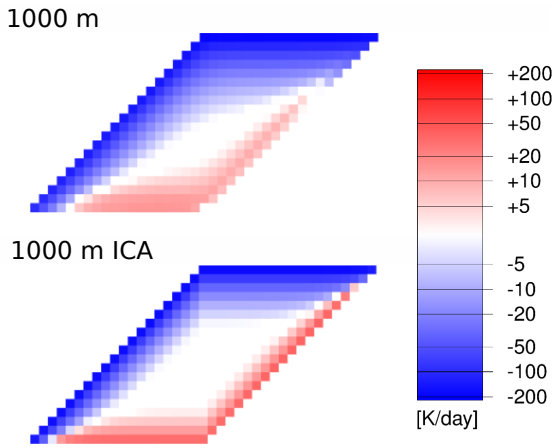

Figure 4.3: Vertical cross section through the middle of the parallelogram cloud (modified from Akansu (2014), Figure 5.19). The heating/cooling rate distribution is shown for a 3D MYSTIC simulations and with a distance of 1000 m between the clouds and the 1D ICA approximation, also with 1000 m distance.

and different distances. The maximum heating or minimum coolings for the 25 m resolution clouds were an order of magnitude higher than the averaged values. Heating rates become larger with increasing model resolution, which is no surprise, because heating rates are located at cloud edges. In coarse model resolution, heating rates are averaged over the grid box volume. If the volume is larger, strong cooling at cloud sides is averaged with nearly no cooling inside the cloud, resulting in lower values. Also, no heating was found in the average values, the cooling was dominating. The smaller the distance between the clouds, the more the average cooling of the 3D calculation resembled the one of the ICA simulation.

4.2 Cloud Resolving Simulations

The effect of thermal radiation on cloud development was studied by performing 3D simulations of clouds with a cloud resolving model. The UCLA-LES was used (Section 3.3). The specific setup for the simulations is described in the same section. First, two types of heat bubble experiments were performed to get a detailed view on the development of a single cloud with and without the effect of radiation. Second, cloud development was investigated in a more complex case. A cumulus cloud field on a large domain (25 x 25 km^2) was studied. Simulations without, with 1D thermal and with 3D thermal radiation (NCA) were compared to each other. If not otherwise stated in the text, the term *simulation with radiation* always refers to simulation with thermal radiation.

4.2.1 Heat Bubble Simulations

For a better understanding of the effects of thermal radiation on cloud development, so called heat bubble simulations were performed (Section 3.3.2). Two different, isolated clouds were simulated: an axially symmetric and a non-symmetric cloud (for more details, see 3.3.2). For each of the two cloud simulations, no-radiation, 1D thermal and 3D (NCA) thermal radiation effects were compared.
Former studies on the effect of thermal radiation on the development of clouds exist and have been pointed out in detail in Section 2.3.2. The following analysis will focus on some of the aspects already found by Guan et al. (1997). They found increased liquid water in the cloud and enhanced downward motion if a cloud develops in interaction with (simplified) 3D thermal radiation compared to no-radiation. Differences between 1D and 3D thermal radiation were not considered and shall be addressed here. The subsiding shell of a cumulus cloud was studied for example by Heus and Jonker (2008), Jiang et al. (2006) and Small et al. (2009). The subsiding shell is a narrow region of subsiding air at the cloud edges which is observed in measurements and simulations of shallow cumulus clouds. While the study of Heus and Jonker (2008) investigated the subsiding shell and what causes it, the studies of Jiang et al. (2006) and Small et al. (2009) focused on the effect of aerosols in simulation and measurement data. They found that enhanced evaporative cooling due to more aerosols (and therefore smaller cloud droplets) causes additional downward motion. In the bubble experiments in this study, the aerosol concentration (that is the number of CCN) was kept constant. The focus was therefore on the effects of thermal radiation and if they also caused such a subsiding shell.

Axially Symmetric Cloud

In the following, the idealized, axially symmetric cloud will be analyzed considering 1D and 3D thermal radiative effects.
The stages of cloud development of the no-radiation simulations are shown in Fig. 4.4. The six vertical cross sections of liquid water mixing ratio represent different stages of the cloud development. Due to the initial temperature perturbation, warm moist air which was positively buoyant started to rise. The positive buoyancy resulted in updrafts which drove the first stage of cloud development. While rising, air was cooled and condensation occurred. At some point, updrafts became weaker and the decaying process of the cloud started. Condensation

occurred early. At 10 min a cloud had already formed and continued ascending. More moist air rose and condensed, which can be seen in the increased liquid water mixing ratio at 17 min. In the following, updrafts became weaker (not shown) and less moist air was moved upward. The environmental temperature profile was stable. While rising, air above the cloud was also lifted upward. This air, in comparison to the warmer air of the initial bubble was cooler than its environment as it was lifted, due to the stable temperature profile. This resulted in negative buoyancy above the cloud (not shown). This negative buoyancy was acting against the upward motion and stopped further rising of the cloud. Therefore cloud development decelerated. While forming, the cloud did not exceed a height of 1500 m. During the rest of the simulation a cloud was located at about 1000 m height. Except for small numerical differences, the cloud developed symmetrically, due to the initial symmetric temperature perturbation. In Fig. 4.4, it can be seen that at 30 min, that the clouds started to disappear because the ascent of air was weaker (not shown). At 67 min, the cloud was located in 900 m to 1300 m height. Due to the rather weak forcing, the cloud remained in this height until it decayed. At 83 min the cloud had almost disappeared. In the following, cloud development with the effect of thermal radiation will be investigated.

To illustrate the difference between 1D and 3D heating rates in this particular model run, Fig. 4.5 shows a vertical cross section (left) and horizontal cross sections in 1200 m height (right) of heating rate differences at 17 min. The differences between the 3D NCA and the 1D ICA approximation are shown. In addition, contours of liquid water mixing ratio are added to show the extent of the cloud. The time snap-shot shown is at an early stage of cloud development, where the development due to the different radiation methods was not yet significant. Therefore, both simulations can nearly directly be compared to each other.

The cloud top cooling is the dominant feature in the top row, which was stronger in the simulation with 3D radiation, with up to 25 K/d difference. The cloud side cooling, which is a 3D effect and the enhanced cooling in the 3D simulation is also visible in the horizontal cross sections at 1200 m height (right). Small areas at the cloud side, where less cooling occurred in the simulation with 3D radiation may be due to a slightly different development of both clouds in both simulations.

Maximum cooling rates of up to 90 K/d were found in the simulation with 3D radiation and 60 K/d in the simulation with 1D radiation at this time step. As pointed out earlier in the previous sections, the heating and cooling rates are located at the cloud edge, the center of the cloud is in radiative equilibrium. For the following analysis, one should keep in mind that 3D cooling effects are stronger than 1D effects, and that additional cloud side cooling takes place in 3D. The question to answer is if and how the heating and cooling rates affect cloud formation.

The temporal development for the maximum values of liquid water mixing ratio, maximum vertical velocity (upward), minimum values for vertical velocity (downward), the liquid water path, and averaged heating and cooling rates (in the cloudy region) are shown in Fig. 4.6. The values were sampled at 600 to 1200 m height, neglecting any newly formed clouds close to the surface during the simulation time. Here, the development of the cloud can be separated into different stages. In the beginning of the cloud lifetime (0-50 min), no significant difference between the no-radiation and the simulations with radiation was found. Only the averaged liquid water path showed higher values in the beginning of the cloud development, for the

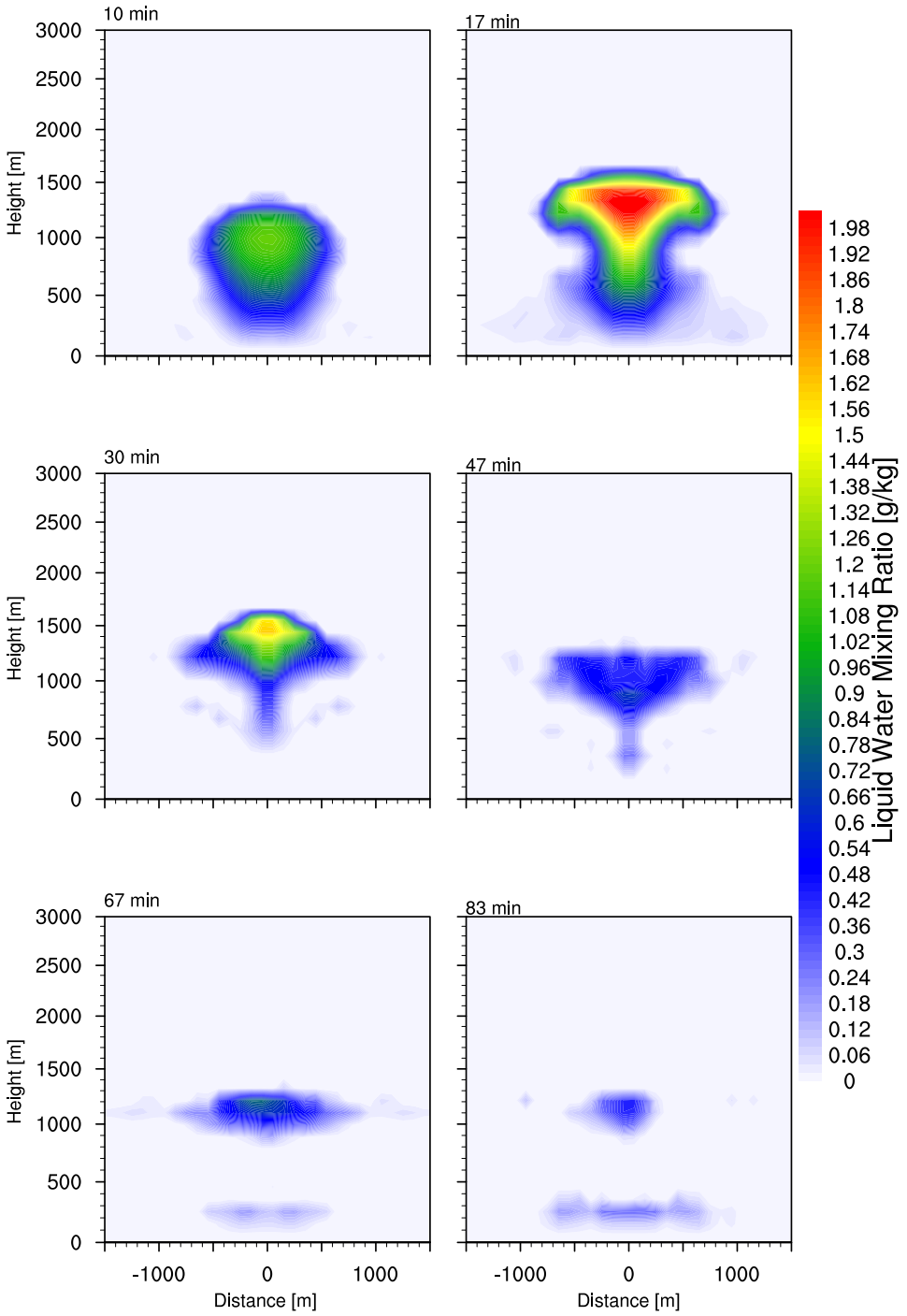

Figure 4.4: Time development of the heat bubble for the no-radiation simulation.

simulations with radiation compared to the no-radiation simulation. This difference was not found in the maximum values, which is not surprising. The maximum values of liquid water mixing ratio were located in the center of the cloud. Thermal radiation, that is cloud top and cloud side cooling, occur at the cloud edge. The increase in the averaged liquid water path

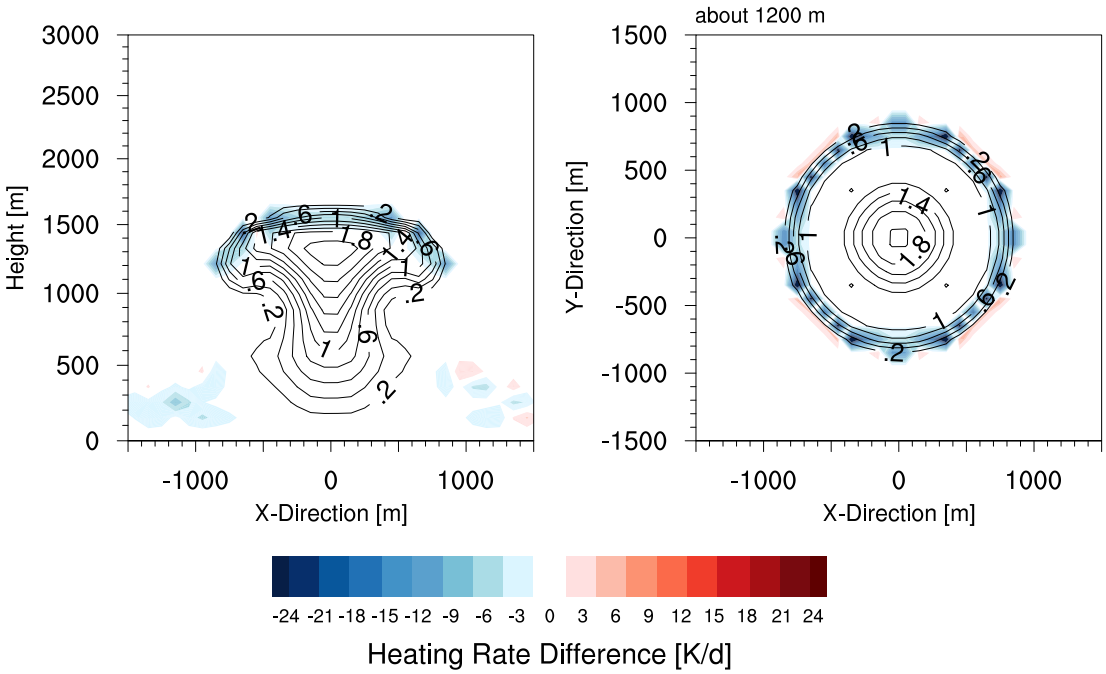

Figure 4.5: Vertical (left) and horizontal cross section at 1200 m (right) of heating rate differences at 17 min. The heating rate difference between the 3D NCA and the 1D ICA approximation is shown. Black lines show contours of liquid water mixing ratio in g/kg of the simulation with 3D radiation.

was therefore occurring at the edges of the cloud, due to radiative cooling and reaches up to 10% higher values than the no-radiation case. This can also be seen in the horizontal cross section of Fig. 4.7. This figure shows the difference in liquid water mixing ratio between the two thermal radiation cases and the no-radiation simulation. Both simulations with radiation showed higher values of liquid water mixing ratio, the 3D case even more.

As the cloud developed, liquid water path and the maximum of liquid water mixing ratio was higher in the simulations with radiation. The increase in liquid water mixing ratio maximum values can not be explained by direct cooling of the cloud, because the maximum values were still located in the center of the cloud where no cooling occurred. But, the vertical winds changed due to thermal cooling enhancing the upward motion within the cloud. The maximum liquid water mixing ratio was increased by 20-35% in case of 1D thermal radiation and by 25-50% in case of 3D thermal radiation. The increase in liquid water path during this time (50 min to 70 min) was, in comparison to the early stage of cloud development a result of the increase of liquid water mixing ratio in the cloud core and the cloud sides. In the beginning, liquid water mixing ratio was increased only at cloud sides. The maximum and minimum vertical velocities (Fig. 4.6, top row), similar to the liquid water mixing ratio, developed differently after 40 min to 50 min in the simulations with radiation compared to the no-radiation simulation. Comparing this behavior to Fig. 4.4, the time around 50 min is the stage of cloud development, where the effects of thermal radiation became visible. The

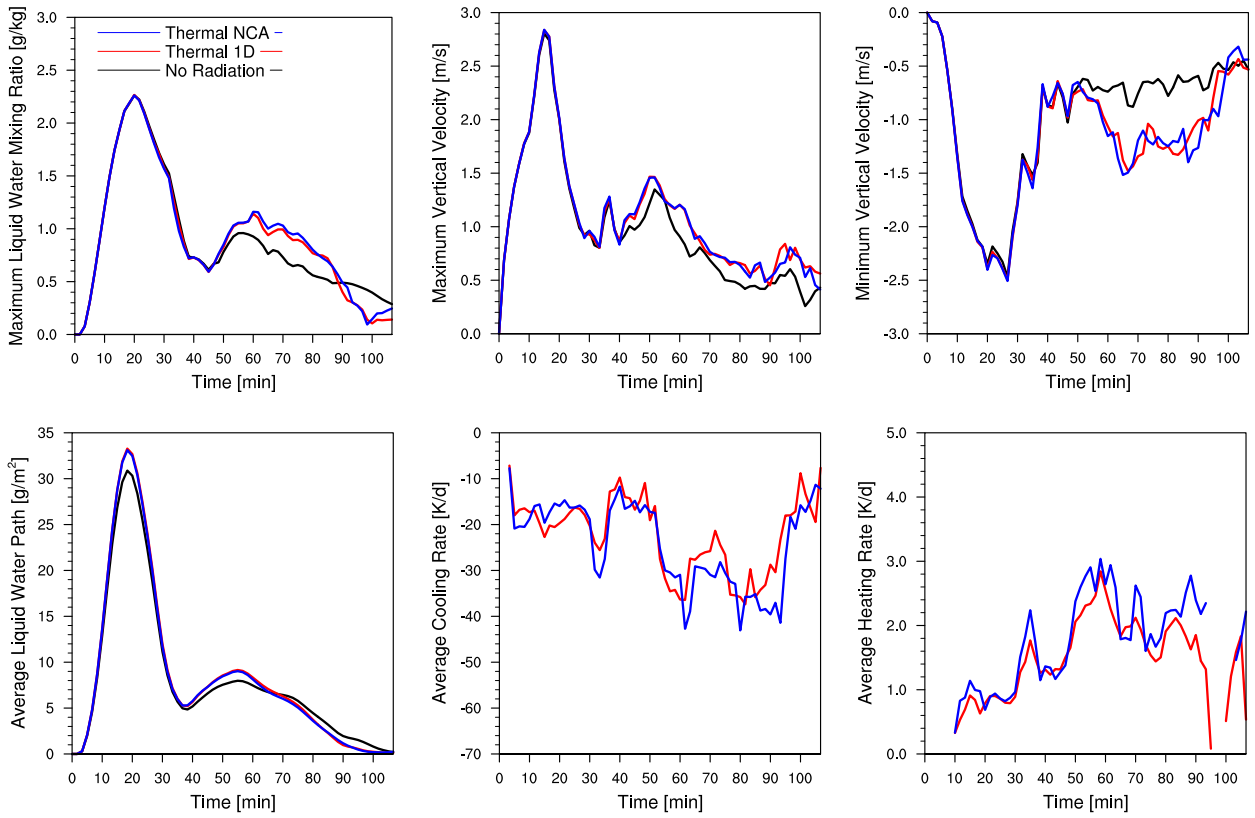

Figure 4.6: Time development of maximal liquid water mixing ratio (left, top), maximum upward vertical velocity (middle, top) and maximum downward vertical velocity (right, top), liquid water path (left, bottom), averaged cooling rates (middle, bottom), and averaged heating rates (right, bottom) of the three heat bubble simulations.

original upward motion, initialized by the perturbation in the beginning slowed down and the cloud was not increasing in depth and height anymore but remained at 900 - 1200 m height. No significant difference in the development of the cloud between the simulations with 1D and 3D radiation was found in terms of vertical velocity. However differences existed between the no-radiation and both simulations with radiation. Upward motion was stronger in the radiation cases compared to the no-radiation simulation. In addition, downward motion became stronger. This indicated that radiation favored a circulation around the cloud, with stronger updrafts in the center and stronger downdrafts at the cloud sides.
At the end of the simulations, the cloud was decaying faster in the simulations with radiation. Looking at the averaged heating and cooling rates in Fig. 4.6 (bottom row), no significant difference between the development of the cloud with 1D and 3D radiation was found. 3D radiation showed (in the average of all cloudy grid boxes) slightly more cooling, from 50 min on. The main difference between 1D and 3D thermal heating rates was the cloud side cooling. This cloud, however, did not have large areas which were denoted as cloud side areas. Looking at the cross section of Fig. 4.4, the cloud was rather oblate. Cloud side grid boxes, where 3D thermal cooling can be found are grid boxes, which are located at the cloud edge, but have a cloudy grid box above and below the grid box under investigation. Grid boxes which are

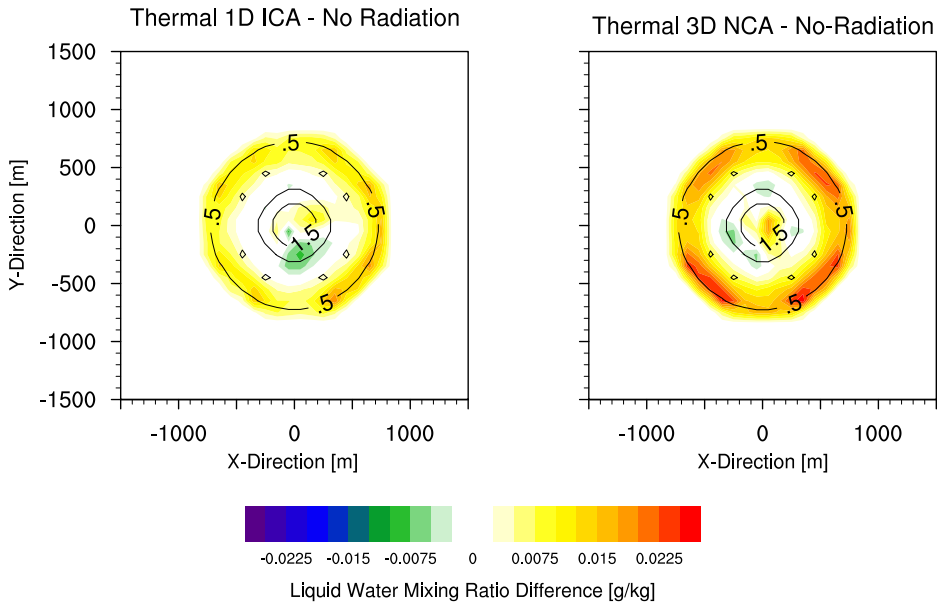

Figure 4.7: Horizontal cross section (in 1100 m height) of liquid water mixing ratio difference after 17 min. The difference was calculated between either 1D or 3D thermal radiation and the no-radiation simulation. Liquid water mixing ratio (black contours) of the cloud indicate the cloud extension.

located at the cloud side, but are also located at cloud top or cloud bottom will have a thermal heating and cooling effect in the simulations with 1D and 3D thermal radiation. This means, that only clouds which have large areas of real cloud sides (grid boxes, where only side faces interact with the clear sky) can show a significant difference between 1D and 3D thermal radiation. Therefore the further investigation of this cloud will focus mainly on general radiation effects, not so much on the difference between 1D and 3D thermal radiation.
Vertical cross section of liquid water mixing ratio, vertical velocity and buoyancy at three different time steps are discussed next (Fig. 4.8, Fig. 4.9, and Fig. 4.10). The cross sections were taken in the middle of the (axially symmetric) cloud. The time steps shown were chosen at 50 min, 67 min and 100 min. From the time-series analysis, 50 min is one of the early time steps where first differences between the no-radiation and simulation with radiation occurred. The last time step is at the end of cloud life time.

Fig. 4.8 shows vertical cross sections of the three properties, at 50 min. The first differences between the no-radiation and the simulations with radiation became visible. The liquid water mixing ratios showed higher values for the radiation cases in the center of the cloud. Also, a stronger upward motion (positive vertical velocity) was found in the center of the cloud for both simulations with radiation. Around the cloud, areas of subsiding air can be seen. The positive buoyancy was a bit stronger, negative buoyant areas were located at the cloud top and a small, but stronger positive region below the center of the cloud at about 400 m height was noticeable.

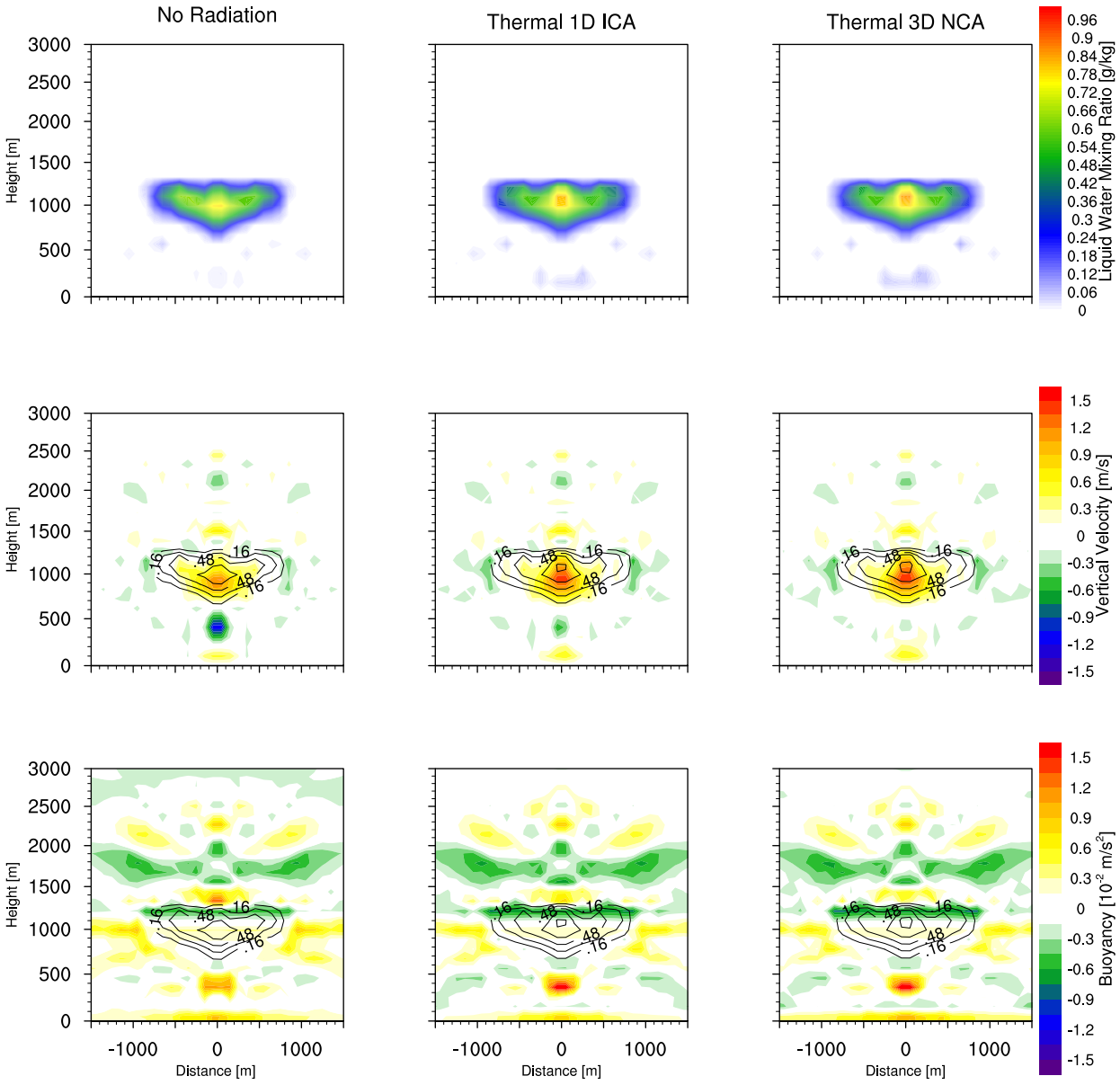

Figure 4.8: Vertical cross section through the middle of the cloud of liquid water mixing ratio (top), vertical velocity (middle) and buoyancy (bottom) after 50 min cloud development. No-radiation (left), 1D thermal radiation (middle) and 3D thermal (NCA) radiation simulations are compared.

The cross section at this time step shows again what was already suggested in the time-series analysis. The circulation in the cloudy region was changing, leading to stronger updraft in the cloud center, which increased the transport of moist air from regions close to the surface. More condensation occurred and more latent heat was released which caused positive buoyancy and strengthened cloud development. In the following 15 minutes, the difference between the radiation and no-radiation simulations became more significant.

After 67 min (Fig. 4.9) the liquid water mixing ratio showed clearly higher values in the

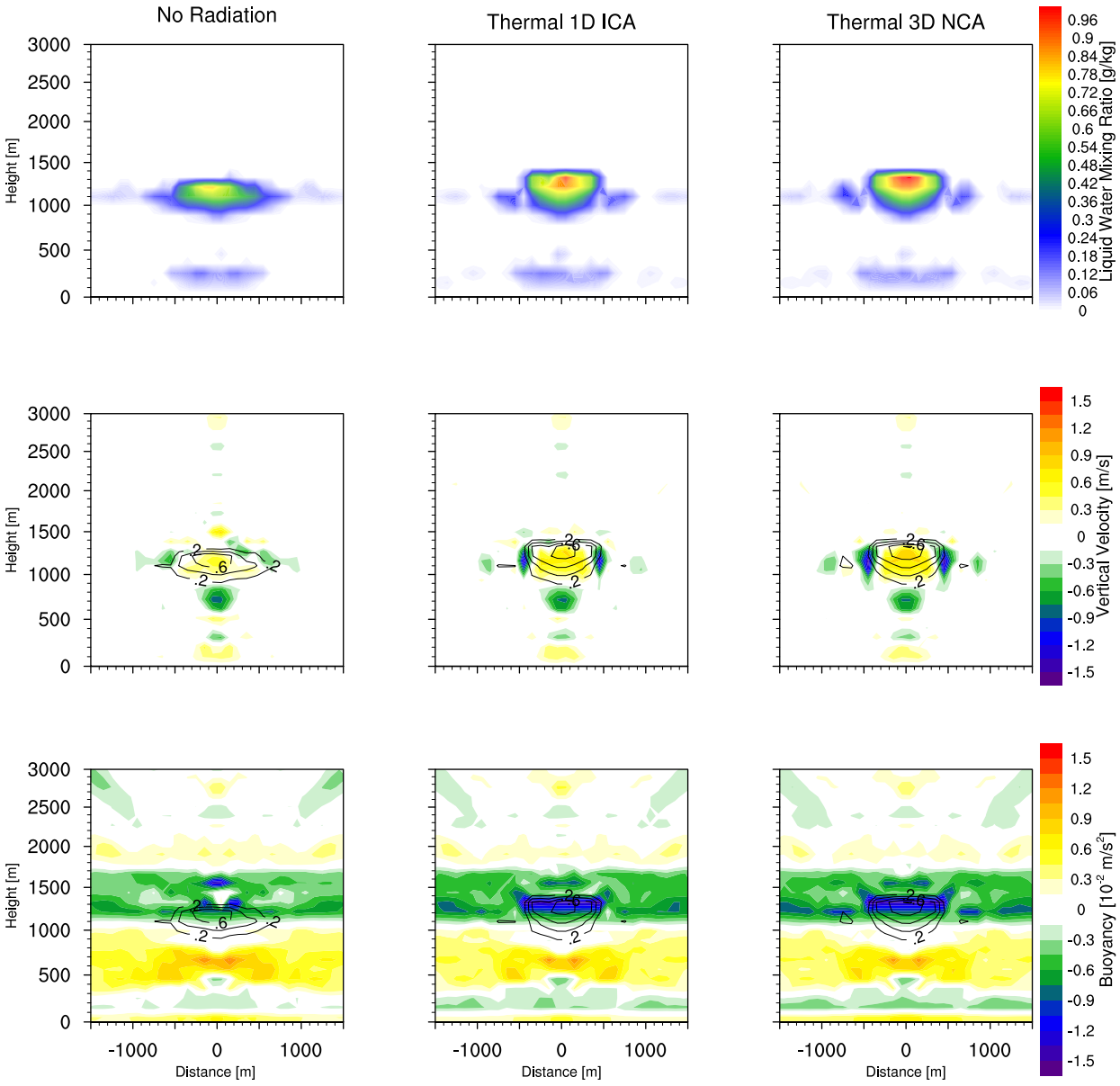

Figure 4.9: As in Fig. 4.8, but after 67 min cloud development.

simulations with radiation than in the simulation without radiation. The subsiding branches at the cloud sides were much more dominant in the simulations with radiation and the core of the cloud still showed positive updraft velocities. Differences between the simulations with 1D and 3D radiation were also visible. As expected, the changes in cloud development were stronger in the simulation with 3D radiation than in the simulation with 1D radiation. The cloud itself, that is, the liquid water mixing ratio, was concentrated in a narrower area in the horizontal but deeper in the vertical. This might have been due to enhanced entrainment caused by enhanced turbulence due to thermal radiation. The negative buoyancy at cloud top

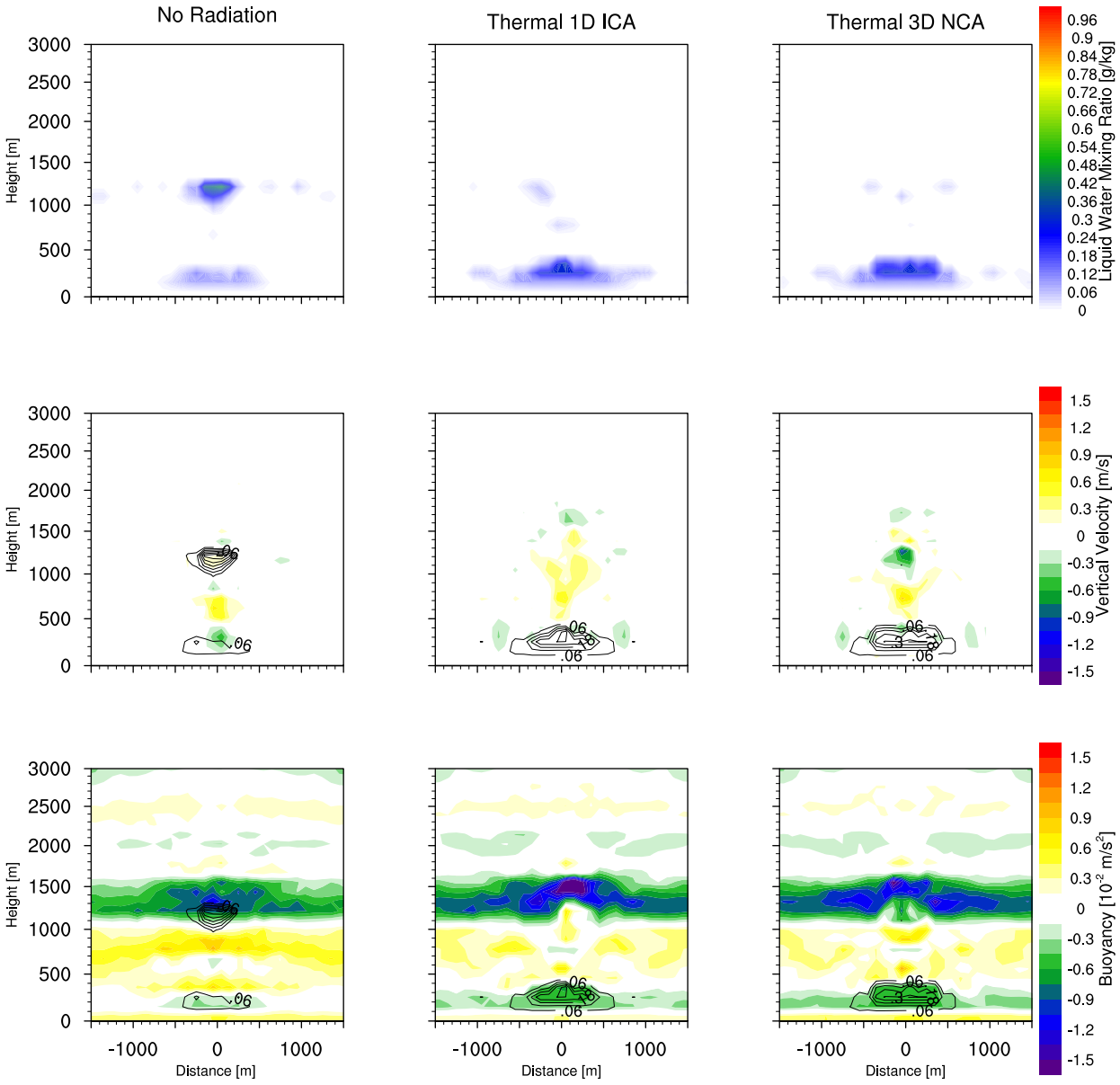

Figure 4.10: As in Fig. 4.8, but after 100 min cloud development.

showed higher values for the simulations with radiation.
The cloud circulation in the simulations with radiation promoted the cloud growth in the middle of the cloud lifetime. However, as could be seen in the time-series analysis, the cloud was decaying faster in the late stage. At 67 min negative buoyancy was created at the cloud top, which acted against the upward motion. After 100 min the constant negative buoyancy at cloud top was still present. In the simulations with radiation, the cloud had almost disappeared (Fig. 4.10) and a new cloud started developing close to the surface, while in the no-radiation simulation, there was still liquid water located at about 1 km height. It seemed

that the enhanced entrainment in combination with the negative buoyancy, acting against the upward motion caused a faster decay of the cloud in the late stage.

To take a closer look at the cloud at 50 min and 67 min, transect of liquid water mixing ratio, vertical velocity and buoyancy are shown in Fig. 4.11. At 50 min liquid water mixing ratio showed slightly higher values for the simulations with radiation, also stronger updrafts in the middle of the cloud and the buoyancy showed negative values at the cloud sides. About 15 minutes later, at 67 min, the shape of the cloud changed (Fig. 4.11, bottom). The horizontal extent of the cloud was smaller for the simulations with radiation, the subsiding branches can be seen in the vertical velocity profile at the cloud sides for the simulations with radiation and the buoyancy changed from positive to negative values. The negative buoyancy at the cloud side (at 50 min, Fig. 4.11, top) caused downward vertical velocity at the edge of the cloud. Also, the narrower shape of the cloud itself indicated higher entrainment at the cloud sides as consequence of thermal radiation.

Fig. 4.12 confirms this conclusion. The pattern of the cooling rates and the liquid water mixing ratio difference resulted from the resolution of the simulation and the cloud development. Although the thermal cooling was stronger in the simulation with 3D radiation (middle) compared to the simulation with 1D radiation (left), the amount of liquid water mixing ratio was

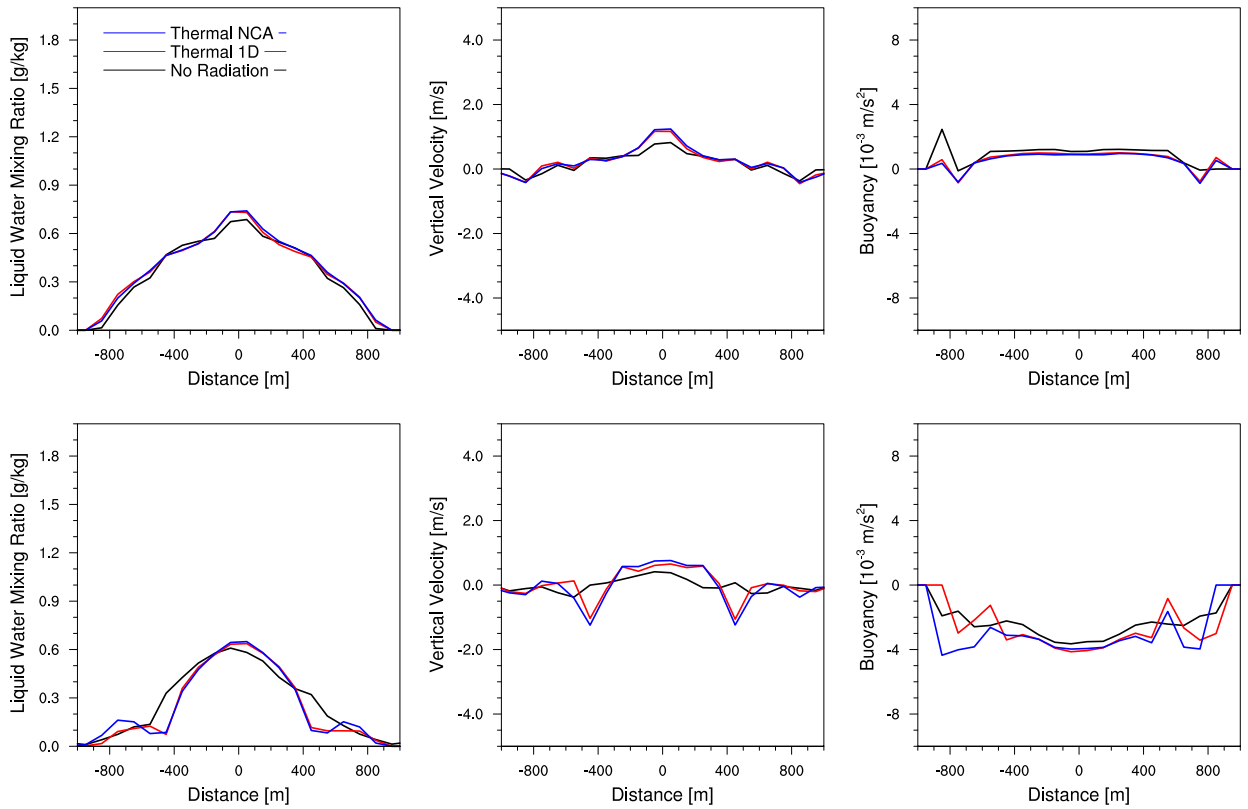

Figure 4.11: Height averaged transect of liquid water mixing ratio (left), vertical velocity (middle) and buoyancy (right) after 50 min (top) and 67 min (bottom). The height between 900-1100 m was averaged. Only cloudy regions (model columns with a liquid water path greater than 10 g/m^2) were considered.

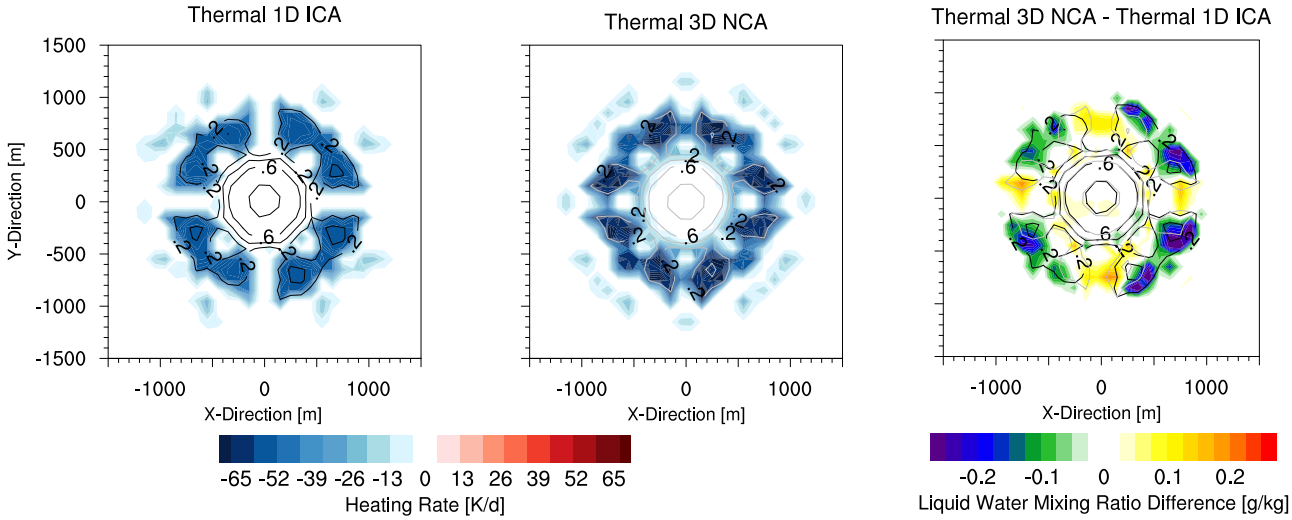

Figure 4.12: Horizontal cross section (in 1200 m height) of thermal heating rates in 1D (left) and 3D (middle) and the liquid water mixing ration difference (right) after 67 min. The difference was calculated between simulation with 3D thermal radiation and the 1D thermal radiation. Liquid water mixing ratio of the simulation with 3D radiation (gray contours) and the simulation with 1D thermal radiation (black) of the cloud indicate the cloud extension.

smaller in the simulation with 3D radiation. At an early stage of cloud development, when the subsiding shell was not yet developed and entrainment was low, the cooling rates at the cloud side of the 3D thermal radiation had caused an increase in condensation and, in consequence, in liquid water mixing ratio at the edges of the cloud. Therefore, it can be concluded that in the late stage of the cloud life cycle, enlarged entrainment and the negative buoyancy in the cloud top area (both caused by thermal radiation) led to a faster decay of the cloud. It can be concluded that thermal radiation over-compensated latent heat release by condensation at the cloud side. That thermal radiative cooling is strong enough to compensate latent heat was for example shown by Curry and Herman (1985).
For another verification of the main hypothesis for the development of this cloud (additional cloud circulation induced by thermal radiation and a faster decay of the cloud at the end of cloud lifetime), profiles of the conditionally sampled, horizontally averaged cloud core vertical velocity and the skewness of the vertical velocity are shown at 50 min and 67 min in Fig. 4.13. The conditionally sampled cloud area is defined as all grid boxes with a liquid water mixing ratio greater than zero. Conditionally sampled cloud core averaged values are defined by a mixing ratio greater than zero and a positive buoyant area. The skewness of the vertical velocity ($S_w = \frac{\bar{w_3}}{\bar{w_2}^{3/2}}$, with w_2 being the second moment of the vertical velocity and w_3 the third moment), is a measure for the structure of the motion of a turbulent flow. If it is positive, the motion is dominated by a narrow updraft while the surrounding downdrafts are broader. Negative values of skewness indicate narrower and stronger regions of downdraft.

At 50 min, the vertical profiles of the cloud core averaged vertical velocity was positive in the cloudy layer. No differences were found between the different simulations at this time,

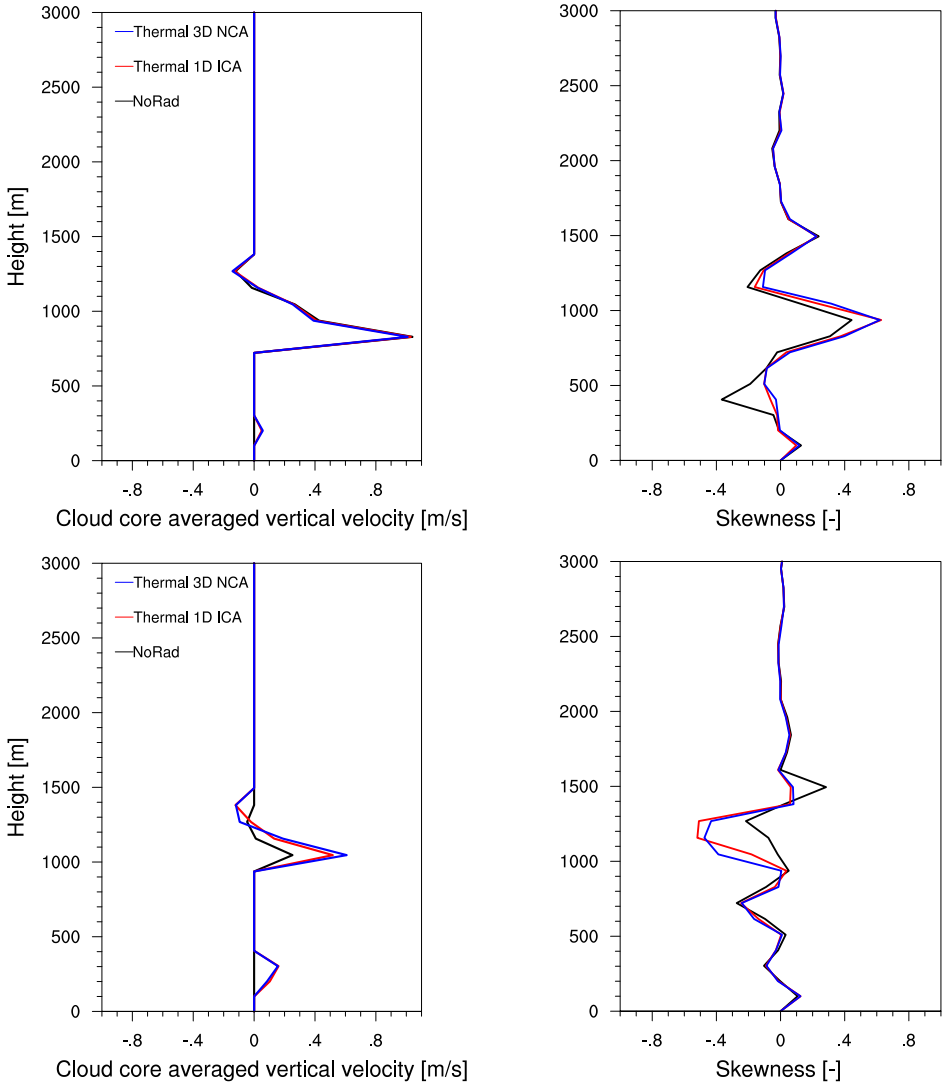

Figure 4.13: Conditionally sampled profiles of cloud average upward velocity, cloud core averaged upward velocity, skewness of the vertical velocity and the absolute value of the horizontal buoyancy gradient at 50 min (top) and at 67 min (bottom).

which might be due to averaging. The skewness was positive in all simulations in the cloudy layers and higher in the simulations with radiation. Above the cloud, skewness was negative, but less negative in the simulations with radiation. Therefore, it can be stated that radiation changed the cloud circulation in this period of cloud lifetime and enhances vertical upward motion in the cloud.

At 67 min, the situation had changed. The profiles of averaged vertical velocity in the cloud core showed clearly higher updraft velocities for the simulations with radiation. Overall, updrafts in the cloud core were stronger for the simulation with 3D radiation in comparison to the simulation with 1D radiation. Also, the skewness had changed sign. The skewness was negative in the cloudy area which would have been expected because the subsiding branches around the cloud had already developed at this time. The area of negative skewness in the

3D simulation was also deeper, which was expected as the subsiding branches reached further down (Fig. 4.9).
In summary, it was shown for a single idealized cloud that:

- Thermal radiation increased the liquid water mixing ratio at cloud edges (in the early stage of cloud development and later on).
- Radiative cooling at cloud top and cloud sides led to additional downward motion at the cloud sides (subsiding shell).
- The downward motion went along with enhanced updrafts in the cloud center which strengthened cloud development (middle stage of cloud cycle).
- Radiative cooling caused enhanced entrainment (especially at the cloud sides) which mixed in dry air from the environment and led to changes in cloud shape and to a faster decay of the cloud (in the late stage of the cloud lifetime).
- Enhanced entrainment reduced the liquid water mixing ratio while thermal cooling increased condensation and liquid water mixing ratio. In the early stage of cloud lifetime, thermal cooling was dominating, in the late stage, entrainment (caused by thermal cooling) was dominating.
- Radiative cooling and enhanced liquid water mixing ratio led to negative buoyancy which caused the cloud to disappear faster in the late stage of the cloud cycle.
- 3D effects were similar to 1D effects, but due to the additional cooling at the cloud sides stronger than the 1D effects.
- 3D effects caused only little change in cloud development in this simulation. This cloud had a small cloud side surface area and therefore only little cloud side cooling, which reduced the 3D effect.

Non-Symmetric Cloud

Similar to the symmetric cloud, a temperature perturbation close to the surface caused positive buoyancy and the air to rise. The air cooled while rising, condensed and formed a cloud. Due to the random noise set on the temperature perturbation, the cloud developed no longer symmetric. The non-symmetric cloud will be investigated in a similar way as the axially symmetric one. However, the time of the snap shots shown will vary, because the cloud develops differently, of course.

Fig. 4.14 shows vertical cross section (left) and horizontal cross section (right) of heating and cooling rate differences of the non-symmetric cloud. The black lines indicate liquid water mixing ratio contours in g/kg to identify the location of the cloud. The horizontal cross section was taken in 1000 m height. The plot shows the cloud after 17 min of development, still at an early stage. Both pictures show that more cooling occurred in the simulation with 3D radiation. The difference is up to 35 K/d. Also, small areas, where less cooling occurred in the simulation with 3D radiation can be seen (for example the red spot in the center of the left figure). This is also a typical 3D effect. While on the one hand, 3D thermal radiation causes more cloud side cooling, less cooling occurs in cloud holes (for example the red dot is in the center of the cloud), because the cloud sides surrounding the hole emit radiation. The ICA approximation, however, can not account for the contribution from the neighboring columns. The maximum cooling rate of the simulation with 3D radiation at this time step was a cooling

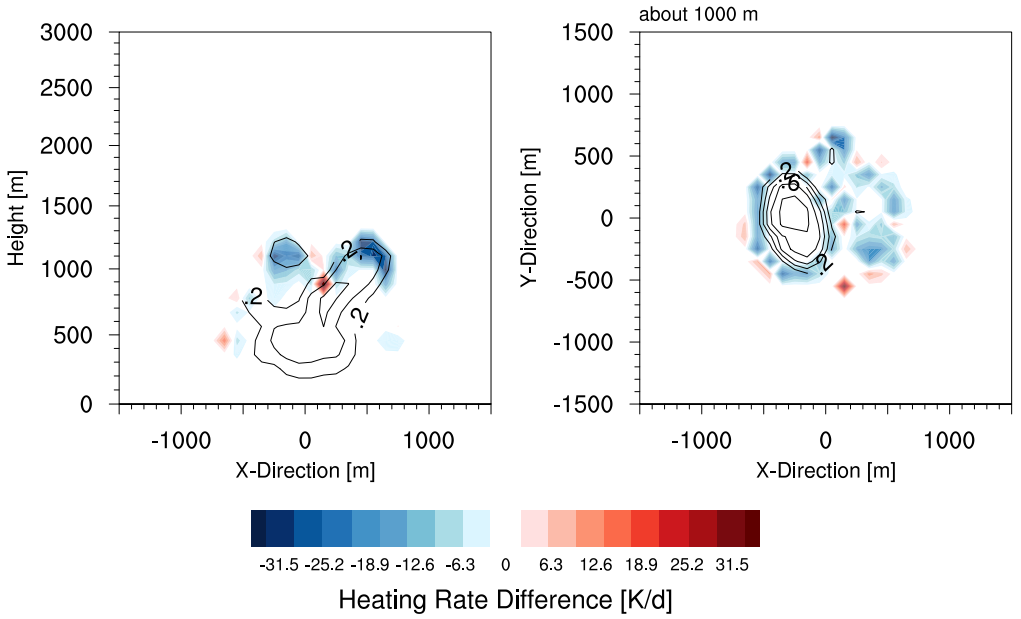

Figure 4.14: Vertical (top) and horizontal heating rate cross sections (middle and bottom) after 17 min development time of the cloud. The horizontal cross sections are taken at about 900 and about 1000 m height. The left side shows 1D, the right side 3D thermal radiative transfer (NCA) results. Black lines show contours of liquid water mixing ratio in g/kg.

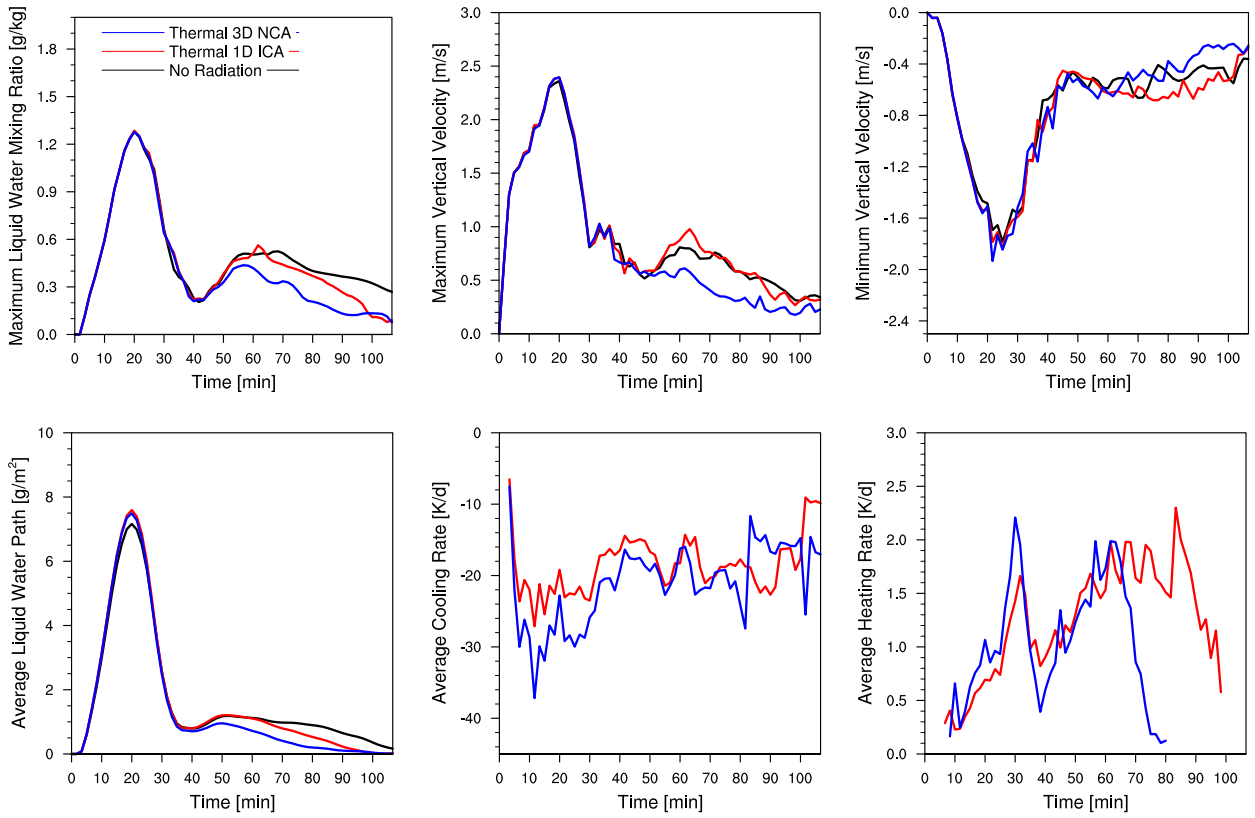

Figure 4.15: Time development of maximum liquid water mixing ratio (left, top), maximum upward vertical velocity (middle, top) and maximum downward vertical velocity (right, top), liquid water path (left, bottom), averaged cooling rates (middle, bottom), and averaged heating rates (right, bottom) of the three heat bubble simulations.

of 89 K/d. In the simulation with 1D radiation, the maximum cooling was 55 K/d. Compared to the axially symmetric cloud, it seemed that 3D heating rates were more dominant in the case of the non-symmetric cloud shown here, because more cloud side surface area existed for this cloud.

Fig. 4.15 summarizes the cloud development. Shown are time series of the maximum liquid water mixing ratio, maximum (upward) vertical velocity, minimum (downward) vertical velocity, averaged liquid water path and averaged negative and positive heating/cooling rates. Averages and maxima/minima were determined for the height range 600 - 2000 m, in order to exclude newly developing clouds.

During the early stage of cloud development, similar to the symmetric bubble, no big differences between the individual simulations occurred. Again, only the liquid water path showed slightly increased values (about 8%) for the simulations with radiation due to the cooling and enhanced condensation at cloud top and cloud sides. The averaged cooling rates showed differences in this simulations. The averaged cooling for the 3D simulation is larger due to the larger cloud side area of this cloud. It can therefore be expected that the cloud development will also be different between both simulations with radiation.

At 50 min, differences between the no-radiation simulation and both simulations with ra-

diation were notable. Liquid water mixing ratio and liquid water path, as well as vertical velocities developed differently in all three simulations. In the simulation with 3D radiation, liquid water mixing ratio maximum and liquid water path decreased from this moment on. In the simulation with 1D radiation, both liquid water quantities increased first, following the no-radiation simulation. Reduction in liquid water mixing ratio set in about 10 to 15 min after the simulation with 3D radiation. Maximum upward vertical velocities also decreased constantly in case of 3D thermal radiation, but increased first in the simulation with 1D radiation. They also became stronger than the values of the no-radiation simulations. Before the maximum upward vertical velocities started decreasing in the 1D case, they followed the no-radiation simulation. Downward velocities of simulation with 3D radiation and the no-radiation simulation were smaller than in the simulation with 1D radiation. At the end of the simulation, the liquid water quantities also decreased in the simulation with 1D radiation.
The axially symmetric heat bubble from the beginning of this section had also shown differences in the development of the liquid water mixing ratio of the cloud due to the effect of thermal radiation. While in the early stage of the cloud, liquid water mixing ratio was increased due to the thermal cooling at cloud top and cloud sides, the changed cloud circulation due to thermal cooling has caused more entrainment and therefore a decrease in liquid water mixing ratio in the late stage of the cloud life cycle. This time-dependent behavior can no longer be observed in the development of the more realistic cloud in this example. The simulation with 1D radiation seemed to follow the behavior of the axially symmetric cloud, with enhanced cloud growth in the middle stage of cloud lifetime, but a faster decay at the end. The simulation with 3D radiation, however, showed a constant decay from 50 min on, compared to the no-radiation simulation.

Fig. 4.16 shows a horizontal cross section of the difference in liquid water mixing ratio between the two simulations with radiation and the no-radiation simulation at 25 min. Liquid water mixing ratio was strongly decreasing in the center of the domain. The cloud had developed two main cores at this stage (one at the left and one to the right of the decreasing area). At cloud sides, subsiding vertical winds (not shown) had formed already and evaporation took place. It can be noted that at this stage of cloud development, the thermal cooling not only caused an increase in liquid water mixing ratio (this was the case in for the axially symmetric cloud), but also caused a decrease in liquid water mixing ratio. A similar behavior was found for earlier time steps (not shown).
For a more detailed picture of the development of this cloud, snap shots at different time steps of the liquid water path are shown in Fig. 4.17. Looking at liquid water path allows to show the full cloud in a 2D projection. In this analysis, only the original cloud at about 1 km height is considered. The liquid water path is calculated from 600 m to 2000 m height. Therefore, any newly formed clouds close to the surface are neglected. This allows to focus on the life cycle of the first cloud.

The liquid water path is shown at 42 min, 67 min and 83 min for the three simulation types. At 42 min, first signs of the radiation effect can be seen. The right part of the cloud seemed to start disappearing in the simulation with radiation which must be due to some change in cloud development caused by thermal radiation. As expected, the effect is more dominant in the simulation with 3D radiation. About half an hour later, at 67 min, this process was even more visible. The cloudy area was much narrower in the thermal simulations. The amount of

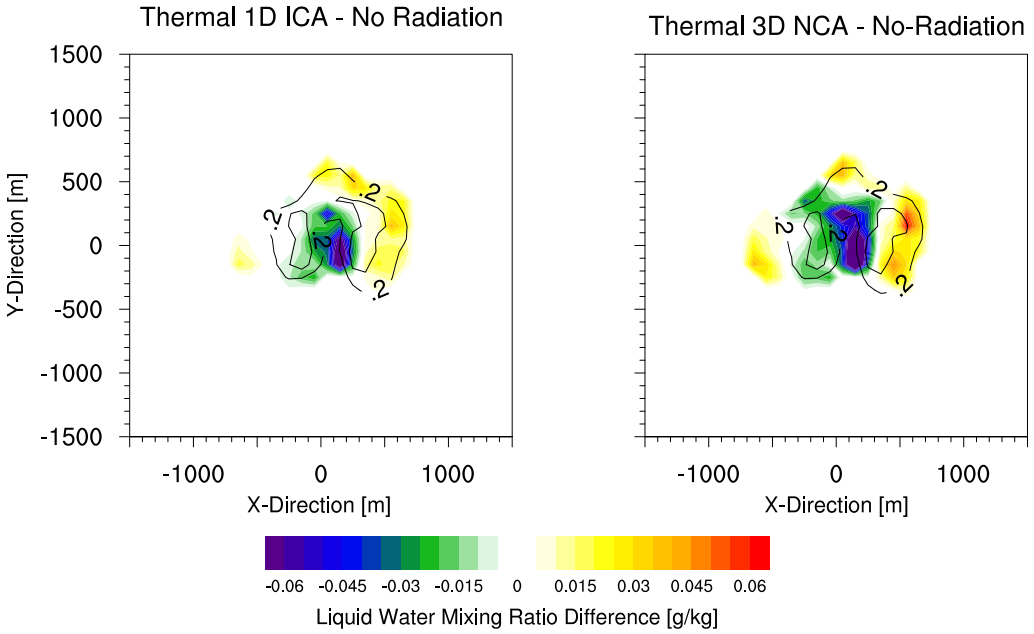

Figure 4.16: Horizontal cross section (in about 1000 m height) of liquid water mixing ratio difference at 17 min (top) and 25 min (bottom). The difference was calculated between either 1D or 3D thermal radiation and the no-radiation simulation. Liquid water mixing ratio (black contours) of the cloud indicate the cloud extension.

liquid water path in the two cloud centers (large red areas) was significantly reduced in the 3D thermal simulation. The radiation effects (probably due to less cooling in the 1D case) needed more time to have a significant effect in the simulation with 1D radiation. Although areas of small liquid water path had disappeared in the simulation with 1D radiation, the cloud cores still showed high values of liquid water. This had changed at 83 min of simulation time. The faster disappearance of the cloud due to thermal radiation was again striking. The cloud had almost disappeared in the 3D simulation and the simulation with 1D radiation also showed decreasing liquid water mixing ratio.

An analysis of up- and downwelling velocities and the buoyancy (not shown) at 42 min showed that downdrafts were stronger and upward motion was weaker in the simulation with radiation and similar to the findings in liquid water mixing ratio, radiation effects were more dominant in case of 3D thermal radiation. The buoyancy at this time was positive in the no-radiation simulation, but already negative in the simulations with radiation. The negative buoyancy slowed down the upward motion further in the simulation with radiation, which, in addition with enhanced entrainment promoted the decay of the cloud. The surroundings of the cloud showed downward motion (subsiding shell) in the following time steps for the no-radiation and simulation with 1D radiation (not shown). The simulation with 3D radiation also showed downward motion at the side of the cloud, but as liquid water mixing ratio and therefore the cloud had decreased already by that time, vertical velocities are no longer directly comparable to the 1D and no-radiation simulation. Upward motion was found however in the cores of the

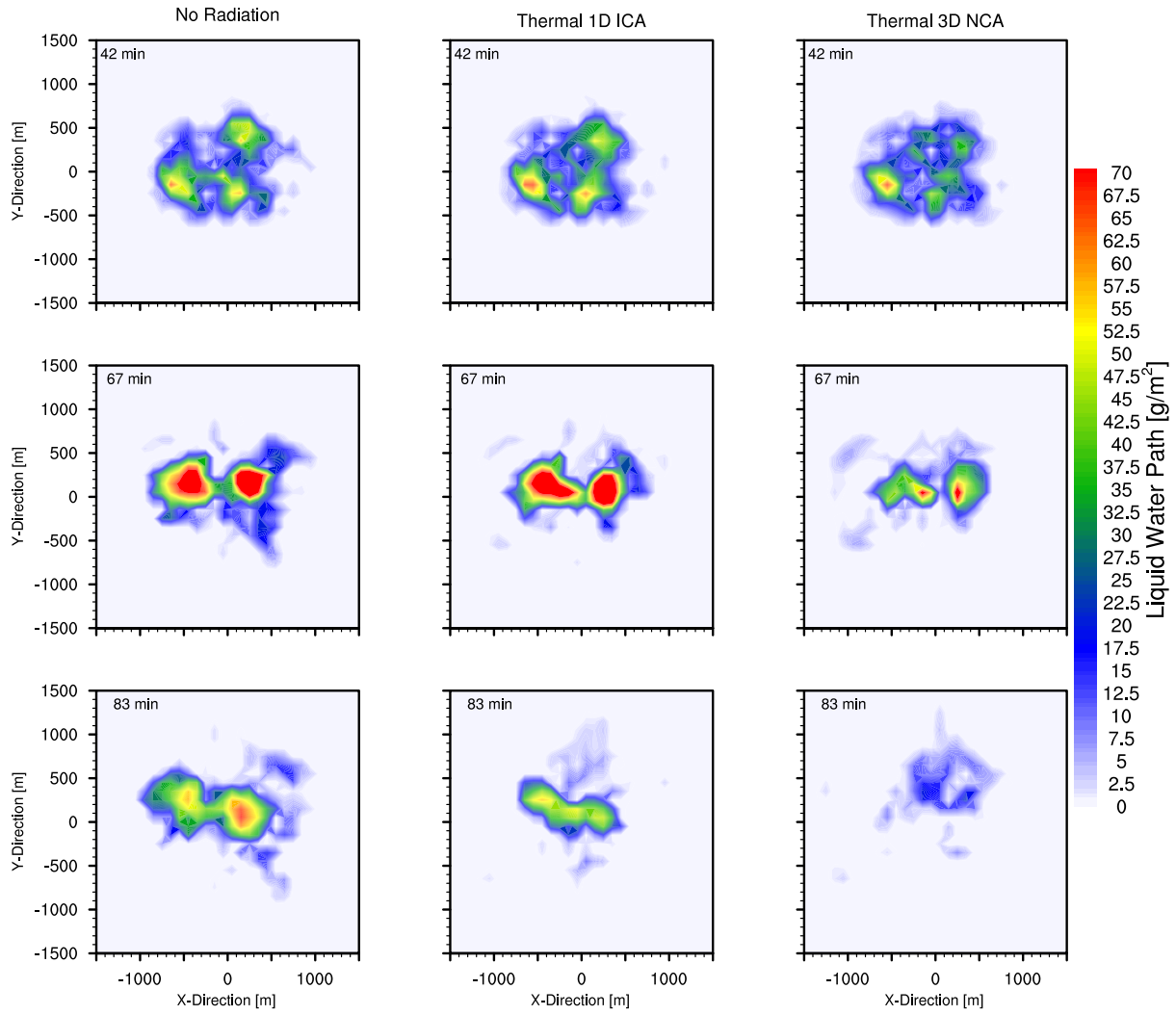

Figure 4.17: Liquid water path at 42 min, 67 min and 83 min for the no-radiation (left), 1D thermal radiation (middle) and 3D thermal radiation (right).

cloud in the 1D and no-radiation simulation.
Fig. 4.18 shows time averaged profiles of the conditionally sampled cloud core averaged vertical velocity and the skewness of the vertical velocity. The time period from 42 min to 67 min was averaged. Cloud averaged vertical velocities were positive in the cloudy region (not shown). The simulations with radiation showed weaker upward motion, the simulation with 3D radiation was weaker than the 1D simulation. This showed that the negative vertical velocities around the cloud increase during the simulation. The cloud core vertical velocity was positive, but weakest for the simulation with 3D radiation. The skewness showed strong rising motion in the cloudy layers for the no-radiation simulation and weaker rising in the simulation with

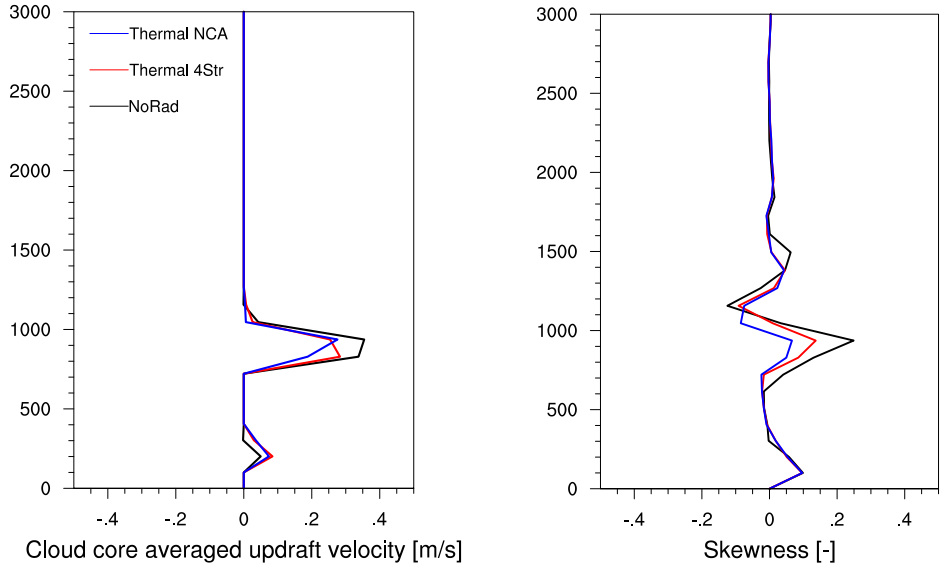

Figure 4.18: Time averaged profiles of conditionally sampled cloud core averaged vertical velocity and the skewness of the vertical velocity. The time period from 42 min to 67 min was averaged.

1D and especially 3D radiation. All statistics indicated again, that radiation speeded up cloud decay, especially the 3D radiation.
In summary:

- The development of the non-symmetric cloud with 1D radiation showed similar differences to the no-radiation simulation compared to the axially symmetric cloud. These differences include increased liquid water mixing ratio at cloud edges, subsiding motion at the cloud edges, stronger updrafts in the cloud core, increased entrainment and the production of negative buoyancy. The cloud decayed faster in the simulation with 1D radiation than in the no-radiation simulation.

- 3D radiation effects were stronger in simulation of the non-symmetric cloud, compared to the axially symmetric cloud. Stronger cooling, resulting from larger cloud side areas was found. This led to a different development of the non-symmetric cloud, in the simulation with 3D radiation, compared to the simulation with 1D radiation. Only small differences in the cloud development between the simulation with 1D and 3D radiation were found for the axially symmetric cloud. After 50 min (after the initial development of the cloud), liquid water mixing ratio decreased and upward as well as downward velocities were weaker in the simulation with 3D radiation compared to the simulation with 1D radiation.

4.2.2 Cloud Field Simulations

After analyzing the effects of 1D and 3D thermal radiation on the development of a single cloud, the question remains if and how thermal radiation has an effect on the development of a whole cloud field in a large domain. For this analysis large scale simulations of a shallow cumulus cloud field in a 25 x 25 km^2 domain were performed. The specific setup was described in Section 3.3.3. Two types of simulations are shown and analyzed in the following. The first had prescribed surface fluxes. Latent heat fluxes were 180 W/m^2 and sensitive heat fluxes 18 W/m^2 during the modeling time. The simulations were run with warm microphysics. Rain was switched off in the first simulation (named SC_fixed_flux). Rain was switched on in the second simulation (SC_fixed_SST). The sea surface temperature was fixed in the second simulation. Therefore surface fluxes were allowed to adjust. The heat fluxes were parameterized as functions of the temperature difference between the fixed ocean surface temperature and the air layers above as well as the horizontal velocities. Interaction between radiation and the surface was not accounted for. Therefore, the two simulations represent the isolated effect of thermal heating and cooling at the clouds and in the atmosphere on cloud development. The simulations were performed for 16 h.
The analysis of this work will focus on the comparison of the simulation without radiation (named no-radiation in the following), the thermal 1D δ-four-stream approximation (named Thermal 1D ICA), the 3D NCA based on the δ-four-stream (named Thermal 3D NCA) and the thermal 3D Tenstream solution (named Thermal 3D Tenstr). All other simulations are not shown in the plots but will be referred to in the text. The variety of possible 1D and 3D thermal radiative transfer solutions can give a hint about the spread different radiation solvers might cause in large scale simulations.
The spectral integration of thermal radiation was performed by using a modified version of the Monte Carlo spectral integration method (MCSI) described by Pincus and Stevens (2009) and Jakub and Mayer (2015b). Due to the fact that only a single wavelength was sampled at each time step and that output files were written every 5 minutes only, it is not possible to show averaged values of the heating or cooling occurring in the simulations. The random choice of wavelength bands at each time step was different in every simulation. 60 bands and sub bands were accounted for by the spectral integration of Fu and Liou (1992). Averaging over about 100 time steps (which is the order of magnitude output was provided in the performed simulations), would still be a noisy average and the heating/cooling effect in the different simulations would be hard to compare. Therefore, one should keep in mind the following: Both 3D thermal radiation approximations, the NCA and the Tenstream solver showed higher cooling rates in cloudy areas compared to the 1D ICA approximation. The NCA showed also slightly higher cooling in the clear sky. This was tested in a different simulation not shown here.
So far, by studying the idealized bubble experiments, differences in cloud development were found, if thermal radiation was accounted for. An increase in updraft velocities, stronger downdrafts at cloud sides, enhanced liquid water mixing ratio in the beginning of the cloud lifetime and stronger evaporation in the late stage of the cloud life have been observed. From former studies, little is known about the effects of thermal radiation on cloud fields. No studies about 3D effects on large domains have ever been performed. A detailed review about studies in the past was given in Section 2.3.2. A short summary shall be given again here: It was

shown in the past that thermal cooling at the cloud top is a generator for turbulence in the cloud, and that the clear sky cooling enhances convection and precipitation (Davies and Alves, 1989; Fu et al., 1995). Increased liquid water content was found due to thermal cooling, but also stronger, radiation induced entrainment (Larson et al., 2001).
Some of these effects have also been found by studying single clouds from the bubble experiments (Section 4.2.1). The investigation of the large scale cloud field will focus on similar variables and quantities. If not otherwise stated in the text, the term *simulation with radiation* always refers to simulations with thermal radiation.

Convective Boundary Layer - Case SC_fixed_flux

In order to give an overview of the simulation, Fig. 4.19 shows a 3D visualization of the development of the cloud field at 16 h, at the end of the no-radiation and the three simulations with radiation. The visualization shows the distribution of liquid water mixing ratio. It is clearly visible that the simulations with radiation developed differently compared to the no-radiation simulation. The clouds seem to be deeper and larger if radiation effects were considered. In addition, both simulations with 3D radiation showed first indications of organization of clouds. The first part of the question to be answered, *if* (3D) thermal radiation has an effect on the development of clouds in a large domain can be answered with yes. The question of the *how* remains. Therefore, a more detailed look into the statistics of the simulations will be given in order to explain the differences in the cloud fields seen in this figure.

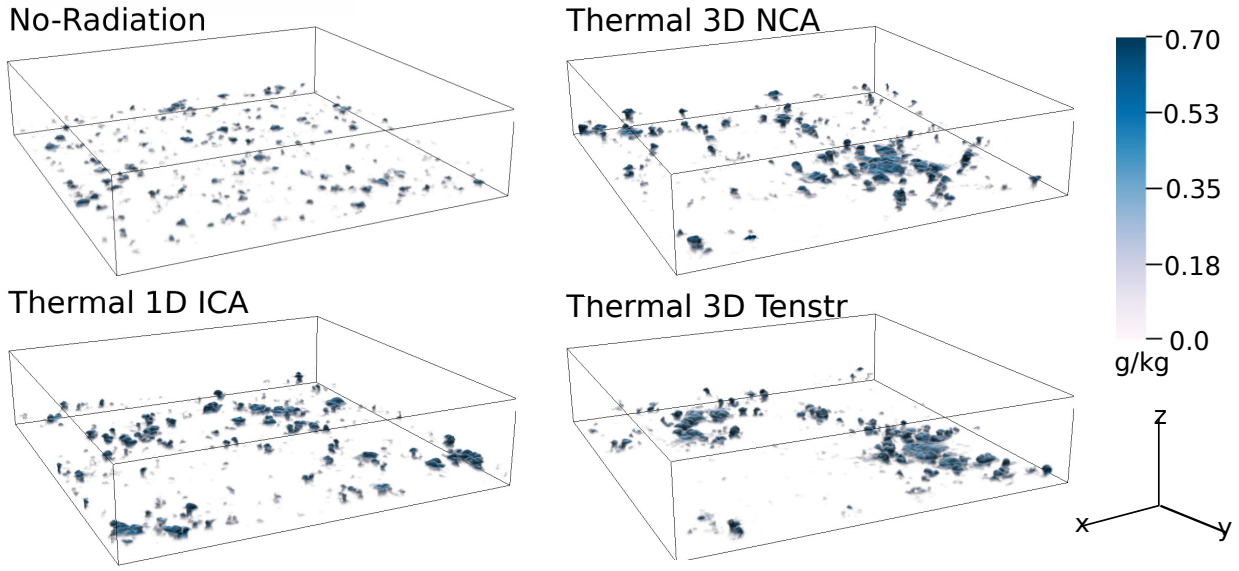

Figure 4.19: 3D visualization of liquid water mixing ratio of the simulated shallow cumulus cloud field. The time snap shots are taken after 16h, at the end of the simulations. Deeper and less clouds occur in the simulations including radiation (δ-four-stream, NCA, Tenstream). Both simulations with 3D radiation (NCA, Tenstream) show organization of clouds.

Fig. 4.20 shows the time development of cloud fraction, liquid water path, maximum upward vertical velocity, maximum liquid water mixing ratio, cloud base and cloud top height as well as the maximum downward vertical velocities (minimum vertical velocity in Fig. 4.20). The first six variables are statistical output, calculated during the simulation. The last, the maximum downward vertical velocity was calculated from the 3D output field, because it was not included in the statistical output of UCLA-LES. 3D output fields were written every 5 min of the simulation. The sampling of the statistics during the simulation included additional time steps which were not accounted for in the maximum downward vertical velocity. In addition, the maximum downward vertical velocities were sampled in non-cloudy area (regions where the liquid water mixing ratio is zero). The thus sampled vertical velocities included the enhanced downward motion at cloud sides. Furthermore, the curves shown in Fig. 4.20 were smoothed by applying a running average over 90 time steps for the statistical output and 9 time steps for the maximum downward vertical velocity (which means over 45 minutes of the simulations in both cases). By looking at these figures one should keep in mind that the simulations with radiation were restarted after 4 hours, based on a 1D solar and thermal simulation, while the no-radiation simulations was done from the very beginning. The time of the restart was chosen shortly before first cloud development occurred in the 1D combined solar and thermal simulation. Vertical profiles of various variables (for example temperature, vertical velocity...) at the time of restart (not shown) did not show significant differences between the no-radiation and the simulations with radiation.

Cloud fraction increased rapidly within 2 h from zero to about $12-15\%$ while it took about 4 h for the no-radiation simulation to develop a cloud cover of 9-10%. The cloud cover was also smaller in the no-radiation simulation. The difference between the simulations with 1D and 3D radiation was not large. The vertical velocities were reduced at first, compared to the no-radiation simulation, but started increasing 2 h after switching on thermal radiation. Liquid water path and the maximum liquid water mixing ratio increased from the moment the simulation was restarted and continued increasing throughout the simulation. The increase in liquid water path was more than a factor of 3 between the no-radiation simulation and the simulations with radiation. 3D radiation led to even more liquid water. Maximum values of cloud top and cloud bottom height showed that condensation occurred at about a height of 500 m in the no-radiation simulation and at about a height of 400 m in the simulations with radiation. In addition, cloud top height increased continuously during the simulation period. Maximum downward vertical velocities decreased during the simulations. At the end of the simulations, maximum downward vertical velocities in the simulations with radiation were about 4 m/s, while those of the no-radiation simulation were weaker with 2 m/s. The development of the vertical velocities showed what has been found in the bubble experiments. Updrafts in the cloud core were stronger and downward motion at the cloud sides was enhanced in the radiation cases. The increase in the liquid water variables in the simulations with radiation can be explained as follows: Thermal cooling, which occurred in the thermal simulations, caused more water to condense. Due to the constant latent heat fluxes, additional water was added continuously to the atmosphere which condensed and forms clouds. The clouds also became deeper. Cloud bottom minimum values were weaker in the radiation cases than in the no-radiation case. This can also be traced back to thermal cooling. Due to the cooling, the whole atmosphere cooled and the temperature profile adjusted to lower temperatures (not shown).

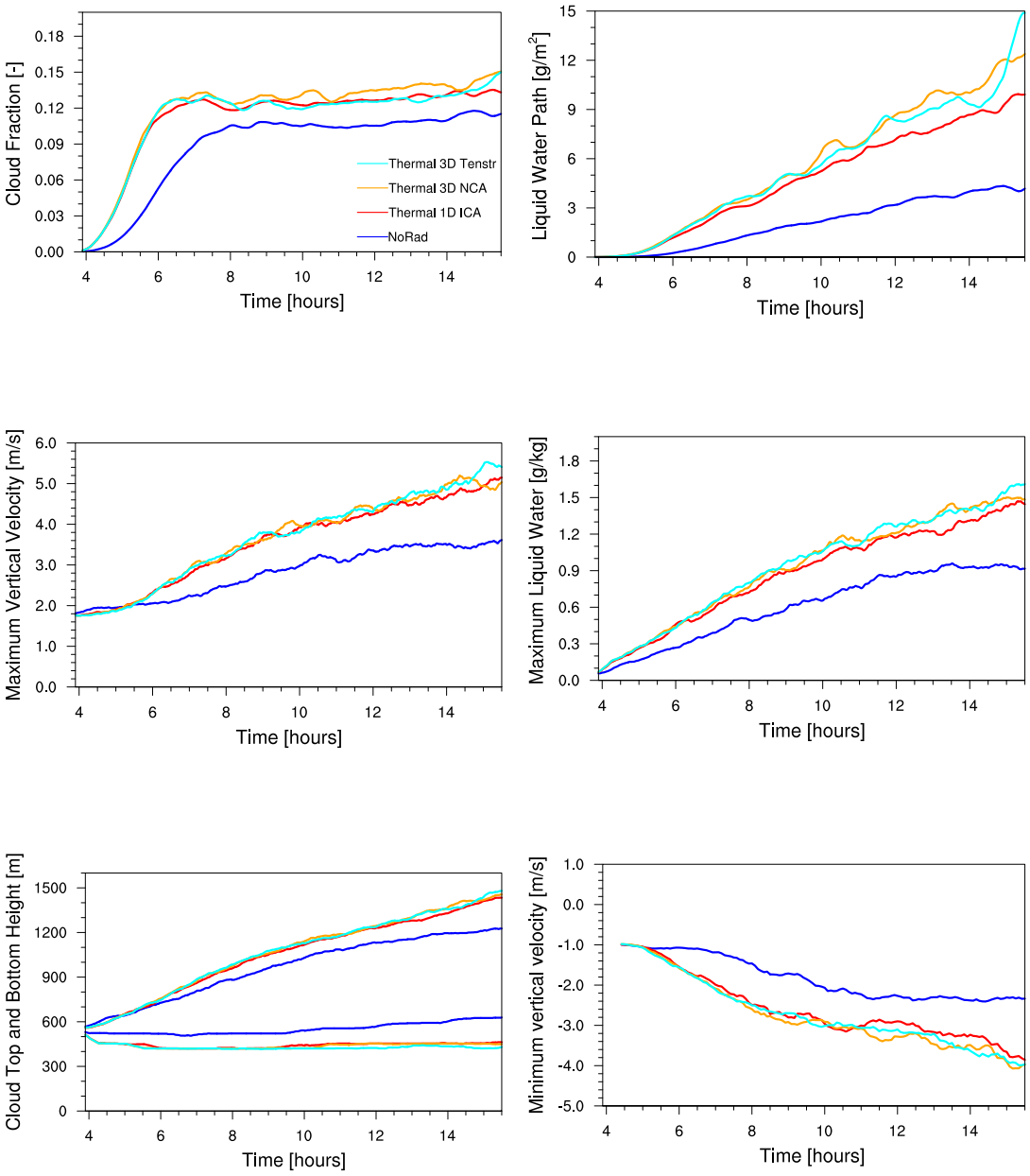

Figure 4.20: Time series of cloud fraction, liquid water path, maximum upward vertical velocity, maximum liquid water mixing ratio, cloud height, and maximum downward vertical velocities (minimum vertical velocity).

In the simulations with radiation, the temperature profile differed by about 1.5 to 2 K during the last 3 hours of the simulation, compared to the no-radiation simulation. The difference in cloud bottom height at the end of the simulation was 150 to 200 m. Condensation occurs when the temperature has decreased to the dew point. The dry adiabatic temperature lapse

rate is about 10 K/km. Therefore a shift in temperature by 2 K to lower temperatures would cause condensation to occur 200 m below the original condensation level, if all other variables stay constant. Cloud top heights rose in the simulations with radiation in comparison to the no-radiation case. This might be due to the stronger updrafts, transporting more moist air to higher levels. The increased cloud cover in the radiation cases might be due to the enhanced condensation and liquid water mixing ratio caused by thermal cooling. The open question is therefore, how the stronger updrafts develop in the radiation cases. This might again be related to thermal cooling causing more condensation. During condensation, latent heat is released, warming the atmosphere locally. The warming results in positive buoyancy which again enhances upward velocities.
Summarizing this first figure, it can be concluded that all shown variables showed an increase in the absolute value in the simulations with radiation. 3D radiation showed slightly stronger effects in the development of the liquid water quantities than the simulation with 1D radiation, although not a significant one. Most of the differences in the development of the variables can be related to the effects of thermal radiation.

A different view on the cloud field is given by Fig. 4.21 which shows vertical profiles of liquid water mixing ratio, conditional sampled cloud averaged vertical velocity, skewness of the vertical velocity, relative humidity, buoyancy production of the resolved turbulent kinetic energy (TKE) and liquid water potential temperature averaged over the last 3 hours of the simulation. The increase in liquid water mixing ratio which was already noted in the time series analysis in the radiation cases was seen here again. It was also seen that the layer of liquid water mixing ratio and therefore the clouds became deeper in the simulations with radiation. The layer of liquid water mixing ratio started at 450 m and went up to 1400 m in the simulations with radiation. For the no-radiation simulations, liquid water mixing ratio was found between 600 m and 1200 m of height. This was in agreement with the development of cloud top and cloud base height which was also shown in the time series figure. Both simulations with 3D radiation showed an increased liquid water mixing ratio in the cloudy layers compared to the simulations with 1D radiation. The increase between the 3D and 1D cases in liquid water mixing ratio was about 20% in the maximum. The cloud averaged vertical velocity showed an increase in vertical velocity in the simulations with radiation compared to the no-radiation case. Most interestingly, the 1D radiation showed slightly higher values (about 0.5 m/s in the maximum) although the maximum upward vertical velocities shown in the time series had shown highest values for the simulations with 3D radiation and not for the 1D radiation case. This might be related to stronger downdrafts at the cloud sides in the simulations with 3D radiation, which in this average quantity compensated the positive updrafts partially. The skewness was positive in the cloudy layers, indicating regions of strong updrafts. Similar to the cloud averaged vertical velocity, the skewness of the simulations with 3D radiation is slightly less positive, which might again be related to downdrafts at the cloud sides. Finally, the profile of relative humidity is shown. The relative humidity also showed that the boundary layer deepened (by 100 - 200 m) in the simulations with radiation compared to the no-radiation simulation. Except for a layer between 700 and 900 m, the boundary layer was moister in the simulations with radiation, compared to the no-radiation simulation. The layer between 700 and 900 m was within the cloudy region. It is possible that due to thermal cooling, entrainment was increased and more dry air was mixed in, thus reducing the relative

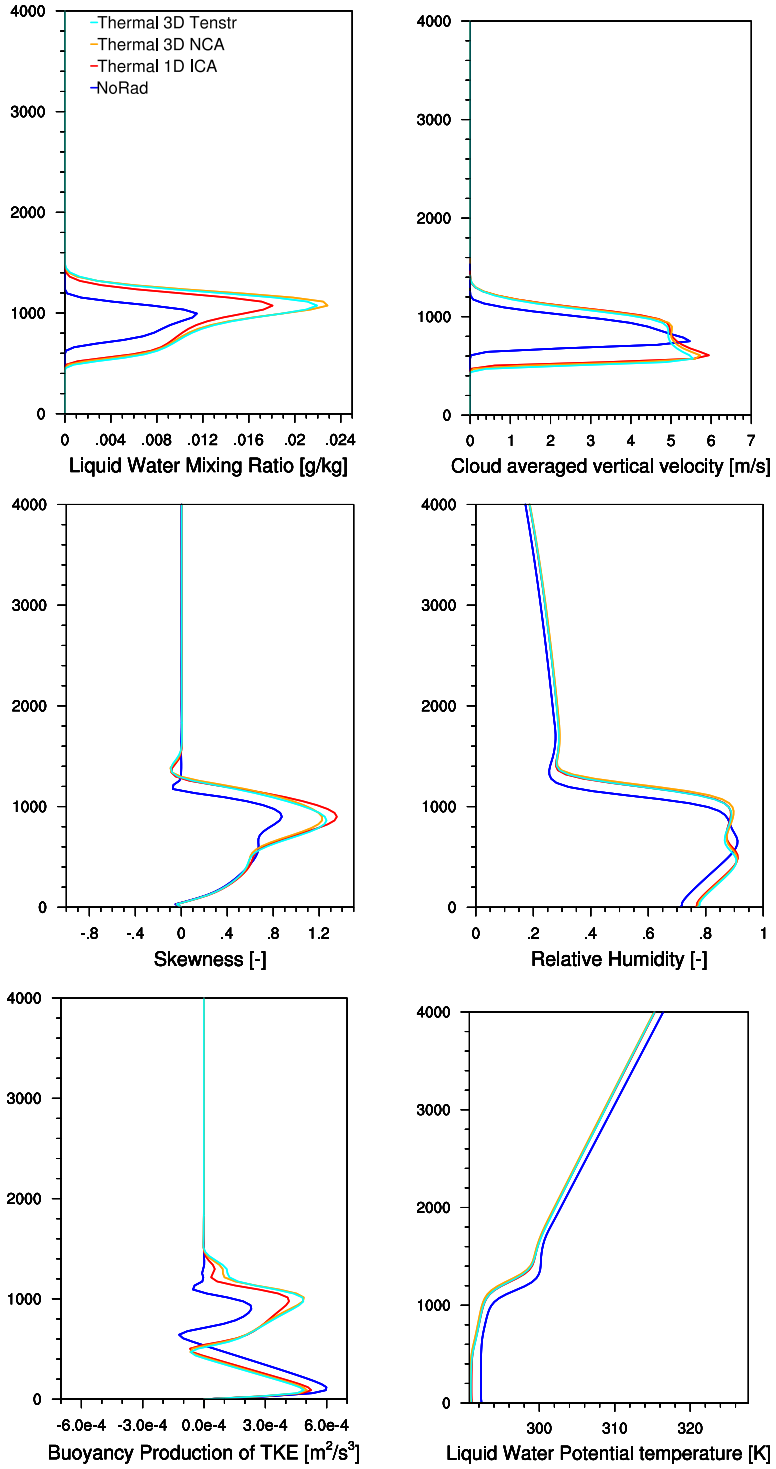

Figure 4.21: Vertical profiles of liquid water mixing ratio, conditional sampled cloud averaged vertical velocity, skewness of the vertical velocity, relative humidity, buoyancy production of the resolved TKE, and liquid water potential temperature. The profiles are averaged over the last 3 hours of the simulation.

humidity. Indeed, the buoyancy production of the resolved TKE showed increased buoyancy production in the cloudy layer.
In the statistical analysis so far, an effect of thermal radiation on the development of the clouds and boundary layer was noted, but differences between 1D and 3D thermal radiation were rare. However, Fig. 4.19 at the beginning of this section showed that the cloud fields looked very differently in terms of horizontal extent and location of the clouds. In the simulations with 3D radiation clouds seemed to organize themselves. Fig. 4.22 shows the spatial auto correlation of the 2D field of liquid water path of the the four simulations shown so far at the last time step (at 16 h). The correlation length was larger in the simulations with 3D radiation, which implies that clouds had a larger horizontal extent in the simulations with 3D radiation, compared to the 1D case. In comparison to the no-radiation simulation, the 1D thermal radiation showed a larger horizontal extent as well. It can therefore be concluded that in general, interactive thermal radiation enhances cloud growth, 3D interactive thermal radiation even stronger than 1D interactive thermal radiation.

Fig. 4.23 compares the correlation length, estimated as the azimuthal averaged radius at which the correlation coefficient drops below exp(-1) at each time step. The correlation length increased with time, especially in the simulation with 3D radiation. The correlation length of

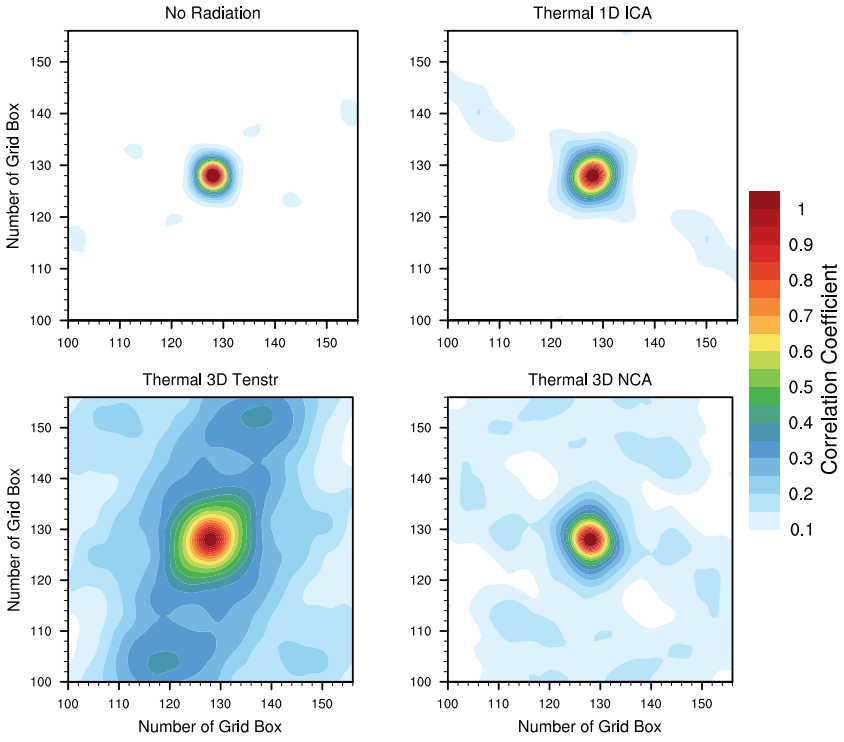

Figure 4.22: Autocorrelation of liquid water path for the no-radiation, the thermal 1D ICA and the two simulations with thermal 3D radiation. The x and y axis show number of grid boxes. Each grid box has an extent of 100 m in the horizontal.

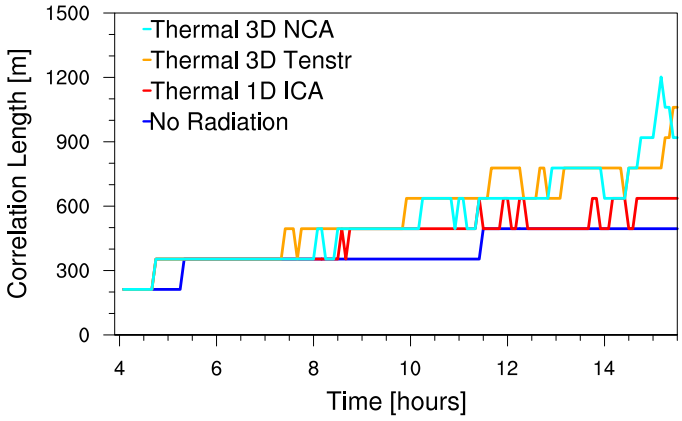

Figure 4.23: Correlation length (at 1/e) per time step of the simulation.

the simulations with radiation was generally larger over the whole modeling time.
A comparison with the results of the two-stream and Schwarzschild 1D simulation and the corresponding NCA simulations showed that all 1D radiation solvers performed very similar if the time series of the shown variables is considered. The NCA approximations based on the two-stream and Schwarzschild 1D approximation showed a slight increase in cloud fraction and liquid water path in the time series analysis compared to the Tenstream and the NCA (based on δ-four-stream) approximation. In terms of the vertical profiles, averaged over the last 3 hours of the simulations, the additional 1D simulations showed lower cloud averaged vertical velocity. All other profiles behaved similar to the δ-four-stream 1D approximation. The additional NCA simulations showed slightly increased values of liquid water mixing ratio, cloud averaged vertical velocities and relative humidity. Buoyancy production and skewness were increased for one of the additional NCA approximations, decreased for the other, compared to the δ-four-stream based NCA simulations. However, all radiation solvers performed very similar in general. In terms of autocorrelation, the same development can be observed as was shown before. For 1D radiation autocorrelation increases compared to the no-radiation simulation. For 3D interactive radiation autocorrelation increases even further.

Convective Boundary Layer - Case SC_fixed_SST

In this simulation experiment, surface fluxes of latent and sensible heat were no longer prescribed (in comparison to the SC_fixed_flux simulations shown before). The sea surface temperature was fixed at 300 K and surface fluxes were allowed to adjust according to the changing temperature profile and horizontal velocities. Therefore, the surface fluxes somehow represented the additional cooling introduced by thermal radiation. To force the simulation to develop clouds within the first few hours of the simulation, the sea surface temperature was set to 300 K although the initial profile of the atmosphere started at 289 K. This setup led

to a unrealistic development of the latent and sensible heat fluxes. This will be addressed during the following analysis. In addition, rain was switched on in the microphysical scheme. The chosen setup was original meant for 'non precipitating shallow cumulus clouds' (Stevens, 2007). Although rain was switched on, only very little amounts of rain develop during the simulation which increased when thermal radiation was switched on. Still, the amount of rain was very little and evaporated completely before it reached the surface. Rain quantities will therefore not be considered in the further analysis. The restart of the simulations with radiation was after 6 h. All other setup specifications remained the same as in the SC_fixed_flux simulations. For the analysis, the same plot types will be shown. At the beginning, Fig. 4.24 shows a 3D visualization at 16 h of liquid water mixing ratio. Like in the previous simulation, SC_fixed_flux, the simulations with radiation showed deeper clouds containing more liquid water. The simulations with 3D radiation indicated again first organization of clouds, as did the 1D radiation simulation, although less.

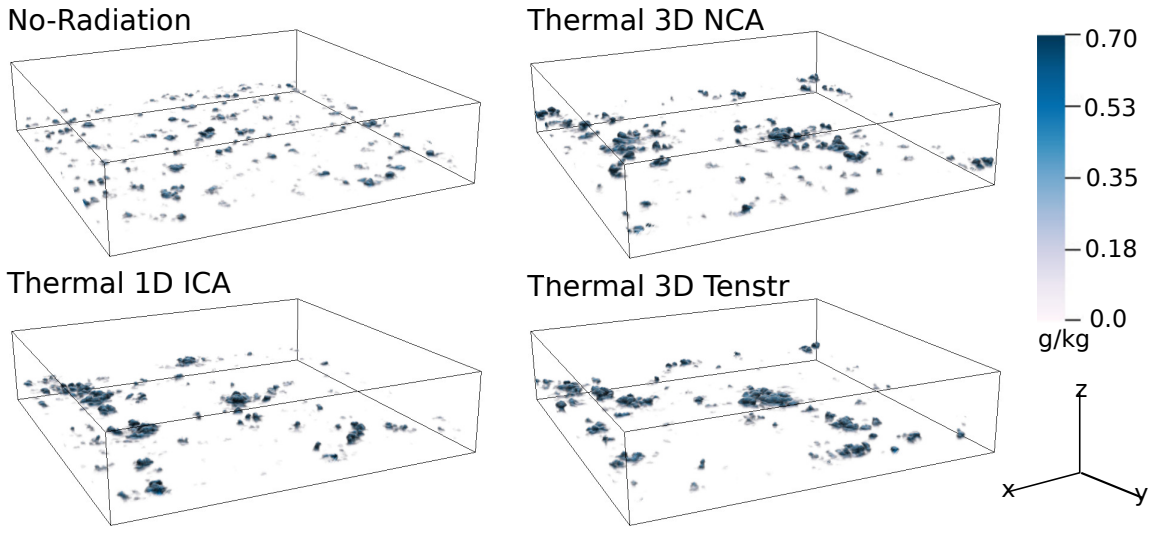

Figure 4.24: 3D visualization of liquid water mixing ratio of the simulated shallow cumulus cloud field. The time snap shots are taken after 16h, at the end of the simulations. Deeper and fewer clouds occur in the simulations including radiation (δ-four-stream, NCA, Tenstream). Both simulations with 3D radiation (NCA, Tenstream) show organization of clouds.

Fig. 4.25 shows the time development of cloud fraction, liquid water path, maximum upward vertical velocity, maximum liquid water mixing ratio, cloud top and bottom height as well as the maximum downward vertical velocity (minimum vertical velocity in Fig. 4.25) in the non-cloudy regions. Similar to Fig. 4.20 a running average of the data is shown. The development of the cloud fraction, shortly after restart, behaved differently, compared to the SC_fixed_flux simulations. In the simulations with radiation, cloud development was first suppressed, before it increased rapidly between 7 and 10 hours of the simulation. The cloud fraction of the simulations with radiation exceeded the cloud fraction of the no-radiation simulation at 10 hours slightly (no-radiation: 16% in the maximum, simulations with radiation: 18% in the maximum). After 12 hours, cloud fraction of the no-radiation simulation and the simulations with

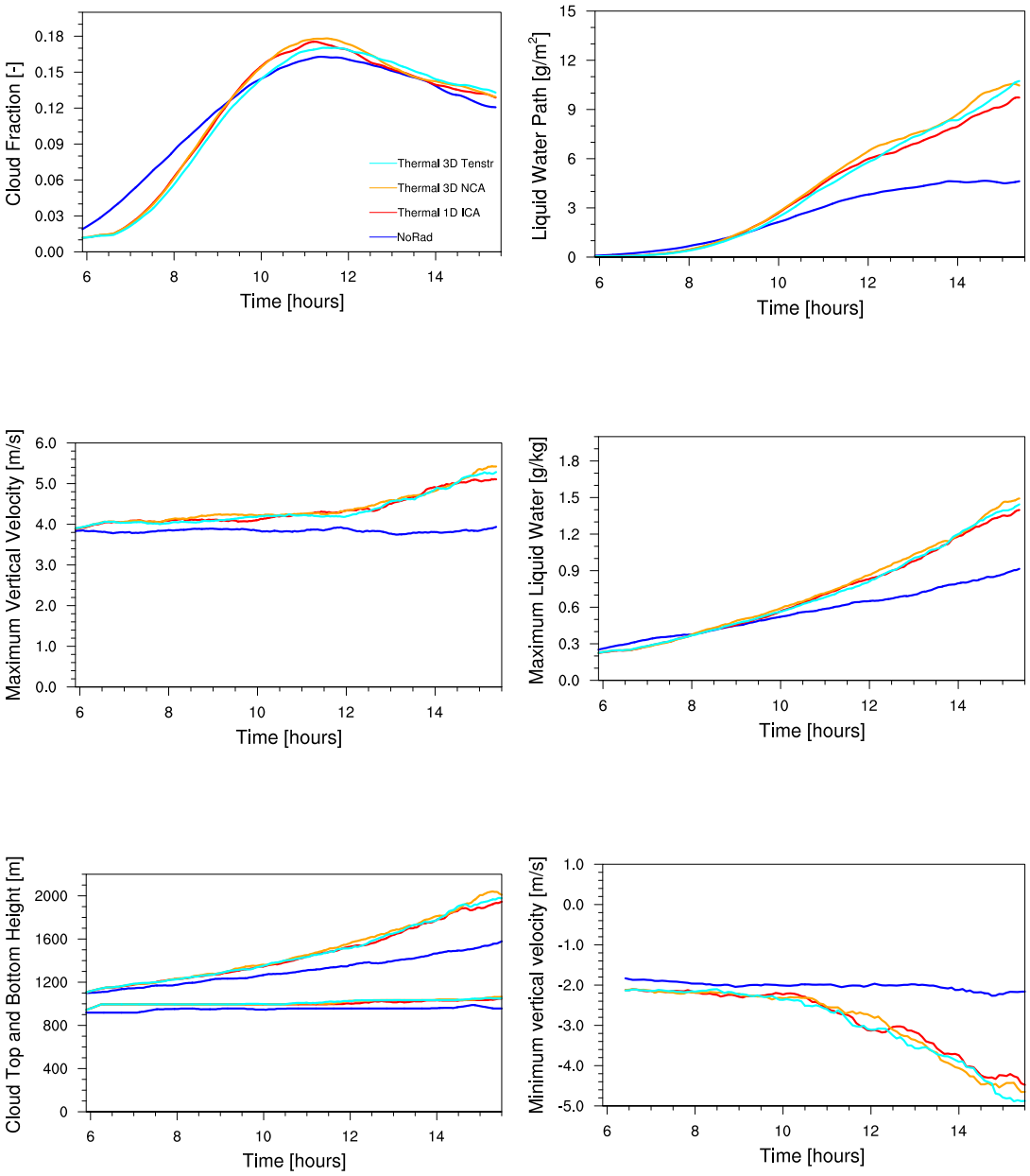

Figure 4.25: Time series of cloud fraction, liquid water path, maximum upward vertical velocity, maximum liquid water mixing ratio, cloud height, and maximum downward vertical velocity (minimum vertical velocity).

radiation converged, but the cloud fraction of the simulations with radiation stayed slightly higher. Liquid water path and maximum liquid water mixing ratio increased after 9 h of the simulations with radiation, compared to the no-radiation case. Liquid water path of the simulations with radiation was about twice as much as in the no-radiation simulation at the

end of the shown simulation time. The same was true for the maximum liquid water mixing ratio. Maximum upward vertical velocities increased (about 25%) with radiation switched on, maximum downward vertical velocities decreased (about 250%). Cloud top height increased with radiation switched on (from 1500 m in the no-radiation simulation to 1900 m in the simulations with radiation, at the last time step) and in comparison to the SC_fixed_flux simulation, cloud bottom height increased slightly (no-radiation: 850 m; radiation: 1100 m at the last time step) too, when thermal radiation was switched on.

Fig. 4.26 showed the time development of the latent and sensible heat fluxes. This was not shown in the SC_fixed_flux simulation, because surface fluxes were prescribed in the former simulation. It can be seen that both sensible and latent heat fluxes decreased with time, but that in the case of thermal radiation, the surface fluxes were higher. The decrease with time can be explained by the temperature profile. In the beginning of the simulation, the difference between the fixed ocean surface temperature (300 K) and the temperature in the lower layers (289 K) was 11 K. This differences decreased with time, because the air layers over the ocean warmed. In the case of latent heat, the fluxes were in the magnitude that was expected over a warm ocean surface, which is the case in this simulation, because the sea surface temperature was set to 300 K. On the other hand the sensible heat fluxes were in a magnitude that would be expected over a warm land surface. The different development of the surface fluxes seemed unrealistic, which they were. However, the simulations were designed to look for effects of thermal radiation on cloud development, not to simulate a perfect realistic environment. The large sensible heat fluxes can be explained with the huge difference in the sea surface temperature (300 K) and the initial profile in the lower layers (289 K). The high sea surface temperatures were necessary to force cloud development after a few hours of simulation. In the first few hours after restart, sensible heat flux was lower in the simulations with thermal radiation than in the no-radiation simulations. When switching on thermal radiation, the atmosphere and clouds were cooled on average, causing a larger temperature gradient between the surface and the atmosphere. If horizontal wind speeds do not differ significantly in the different simulation types, the change in sensible and latent heat fluxes must be due to the change in atmospheric temperature. The answer is given by looking at the profiles

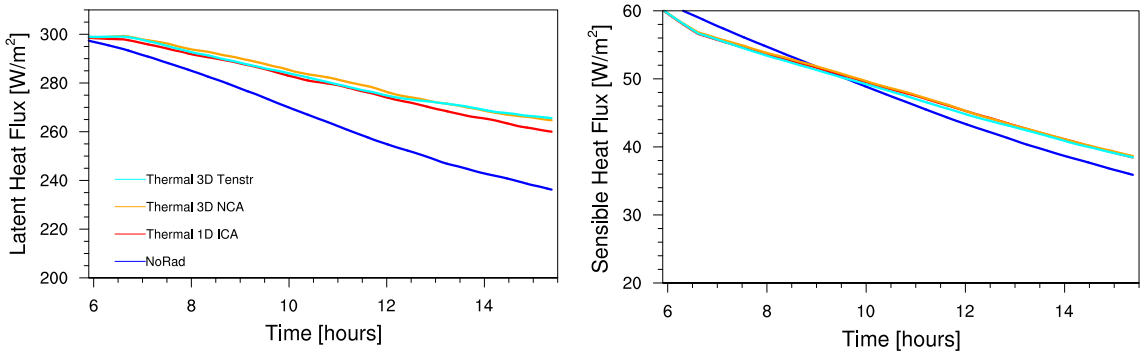

Figure 4.26: Time series of latent and sensible heat flux.

of temperature at the time of restart. Due to the base simulation (1D solar and thermal), the temperature profile at 6 h (not shown) showed higher temperatures in the simulations with radiation than the no-radiation simulation. Therefore, sensible heat fluxes decrease at first, as long as the temperature profile shows higher temperatures for the simulations with radiation. At about 9 h, the profiles were very much alike, and due to the thermal cooling of the atmosphere and increased horizontal wind speeds, sensible heat fluxes became now higher in the simulations with radiation than in the no-radiation simulation.
The development of the sensible heat fluxes can help explaining some of the features seen in the other time-series variables. Until 9 h, cloud cover and both liquid water quantities were lower in the simulations with radiation compared to the no-radiation simulations. This changed after 9 h. From 9 h on, the development of the variables in the time series analysis was similar as in the SC_fixed_flux case. To further interpret the results the vertical profiles of different variables were shown in Fig. 4.27. It can be seen that the cloud layer was much deeper and the cloud base and top were lifted higher up in the vertical profile of the liquid water mixing ratio. Also, the magnitude of liquid water mixing ratio increased in the simulations with radiation, the 3D even more. This was in agreement with the development of the liquid water variables and the cloud top/base height in the time series analysis. The lift in cloud bottom height resulted from the warmer temperature profile, which was due to the base simulation from which the thermal simulations were restarted. The increase in liquid water variables was due to the cooling of the atmosphere over time due to thermal radiation. Averaged vertical velocities in the cloudy region (middle figure on the left) showed also the deeper cloud layer. The magnitude of the averaged velocity was also higher in simulations with radiation compared to the no-radiation simulation. The same was found for cloud core regions (not shown). The updrafts in the cloud core regions were stronger (about 1 m/s) in the simulations with radiation. Looking at the time series, it was found that the maximum upward vertical velocity were larger in the simulations with radiation. The maximum upward vertical velocities were located in the cloud cores. So this is in agreement. The skewness also showed stronger updraft regions for the simulations with radiation (being more positive in the cloudy area) and small negative values above the cloud layer. The buoyancy production was stronger in the cloudy layer and the profile of liquid water potential temperature in the last 3 h showed lower temperatures in and above the clouds. The relative humidity can explain the development of the latent heat fluxes. Latent heat fluxes were stronger in the simulations with radiation. The profile of the relative humidity averaged over the last 3 hours of the simulations showed that the boundary layer below the clouds was dryer. Latent heat fluxes increased to compensate the dryer boundary layer.
Similar to the SC_fixed_flux experiment, the differences between 1D and 3D thermal radiation was visible in the liquid water variables, but all other variables behaved similar in the statistical analysis. However, again, the spatial distribution of the clouds changed.
Fig. 4.28 shows the spatial autocorrelation of liquid water path at the last time step. Clouds were overall larger in horizontal extent in the simulations with radiation, which could already be guessed in Fig. 4.24. Finally, Fig. 4.29 shows the time development of the 1/e correlation length. The difference between 1D and 3D thermal radiation was not as large as in the SC_fixed_flux simulation, but the increase in all simulations with radiation in comparison to no-radiation simulation was significant.

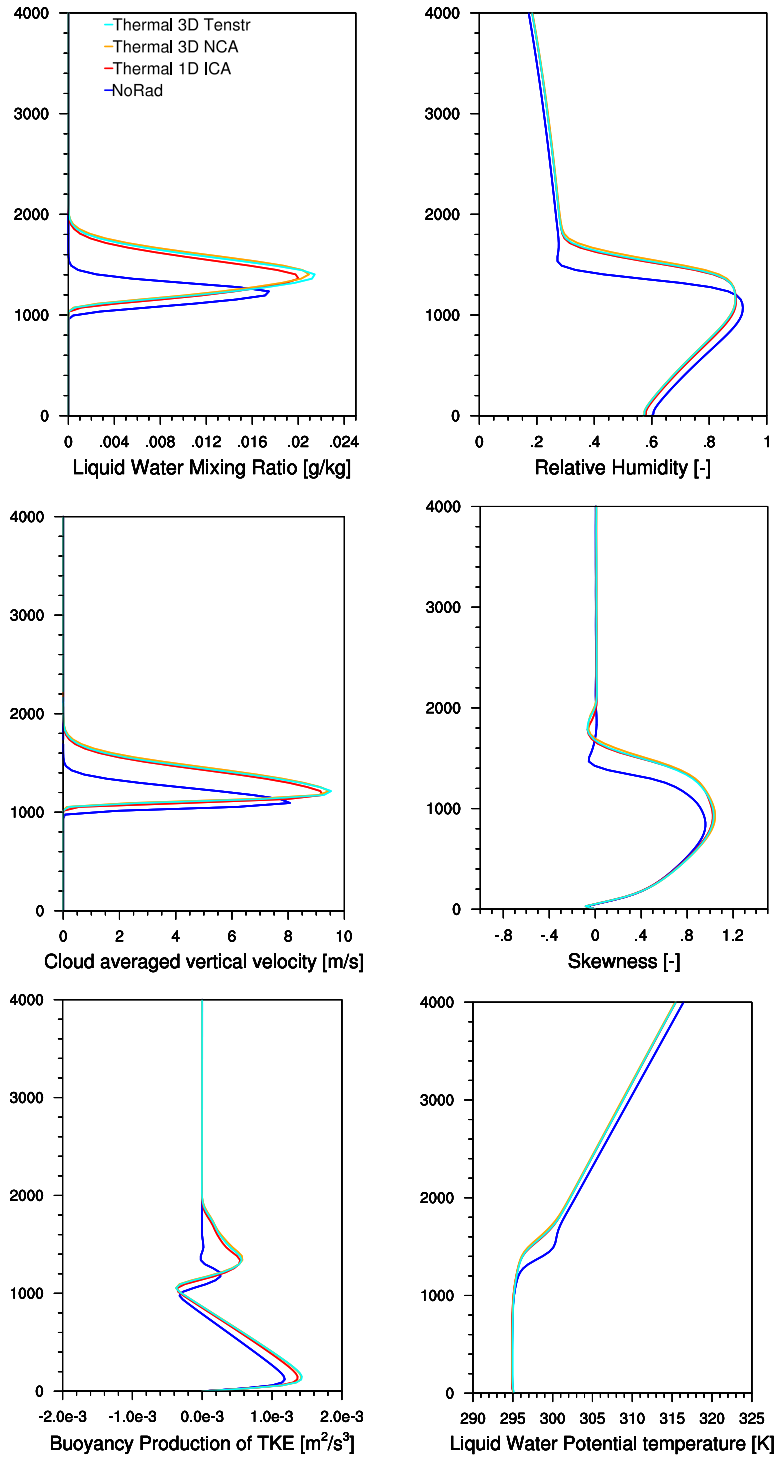

Figure 4.27: Vertical profiles of liquid water mixing ratio, conditional sampled cloud averaged vertical velocity, skewness of the vertical velocity, relative humidity, buoyancy production of the resolved TKE, and liquid water potential temperature. The profiles are averaged over the last 3 hours of the simulation.

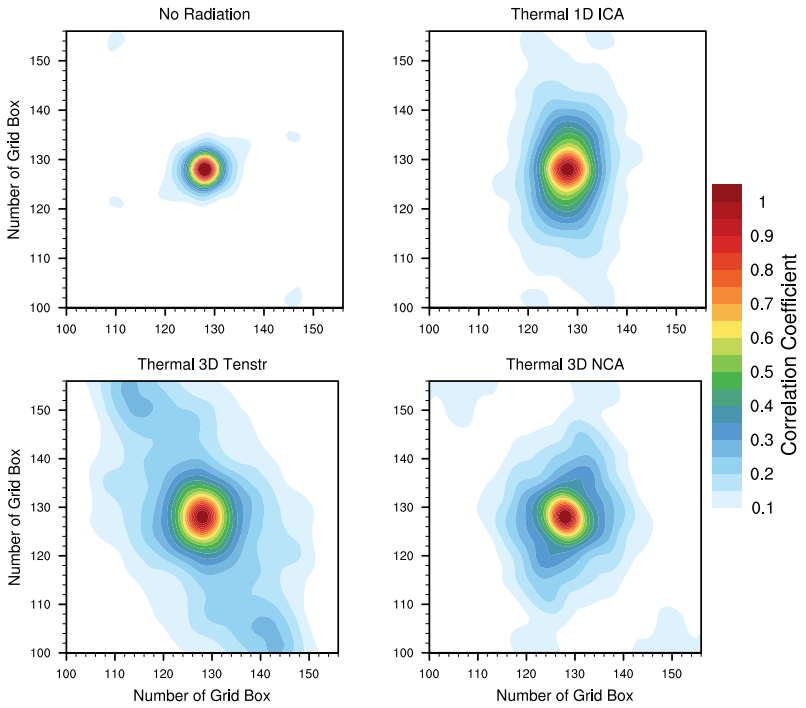

Figure 4.28: Autocorrelation of liquid water path for the no-radiation, the thermal 1D ICA and the two simulations with 3D radiation. The x and y axis show number of grid boxes. Each grid box has an extent of 100 m in the horizontal.

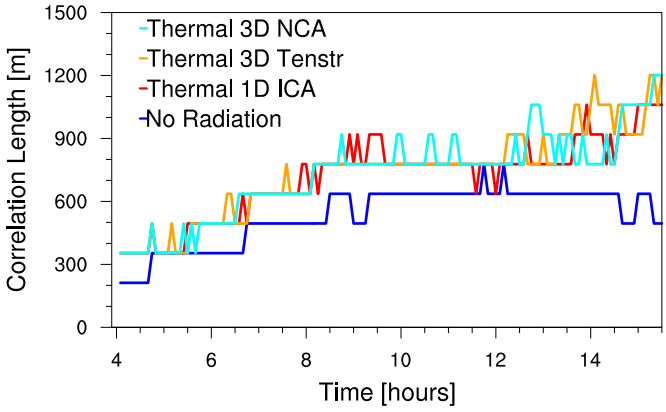

Figure 4.29: Correlation length (at 1/e) per time step of the simulation.

Summary of the Large Scale Simulations

Summarizing the effects of thermal radiation on cloud development in a large domain (SC_fixed_flux and SC_fixed_SST), it was found:

- Thermal radiation increases condensation and therefore liquid water mixing ratio of the clouds.
- Due to the enhanced condensation, latent heat was released locally, causing positive buoyancy and therefore stronger updraft velocities in the cloud cores.
- Next to the stronger upward motion in the cloud core, downward motion at the cloud sides was increased in the simulations with radiation.
- The boundary layer and clouds become deeper in the simulations with thermal radiation, which can be a result of the stronger updraft velocities, transporting more moist air to higher levels.
- More turbulence and entrainment was found in simulations with radiation.
- Clouds showed a larger horizontal extend and it seemed that convective organization is triggered if 3D thermal radiation is accounted for. A general effect of thermal radiation on cloud development was found, but 3D and 1D thermal radiation do not differ much in most of the variables of the statistical analysis of the simulations.

4.3 Impact of 3D Thermal Radiation on Cloud Droplet Growth

Estimates about the effect of (3D) thermal radiation on cloud droplet growth were made in a bachelor thesis under my supervision (Gödde, F., 2015). Former studies on this subject (Section 2.3.2) found increased cloud droplet growth due to the effect of thermal radiation. However, only the effects of 1D thermal radiation were considered in the past. In the bachelor thesis (Gödde, F., 2015), first, idealized studies of the effect of 3D thermal radiation were made. A short summary of the results of this thesis is given here:
In the first part of the study, a diffusional droplet growth equation (Eq. 2.41) considering radiation effects was derived. Considering radiation effects in the diffusional droplet growth equation is essential, because radiation effects at cloud top and sides affect droplet growth. Applying heating and cooling rates only in volumes (which was done for example in Section 4.2.2), neglects the effect on cloud microphysics. The idealized estimations of the effect of thermal radiation on droplet growth were not performed in a time developing model. Radiation effects on idealized clouds (a cubic cloud in 3D and a plane parallel cloud in the 1D case) were calculated with the 3D Monte Carlo model MYSTIC (Mayer, 2009) and the simulations with 1D radiation were performed with DISORT (Stamnes et al., 1988). Radiation effects were calculated for two different height levels of the cloud in the atmosphere. Different effects were estimated:

- Constant effect of thermal radiation on a cloud droplet
- Effect of thermal radiation along a realistic cloud droplet trajectory in the 1D case
- Effect of 3D thermal radiation along an idealized trajectory (given a maximum estimation).

The trajectories used in this work were similar to those found by Harrington et al. (2000) who simulated different types of trajectories in a stratocumulus cloud. Simulations with radiation were performed with two resolutions and for different liquid water contents and effective radii of the cloud. This allowed to perform the droplet growth calculation with a realistic estimate of the radiation effect (which changed with droplet size and the height of cloud and the location of the droplet within the cloud). For more details, the reader is referred to the thesis.
Fig. 4.30 shows droplet growth with and without the effect of thermal radiation. Thermal radiation was acting on the cloud droplet during the whole simulation time. The net emitted irradiance of a cloud droplet at the cloud droplet surface (last term in Eq. 2.41; 10, 30 and 50 W/m^2) was estimated from cooling rates calculated by Klinger and Mayer (2014). The stronger the cooling, the faster the cloud droplet grew.
A constant cooling on a cloud droplet would only occur in reality, if the cloud droplet would be located at the edge or top of the cloud during its whole lifetime. This is unrealistic. In a dynamical system like a cloud, cloud droplets are moved constantly. For a more realistic estimate, the growth of cloud droplet with the effect of thermal radiation was studied along a cloud droplet trajectory. Fig. 4.31 shows such a trajectory on the left. The droplet moved

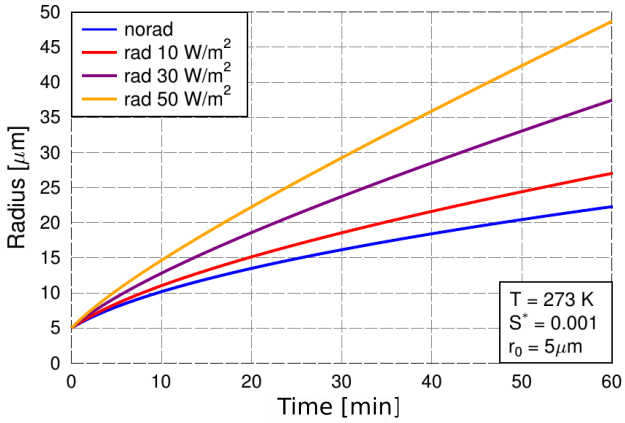

Figure 4.30: Cloud droplet growth with time by emission of a constant net irradiance of 10, 30 and 50 W/m^2. For comparison, the blue line shows cloud droplet growth without the impact of thermal radiation. (From Gödde, F. (2015), Figure 3.3.)

along the black line. Depending on its location in the cloud, thermal cooling (cloud top) or warming (cloud bottom) was influencing droplet growth. The figure on the right shows the droplet growth. In the beginning, when the droplet moved in the cloud center where no heating or cooling occurred, the droplet growth was the same in the radiation and the no-radiation simulation. As soon as the droplet reached cloud top, it started growing faster in the simulation with thermal radiation. While descending, the air was warmed adiabatically and the droplet started to evaporate. Due to the warming at cloud base in the simulation with radiation, only a small increase in cloud droplet size remained after half of the simulation time (60 min). The same processes started again in the second half of the simulation. In summary, the droplet grew faster due to the effect of thermal radiation. The simulation time was 120 min for the long lasting type of a stratus cloud shown here.

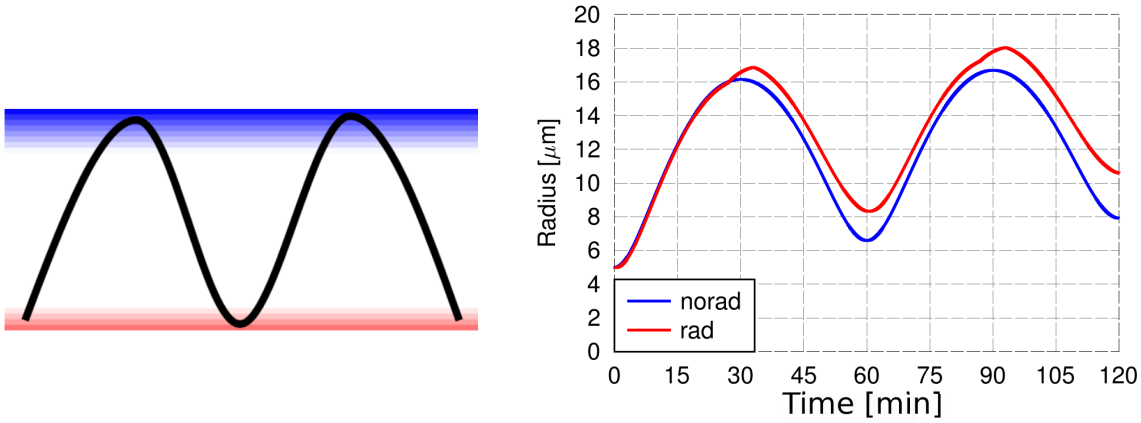

Figure 4.31: Schematic trajectory of the cloud droplet and heating (red) and cooling rates (blue) of the 1D cloud (left), cloud droplet growth in a 120 min simulation with and without the effect of thermal radiation (right). (Modified from Gödde, F. (2015), Figure 4.4 and Figure 4.7.)

In the example of the 3D cloud (Fig. 4.32), the trajectory (along the edges of the cloud, left figure) can be seen as a maximum estimate of the effect of thermal radiation on droplet growth. Cloud droplets started in the center at the cloud bottom and moved up through the cloud. At cloud top, radiation affects on droplet growth occurred for the first time, again increasing the growth rate. Even during descending and the adiabatic warming, the cooling at cloud sides in this 3D case reduced evaporation. The figure shows the development for the two cloud heights simulated. Again, thermal radiation enhances cloud droplet growth.

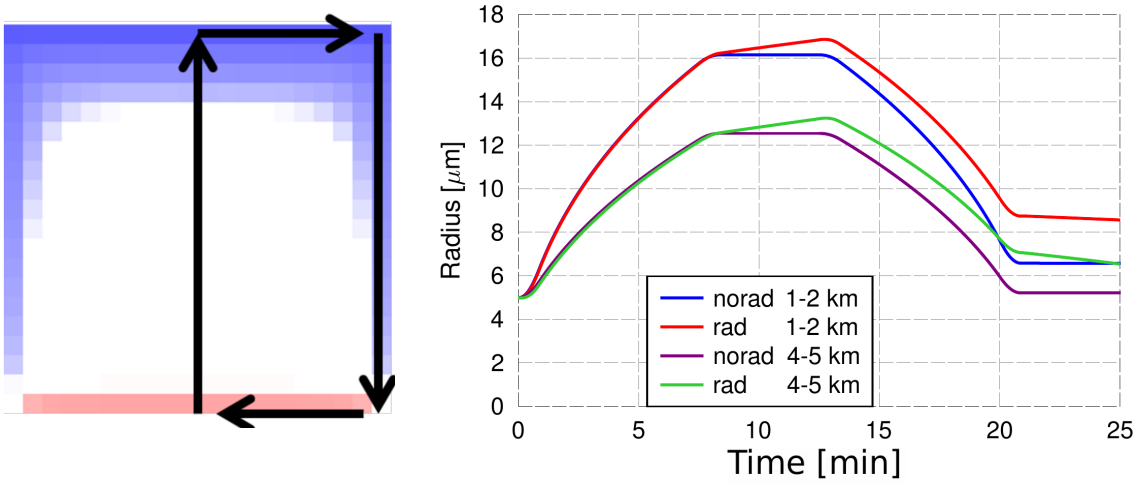

Figure 4.32: Schematic trajectory of the cloud droplet and heating (red) and cooling rates (blue) of the 3D cloud (left), cloud droplet growth in a 25 min simulation with and without the impact of thermal radiation (right). (Modified from Gödde, F. (2015), Figure 4.10 and Figure 4.11.)

Chapter 5

Summary and Discussion

The aim of this thesis is to answer the question if and how thermal radiation affects the development of clouds. Three steps were necessary in order to study the effects of 3D thermal radiation on cloud development:

1) Quantify magnitude of typical thermal heating rates and provide accurate benchmark results by performing 3D radiative transfer simulations with an accurate radiative transfer model.

2) Develop a fast, but still reasonably accurate parameterization for the calculation of 3D thermal heating rates which can be implemented in a cloud resolving model, based on the knowledge gained in 1).

3) Implement the newly developed 3D thermal parameterization into a cloud resolving model and estimate the effect of thermal radiation on cloud development by a set of cloud simulations.

The methods developed in this work and the results are summarized in the following. For the first two items, the summary is taken from the corresponding paper of Klinger and Mayer (2014) and Klinger and Mayer (2016), with only a few editorial changes. Finally, conclusions and an outlook are presented.

3D Radiative Transfer with a Monte Carlo Model

Three fundamentally different Monte Carlo methods (one forward and two backward) to calculate 3D thermal heating rates in the atmosphere were developed. All three methods have been implemented into the MYSTIC Monte Carlo code. All three methods are physically correct: no approximations were introduced which might bias the results. The results have been shown to agree with each other within the inherent statistical noise of the Monte Carlo approach. The methods include the calculation of thermal emission, absorption, and scattering effects. Backward photon tracing is more efficient than forward tracing for thermal heating rate calculations. Two different approaches have been developed. In the first (EMABS) the difference between the emission and absorption of a grid box is used to calculate the heating

rates. A sophisticated variance reduction method was implemented (EMABS_OPT) which reduces the computational time for a given Monte Carlo noise by an order of magnitude for grid box optical thicknesses of more than 100 (which are common in the thermal spectral range). The second backward method (DENET) is based on a net-flux difference approach. DENET reduces the computational time for large grid box optical thicknesses by another order of magnitude. The results of all forward and backward methods agreed with each other and with the completely different DISORT method (for a 1D case) within the Monte Carlo noise. A hybrid method (HYBRID) was developed which combines EMABS_OPT for small optical thickness with DENET for large optical thickness to maximize the performance of the model.
The methods have been used to study the dependence of thermal heating and cooling rates in different geometries and in realistic cloud fields. It was found that thermal cooling occurs at the cloud sides and cloud tops within the first 100-200 m of the cloud edge. The interior of the cloud shows no heating or cooling. In addition modest cloud bottom warming is found. The larger the distance between neighboring clouds, the more the cloud sides cool.
The magnitude of the heating rates and the location of the maximum values depend on the cloud shape, the geometry of the cloud field, and the optical properties. The 1D independent column apprixmation fails to reproduce the cloud side cooling which is a clear 3D effect.

3D Parameterization for Atmospheric Thermal Heating Rates

A fast and accurate method to calculate 3D thermal heating rates has been developed. The method uses only input from the directly neighboring columns of a column in a model domain and is therefore called Neighboring Column Approximation (NCA). The NCA may use the existing 1D ICA radiation code of a cloud resolving model or can be used with any 1D radiation code. It can therefore be easily applied in any cloud resolving model where a 1D radiation solver is implemented. Several assumptions were made to make this radiative transfer solution an analytic and fast approximation. Next to the neglect of horizontal transport of radiation beyond one neighboring column, scattering is neglected and radiation transport is approximated by using an effective zenith angle of 45°, perpendicular to the grid box faces in the horizontal. For the uncertainties introduced by the latter two assumptions, a correction function was developed. An important advantage of the method is that it can be used in parallelized models without breaking the parallelization. The computational costs for a LES simulation with the NCA are only a factor of 1.5 - 2 higher compared to a 1D radiation approximation. The method performs best for model resolutions of about 100 m or coarser and a significant improvement of the accuracy compared to common 1D radiative transfer solutions was shown. For isolated grid boxes, the NCA differed about 10% from an exact 3D Monte Carlo simulation. For a cloud field application with a resolution of 100 m, the RMSE for all cloudy grid boxes in the domain decreased from 13.6 K/d (ICA vs. MYSTIC) to 9.6 K/d (NCA vs. MYSTIC). Maximum cooling rates for the full 3D simulation with MYSTIC showed values of -150 K/d (100 m resolution) while the 1D solution shows maximum coolings of -100 K/d. The NCA however is capable of reproducing the stronger 3D cooling rates.
To my best knowledge, the NCA is next to the Tenstream solver (Jakub and Mayer, 2015a)

the only known parameterization for the calculation of 3D thermal heating rates in a cloud resolving model. Only Guan et al. (1995, 1997) used 3D thermal radiation in a cloud resolving model. Their method, however, is limited to axially symmetric cases. Accurate 3D radiative transfer models (for example MYSTIC (Mayer, 2009) or SHDOM (Evans, 1998)) are far expensive to be used in cloud resolving numerical models. The advantage of the NCA is the little extra computational costs compared to a 1D radiative transfer approximation and the ability to use it in parallelized models by only considering the neighboring columns for the calculation of the heating/cooling rates. At climate model scale, a fast 3D radiative transfer approximation of irradiance (in the solar spectral range), based on a 2-stream radiative transfer scheme was developed by Hogan and Shonk (2013). Thermal parameterizations of irradiance at GCM scale are currently developed at the ECMWF and the University of Reading.

Cloud Resolving Simulations

Two different types of cloud resolving simulations were performed, to study the effects of 1D and 3D thermal radiation on cloud development. So called bubble experiments and large scale simulation of a shallow cumulus cloud field were performed.
In a bubble experiment, the development of a single cloud is initialized by a temperature perturbation in the lower layers of the model. The warm bubble, the perturbation, causes air to rise and water vapor to condense. A single cloud forms.
Two different bubble experiments were performed. The first simulations used a axial symmetric perturbation, the second simulations used a non-symmetric perturbation, resulting in a non-symmetric cloud, which was probably the more realistic case. In both simulations, the temporal development of the resulting cloud was studied with and without the effects of 1D and 3D thermal radiation. It was shown that in both simulations, thermal radiation affects the cloud growth by increasing liquid water content in the early stage of cloud development. In the further development of the axial symmetric cloud, the cloud circulation changed. Updrafts in the cloud core and downdrafts at the cloud sides became stronger. This led, in the beginning, to an enhanced cloud growth, but finally to a faster decay of the cloud. The differences between the simulations with 1D and 3D thermal radiation were small. The effect of 3D thermal radiation strengthened the radiation effects slightly, but overall, no large differences existed. This can be due to the small cloud side surface area of the axial symmetric cloud: the main difference between 1D and 3D thermal radiative effects is the cloud side cooling, which, however is small, if cloud side surface area is small.
The more realistic, non-symmetric cloud showed a different behavior in the cloud development between the no-radiation simulation and the simulations with 1D and 3D thermal radiation. From the beginning of cloud lifetime, the cloud developed differently with 3D thermal radiation. From a certain time step on, liquid water content decreased constantly in the 3D thermal simulation, while an increase was found for the 1D thermal simulation and the no-radiation simulation. In addition, updrafts were weaker in the 3D case. It seemed that the additional cooling in the simulation with 3D thermal radiation caused a faster and stronger decay of the cloud.
The main findings are summarized in the following:

- The axially symmetric cloud and the non-symmetric cloud simulated with 1D thermal radiation showed similar differences compared to the no-radiation simulation. These differences include increased liquid water content at cloud edges, subsiding motion at the cloud edges, stronger updrafts in the cloud core, increased entrainment and the production of negative buoyancy. The cloud decayed faster in the simulation with 1D thermal radiation than in the no-radiation simulation.

- 3D radiation effects were stronger in simulation of the non-symmetric cloud compared to the axially symmetric cloud. Larger areas of cloud side cooling, resulting from larger cloud side areas were found. This led to a different development of the non-symmetric cloud in the simulation with 3D thermal radiation, compared to the simulation with 1D thermal radiation. Only small differences in the cloud development between the simulation with 1D and 3D thermal radiation were found for the axially symmetric cloud. After 50 min (after the initial development of the non-symmetric cloud), liquid water mixing ratio decreased and updraft as well as downdraft velocities were weaker in the simulation with 3D thermal radiation compared to the simulation with 1D thermal radiation for the non-symmetric cloud.

From this first simple example, it can be concluded that thermal radiation in general affects cloud formation. The effect of radiation and no-radiation was stronger than the difference between the 1D and 3D approximations.
Similar effects of thermal radiation on the development of clouds were found in former studies: Guan et al. (1997) showed increased liquid water in the cloud and enhanced downward motion if a cloud develops in interaction with (simplified 3D) thermal radiation. The subsiding shell of a cumulus cloud (downdrafts at the cloud sides) was studied for example by Heus and Jonker (2008), Jiang et al. (2006) and Small et al. (2009). While the study of Heus and Jonker (2008) investigated the subsiding shell and what causes it, the studies of Jiang et al. (2006) and Small et al. (2009) focused on the effect of aerosols in simulation and measurement data. They found that enhanced evaporative cooling due to more aerosols (and therefore smaller cloud droplets) causes additional downward motion. In the bubble experiments in this study, the aerosol concentration (that is the number of CCN) was kept constant. Therefore, thermal cooling at cloud top and cloud sides can be another effect causing the subsiding shell to develop.

Finally, large scale simulations of shallow cumulus clouds were performed. Two different simulation types were shown. Both simulation types were initialized with the same temperature and moisture sounding. In the first simulation (SC_fixed_flux), surface fluxes were kept constant during the simulation time. In the second type of simulations, the sea surface temperature was kept constant and surface fluxes were allowed to adjust (SC_fixed_SST). Both simulation types were run for 16 h. The simulations with the different radiation solvers were restarted at 4 h and 6 h, based on a 1D solar and thermal base simulation, to save computational time. The time of the restart was chosen at the moment when first cloud development occurred.
In both simulations, an effect of thermal radiation on the development of the clouds was shown. Cloud fraction, liquid water content and vertical velocities increased when thermal radiation was considered. The cloud layer and the boundary layer became deeper in both simulations.

While most variables did not show significant systematic difference between no-radiation simulation and the simulations with 1D and 3D thermal radiation, the cloud size (or horizontal extent) was larger in the simulations with interactive 3D thermal radiation. This is a clear indication that 3D thermal radiation could trigger convective organization.
In the following, the key aspects are summarized once more:

- Thermal radiation increased condensation and therefore liquid water mixing ratio of the clouds.
- Due to the enhanced condensation, latent heat was released locally, causing positive buoyancy and therefore stronger updraft velocities in the cloud cores.
- Next to the stronger upward motion in the cloud core, downward motion at the cloud sides was increased in the simulations with radiation.
- The boundary layer and clouds became deeper, which can be a result of the stronger updraft velocities, transporting more moist air to higher levels.
- More turbulence or entrainment was found in simulations with radiation.
- 3D and 1D thermal radiation did not differentiate much in most model variables, but 3D thermal radiation might accelerate convective organization.

The results from the large scale simulations are in agreement with former studies, as far as radiation results in general are concerned. An increase in turbulence was found in different studies with 1D radiation. Davies and Alves (1989) and Fu et al. (1995) showed that cooling at the cloud top is a generator for turbulence in the cloud. Fu et al. (1995) also found that the clear sky cooling enhances convection. Larson et al. (2001) showed an increased liquid water content due to thermal cooling, but on the other hand more entrainment induced by radiation which in turn decreases liquid water content. Curry and Herman (1985) also looked at the balance between latent heat release, evaporative cooling and radiative cooling in arctic stratocumulus clouds. According to them 10% of the cloud top thermal cooling can be compensated by sensible heat fluxes from below, but some cooling always remains. They also found increased convection due to radiation, and increased liquid water. Tao et al. (1996) saw an increase in relative humidity and enhanced circulation due to thermal cooling. Seifert et al. (2015) compared the development of a cloud field with a prescribed, constant cooling to the development with interactive 1D solar and thermal radiation. They found that equilibrium is reached sooner in the simulations with interactive radiation. Furthermore, similar to this study, they found more destabilization, enhanced updrafts and a deeper cloud layer in the simulations with interactive radiation. This result is interesting, for the interpretation of the results of this thesis. While the 1D and 3D radiation effects were compared to a no-radiation simulation in this thesis, the work by Seifert et al. (2015) bridges the gap, between the effects of prescribed constant cooling and interactive 1D radiation.
Finally, recent studies of Muller and Held (2012) and Muller and Bony (2015) showed that interactive thermal radiation is essential for convective organization of clouds. The results found in this thesis suggest that interactive 3D thermal radiation promotes convective organization even further.

Conclusion, Discussion and Future Work

The presented work offers by no means a full and complete study of the effect of thermal radiation on clouds. The work presented is a first step into a research area that has to be investigated further. For the first time it was possible to simulate cloud development with interactive 3D thermal radiation in a cloud resolving model. Two idealized examples of single clouds as well as two large scale simulations of a shallow cumulus cloud field have been presented. Both, the single cloud and the cloud field simulations are idealized. Never the less, they provide first useful insights into radiation cloud interactions.

It could be shown, that radiation in general affects the development of clouds and cloud fields. The effects of 3D thermal radiation were shown to increase the effect of 1D approximations. Depending on the setup, 3D radiation changes cloud development more or less. The NCA is only little more expensive than common 1D radiation approximations and could be a way to replace 1D approximations with more accurate parameterizations in cloud-resolving models.

Both, the single cloud experiments and the large scale experiments need further study and analysis. It would be interesting to repeat the single cloud simulations with different initial background states and perturbation. What would happen if updrafts are stronger? Or, if the atmosphere is less stable and the cloud is allowed to rise further to from deep convection? What happens if rain is accounted for? Also, the sensitivity due to thermal radiation could be tested. Are the changes in cloud development a mere effect of more overall cooling in simulations with 3D thermal radiation or do they depend on the location of the heating and cooling rates?

Similar question apply also to the large scale simulations. Different background profiles and the effect of rain would be interesting to study. How does the cloud field develop if the simulation is performed longer than 16 h. What happens in a completely different meteorological environment, if deeper clouds are accounted for, for example. The interaction of surface fluxes with radiation was neglected completely in this thesis, but should be considered in the future.

Solar radiation is another important component which needs investigation, in particular the combination of thermal and solar radiation. In former studies it was shown that the magnitude of the thermal radiative effect on cloud development depends on the height of the clouds in the atmosphere. Warm clouds behave differently than cold clouds. Ice clouds would be another object where the interaction of radiation with the cloud should be studied.

A more systematic study of the effects of radiation is necessary in future work. If certain effects of radiation on cloud development can be related to specific processes or situation, further development of current cloud parameterizations in weather and climate models would be possible. Parameterizations for large scale models should include systematic enhancements of cooling rates due to 3D radiative transfer effects.

Further advance in the field will require a closer coupling of the radiation to the cloud physics, in particular the microphysical scheme. To fully consider (3D) radiation, schemes beyond the often-used one- or two-moment schemes are required, for example an explicit bin model.

Appendix A

List of Abbreviations

1D	One Dimensional
3D	Three Dimensional
AGCM	Atmospheric General Circulation Model
BOMEX	Barbados Oceanographic and Meteorological Experiment
CAPE	Available Convective Potential Energy
CCL	Convective Condensation Level
CCN	Cloud Condensation Nuclei
COSMO-DE	Numerical Weather Prediction Model of the German Weather Service
CPU	Central Processing Unit
DNS	Direct Numerical Simulation
DENET	Monte Carlo Heating Rate Method, Flux Divergence (Klinger and Mayer, 2014)
DISORT	Discrete Ordinates Radiative Transfer Program for a Multi-Layered Plane-Parallel Medium (Stamnes et al., 1988)
DKRZ	Deutsches Klima Rechenzentrum
DYCOMS	Dynamics and Chemistry of Marine Stratocumulus field study
EMABS	Monte Carlo Heating Rate Method, Emission Absorption (Klinger and Mayer, 2014)
EMABS_OPT	Monte Carlo Heating Rate Method, Emission Absorption Optimized (Klinger and Mayer, 2014)
FORWARD	Foward Monte Carlo Heating Rate Method (Klinger and Mayer, 2014)
GCM	General Circulation Model
HD(CP)^2	High Definition Clouds and Precipitation Project
HYBRID	Optimized Monte Carlo Heating Rate Method (Klinger and Mayer, 2014)

ICA	Independent Column Approximation
LCL	Lifting Condensation Level
LES	Large Eddy Simulation
LMU	Ludwig Maximilians University Munich
MCSI	Monte Carlo Spectral Integration (Pincus and Stevens, 2009)
MYSTIC	Monte Carlo Code for the physically correct tracing of photons in the atmosphere
NCA	Neighboring Column Approximation
NWP	Numerical Weather Prediction
POST	Physics of Stratocumulus
RCE	Radiative Convective Equilibrium
RMSE	Root Mean Square Error
RICO	Rain in Cumulus over the Ocean field study
RTE	Radiative Transfer Equation
SC_fixed_flux	UCLA-LES Simulation of shallow cumulus cluods; fixed surface fluxes
SC_fixed_SST	UCLA-LES Simulation of shallow cumulus clouds; fixed SST
SHDOM	Spherical Harmonic Discrete Ordinate Method
TKE	Turbulent Kinetic Energy
TOA	Top of Atmosphere
UCLA-LES	University of California, Los Angeles Large Eddy Simulation Model
UTC	Coordinated Universal Time

Bibliography

Ackerman, T., K.-N., L., Valero, F., and Pfister, L. (1988). Heating rates in tropical anvils. *Journal of the Atmospheric Sciences*, 45:1606–1623.

Akansu, E. F. (2014). *Der Einfluss der Wolkengeometrie auf Wolken-Strahlungs-Wechselwirkung im thermischer Spektralbereich*. Bachelor Thesis, Fakultät für Physik der Ludwig-Maximilians-Universität München.

Anderson, G., Clough, S., Kneizys, F., Chetwynd, J., and Shettle, E. (1986). AFGL Atmospheric Constituent Profiles (0-120 km). Technical Report AFGL-TR-86-0110, AFGL (OPI), Hanscom AFB, MA 01736.

Arakawa, A. (2004). The Cumulus Parameterization Problem: Past, Present, and Future. *Journal of Climate*, 17:2493–2525.

ARM (2010). Atmospheric System Research (ASR) Science and Program Plan. U.S. Department of Energy, Office of Science.

Arrhenius, S. (1896). On the influence of carbonic acid in the air upon the temperature of the ground. *London, Edinburgh and Doublin Philosophical Magazine and Journal of Science (fifth series)*, 41:237–275.

Austin, P. H., Siems, S., and Wang, Y. (1995). Constraints on droplet growth in radiatively cooled stratocumulus clouds. *Journal of Geophysical Research*, 100(D7):14231–14242.

Barkstrom, B. R. (1978). Some effexts of 8-12μm radiant energy transfer on the mass and heat budgets of cloud droplets. *Journal of the Atmospheric Sciences*, 35:665–673.

Benassi, A., Szczap, F., Davis, A., Masbou, M., Cornet, C., and Bleuyard, P. (2004). Thermal radiative fluxes through inhomogeneous cloud fields: a sensitivity study using a new stochastic cloud generator. *Atmospheric Research*, 72:291–315.

Bohren, C. F. and Albrecht, B. A. (1998). *Atmospheric thermodynamics*. Oxford Univ. Press, New York.

Bony, S., Stevens, B., Frierson, D. M. W., Jakob, C., Kageyama, M., Pincus, R., Shepherd, T. G., Sherwood, S. C., Siebesma, A. P., Sobel, A. H., Watanabe, M., and Webb, M. J. (2015). Clouds, circulation and climate sensitivity. *Nature Geosci*, 8:261–268.

Boucher, O., Randall, D., Artaxo, P., Bretherton, C., Feingold, G., Forster, P., Kerminen, V.-M., Kondo, Y., Liao, H., Lohmann, U., Rasch, P., Satheesh, S., Sherwood, S., Stevens, B., and Zhang, X. (2013). Clouds and aerosols. In Climate Change 2013: The Physical Science Basis. Contribution of Working Group I to the Fifth Assessment Report of the Intergovernmental Panel on Climate Change. pages 571–657. Cambridge University Press.

Brewster, M. (2015). Evaporation and condensation of water mist/cloud droplets with thermal radiation. *International Journal of Heat and Mass Transfer*, 88:695 – 712.

Bronstein, I., Semendjajew, K., Musiol, G., and Mühlig, H. (2006). *Taschenbuch der Mathematik*, volume 6. Verlag Harri Deutsch.

Buras, R., Dowling, T., and Emde, C. (2011). New secondary-scattering correction in disort with increased efficiency for forward scattering. *J. Quant. Spectrosc. Radiat. Transfer*, 112:2028–2034.

Cahalan, R., McGill, M., Kolasinski, J., Varnai, T., and Yetzer, K. (2005). THOR – Cloud Thickness from Offbeam Lidar Returns. *Journal of Atmospheric and Oceanic Technology*, 22:605–627.

Chandrasekhar, S. (1950). *Radiative transfer*. Oxford Univ. Press, London, UK.

Cheng, A., Xu, K.-M., and Stevens, B. (2010). Effects of resolution on the simulation of boundary-layer clouds and the partition of kinetic energy to subgrid scales. *Journal of Advances in Modeling Earth Systems*, 2(1).

Curry, J. A. and Herman, G. F. (1985). Infrared radiative properties of Arctic stratus clouds. *J. Clim. Appl. Met.*, 24:525–538.

Davies, R. and Alves, A. (1989). Flux divergence of thermal radiation within stratiform clouds. *Journal of Geophysical Research*, 94(D13):16277–16286.

Ellingson, R. (1982). On the effects of cumulus dimensions on longwave irradiance and heating rate calculations. *Journal of the Atmospheric Sciences*, 39:886–896.

Ellingson, R. and Kolczynski, E. (1980). Cumulus clouds and infrared heating of the atmosphere. In Vonder Haar, T. V., editor, *Volume of Extended Abstracts of the 1980 International Radiation Symposium*, pages 474–476. Dept. Atmos. Sci, Colorado State University, Fort Collins.

Evans, K. (1998). The spherical harmonics discrete ordinate method for three-dimensional atmospheric radiative transfer. *Journal of the Atmospheric Sciences*, 55:429–446.

Fourier, J. (1824). Remarques Générales Sur Les Températures Du Globe Terrestre Et Des Espaces Planétaires. *Annales de Chimie et du Physique*, 27:136–167.

Fu, Q., Krueger, S., and Liou, K. (1995). Interactions of radiation and convection in simulated tropical cloud clusters. *Journal of the Atmospheric Sciences*, 52:1310–1328.

Fu, Q. and Liou, K. (1992). On the correlated k-distribution method for radiative transfer in nonhomogeneous atmospheres. *Journal of the Atmospheric Sciences*, 49:2139–2156.

Gerber, H., Frick, G., Malinowski, S. P., Jonsson, H., Khelif, D., and Krueger, S. K. (2013). Entrainment rates and microphysics in POST stratocumulus. *Journal of Geophysical Research: Atmospheres*, 118(21):12,094–12,109.

Gerber, H., Malinowski, S. P., Bucholtz, A., and Thorsen, T. (2014). Radiative cooling of stratocumulus. AMS 14th Conference, Atmospheric Radiation.

Gödde, F. (2015). *Einfluss thermischer Strahlung auf das Wachstum von Wolkentröpfchen*. Bachelor Thesis, Fakultät für Physik der Ludwig-Maximilians-Universität München.

Goody, R., West, R., Chen, L., and Crisp, D. (1989). The correlated-k method for radiation calculations in non-homogeneous atmospheres. *J. Quant. Spectrosc. Radiat. Transfer*, 42:539–550.

Gu, Y. and Liou, K. N. (2000). Interactions of radiation, microphysics, and turbulence in the evolution of cirrus clouds. *Journal of the Atmospheric Sciences*, 57:2463–2479.

Guan, H., Davies, R., and Yau, M. (1995). Longwave radiative cooling rates in axially symmetric clouds. *Journal of Geophysical Research*, 100(D3):3213–3220.

Guan, H., Yau, M., and Davies, R. (1997). The Effects of Longwave Radiation in a Small Cumulus Cloud. *Journal of the Atmospheric Sciences*, 54:2201–2214.

Han, D. and Ellingson, R. (1999). Cumulus cloud formation for longwave radiation calculation. *Journal of the Atmospheric Sciences*, 56:837–851.

Harrington, J., Feingold, G., and Cotton, W. (2000). Radiative Impacts on the Growth of a Population of Drops within Simulated Summertime Arctic Stratus. *Journal of the Atmospheric Sciences*, 57:766–785.

Harshvardhan and Weinman, J. (1982). Infrared radiative transfer through a regular array of cuboidal clouds. *Journal of the Atmospheric Sciences*, 39:431–439.

Harshvardhan, Weinman, J., and R., D. (1981). Transport of infrared radiation in cuboidal clouds. *Journal of the Atmospheric Sciences*, 38:2500–2513.

Hartman, C. and Harrington, J. (2005a). Radiative impacts on the growth of drops within simulated marine stratocumulus. Part I: Maximum solar heating. *Journal of the Atmospheric Sciences*, 62:2323–2338.

Hartman, C. and Harrington, J. (2005b). Radiative impacts on the growth of drops within simulated marine stratocumulus. Part II: Solar zenith angle variations. *Journal of the Atmospheric Sciences*, 62:2339–2351.

Heidinger, A. and Cox, S. (1996). Finite-cloud effects in longwave radiative transfer. *Journal of the Atmospheric Sciences*, 53:953–963.

Heinze, R., Moseley, C., Böske, L., Raasch, S., and Stevens, B. (2015). Evaluation of large eddy simulations forced with mesoscale model output for a period during hope. *Atmos. Chem. Phys.*, page in preparation.

Heus, T. and Jonker, H. J. J. (2008). Subsiding shells around shallow cumulus clouds. *Journal of the Atmospheric Sciences*, 65:1003–1081.

Heymsfield, A. J., Miloshevich, L. M., Slingo, A., Sassen, K., and Starr, D. O. (1991). An observational and theoretical study of highly supercooled altocumulus. *Journal of the Atmospheric Sciences*, 48:923–945.

Hogan, R. J. and Shonk, J. K. P. (2013). Incorporating the effects of 3d radiative transfer in the presence of clouds into two-stream multilayer radiation schemes. *Journal of the Atmospheric Sciences*, 70:788–724.

Holton, J. R., editor (2003). *Encyclopedia of Atmospheric Sciences*. Academic Press, Oxford.

Houze, R. A., J. (1993). *Cloud Dynamics*. Academic Press, Inc.

Hu, Y. X. and Stamnes, K. (1993). An accurate parameterization of the radiative properties of water clouds suitable for use in climate models. *Journal of Climate*, 6:728–742.

Jakub, F. and Mayer, B. (2015a). A three-dimensional parallel radiative transfer model for atmospheric heating rates for use in cloud resolving models – The TenStream solver. *Journal of Quantitative Spectroscopy and Radiative Transfer*, 163(0):63 – 71.

Jakub, F. and Mayer, B. (2015b). 3-D radiative transfer in large-eddy simulations – experiences coupling the TenStream solver to the UCLALES. *Geoscientific Model Development Discussions*, 8(10):9021–9043.

Jiang, H., Xue, H., Teller, A., Feingold, G., and Levin, Z. (2006). Aerosol effects on the lifetime of shallow cumulus. *Geophysical Research Letters*, 33. L14806.

Joseph, J., Wiscombe, W., and Weinman, J. (1976). The Delta-Eddington approximation for radiative flux transfer. *Journal of the Atmospheric Sciences*, 33:2452–2459.

Kablick, G., Ellingson, R., Takara, E., and Gu, J. (2011). Longwave 3D Benchmarks for Inhomogeneous Clouds and Comparisons with Approximate Methods. *Journal of Climate*, 24:2192–2205.

Kato, S., Ackerman, T., Mather, J., and Clothiaux, E. (1999). The k-distribution method and correlated-k approximation for a shortwave radiative transfer model. *J. Quant. Spectrosc. Radiat. Transfer*, 62:109–121.

Khain, A. P., Beheng, K. D., Heymsfield, A., Korolev, A., Krichak, S. O., Levin, Z., Pinsky, M., Phillips, V., Prabhakaran, T., Teller, A., van den Heever, S. C., and Yano, J.-I. (2015). Representation of microphysical processes in cloud-resolving models: Spectral (bin) microphysics versus bulk parameterization. *Reviews of Geophysics*, 53(2):247–322.

Kirchhoff, G. (1890). Über das Verhältniss zwischen dem Emissionsvermögen und dem Absorptionsvermögen der Körper für Wärme und Licht. *Annalen der Physik und Chemie*, 109:275–301.

Klinger, C. and Mayer, B. (2014). Three-dimensional Monte Carlo calculation of atmospheric thermal heating rates . *Journal of Quantitative Spectroscopy and Radiative Transfer*, 144:123 – 136.

Klinger, C. and Mayer, B. (2016). The Neighboring Column Approximation (NCA) - A fast approach for the calculation of 3D thermal heating rates in cloud resolving models . *Journal of Quantitative Spectroscopy and Radiative Transfer*, 168:17 – 28.

Köhler, H. (1936). The nucleus in and the growth of hygroscopic droplets. *Trans.Faraday Soc.*, 32:1152 – 1161.

Kourganoff, V. (1952). *Basic Methods in Transfer Problems*. Oxford, England: Clarendon Press.

Lábó, E. and Geresdi, I. (2016). Study of longwave radiative transfer in stratocumulus clouds by using bin optical properties and bin microphysics scheme. *Atmospheric Research*, 167:61 – 76.

Larson, V. E., Fleishauer, R. P., Kankiewicz, J. A., Reinke, D. L., and Vonder Haar, T. H. (2001). The death of an altocumulus cloud. *Geophysical Research Letters*, 28(13):2609–2612.

Lebo, Z. J., Johnson, N. C., and Harrington, J. Y. (2008). Radiative influences on ice crystal and droplet growth within mixed-phase stratus clouds. *Journal of Geophysical Research*, 113(D9). D09203.

Liou, K. (2002). *An Introduction to Atmospheric Radiation*, volume 84 of *International Geophysics*. Academic Press.

Liou, K. and Ou, S. (1979). Infrared radiative transfer in finite cloud layers. *Journal of the Atmospheric Sciences*, 36:1985–1892.

Liou, K.-N. (1973). A numerical experiment on Chandrasekhar's discrete-ordinat method for radiaitve transfer: Applications to cloudy and hazy atmospheres. *Journal of Applied Meteorology*, 30:1303–1326.

Liou, K.-N., Fu, Q., and Ackerman, T. (1988). A simple formulation of the delta-four-stream approximation for radiative transfer parameterizations. *Journal of the Atmospheric Sciences*, 45(13):1940–1947.

Liu, H., Wang, P. K., and Schlesinger, R. E. (2003). A Numerical Study of Cirrus Clouds. Part II: Effects of Ambient Temperature, Stability, Radiation, Ice Microphysics, and Microdynamics on Cirrus Evolution. *Journal of the Atmospheric Sciences*, 60:1097–1119.

Markowski, P. and Harrington, J. (2005). A simulation of a supercell thunderstorm with emulated radiative cooling beneath the anvil. *Journal of the Atmospheric Sciences*, 62:2607–2617.

Marquis, J. and Harrington, J. (2005). Radiative influences on drop and cloud condensation nuclei equilibrium in stratocumulus. *Journal of Geophysical Research*, 110(D10):doi:10.1029/2004JD005401.

Marshak, A. and Davis, A., editors (2005). *3D radiative transfer in cloudy atmospheres*. Springer, Berlin, Heidelberg, New York.

Mason, B. (1960). The evolution of droplet spectra in stratus clouds. *J. Meteor.*, 17:459–462.

Mayer, B. (2009). Radiative transfer in the cloudy atmosphere. *European Physical Journal Conferences*, 1:75–99.

Mayer, B. and Kylling, A. (2005). Technical Note: The libRadtran software package for radiative transfer calculations: Description and examples of use. *Atmos. Chem. Phys.*, 5:1855–1877.

McDonald, J. E., editor (1958). *The physics of cloud modification*, volume 5 of *Advances in Geophysics*. Academic Press Inc., New York.

Mechem, D. B., Kogan, Y. L., Ovtchinnikov, M., Davis, A., Evans, K., and Ellingson, R. (2008). Multi-Dimensional Longwave Forcing of Boundary Layer Cloud Systems. *Journal of the Atmospheric Sciences*, 65:3963–3977.

Mlawer, E., Taubman, S., Brown, P., Iacono, M., and Clough, S. (1997). Radiative transfer for inhomogeneous atmospheres: RRTM, a validated correlated-k model for the longwave. *Journal of Geophysical Research*, 102(D14):16663–16682.

Muller, C. and Bony, S. (2015). What favors convective aggregation and why? *Geophysical Research Letters*, 42(13):5626–5634. 2015GL064260.

Muller, C. J. and Held, I. M. (2012). Detailed investigation of the self-aggregation of convection in cloud-resolving simulations. *Journal of the Atmospheric Sciences*, 69:2551–2565.

O'Hirok, W. and Gautier, C. (2005). The impact of model resolution on differences between independent column approximation and Monte Carlo estimates of shortwave surface irradiance and atmospheric heating rate. *Journal of the Atmospheric Sciences*, 62:2939–2951.

Petters, J., Harrington, J., and Clothiaux, E. (2012). Radiativedynamical feedbacks in low liquid water path stratiform clouds. *Journal of the Atmospheric Sciences*, 69:14981512.

Pincus, R. and Stevens, B. (2009). Monte carlo spectral integration: A consistent approximation for radiative transfer in large eddy simulations. *Journal of Advances in Modeling Earth Systems*, 1.

Planck, M. (1901). Über das Gesetz der Energieverteilung im Normalspektrum. *Annalen der Physik*, 4:533 ff.

Ramaswamy, V.and Detwiler, A. (1986). Interdependence of radiation and microphysics in cirrus clouds. *Journal of the Atmospheric Sciences*, 143:2289–2301.

Roach, W. T. (1976). On the effect of radiative exchange on the growth by condensation of a cloud or fog droplet. *Quart. J. Roy. Meteor.*, 102:361–372.

Rogers, R. (1979). *Short Course in Cloud Physics (Monographs in Natural Philosophy)*. Pergamon Press.

Schumann, U., Dörnbrack, A., and Mayer, B. (2002). Cloud-shadow effects on the structure of the convective boundary layer. *Meteorologische Zeitschrift*, 11(4):285–294.

Seifert, A. and Beheng, K. D. (2001). A double-moment parameterization for simulating autoconversion, accretion and self collection. *Atmos. Res.*, 59-60:256–382.

Seifert, A., Heus, T., Pincus, R., and Stevens, B. (2015). Large-eddy simulation of the transient and near-equilibrium behavior of precipitating shallow convection. *Journal of Advances in Modeling Earth Systems*, pages n/a–n/a.

Smagorinsky, J. (1963). General circulation experiments with the primitive equations. *Monthly Weather Review*, 93(3).

Small, J., Chuang, Y., Feingold, G., and Jiang, H. (2009). Can aerosol decrease cloud lifetime? *Geophysical Research Letters*, 36. L16806.

Smith, A. J., Larson, V. E., Niu, J., Kankiewicz, J. A., and Carey, L. D. (2009). Processes that generate and deplete liquid water and snow in thin midlevel mixed-phase clouds. *Journal of Geophysical Research*, 114(D12).

Sommerai, G. (1976). Three-dimensional simulation of turbulent processes in an undisturbed trade wind boundary layer. *Journal of the Atmospheric Sciences*, 33:216–241.

Stamnes, K., Tsay, S., Wiscombe, W., and Jayaweera, K. (1988). A numerically stable algorithm for discrete-ordinate-method radiative transfer in multiple scattering and emitting layered media. *Applied Optics*, 27(12):2502–2509.

Stephens, G. (1978). Radiation profiles in extended water clouds. II: Parameterization schemes. *Journal of the Atmospheric Sciences*, 35:2123–2132.

Stephens, G. L. (1983). The Influence of Radiative Transfer on the Mass and Heat Budgets of Ice Crystals Failing in the Atmosphere. *Journal of the Atmospheric Sciences*, 40:1729–1739.

Stevens, B. (2007). On the growth of layers of non-precipitating cumulus convection. *J. Atmos. Sci*, 64:2916–2931.

Stevens, B., Moeng, C., Ackerman, A., Bretherton, C., Chlond, A., De Roode, S., Edwards, J., Golaz, J., Jiang, H., Khairoutdinov, M., Kirkpatrick, M., Lewellen, D., Lock, A., Muller, F., Stevens, D., Whelan, E., and Zhu, P. (2005). Evaluation of large-eddy simulations via observations of nocturnal marine stratocumulus. *Mon. Weather Rev.*, 133:1443–1462.

Takara, E. and Ellingson, R. (1996). Scattering effects on longwave fluxes in broken cloud fields. *Journal of the Atmospheric Sciences*, 53:1464–1476.

Takara, E. and Ellingson, R. (2000). Broken cloud field longwave-scattering effects. *Journal of the Atmospheric Sciences*, 57:1298–1310.

Tao, W.-K., Lang, S., Simpson, J., Sui, C. H., Ferrier, B., and Chou, M. D. (1996). Mechanisms of cloud-radiation interaction in the tropics and midlatitudes. *Journal of the Atmospheric Sciences*, 53:2624–2651.

Tao, W.-K., Simpson, J., Sui, C. H., Ferrier, B., Lang, S., Scala, J., Chou, M. D., and Pickering, K. (1993). Heating, moisture, and water budgets of tropical and midlatitude squall lines: comparisons and sensitivity to longwave radiation. *Journal of the Atmospheric Sciences*, 50:673–690.

Taylor, F. W. (2005). *Elementary Climate Physics*. Oxford Univ. Press, London, UK.

Trenberth, K., Fasullo, J., and Kiehl, J. (2009). Earth's Global Energy Budget. *Bulletin of the American Meteorological Society*, 90:311–323.

van Zanten, M., Stevens, B., Nuijens, L., Siebesma, A., Ackerman, A., Burnet, F., Cheng, A., Couvreux, F., Jiang, H., Khairoutdinov, M., Kogan, Y., Lewellen, D., Mechem, D., Nakamura, K., Noda, A., Shipway, B., Slawinska, J., Wang, S., and Wyszogrodzki, A. (2011). A., Shipway, B., Slawinska, J., Wang, S., and Wyszogrodzki, A.: Controls on precipitation and cloudiness in simulations of trade-wind cumulus as observed during RICO. *J. Adv. Model. Earth Syst.*, 3.

von Helmholtz, H. (1853). Über einige Gesetze der Vertheilung elektrischer Ströme in körperlichen Leitern, mit Anwendung auf die thierisch-elektrischen Versuche. *Annalen der Physik und Chemie*, 89:211–233, 353–377.

Wapler, K. (2007). *Der Einfluss des dreidimensionalen Strahlungstransportes auf Wolkenbildung und -entwicklung*. PhD thesis, Fakultät für Physik der Ludwig-Maximilians-Universität München.

Wapler, K. and Mayer, B. (2008). A fast method for the three-dimensional calculation of surface irradiance within a cloud resolving model. *Journal of Applied Meteorology and Climatology*, 47:3061–3071.

Wißmeier, U. and Buras, R. (2012). Accounting for 3D-effects in 1D-radiative transfer calculations in the solar spectral range. *In preparation*.

World Meteorological Organization, editor (1975). *International Cloud Atlas. Volume I – Manual on the observation of clouds and other meteors*. WMO.

Xu, K.-M. and Randall, D. A. (1995). Impact of interactive radiative transfer on the macroscopic behavior of cumulus ensembles. Part II: Mechanisms for cloud-radiation interactions. *Journal of the Atmospheric Sciences*, 52:800–817.

Yamaguchi, T. and Randall, D. A. (2012). Cooling of entrained parcels in a large-eddy simulation. *Journal of the Atmospheric Sciences*, 69:1118–1136.

Yano, J.-I. (2014). Basic convective element: bubble or plume? a historical review. *Atmospheric Chemistry and Physics*, 14(13):7019–7030.

Zdunkowski, W., Trautmann, T., and Bott, A. (2007). *Radiation in the atmosphere - A course in theoretical meteorology*. Cambridge University Press.

Acknowledgments

First, I want to thank my supervisor Prof. Dr. Bernhard Mayer for constant support and advice, many helpful discussion, guideline and motivation. His help contributed significantly to this work.

Furthermore, I want to thank Prof. Dr. Markus Rapp for reviewing this thesis as coexaminer.

I am also grateful to Fabian Jakub for many helpful discussions about the work during the last three and a half years, his help by setting up the UCLA-LES at DKRZ, by implementing the NCA into ULCA-LES and for his support in the last weeks of finishing. Furthermore, I want to thank Claudia Emde and Leonhard Scheck for the internal reviews of the papers. Claudia Emde, Tobias Zinner and Christoph Knote are acknowledged for helpful discussions. Elisa Akansu, Felix Gödde and Annette Schütt shall be mentioned. Elisa and Felix contributed directly to this work with their Bachelor theses. Annette already started with future work. I had a lot of fun and learned a lot while supervising them.
A big thanks goes to Bjorn Stevens and Raphaela Vogel for help and advice in setting up the UCLA-LES simulations and to Louise Nuijens and Gerard Kilroy for help with the interpretation of the UCLA-LES simulation results. Rieke Heinze and Christopher Moseley are acknowledged for providing the UCLA-LES simulation data from the HD(CP)^2 prototype simulations which were used for evaluating the NCA.
Also, I'd like to thank my colleagues at the Meteorological Institute at LMU for the friendly working environment. Especially the colleagues from the "Lehrstuhl of Experimentelle Meteorologie". Discussions in the "Strahlungstreffen" were always helpful in proceeding this work.

Special thanks go to my friends. Two shall be mentioned by name: Judith Mittag and Viviane Nowotny.

Finally, I would also like to thank my family for constant support, especially my parents Marianne and Walter and my brother Maximilian.

This work was funded by the Federal Ministry of Transport, Building and Urban Development (BMVBS) through the German Weather Service (Extramurales Forschungsprojekt FKZ 8), the Federal Ministry of Education and Research (BMBF) through the High Definition Clouds and Precipitation for Climate Prediction (HD(CP)^2) project (FKZ: 01LK1208A) and the DFG Transregio 165 "Waves to Weather".